# Thermodynamics and Transport in Fermi Gases near Unitarity

Dissertation

vorgelegt von

Bernhard Frank

November 2018

Physik Department T34
Technische Universität München

Technische Universität München

Physik Department
Lehrstuhl T34, Prof. Dr. Wilhelm Zwerger

# Thermodynamics and Transport in Fermi Gases near Unitarity

Bernhard Otto Frank

Vollständiger Abdruck der von der Fakultät für Physik der Technischen Universität München zur Erlangung des akademischen Grades eines

Doktors der Naturwissenschaften (Dr. rer. nat.)

genehmigten Dissertation.

| | |
|---|---|
| Vorsitzender: | Prof. Dr. Peter Böni |
| Prüfer der Dissertation: | 1. Prof. Dr. Wilhelm Zwerger |
| | 2. Prof. Dr. Matthias Punk (Ludwigs-Maximilians-Universität München) |

Die Dissertation wurde am 22.11.2018 bei der Technischen Universität München eingereicht und durch die Fakultät für Physik am 09.01.2019 angenommen.

**Abstract**

In this thesis, we address the thermodynamics and the phase diagram of the BCS-BEC crossover in the presence of spin imbalance at by a Luttinger-Ward approach. The latter gives rise to a Schwinger-Dyson equation for the interacting fermionic Green's function $G$, that we numerically solve within the ladder approximation in a fully self-consistent manner. $G$ allows to compute all thermodynamic quantities and therefore to obtain quantitative results for the universal scaling functions associated with the strong-coupling fixed point of the unitary Fermi gas at zero density, discussed by Nikolič and Sachdev [1]. Apart from the transition to a homogeneous superfluid, we observe the instability to an FFLO state characterized by an order-parameter that varies periodically in space and whose phase boundary extends from the BCS-side of the crossover to the unitary limit. This result agrees with the qualitative picture obtained by Son and Stephanov [2] within an effective field theory approach. Solving the self-consistent equations requires an efficient numerical Fourier transformation of functions varying over many orders of magnitude. To accomplish that task we use a combination of a logarithmic and a spline-interpolated, discrete Fourier transform and a specifically-designed subtraction scheme for the known analytic asymptotics. Finally, we consider transport properties of the unitary gas in the quantum critical regime above the quantum critical point. In particular, the heat conductivity is computed by a large-N approach and we compare the shear viscosity with universal quantum bounds.

**Zusammenfassung**

In dieser Arbeit wird der Einfluss von Spinungleichgewicht auf das Phasendiagram und die Thermodynamik des BCS-BEC Crossovers untersucht. Dazu wird der Luttinger-Ward Formalismus verwendet, aus dem wir, innerhalb der Leiternäherung eine Schwinger-Dyson Gleichung für die Greensche Funktion $G$ der Fermionen ableiten und selbstkonsistent lösen. Mithilfe von $G$ berechnen wir die thermodynamischen Größen und erhalten quantitative Ergebnisse für die universellen Skalenfunktionen, die mit dem stark wechselwirkenden RG Fixpunkt des unitären Gases bei verschwinder Dichte, welcher von Nikolič und Sachdev [1] beschrieben worden ist, verknüpft sind. Neben dem Übergang zur räumlich homogenen Supraflüssigkeit finden wir auch eine FFLO-Phase, die durch einen periodischen Ordnungsparameter charakterisiert ist. Diese erstreckt sich bei sehr niedrigen Temperaturen von der BCS-Seite des Crossovers bis hin zum stark wechselwirkenden unitären Grenzfall. Diese Resultat steht im Einklang mit dem Bild von Son und Stephanov [2], welches auf einer effektiven Feldtheorie beruht. Die selbstkonsistente Lösung benötigt eine effiziente, numerische Fouriertransformation von Funktionen, die über viele Größenordnungen variieren. Dazu verwenden wir eine Kombination aus einer logarithmischen und einer diskreten Fouriertransformation und subtrahieren die führende analytische Asymptotik in hinreichend hoher Ordnung. Abschließend betrachten wir Transporteigenschaften des unitären Fermigases im quantenkritischen Regime über dem quantenkritischen Punkt. Insbesondere berechnen wir die Wärmeleitfähigkeit des unitären Fermigases mit Hilfe einer large-N Entwicklung und vergleichen die Scherviskosität mit universellen, quantenmechanischen Schranken.

# Contents

# List of Figures

# Chapter 1

# Introduction

The experimental achievement of cooling trapped fermionic atom clouds at JILA [3], Innsbruck [4] and MIT [5] below the threshold for the condensation of molecules formed by fermionic pairs in the year 2003, added a new chapter to the story of fermionic superfluidity, which had begun almost a century ago in 1911, when Kammerlingh Onnes [6] discovered superconductivity in Hg below temperatures of 4.19 K. While conventional superconductors are well described by the BCS theory [7] of Bardeen, Cooper and Schrieffer in terms of a coherent state formed by electronic Cooper pairs [8], the observation of superconductivity above 30 K in the ceramic compound La-Ba-Cu-O by Bednorz and Müller [9] opened the route to novel superconducting systems and increasingly higher critical temperatures. Currently, $H_2S$ holds the record of the highest transition temperature ever achieved with $T_c = 203\,\mathrm{K}$ [10], however, it requires the enormous pressure of 155 GPa. In contrast, at ambient pressure the largest known $T_c = 133\,\mathrm{K}$ [11] has been realized in the cuprate Hg-Ba-Ca-Cu-O. So far, these systems unfortunately lack a complete theoretical description [12].

The motivation to study superfluidity also in ultracold fermionic atoms relies on the unique properties of these systems. They provide the only neutral condensed matter example for fermionic superfluids, apart from $^3$He, where the phase transition takes place in the mK regime, as observed by Osherhoff et al. [13, 14] in 1972 (for an overview see Ref. [15]). In particular, at ultralow temperatures the mutual interactions of the atoms can be described in terms of the scattering length $a$ [16, 17] only. Quite importantly, the latter can be adjusted freely by Feshbach resonances [18]. Moreover, the standard model Hamiltonian of an instantaneous, zero-range interaction due to Gorkov applies in quantitative terms. As was first considered by Eagles [19] and Leggett [20] in the ground state, this enables one to realize the BCS-BEC crossover from a superfluid of Cooper pairs in the presence of weak attractive interactions to the Bose-Einstein condensate of tightly bound diatomic molecules at very strong attractions. In addition, the corresponding finite-temperature transition to a normal state has first been discussed by Nozières and Schmidt-Rink [21]. Furthermore, the gas at resonance, where the scattering cross section becomes unitarily limited due to the divergence $|a| \to \infty$, realizes a novel strong-coupling RG fixed point, as observed by Nikolič and Sachdev [1]. This quantum critical point gives rise to a universal thermodynamic phase-diagram. The scale

invariance of the unitary gas, which was first implicitly noted by Ho [22], is related to the fact that the unitary gas exhibits both scale and conformal invariance in addition to the Galilean invariance, as was shown by Nishida and Son [23]. Quite remarkably, this entails scaling laws not only for thermodynamic quantities but even for transport coefficients.

Another interesting direction for investigations is provided by the fermionic spin degree of freedom. In particular, the response to a population imbalance of the allowed spin orientations or equivalently a Zeeman field $h$, which couples only to the spin, has been addressed soon after the advent of BCS theory in 1957. In 1962 Clogston [24] and Chandrasekhar [25] found that the spin-balanced BCS ground state is stabilized by its excitation gap $\Delta_0$ against values of $h$ below the critical field $h_c = \Delta_0/\sqrt{2}$ but turns normal again for larger $h$. While Sarma [26] investigated the $T > 0$ case, Fulde and Ferrell [27] and independently Larkin and Ovchinnikov [28] showed that the transition to the normal phase is actually preempted by a new kind of superfluid state. This FFLO-state is characterized by a periodically modulated order-paramter, where the Cooper pairs acquire a finite center-of-mass momentum. Unfortunately, the orbital effects of the electronic motion usually prevent the study of Zeeman fields in bulk superconductors, which is why lower dimensional organic superconductors [29] with in-plane magnetic fields are considered as promising candidates for the detection of FFLO-type order. Neutral fermionic atoms in turn allow to control the densities of the hyperfine states individually, which led to the first experimental studies by Patridge et al. [30, 31] and Zwierlein [32] on spin-imbalanced ultracold atom samples in the strong-coupling regime. Furthemore, Shin et al. have observed the Clogston-Chandraskhar(CC) limit at the Feshbach resonance by phase-contrast imaging of a trapped gas [33, 34], as well as the equation of state [35]. More recently the CC threshold of the unitary gas has also been investigated by Navon et al. [36]. From the theoretical perspective Son and Stephanov [2] developed a qualitative, yet very complete picture for the ground state of the BCS-BEC crossover in the presence of finite spin-imbalance in terms of an effective field theory. The latter predicts, besides the balanced superfluid at small $h$ and the trivial fully-polarized gas at large $h$, several partially polarized superfluid phases. In particular, it includes an FFLO-phase, which extends beyond the unitary limit onto the bosonic side of the crossover.

Our aim in the present thesis is to extend a previous Luttinger-Ward study of the balanced BCS-BEC crossover by Haussmann et al. [37] to the presence of Zeeman fields and to obtain a quantitative description of the phase diagram. This diagrammatic method includes the effects of strong interactions by resumming particle-particle ladders, responsible for the transition to the symmetry-broken phase, to arbitrary order. Quite importantly, we solve the resulting Schwinger-Dyson equation for the fermionic single-particle Green's function fully self-consistently, without incorporating further approximations and use the Tan relations [38–40] as a consistency check. Apart from thermodynamics, we also consider transport properties of the unitary gas. In this regard, we discuss the shear viscosity $\eta$ and the quantum

bounds appearing in universal ratios $\eta/s$ and $\eta/n$, where $s$ denotes the entropy density and $n$ the total density. Finally, we perform a large-N expansion to compute the heat conductivity

The thesis is organized as follows: In Chapter 2 we review the standard description of interactions in ultracold atomic systems and focus in particular on Feshbach resonances before we turn to the universal phase diagram of the imbalanced Fermi gas in the ground state in Chapter 3. In Chapter 4 we set up the Luttinger-Ward formalism. Moreover, we introduce the particle-particle ladder approximation for the interactions and the resulting Schwinger-Dyson equation for the fermionic Green's function, as well as the vertex function. We show the results for the phase diagram and the thermodynamic quantities in Chapter 5. The following two chapters are dedicated to the numerical solution of the Schwinger-Dyson equation. Chapter 6 presents the two kinds of Fourier transformations that we use: a logarithmic one and a discrete one in combination with a spline interpolation, while Chapter 7 summarizes how we subtract the analytically known asymptotics of the Green's and vertex functions. In addition, we develop a similar subtraction for the expressions of the pressure, the internal energy and the entropy. Then we turn to transport in Chapter 8, before we close the thesis with an outlook on how the Luttinger-Ward computations can be extended to capture also the symmetry-broken phase in Appendix A.

A list of the papers that have been published during this PhD-project can be found in Appendix E.

# Chapter 2

# Many-body physics with ultracold Fermions

This chapter summarizes the framework that underlies the description of the physics encountered in ultracold fermionic atoms. In Section 2.1 we start with an overview how to formulate the interactions at the two-particle level in ultracold quantum gases and how Feshbach resonances can be used to adjust the scattering properties. In Sec. 2.2 we introduce the single-channel model and the related renormalization scheme, which provides the central basis for the remainder of the thesis. Afterwards, in Sec. 2.3 we present the results for the BCS-BEC crossover that have been obtained so far, thereby relating the thesis with previous work and motivating the study on spin imbalance, presented here. Finally, we review the Tan relations in Sec. 2.4, which give rise to a convenient way to present thermodynamics and also will play an important role in the evaluation of our data.

## 2.1 Interactions in ultracold gases and Feshbach resonances

This chapter provides a summary of the well-established effective theory for ultracold interactions [16, 17] in terms of the scattering length $a$, which underlies many phenomena in the entire field of ultracold atoms [41]. Furthermore, we introduce the concept of Feshbach resonances and the related tunability of the interaction strength. An in-depth review on this special topic has been provided by Chin et. al. [18]. Finally, we take a short detour and consider the stability of strongly attractive Fermion systems at finite density, which also touches the interaction properties of bound dimers. We follow the lectures by Zwerger [42], where further details can be found.

### 2.1.1 Two-body scattering of ultracold atoms

In general, a gas is a low-density system, where the mean spacing between particles $\sim n^{-1/3}$ is much larger than the range of the interaction potential. Consequently, the many-body Hamiltonian can be restricted to include a sum of two-body interactions only. However, at very low temperatures one automatically enters the regime of a degenerate gas, which is characterized by $n\lambda_T^3 \gg 1$, with the thermal de

Broglie wavelength $\lambda_T = \hbar\sqrt{2\pi/(mT)}$. Here $\hbar$ denotes the reduced Planck's constant, $m$ the particle mass and $T$ the temperature, while we have set the Boltzmann constant to unity. Physically, this criterion implies that the atoms cannot be considered anymore as individual, point-like particles, since the associated quantum wave packets overlap and therefore quantum mechanical scattering theory has to be applied. At large separations, neutral atoms interact with a van der Waals force, due to spontaneously induced dipole-dipole interactions. They yield an attractive two-body potential of the form

$$V_{\mathrm{vdW}}(r) = -C_6/r^6\,, \tag{2.1}$$

when the atoms are far apart. The positive coefficient $C_6$, depends on the chemical element. The corresponding values of the experimentally relevant alkali atoms are listed in Ref. [16]. In turn, the short-distance behavior constitutes a genuine many-body problem, since it includes all the electronic degrees of freedom of the two atoms that participate in the scattering process. Consequently, it is hard to determine $V(r \to 0)$ a priori from theoretical considerations. However, in the situation $k_F r_e \ll 1$ and $k_{\mathrm{th}} r_e \ll 1$, where $k_F$ denotes the Fermi wave vector[1] $k_F \simeq n^{1/3}$, $k_{\mathrm{th}} \simeq 1/\lambda_T$ the typical thermal momentum and $r_e$ the effective range introduced in eq. 2.4 below, one can deploy a description based on an effective interaction. The latter does not require a precise knowledge of the complete potential, yet leads to a very simple characterization of the interactions in terms of a single parameter. To obtain such a simplified description, we first note that the asymptotics of $V_{\mathrm{vdW}}$ gives rise to an intrinsic length scale, called van der Waals length

$$l_{\mathrm{vdW}} = \frac{1}{2}\left(\frac{mC_6}{\hbar^2}\right)^{1/4} \tag{2.2}$$

and a related van der Waals energy $E_{\mathrm{vdW}} = \hbar^2/(m l_{\mathrm{vdW}}^2)$. In general, the range of the interactions is on the order of $l_{\mathrm{vdW}}$, as we will see below. Thus, we find a separation of length scales

$$l_{\mathrm{vdW}} \ll n^{-1/3} \ll \lambda_T\,, \tag{2.3}$$

which defines the ultracold regime of dilute quantum gases. Under these conditions all but the s-wave scattering channel are frozen out due to the angular momentum barrier. The latter is determined by the potential range and accordingly is on the order of the van der Waals energy, which exceeds the thermal energy by far. The associated quantum mechanical s-wave scattering amplitude is isotropic and takes the low-energy form [43]

$$f(k) = \frac{1}{\cot\delta_0(k) - ik} \to \frac{-1}{\frac{1}{a} - \frac{1}{2}r_e k^2 + ... + ik}\,, \tag{2.4}$$

[1] We will define the proportionality later on, when we have introduced the density imbalance. Here only the order of magnitude matters.

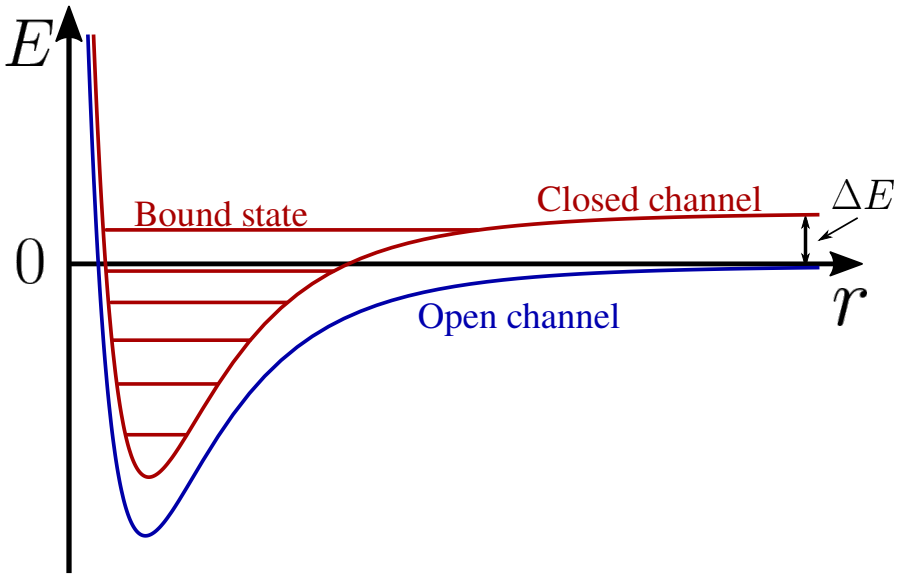


Figure 2.1: Schematic representation of a Feshbach resonance. $r$ denotes the distance between the atoms, which scatter at vanishing incident energy. The bound state just below the incident energy $E = 0$ is close to resonance.

when the collision takes place at energy $E = \hbar^2 k^2/m \to 0$. In this limit the interactions are described by the scattering length $a$ and the effective range $r_e$ only. Typically, both are on the order of the van der Waals length, unless $V(r)$ exhibits a zero-energy resonance, where one additional bound state is about to be present. Thus, knowledge of these two parameters suffices to describe the two-body interactions in ultracold quantum gases. Nevertheless, $a$ and $r_e$ depend on the scattering properties at short distances[2]. Yet, a theoretical solution of the involved short-range problem becomes obsolete, if one admits an experimental input for $a$ and the limits $k_F r_e \ll 1$ $k_{\mathrm{th}} r_e$ are satisfied, which renders the effective range irrelevant.

### 2.1.2 Feshbach resonances

A particularly interesting feature of ultracold atoms is provided by Feshbach resonances[3], which were introduced to the field of cold atoms by Tiesinga et al. [48].

[2] A toy model which illustrates the relations of the involved length scales is discussed in Refs. [44, 45]. In those papers the short-range properties are simply replaced by an infinitely high potential barrier at a short-distance cutoff $r_c \ll l_{\mathrm{vdW}}$. As a result, both the scales $a$ and $r_e$ are set by $l_{\mathrm{vdW}}$, however, by fine-tuning $r_c$ one can either reach the limit $a \gg l_{\mathrm{vdW}}$ or $r_e \gg l_{\mathrm{vdW}}$, while the other variable remains of order $\mathcal{O}(l_{\mathrm{vdW}})$.

[3] This concept has originally been developed in the context of nuclear reactions by Feshbach [46] and for configuration interactions in many-electron atoms by Fano [47].

They allow to tune the scattering length to values $a \gg l_{\mathrm{vdW}}$, while keeping $r_e$ of the order of the van der Waals length by adjusting an external magnetic field[4] $\mathbf{B}$. This limit entails a regime of strong interactions, since the gas parameter $na^3$ reaches values much larger than unity and the standard perturbation expansion in its powers breaks down. The physical mechanism behind Feshbach resonances originates from the existence of different scattering channels. It is depicted schematically in Figure 2.1. In the following, we will describe the physical picture encountered at the experimentally relevant Feshbach resonance at $B_0 \sim 832\mathrm{G}$ in $^6$Li, that has been measured by Zürn et al. [51]. We choose the magnetic field $\mathbf{B} = B\hat{\mathbf{e}}_z$ to point along the $z$ direction without loss of generality. For field strengths on the order of $B_0$ the electron spins become almost perfectly polarized, because they react to the external field with a coupling strength that is by a factor of the ratio proton mass over electron mass $m_p/m_e \simeq 2000$ larger than the coupling between the nuclear spins and $\mathbf{B}$. Accordingly, collisions of two initially well-separated atoms mainly take place in the electronic triplet configuration, that is called the open channel. In contrast, in the limit of vanishing scattering energy the singlet channel is closed, due to its additional Zeeman energy $\Delta E = \Delta\mu\, B$. The latter arises from the difference of the magnetic moments $\Delta\mu$ of the triplet and singlet channels adds to the van der Waals asymptotics in equation (2.1). As we detail in a moment, it originates from the different combinations of electronic and nuclear spin projections on the magnetic field axis encountered in the two channels. However, at shorter distances the singlet potential becomes much more attractive than its triplet counterpart, since the spatial part of the scattering wave function occupied by the two Fermions, is symmetric. Thus, the singlet potential exhibits many bound states, whose energies can be detuned against the energy of the incoming open-channel atoms by varying $B$. At any finite magnetic field the electron triplet is not a perfect eigenstate of the Hamiltonian and every scattering event will have an admixture of the singlet configuration. In particular, there exists a finite off-diagonal potential $\hat{W}(\mathbf{x})$ that couples the triplet and the singlet channel. Physically, it originates from the fact that quanta of electronic and nuclear spin projections on the $z$-axis can be exchanged during the collision, as only the total hyperfine angular momentum $m_z^F$ is conserved by the reduced rotational invariance in the presence of $\mathbf{B} \sim \hat{\mathbf{e}}_z$. The different coupling strengths between $B$ and the nuclear and electronic spins therefore give rise to a finite $\Delta\mu$ and consequently, one can shift the singlet potential relative to the triplet potential by the Zeeman effect. If one adjusts $B$, such that one of the bound states of the singlet potential comes energetically close to resonance with the incident open-channel state, it will drastically influence the scattering properties. Phenomenologically, the dependence of the scattering length on the magnetic field

[4] In thesis we only consider magnetic Feshbach resonances. However, they can be induced by optical methods, too, as was first proposed in [49] and realized in $^{87}$Rb [50]. See also [18].

$B$ can be parametrized as

$$a\,(B) = a_{\mathrm{bg}}\left(1 - \frac{\Delta B}{B - B_0}\right) \to -\frac{\hbar^2}{m r^\star \nu\,(B)} + \ldots\,, \tag{2.5}$$

where the resonance is characterized by a width $\Delta B$ in magnetic units around the resonant field strength $B_0$. Its scale is set by the background scattering length $a_{\mathrm{bg}}$, which would be obtained, if the closed channel were completely neglected. Close to resonance, it suffices to include only the resonant contribution, which leads to the second parametrization above. It describes the Feshbach resonance in terms of the detuning $\nu(B) = \Delta\mu(B - B_0)$ of the open and the closed-channel bound state. Furthermore, a new intrinsic length scale $r^\star$ has been introduced for the width of the resonance. Physically, its inverse quantifies the coupling strength of the open and closed channels independent of the parametrization of the resonance, which will become clear in equation (2.12) below.

A simple model that describes the conversion of pairs of fermionic atoms from the open channel to bound-state dimers is the two-channel model or equivalently the Bose-Fermi resonance model, first considered in this context by Holland et al. [52] and Timmermans et al. [53]. Its effective Hamiltonian

$$\begin{aligned}\hat{H}_{\mathrm{Feshbach}} = \int_{\mathbf{x}} \Bigg[ \sum_\sigma \hat{\psi}^\dagger_\sigma(\mathbf{x})\Big( -\frac{\hbar^2}{2m}\nabla^2\Big)\hat{\psi}_\sigma(\mathbf{x}) \; + \hat{\Phi}^\dagger(\mathbf{x})\Big( -\frac{\hbar^2}{4m}\nabla^2 + \nu_c(B)\Big)\hat{\Phi}(\mathbf{x}) \\ + \tilde{g}\int_{\mathbf{x}'} \chi(|\mathbf{x}-\mathbf{x}'|)\Big(\hat{\Phi}^\dagger\left(\frac{\mathbf{x}+\mathbf{x}'}{2}\right)\,\hat{\psi}_\uparrow(\mathbf{x})\hat{\psi}_\downarrow(\mathbf{x}') + \mathrm{h.c.}\Big)\Bigg]\,,\end{aligned} \tag{2.6}$$

allows in particular to compute the resonant contribution of the scattering amplitude (2.4). The fermionic field operators $\hat{\Psi}_\sigma\,(\mathbf{x})$ $\left(\hat{\Psi}^\dagger_\sigma\,(\mathbf{x})\right)$ annihilate (create) an open-channel atom. The index refers to the hyperfine state, which we formally denote as $\sigma = \uparrow, \downarrow$. Furthermore, the so-called dimer field $\hat{\Phi}(\mathbf{x})$, which obeys Bose statistics, represents the closed-channel bound state, whose energy is shifted by the *bare* detuning $\nu_c(B) = \Delta\mu(B - B_c)$ with respect to the open channel. Both channels are coupled by the Yukawa-like term in the second line. The form factor $\chi\,(|\mathbf{x} - \mathbf{x}'|)$ regularizes the theory by cutting-off the transfer between the open and closed channel at large separations of the $\uparrow\downarrow$ Fermion pair and the closed channel dimer, while its rotational isotropy restricts the interactions to the s-wave channel. It is normalized by the condition $\int d^3x\,\chi(|x|) = 1$, such that the overall interaction strength of the two channels is given by the coupling constant $\tilde{g}$. A convenient choice for the form factor in momentum space is a Lorentzian

$$\chi(q) = \frac{1}{1 + \mathbf{q}^2\tilde{\sigma}^2}\,, \tag{2.7}$$

which implies a further length $\tilde{\sigma}$ that quantifies the cut-off scale[5]. From the arguments below, it will turn out that $\tilde{\sigma}$ is of order $l_{\mathrm{vdW}}$. At the level of two atoms with opposite spins the Yukawa interaction in eq. (2.6) leads to an-off diagonal potential $\hat{W}$, which acts in the center-of-mass reference frame as [42, 55]

$$\hat{W}|\phi_{\mathrm{res}}\rangle = \tilde{g}\sum_{\mathbf{k}}\chi(\mathbf{k})||\mathbf{k}\rangle \tag{2.8a}$$

$$\hat{W}||\mathbf{k}\rangle = \tilde{g}\chi(\mathbf{k})\,|\phi_{\mathrm{res}}\rangle\,, \tag{2.8b}$$

on the zero-momentum bound state $|\phi_{\mathrm{res}}\rangle$ and the open-channel scattering state $||\mathbf{k}\rangle = |\mathbf{k},-\mathbf{k}\rangle$, consisting of two atoms carrying opposite momenta $\pm\mathbf{k}$. The Schrödinger equation for the eigenenergy $E = \hbar^2\mathbf{k}_0^2/m$ can be solved by plugging in the ansatz

$$|\Psi\rangle = \sqrt{Z}|\phi_{\mathrm{res}}\rangle + \sum_{\mathbf{k}}\alpha(k)||\mathbf{k}\rangle\,. \tag{2.9}$$

Eliminating the closed-channel admixture $Z$ yields an effective scattering problem for the open-channel state, whose solution is demonstrated explicitly in Refs. [42] and [55]. As a result, the scattering amplitude reads

$$f(k) = \frac{m}{4\pi\hbar^2}\frac{\tilde{g}^2\chi^2(k)}{\nu_c(B) - \frac{\hbar^2k^2}{m} + \frac{m\tilde{g}^2}{\hbar^2} + \int_q \frac{\chi^2(q)}{k^2-q^2+i0}}\,, \tag{2.10}$$

which in the low-energy limit is consistent with the form of equation (2.4), whose two lengths become [56]

$$\frac{1}{a} = -\frac{mr^\star}{\hbar^2}\nu_c\,(B) + \frac{1}{2\tilde{\sigma}} \tag{2.11a}$$

$$r_e = -2r^\star + 3\tilde{\sigma}\left(1 - \frac{4\tilde{\sigma}}{3a}\right)\,. \tag{2.11b}$$

Quite importantly, the intrinsic length scale $r^\star$, introduced in the phenomenological parametrization of the Feshbach resonance (2.5) is connected to the coupling constant $\tilde{g}$ by

$$r^\star = \frac{4\pi\hbar^4}{m^2\tilde{g}^2}\,. \tag{2.12}$$

Thus, indeed, it quantifies the coupling strength between the two channels. Furthermore, the scattering length acquires the phenomenologically suggested form,

[5] Alternatively, a Gaussian form factor is used in Ref. [54]. However, the Lorentzian cut-off yields results that coincide more closely with those from single-channel computations, as will become clear in a moment.

too. Yet, the position of the Feshbach resonance, where the scattering length diverges, is shifted from the bare $B_c$ by an amount

$$\Delta\mu(B_0 - B_c) = \frac{\hbar^2}{2mr^\star\tilde{\sigma}}\,. \tag{2.13}$$

From a physical point-of-view, this difference originates from the level repulsion of the interacting states, induced by the off-diagonal coupling $\tilde{g}$. Furthermore, it provides a way to determine the value of the cut-off length scale $\tilde{\sigma}$ by matching this resonance shift to the results from microscopic computations for potentials with van der Waals tails [57]. This procedure leads to the identification $\tilde{\sigma} = \bar{a} = 0.956\, l_{\mathrm{vdW}}$ [56], which therefore essentially coincides with the van der Waals length[6].

On the two-particle level one can classify Feshbach resonances in terms of the resonance strength $s_{\mathrm{res}}$, defined as the ratio of the two relevant microscopic length scales

$$s_{\mathrm{res}} = \frac{\bar{a}}{r^\star}\,. \tag{2.14}$$

Feshbach resonances satisfying $s_{\mathrm{res}} \gg 1$ are called open-channel dominated. In this case, the open and closed channel are strongly coupled according to relation (2.12). The name relates to the fact that the closed-channel admixture $Z$ is negligible, as long as the detuning remains within the resonance width, i.e. for values of $B$ that satisfy $|B - B_0| \lesssim |\Delta B|$. Indeed, for $a > 0$, the dressed bound state can be written as a linear combination similar to eq. (2.9). Close to resonance it has a universal binding energy $\varepsilon_B = \hbar^2/(ma^2) = \nu^2/\varepsilon^\star$, that depends quadratically on the detuning $\nu = \Delta\mu\,(B - B_0)$, divided by the characteristic energy $\varepsilon^\star = \hbar^2/(m(r^\star)^2)$. Applying the Hellman-Feynman theorem to the binding energy, reveals that [18, 42]

$$Z = \frac{\partial\,(-\varepsilon_B)}{\partial\nu_c} = 2\frac{|\nu|}{\varepsilon^\star} = 2\frac{r^\star}{a} = 2\frac{r^\star}{|a_{\mathrm{bg}}|}\frac{|B - B_0|}{|\Delta B|}\,, \tag{2.15}$$

vanishes linearly with the magnetic field upon the approach to resonance. To confirm this result, one first uses $a$ from (2.11a) and subsequently the parametrization (2.5). As stated above, if $s_{\mathrm{res}} \gg 1$, $Z$ remains much smaller than one over a wide range of detunings, as $a_{\mathrm{bg}}$ typically is of the order of the van der Waals length. In addition, the effective range in (2.11b) is positive and tends to $r_e \to 3\sigma \simeq l_{\mathrm{vdW}}$. This agrees very well with the result $r_e = 2.92\bar{a}$ obtained from the computations for a single-channel potential with $1/r^6$-asymptotics [45].

The opposite limit of $s_{\mathrm{res}} \ll 1$ gives rise to closed-channel dominated resonances, since the admixture of the closed-channel state can be neglected only for very small detunings $\nu \ll \varepsilon^\star$. Furthermore, we observe that the effective range in equation (2.11b) tends to $-2r^\star$, which is negative but has an absolute value much larger

[6] The quantity $\bar{a}$ appears in the discussion of the toy model for vdW interactions [44] and is the standard choice to denote the length scale for the short-distance physics.

than $l_{\mathrm{vdW}}$. Consequently, $r_e$ cannot be neglected and one does not expect to find universal many-body physics in the sense that interactions are described in terms of the tunable scattering length only.

From an experimental perspective the element $^6$Li, which is frequently used for experiments on the strongly-interacting regime of the BCS-BEC crossover, for example at MIT [58] and at ENS [59], has an open-channel dominated Feshbach resonance[7] at $B_0 \sim 832$G [51] with a resonance strength $s_{\mathrm{res}} \simeq 59$. Therefore, we will focus in the remainder of the thesis on open-channel dominated Feshbach resonances.

### 2.1.3 A short note on stability

One important question in the context of strongly attractive Fermions concerns the stability of a trapped gas. Typically, three-body losses limit the lifetimes of ultracold atomic clouds. In such a process three atoms approach each other within a small volume, whose spatial extend is comparable to the effective range or equivalently $l_{\mathrm{vdW}}$. Two of them then form a dimer in one of the deeply bound states of the atomic potentials, while the third atom carries the binding energy in form of kinetic energy and thereby heats the system via two-body collisions with the background atoms. One might expect that the three-body loss rates increase, when the attractions are enhanced, which makes configurations of three atoms close to each other more favorable. However, in case of two-component fermionic gases two of the atoms necessarily have identical spin orientations and the Pauli exclusion principle suppresses the probability for the occurrence of these configurations. Therefore, one encounters lifetimes long enough for equilibration to take place. In contrast, the lifetime of unitary Bosons tends to zero. A more in-depth discussion of this issue may be found in Ref. [42].

Regarding Fermions, the short-distance asymptotics of the three-particle wave function at zero energy is restricted by dimensional analysis to $\Psi(r \to 0) = a^{-3/2}(r/a)^{\gamma}F(\Omega) = A(a)r^{\gamma}F(\Omega)$, as discussed by Petrov et al. [60]. The variable $r = \sqrt{r_{12}^2 + r_{13}^2 + r_{23}^2}$ is called the hyperradius, while $F(\Omega)$ contains the angular degrees of freedom, Furthermore, the authors compute the dominant anomalous dimension $\gamma = -0.2273...$. The resulting relaxation rate $\alpha_3(a) \sim |A(a)|^2$ into deeply bound states, obeys the power law

$$\alpha_3(a) = \mathrm{const}\frac{\hbar\, l_{\mathrm{vdW}}}{m}\left(\frac{l_{\mathrm{vdW}}}{a}\right)^{3+2\gamma}, \tag{2.16}$$

where the proper dimensions of cm$^3$/s are obtained by inserting corresponding factors of $l_{\mathrm{vdW}}$. The numerical constant depends on the short-distance physics and

[7] It turns out that $^6$Li has a background scattering length that exceeds the van der Waals length. Under these circumstances $Z$ is suppressed over an even larger range of magnetic fields around the resonance.

cannot be calculated from the effective Hamiltonian (2.6). Experiments on both $^{40}$K [61] and $^{6}$Li [62] agree with eq. (2.16). However, the available accuracy does not allow to compare with the theoretical prediction for $\gamma$.

The fundamental question for the study of many-body effects is whether thermal equilibrium can be reached fast enough by two-particle collisions, before three-body losses distort the cloud too strongly. At unitarity the two-particle scattering rate scales like $\Gamma_2 = n\sigma_{\rm scatt} v_F \sim \varepsilon_F/\hbar$, as the total scattering cross-section $\sigma_{\rm scatt}$ is trivially related to the differential cross-section $d\sigma_{\rm scatt}/d\Omega = |f(k)|^2 \propto 1/k_F^2$ in accordance with eq. (2.4). Regarding the three-body loss rate $\Gamma_3 = -\dot{N}_3/N = n\,\alpha$ we make use of the fact that the power law in eq. (2.16) saturates at scales $k_F a \simeq 1$ in finite density systems. Hence, we find for the ratio

$$\frac{\Gamma_3}{\Gamma_2} = \frac{\hbar\, n\, \alpha\left(a^{-1} \to k_F\right)}{\varepsilon_F} \simeq (k_F l_{\rm vdW})^{4+2\gamma} \ll 1\,, \tag{2.17}$$

where the last inequality follows from the hierarchy of length scales (2.3), realized in an ultracold gas. Consequently, the unitary gas is stable enough to thermalize. For example at the 832.18 G resonance in $^{6}$Li one encounters lifetimes of up to one minute [63].

Another important aspect of stability concerns the interaction strength between single atoms and bound dimers, as well as the mutual dimer-dimer interaction at positive scattering lengths. In the first case one considers a dimer, represented by the universal two-body bound state wave function $\phi_0(r) = \exp(-r/a)/(\sqrt{2\pi a} r)$ of spatial extent $a$, and an additional atom at a distance $R \gg a$. The solution of the Schrödinger equation for three-body wave function acquires the asymptotic form [64]

$$\Psi(\mathbf{r}, \mathbf{R}) = \phi_0(r)\left(1 - \frac{a_{\rm ad}}{R}\right)\,, \tag{2.18}$$

with the atom dimer scattering length $a_{\rm ad} = 1.18$. In the dimer-dimer problem one has two bound states at distance $R \gg a$, which gives rise to the asymptotic result [60]

$$\Psi(\mathbf{r}_1, \mathbf{r}_2, \mathbf{R}) = \phi_0(r_1)\phi_0(r_2)\left(1 - \frac{a_{\rm ad}}{R}\right)\,, \tag{2.19}$$

with a dimer-dimer scattering length $a_{\rm dd} = 0.6a > 0$. The positivity of both scattering lengths implies repulsive interactions and the encountered molecular BECs are stable. An alternative derivation of the latter value, based on a diagrammatic method, has been given in Refs. [65, 66].

## 2.2 Single-channel model and renormalization

After having summarized the basic physics of magnetic Feshbach resonances in the context of ultracold Fermions, we can now transform the two-channel model (2.6)

into a single-channel model, which is more convenient regarding the computations of the thermodynamic quantities within the Luttinger-Ward formalism. As $\hat{H}_{\text{Feshbach}}$ is quadratic in the dimer field $\hat{\Phi}$, the latter can be formally integrated out, which gives rise to a quartic fermionic coupling in the pairing channel. With the abbreviations $x = (t, \mathbf{x})$ in real space and $q = (\omega, \mathbf{q})$ in momentum space, the new form of the interaction term reads at the level of the action

$$\begin{aligned}
&\tilde{g}^2 \int\limits_{x,x'} \int\limits_{y,y'} \chi(|\mathbf{y}|)\, \hat{\Psi}^\dagger_\uparrow\Big(x + \frac{y}{2}\Big) \hat{\Psi}^\dagger_\downarrow\Big(x - \frac{y}{2}\Big) \mathcal{G}^{-1}_{\Phi,0}\left(x - x'\right) \hat{\Psi}_\downarrow\Big(x' + \frac{y'}{2}\Big) \hat{\Psi}_\uparrow\Big(x' - \frac{y'}{2}\Big) \chi(|\mathbf{y}'|) \\
&= \tilde{g}^2 \int\limits_{Q,q,q'} \chi(|\mathbf{q}|)\chi(|\mathbf{q}'|) \hat{\Psi}^\dagger_\uparrow\left(\frac{Q}{2} + q\right) \hat{\Psi}^\dagger_\downarrow\left(\frac{Q}{2} - q\right) \mathcal{G}^{-1}_{\Phi,0}\left(Q\right) \hat{\Psi}_\downarrow\left(\frac{Q}{2} + q'\right) \hat{\Psi}_\uparrow\left(\frac{Q}{2} - q'\right).
\end{aligned} \tag{2.20}$$

$\mathcal{G}_{\Phi,0}(Q)$ denotes the bare propagator of the dimer field. In this new formulation the scattering amplitude of two Fermions with opposite spin in their center-of-mass frame is given by

$$f(k) = \frac{m}{4\pi\hbar^2} \tilde{g}^2 \chi^2(k)\, \mathcal{G}^{-1}_{\Phi}(E = 2\varepsilon_k, \mathbf{Q} = 0)\,, \tag{2.21}$$

where the incoming Fermions carry momenta $\pm\mathbf{k}$ and the scattering takes place at the total energy $E = 2\varepsilon_k$. Quite importantly, the propagator $\mathcal{G}_\Phi(Q)$ is dressed by repeated inclusions of fermionic bubbles, which are the only possible diagrammatic corrections at the two-particle level. Note also that the isotropy of the form factor $\chi(|\mathbf{x}|)$ gives rise to a purely s-wave interaction. As discussed in Ref. [42], inserting the propagator with the interaction contributions corresponding to the bubbles

$$\mathcal{G}^{-1}_{\Phi}(E = 2\varepsilon_k, \mathbf{Q} = 0) = -\frac{\hbar^2 k^2}{m} + \nu_c(B) + \frac{\tilde{g}^2 m^2}{\hbar^2} \int\limits_{\mathbf{q}} \frac{\chi(q)^2}{k^2 - q^2 + i0^+}\,, \tag{2.22}$$

returns exactly the result from the two-channel model in eq. (2.10) for $f(k)$. Consequently, the scattering amplitude obtained in this way admits the identical low-energy expansion in terms of the scattering length and effective range given in eq. (2.11a) and (2.11b), respectively.

To simplify the model, one replaces the full scattering amplitude by $f(k) = -1/(a^{-1} + ik)$, which merely depends on the scattering length. From quantum mechanics it is known that this particular form of the scattering amplitude arises for all $\mathbf{k}$ from a Fermi pseudo-potential. However, in the context of Feshbach resonances this approximation is justified only, if the effective range corrections can be neglected at all relevant momentum scales. In other words the condition

$$k_F\, r_e \ll 1\,, \tag{2.23}$$

which is termed the zero-range limit, must be satisfied. Open-channel dominated resonances comply $r_e \sim l_{\text{vdW}}$ (see eq. (2.11a)) and thus automatically realize this

relation, due to the separation of length scales in a quantum gas (2.3)[8]. For a closed-channel dominated resonance in contrast, the effective range approaches $r_e \to -2r^\star$, where in this case $r^\star \gg l_{\mathrm{vdW}}$ according to eq. (2.14), such that the zero-range limit is ruled out. Furthermore, as discussed by Zwerger [42], the density of closed-channel bound states close to resonance in a homogeneous system is given by

$$n_b(B \simeq B_0) = \frac{r^\star \tilde{\mathcal{C}}\, k_F^4}{4\pi}\,, \tag{2.24}$$

which entails a closed channel admixture $\tilde{Z} = 2n_b/n$ at the many-body level. Here $\tilde{\mathcal{C}} = \mathcal{C}/k_F^4$ denotes the dimensionless contact density, defined in eq. (2.53) below, that in particular is finite around the Feshbach resonance. In case of only two atoms one recovers $Z$ from eq. (2.15). With the result from above we have for the closed channel admixture of a strongly interacting, dilute gas $\tilde{Z} \sim \tilde{c}\, r^\star k_F$, which can only be neglected in case of an open-channel dominated resonance. In contrast, in case of closed-channel dominated resonance one always has to take into account the bound-state. However, the weak coupling between the open and the closed channel allows to effectively replace the dimer field in the two-channel model (2.6) by its expectation value

$$\tilde{g} \int_{\mathbf{x}'} \chi\left(|\mathbf{x}-\mathbf{x}'|\right)\, \hat{\Phi}^\dagger\left(\frac{\mathbf{x}+\mathbf{x}'}{2}\right) \;\to\; \Delta(\mathbf{x})\,, \tag{2.25}$$

which gives rise to a c-number-valued gap function. The resulting Hamiltonian acquires the standard BCS form [67] throughout the crossover and mean-field theory can be applied. This procedure underlies the works of Parish et al. [68], Sheehy and Radzihovsky [69] and Veillette and Radzihovsky [70], but gives rise to the BCS universality class, where the energy cutoff $\bar{E} = \hbar^2/(m\bar{a}^2) \sim E_{\mathrm{vdW}}$ remains manifest [42]. For example the critical temperature $k_B T_c \sim \bar{E}\exp(-\pi/(2k_F|a|))$ depends on the non-universal energy scale $\bar{E} \ll \varepsilon_F$, while the proportionality constant is of order one. In fact, this approach amounts to a high-density expansion in inverse powers of $k_F|r_e| \sim k_F r^\star \gg 1$ around a narrow Feshbach resonance (see footnote 8), as discussed in Ref [69], which actually contradicts the notion of a gas.

Returning now to the open-channel dominated resonances, which we concentrate on in this thesis, we introduce the single-channel model

$$\hat{H} = \int_{\mathbf{x}} \Big[ \sum_\sigma \hat{\psi}_\sigma^\dagger(\mathbf{x}) \big( -\frac{\hbar^2}{2m}\nabla^2\big)\hat{\psi}_\sigma(\mathbf{x}) \;+ \bar{g}(\Lambda)\, \hat{\psi}_\uparrow^\dagger(\mathbf{x})\hat{\psi}_\downarrow^\dagger(\mathbf{x})\hat{\psi}_\downarrow(\mathbf{x})\hat{\psi}_\uparrow(\mathbf{x})\Big]\,, \tag{2.26}$$

which is characterized by the bare coupling constant $\bar{g}(\Lambda)$. For convenience, we choose it as the scattering length in Born approximation of the full atomic inter-

[8] Note that $k_F l_{\mathrm{vdW}} \ll 1$ poses a stronger constraint than the frequently applied criterion $k_F r^\star \ll 1$, which characterizes a so-called broad Feshbach resonance. In contrast, a narrow Feshbach resonance is defined by the opposite limit $k_F r^\star \gg 1$. We will refrain from distinguishing the influence of interactions in this way, since it explicitly depends on the density.

action potential $V(\mathbf{x})$

$$\bar{g}\left(\Lambda\right) = \frac{4\pi\hbar^2 a_B\left(\Lambda\right)}{m} = \int d^3x\, V(\mathbf{x})\,. \tag{2.27}$$

The high-momentum cutoff $\Lambda$ keeps track of the physically finite effective range. As a result, it scales inversely proportional $\Lambda \sim 1/r_e$ to $r_e$ and the zero-range limit is obtained by $\Lambda \to \infty$. On a technical level $\Lambda$ is required to regularize the otherwise divergent loop integrals and implies a fine-tuning scheme for the limit $\Lambda \to \infty$, which ascertains that the physical scattering length $a$ is recovered. The necessity of this procedure can already be observed at the two-body level where the Lippmann-Schwinger equation

$$\tilde{f}(\mathbf{k} \to \mathbf{k}') = v(\mathbf{k} - \mathbf{k}') + \int \frac{d^3q}{\left(2\pi\right)^3} \frac{v\left(\mathbf{k}' - \mathbf{q}\right) \tilde{f}(\mathbf{k} \to \mathbf{q})}{k^2 - q^2 + i\varepsilon}\,, \tag{2.28}$$

determines the exact scattering amplitude $\tilde{f} = -4\pi f$. The function $v(\mathbf{k})$ denotes the momentum-space representation of the rescaled potential $mV(\mathbf{x})/\hbar^2$. Substituting the latter by $4\pi a_B(\Lambda)$ and taking the low-energy limit $\tilde{f} \to 4\pi a = mg/\hbar^2$ , which defines the physical coupling constant $g$, the Lippmann-Schwinger equation becomes

$$\frac{1}{g} = \frac{1}{\bar{g}\left(\Lambda\right)} + \int_{q<\Lambda} \frac{1}{2\varepsilon_q}\,. \tag{2.29}$$

The integral is restricted to momentum scales $q < \Lambda$, while higher momenta are sharply cut-off, such that the integral is rendered finite. Note that the value of $\bar{g}(\Lambda)$ has to be adjusted carefully, such that the right-hand side returns the correct physical $g$, that is consistent with the left-hand side. In particular, the limit $\Lambda \to \infty$ requires the bare coupling constant to vanish $\bar{g}(\Lambda \to \infty) \to 0^-$. This observation will affect the diagrammatic expansion performed in Section 4 on the Luttinger-Ward formalism. Finally, note that the Lippmann-Schwinger equation (2.28), which provides a convenient and exact reformulation of the Schrödinger equation for two-body scattering problems, already contains all orders of the interaction. Therefore, the renormalization prescription (2.29) already resums arbitrary orders of the interaction. An illustration how to perform perturbative renormalization and how it relates to the formulation used here is given in the review by Braaten and Hammer [71], which however focuses on the scaling limit $r_e/a \to 0$. Furthermore, the $\Lambda$-dependence gives rise to a flow of the coupling constant, which in turn determines the fixed points and the universal phase diagram, discussed in the next section.

## 2.3 Quantum critical point and universal phase diagram of the BCS-BEC crossover

From the point of view of critical phenomena the single-channel model (2.26) gives rise to a universal phase diagram for the BCS-BEC crossover, as was first discussed

by Nikolič and Sachdev [1]. The central insight that one gains from this perspective is the existence of a new, strongly interacting quantum critical point, located at the Feshbach resonance at $1/a = 0$ and at zero chemical potentials[9] $\mu_\uparrow = 0 = \mu_\downarrow$ or equivalently $\mu = 0 = h$. We define $\mu$ as the average chemical potential and $h$ as the potential difference, which plays the role of the Zeeman field, via

$$\mu = \frac{1}{2}\left(\mu_\uparrow + \mu_\downarrow\right) \tag{2.30a}$$

$$h = \frac{1}{2}\left(\mu_\uparrow - \mu_\downarrow\right) , \tag{2.30b}$$

where the latter controls the spin imbalance. Without loss of generality we assume that $h > 0$, thereby defining the $\uparrow$-atoms as majority component.

Let us return to the phase diagram. When one continuously increases the chemical potentials $\mu_\uparrow$ and $\mu_\downarrow$ of the two spin-components, starting at $-\infty$, the ground state of the system undergoes a quantum phase transition from the vacuum state to a finite density state, irrespective of the value of $a^{-1}$. The vacuum formally is an incompressible state, since the density remains fixed upon changing the chemical potentials as long as one does not cross the phase boundary. In turn, the detailed nature of the finite-density phase depends both on the scattering length $a$ and on the chosen values of the chemical potentials. From the point of critical phenomena one mostly discusses the onset of a finite population and the characterization of the underlying states. The three quantities $1/a, \mu, h$ exhaust the list of relevant perturbations around the fixed point, whereas a finite temperature always leads to a breaking of scale invariance due to the compact imaginary time interval.

In the following, we discuss the basic features of the RG flow towards the infrared regime and the consequences that arise for the phase diagram. Furthermore, we summarize the results known in the literature for $h \geqslant 0$ and state the open questions in connection with a finite population imbalance, which are addressed in this thesis.

### 2.3.1 RG-flow

We first consider $T = 0$ and vanishing chemical potentials, such that all correlation functions reduce to vacuum expectation values. In this situation the cutoff-dependence of the coupling constant can be determined from (2.29), assuming a sharp cutoff at $q_{\max} = \Lambda$. In $d$-dimensions we have

$$\bar{g}(\Lambda) = \frac{g}{1 - g\frac{\Omega_d}{(2\pi)^d}\frac{m}{\hbar^2(d-2)}\Lambda^{d-2}} , \tag{2.31}$$

where $\Omega_d = 2\pi^{(d/2+1)}/\,\Gamma(d/2+1)$ denotes the surface of a units sphere. With the definition of the dimensionless coupling constant $u_d(\Lambda) = 2\Omega_d m/((2\pi)^d\hbar^2)\Lambda^{d-2}\bar{g}(\Lambda)$,

[9] Furthermore, the authors argue that both the single-channel (2.26) and the two-channel model (2.6) belong to the same universality class.

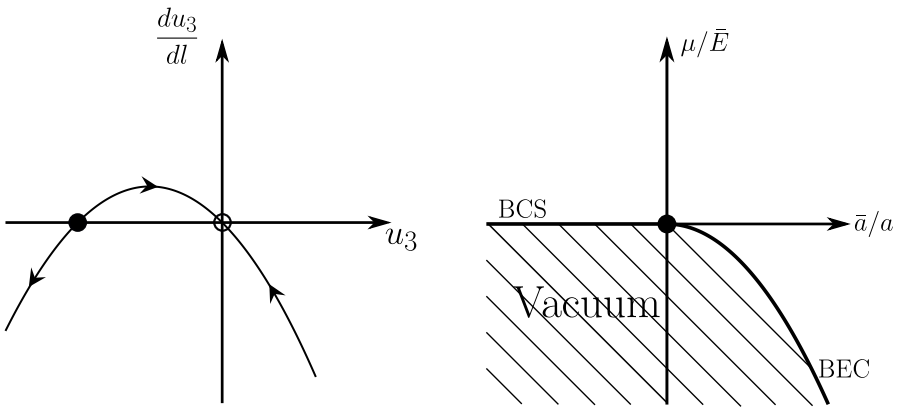


Figure 2.2: Left: RG flow in $d = 3$ with the unstable fixed point at $u_3^\star = -2$ (disk), representing the Feshbach resonance, and the stable one at $u_3 = 0$ (circle). Right: Universal ground state phase diagram of the BCS-BEC crossover without spin imbalance, following Ref. [1].

the latter result gives rise to the flow equation [1]

$$\beta_d(u) = \frac{du_d}{dl} = (2-d)u_d - \frac{u_d^2}{2}\,, \tag{2.32}$$

which describes the change of $u_d$, when the cutoff scale is reduced via $\Lambda \to e^{-l}\Lambda$, with $l \geqslant 0$. Quite remarkably, this relation is exact to all orders in the coupling constant, as in the vacuum state only particle-particle ladder diagrams contribute to the renormalization of $\bar{g}(\Lambda)$ within the field theory (2.26). Other diagrams would require the presence of additional particles [72,73]. Note that the Lippmann-Schwinger equation (2.28), which (2.31) is based upon, exactly represents the quantum mechanical equivalent of this particular class of diagrams.

In three dimensions the flow equation has a stable fixed-point at $u_3 = 0$ and an unstable one at $u_3^\star = -2$, which corresponds to the unitary gas at the Feshbach resonance. A graphical representation of the flow is given in Fig. 2.2. Moreover, detunings away from $u_3^\star$ can be identified with finite values of the inverse scattering length, i.e. $\delta u_3 = u_3 - u_3^\star = -\bar{a}/a$. For initial values $u_3^\star < u_3 < 0$ the flow is directed towards $u_3(l \to \infty) \to 0^-$ corresponding to a weakly attractive Fermi gas in the limit $a \to 0^-$. In the absence of two-particle bound states at negative scattering lengths, the onset of a finite density of particles is reached, when at least one of the chemical potentials $\mu_\sigma$ is positive. The increase of the densities with the chemical potential follows like in the non-interacting case $n_\sigma \propto \mu_\sigma^{3/2}$, since in the presence of just a single-component Fermi gas s-wave interactions are ruled out by the Pauli principle, while pairing effects, caused by the attraction in the case of a two-component gas, only give rise to exponentially small corrections.

On the other hand starting the flow at $u_3 < u_3^\star$, the coupling constant is driven towards $u_3(l \to \infty) \to -\infty$ or correspondingly $a \to 0^+$, indicating very strong,

attractive interactions. Therefore, particles of opposite spin form tightly-bound molecules with bosonic statistics. The chemical potential for these dimers is given by $\mu_B = \mu_\uparrow + \mu_\downarrow + \varepsilon_B = 2\mu + \varepsilon_B$, where $\varepsilon_B = \hbar^2/(ma^2)$ denotes the binding energy of the two-body s-wave bound state, which indeed exists at $a > 0$. From a fermionic perspective, a finite dimer density $n_d$ is admitted already above the threshold $\mu_B = 0$ or equivalently above $\mu = -\varepsilon_B < 0$. Apart from the possibility to create molecules, a single-component gas forms, if $\mu_\uparrow > 0$ and simultaneously $\mu_\downarrow \leqslant -\varepsilon_B - \mu_\uparrow$. We discuss the possible phases in this regime, including possible mixtures of dimers and unpaired atoms, in more detail in Chap. 3. If a finite $n_d$ is present, a weakly-coupled, stable BEC forms, since both the dimer-dimer interactions with scattering length $a_{\mathrm{dd}} = 0.6a > 0$ [60] as well as the interactions between dimers and excess atoms with $a_{\mathrm{ad}} = 1.18a > 0$ [64] are of a repulsive nature. In addition, they only give rise to small corrections, due to the limit $a \to 0^+$. As $d = 3$ is above the upper critical dimension of the condensation transition [72], mean-field theory applies and in the limit $n_d a^3 \to 0$ the system is described by the Gross-Pitaevskii equation, which yields a linear dependence on the bosonic chemical potential $n_d = \mu_B/g_{\mathrm{dd}}$, with the coupling constant $g_{\mathrm{dd}} = 4\pi\hbar^2 a_{\mathrm{dd}}/m_B = 2\pi\hbar^2 a_{\mathrm{dd}}/m$ for the molecules of mass $m_B = 2m$ [42].

Both of the latter limits share the common feature that one automatically enters a perturbative regime in the dilute limit, which is caused by the smallness of the gas parameters $na^3 \ll 1$ or $n_d a^3 \ll 1$, respectively. The corresponding theories are either the BCS theory, if $a < 0$, which takes pairing effects into account or for positive $a$ the theory of a BEC of weakly repulsive diatomic molecules. The name BCS-BEC crossover refers to the fact, that the ground-state at finite and equal spin-populations forms a superfluid, irrespective from the value of $a$. Moreover, the thermodynamic quantities evolve smoothly through the unitary limit $a^{-1} = 0$ when changing the scattering length from negative to positive values or vice versa. Further information on this subject can be found in the book [74] and in the reviews [41, 75, 76].

In contrast to the BCS or BEC limit, the strongly interacting regime in the vicinity of the critical point $a^{-1} = 0$ can never be treated by an expansion in terms of a small gas parameter. However, the fact that $\mu = h = 1/a = 0$ defines a scale-invariant fixed point allows to obtain a large amount of information about the system, despite the presence of strong correlations, since the existence of the fixed point gives rise to a universal regime, where scaling theory applies [72]. Universality in the context of ultracold atoms means that the only relevant intrinsic length scale is the (inverse) scattering length $a^{-1}$, which can be tuned by an external magnetic field, according to eq. (2.5). This implies that thermodynamic quantities follow from universal scaling functions, whose arguments are given by the ratios of the relevant perturbations $T, \mu, h$ and $a^{-1}$ around the critical point. The range of validity of these scaling forms is restricted to energy scales smaller than the microscopic energy scale $\bar{E} = \hbar^2/(m\bar{a}^2) \simeq E_{\mathrm{vdW}}$ or equivalently to lengths scales larger than the corresponding microscopic length $\bar{a} \simeq l_{\mathrm{vdW}}$, respectively. Beyond

those boundaries non-universal effects, for example due to the finite effective range, have to be taken into account.

The standard grand potential, which contains all thermodynamic information, becomes in this setup

$$\begin{aligned}\Omega(T,\mu_\uparrow,\mu_\downarrow,1/a,V) &= -T\log\mathrm{Tr}\exp\left[-\beta(\hat{H}-\mu_\uparrow\hat{N}_\uparrow-\mu_\downarrow\hat{N}_\downarrow)\right]\\ &= -T\log\mathrm{Tr}\exp\left[-\beta(\hat{H}-\mu\hat{N}-h\,\delta\hat{N})\right]=\Omega(T,\mu,h,1/a,V)\,,\end{aligned} \tag{2.33}$$

where $\hat{N}$ corresponds to the total particle number operator, while $\delta\hat{N}$ measures the difference of the spin populations. Within the universal regime one can now express the pressure, which is directly proportional to the grand potential, in terms of a universal scaling function $f_p$

$$p(T,\mu,h,a^{-1}) = -\frac{\Omega(T,\mu,h,a^{-1})}{V} = p^{(0)}(T,\mu)f_p\left(\beta\mu,\beta h,\frac{\lambda_T}{a}\right)\,, \tag{2.34}$$

where

$$p^{(0)}(T,\mu) = 2\frac{T}{\lambda_T^3}\mathrm{Li}_{5/2}(-e^{\beta\mu}) \tag{2.35}$$

defines the pressure of a non-interacting, balanced Fermi gas [77] and

$$\mathrm{Li}_s(z) = \sum_{k=1}^{\infty}\frac{z^k}{k^s} \tag{2.36}$$

denotes the polylogarithm. Using the standard thermodynamic relations for the density and the definitions eqs. (2.30) and (2.33), one can determine the total density $n$ and the density difference $\delta n$ via

$$n = n_\uparrow + n_\downarrow = \left(\frac{\partial p}{\partial\mu}\right)_{T,h,a} \tag{2.37a}$$

$$\delta n = n_\uparrow - n_\downarrow = \left(\frac{\partial p}{\partial h}\right)_{T,\mu,a}\,. \tag{2.37b}$$

Note that in a phase with equal spin populations, that is $\delta n \equiv 0$, the thermodynamic potential does not depend on $h$. This will be of interest especially in the $T = 0$ case, where thermal fluctuations of the particle number are absent. Furthermore, we introduce the spin polarization

$$\sigma = \frac{n_\uparrow - n_\downarrow}{n_\uparrow + n_\downarrow} = \frac{\delta n}{n}\,, \tag{2.38}$$

that varies between $\sigma = 0$, in the spin-balanced situation, where $n_\uparrow = n/2 = n_\downarrow$ and $\sigma = 1$ in the fully polarized case $n_\uparrow = n$, $n_\downarrow = 0$. To study the ground state

properties in the crossover regime at finite $1/a \neq 0$ a more convenient representation of $f_p$ is obtained by rescaling all energies by the binding energy (also for $a^{-1} < 0$, despite the absence of a two-body bound state). In the corresponding units $\bar{\mu} = 2\mu/(\varepsilon_B)$ and $\bar{h} = 2h/\varepsilon_B$, where the factor of two has been introduced for later convenience, the pressure scaling function reads

$$p(0, \mu, h, a^{-1}) = p^{(0)}(0, \mu) f_p^{(\pm)}(\bar{\mu}, \bar{h}) \,. \tag{2.39}$$

This form, which has been introduced in Ref. [78] generalizes previous formulations for the ground state thermodynamics [79,80]. In particular, $f_p^{(\pm)}$, whose superindex refers to the sign of $a^{-1}$, indicates that the ground-state phase diagram separates into three regimes. In the limit $\bar{\mu} \ll 1$ one recovers either the BCS physics, if $a^{-1} < 0$, or the weakly-repulsive BEC, if $a^{-1} > 0$. On the other hand the unitary regime, where the pressure reduces to a function of merely two arguments $p(0, \mu, h, 0)$, is encountered for $\bar{\mu} \gg 1$. Since the scaling function $f_p^{(\pm)}$ has to smoothly cross over from finite scattering lengths to the limit $a^{-1} \to 0^{\pm}$, where the scattering length has to drop out, it can only depend on the ratio $\bar{\mu}/\bar{\mu} = \mu/h$ at the resonance. Therefore, we obtain the following evolution of the scaling form

$$f_p^{(\pm)}(\bar{\mu}, \bar{h}) \to f_p(h/\mu) \,, \tag{2.40}$$

for the approach to unitarity. In Chapter 3 we show the universal phase boundaries in the $\bar{h}$ vs. $\bar{\mu}$ representation at $1/a = 0$ and for positive and negative scattering length. In Section 5 we use our Luttinger-Ward data to determine quantitatively at which value of $\bar{\mu}$ the crossover between the weak and strong coupling regimes takes place.

At finite $T$ the scaling function of the unitary gas becomes $f_p(\beta\mu, \beta h, 0) \equiv f_p(\beta\mu, \beta h)$, which has first been noted by Ho [22]. So far, mainly the restriction $f_p(\beta\mu, 0)$ to the balanced case has been addressed both theoretically and experimentally. The obtained results will be detailed in the next section, but for now we focus on the general statements that can be deduced from the scaling arguments. In particular, $f_p(\beta\mu, \beta h)$ gives rise to a set of universal numbers, that characterize the thermodynamic properties of the gas at resonance and therefore have attracted considerable interest. First of all, there is the critical temperature of the normal-to-superfluid transition $\theta_c = T_c/\varepsilon_F$, where $\varepsilon_F = \hbar^2/(2m)(3\pi^2 n)^{2/3}$ denotes the Fermi-energy of an ideal Fermi gas of the same density $n$. In addition, the ground state pressure at $h = 0$ acquires the form

$$p(0, \mu, 0, 0) = p^{(0)}(0, \mu) f_p(0) = \xi_s^{-3/2} p^{(0)}(0, \mu) \,, \tag{2.41}$$

which is directly proportional to the Pauli pressure of an ideal Fermi gas, according to (2.39) and (2.40). The proportionality constant is called the Bertsch parameter[10] $\xi_s$. Another universal quantity of interest is the ratio $(h/\mu)_c$, describing the

[10] The power $\xi_s^{-3/2}$ follows from the original definitions of the chemical potential $\mu$ and the pressure $p$ of the balanced unitary gas at $T = 0$ in terms of the density: $\mu = \xi_s \varepsilon_F[n]$ and $p = \xi_s p^{(0)}[n]$, which yields $p = \xi_s^{-3/2} 2/5 \cdot (3\pi^2 m\mu/\hbar^2)^{3/2} \mu^{5/2} = \xi_s^{-3/2} p^{(0)}(0, \mu)$.

Clogston-Chandrasekhar limit of the unitary gas. In particular, it is one of the goals of this work to determine $(h/\mu)_c$.

We postpone the summary of the available results on these universal numbers to the next section on the BCS-BEC crossover, but first note, that these scaling arguments rely on the observation that the scattering length is the only relevant internal length scale, which drops out in the unitary limit. As a result, the unitary gas obeys the standard relation [22]

$$p = \frac{2}{3}\,\varepsilon\,, \tag{2.42}$$

between the pressure and the energy density $\varepsilon$ of any scale-invariant system with Galilean symmetry, which usually is encountered in the noninteracting case. The origin of this equation and the behavior away from unitarity are summarized in Chapter 2.4, that deals with the Tan relations for systems with zero-range interactions[11].

Furthermore, also transport properties of the unitary gas are influenced by the scale invariance. In particular, the conformal symmetry at the Feshbach resonance implies that the bulk viscosity

$$\zeta(T) \equiv 0 \tag{2.43}$$

vanishes [81] identically in the normal phase. We return to the generalization for the superfluid phase, where one actually distinguishes between three different bulk viscosities, in Section 8. A more thorough discussion can be found in Ref. [42].

### 2.3.2 The BCS-BEC crossover of the balanced Fermi gas

After the first experimental realizations of strongly interacting Fermi gases in the regime $|k_F a| \gg 1$ by O'Hara et al [82] in 2002 and the creation of molecular, fermionic BECs [3–5], many experimental groups began to investigate the physics of strongly interacting Fermi gases and the BCS-BEC crossover [62, 83–85]. In particular, Chin et al. [86] used rf spectroscopy to reveal fermionic pairing caused by the many-body character of the system. Direct experimental evidence for the existence of a fermionic superfluid both at positive and negative scattering lengths was given by Zwierlein et al., who showed that a vortex lattice persists, while sweeping the scattering length back and forth through the Feshbach resonance. A major experimental step has been achieved in 2012 by Ku et al. [58], who measured the universal pressure and density equations of state of the unitary, spin-balanced Fermi gas from in-situ imaging with unprecedented precision. Furthermore, Ku et al. observed the normal-to-superfluid phase transition and determined the critical temperature $T = 0.16...T/T_F$ and the Bertsch parameter $\xi_s = 0.37...$ introduced

[11] Alternatively, eq. (2.42) can be quite easily proven from the relation $\Omega = U - TS - \mu N - hN$ together with the standard thermodynamic derivatives and the equation (2.34) at $1/a = 0$.

in eq. (2.41). The latter value results from using the most precise detection of the Feshbach resonance in $^6$Li at 832.16G by Zürn et al. [51].

Motivated by the experiments a great theoretical effort has been expended to improve the understanding for the phase diagram beyond the original mean field approaches by Eagles [19], Leggett [20] and Nozières and Schmidt-Rink [21]. In particular, the measurements by Ku et al. [58] allow for a parameter-free comparison between the experimental results and the predictions of different quantum many-body theories on a quantitative level. A fully self-consistent Luttinger-Ward computation based on ladder-diagrams consisting of interacting Green's functions has been developed by Haussmann [87] already in 1994 for the normal fluid and later extended to the superfluid phase by Haussmann et al. [37]. It yields $T_c \simeq 0.16 T_F$ right at the resonance in very good agreement with the experiment. Furthermore, this method is able to obtain quantitative results for the thermodynamics of the Fermi gas also at finite values of the scattering length, e.g. the critical temperature $\theta = T_c/\varepsilon_F$ as a function of the dimensionless coupling constant $v = 1/(k_F a)$ is depicted in Fig. 2.3. In this thesis we will extend this approach to finite Zeeman fields $h \neq 0$. Moreover, due to the availability of precise experimental data and the scale invariance of the unitary Fermi gas, a variety of nonperturbative quantum many-body methods has been applied to the system at infinite scattering length, including Quantum Monte Carlo approaches [88–90], an $\epsilon$ expansion both around $d = 2$ and $d = 4$ dimensions [91, 92] and Bold Diagrammatic Monte Carlo computations [93]. We will summarize the main approaches and their results below. Further information can be found in the reviews by Bloch et al. [41], the book edited by Zwerger [74] and the lectures by Zwerger [42].

Before we describe the strongly interacting regime around unitarity, let us first briefly review the asymptotic behavior in the BCS and BEC limits, which will also serve as checks for our results in the spin-imbalanced case. For $v \to -\infty$ one encounters the weak-coupling limit, that can be described by applying the BCS-pairing mechanism to ultracold Fermions [94]. The critical temperature and the $T = 0$ superfluid excitation gap are of the form obtained by Gorkov and Melik-Barkhudarov [95] already in 1961:

$$T_c = \frac{8e^{\gamma}}{(4e)^{1/3}\pi e^2}\varepsilon_F \exp(-\frac{\pi}{2}|v|) \tag{2.44}$$

and

$$\Delta_0 = \frac{8}{(4e)^{1/3}e^2}\varepsilon_F \exp(-\frac{\pi}{2}|v|)\,, \tag{2.45}$$

which are asymptotically exact results for the basic underlying model (2.26) In particular, their ratio gives rise to the universal value from BCS theory

$$\frac{\Delta_0}{T_c} = \pi e^{-\gamma_E} \simeq 1.76\,, \tag{2.46}$$

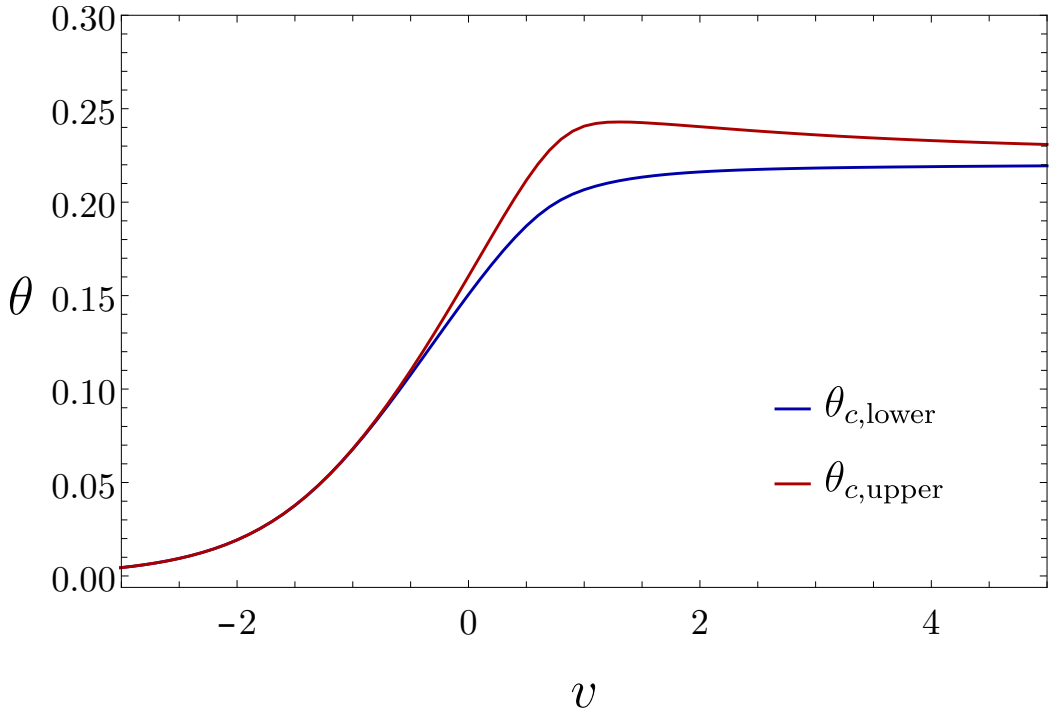


Figure 2.3: Critical temperature as function of the dimensionless coupling strength for spin balance, from [37]. The red line indicates the physical transition line, while the blue one is an artifact of the Luttinger-Ward method, which is explained in the text.

where $\gamma_E = 0.577...$ denotes the Euler-Mascheroni constant. The prefactor of $T_c$ and $\Delta_0$ includes corrections from density fluctuations by taking into account all second order contributions of the interactions exactly [96]. In fact, this entails a change of the physical coupling strength by

$$g \to g\left(1 + gN(0)\frac{1+2\ln 2}{3}\right), \tag{2.47}$$

with $N(0)$ referring to the density of states at the Fermi level. The standard BCS theory without these induced interaction corrections yields a critical temperature that is enlarged by a factor of $(4e^2)^{1/3} \approx 2.22$. Note that the asymptotic critical temperature from the Luttinger-Ward approach [37] in Fig. 2.3 follows this BCS asymptotics, due to the absence of particle-hole fluctuations in the underlying particle ladder approximation (see also Section 4.4.2). From the perspective of

universality we can transform eq. (2.44) to

$$\bar{T}_c = \frac{8e^\gamma}{(4e^2)^{1/3}\pi e^2}\bar{\mu}\exp\left(-\frac{\pi}{2\sqrt{\bar{\mu}}}\right), \tag{2.48}$$

where we have defined the dimensionless temperature $\bar{T} = T/(\varepsilon_B/2)$ in analogy to $\bar{\mu}$ and $\bar{h}$ in the zero-temperature scaling function (2.39). Furthermore, we have identified $\mu = \varepsilon_F$, which holds in the BCS limit up to exponentially small corrections of order $\Delta^2$. Finite critical temperatures are only possible for $\bar{\mu} > 0$, which is a prerequisite for a finite density of atoms.

In the opposite limit of $v \to \infty$, the dimer-dimer interactions become negligible and one expects to recover asymptotically the critical temperature of an ideal BEC, consisting of $n_d = n/2$ pairs of mass $m_B = 2m$, which reads [16]

$$T_c^{\mathrm{BEC}} = \frac{2\pi}{[\zeta(3/2)]^{3/2}}\frac{\hbar^2 n_d^{2/3}}{m_d} = 0.218\,\varepsilon_F\,. \tag{2.49}$$

Away from the extreme BEC limit the mutual interactions of dimers imply additional corrections . The leading contribution in the weak coupling limit $n_d\, a_{\mathrm{dd}}^3 \ll 1$ yields an increase of the critical temperature [97–99]

$$\frac{T_c}{T_c^{\mathrm{BEC}}} = 1 + c\, n_d^{1/3} a_{\mathrm{dd}} + \dots\,, \tag{2.50}$$

where $c \simeq 1.31$ [100, 101] denotes a numerical constant. Physically, this effect can be interpreted as a reduction of the volume per particle due to the repulsion, which effectively increases the phase space density $n\lambda_T^3$ in comparison to the ideal gas and therefore the critical temperature grows.

Despite the continuous nature of the normal-to-superfluid transition, the Luttinger-Ward formalism turns out to give rise to a weak first order transition, as shown in Ref. [37], which is signaled by a hysterisis of the normal solution with $\Delta \equiv 0$ and the superfluid branch with finite order parameter. This effect has already been observed a long time ago in a Luttinger-Ward study of the weakly-interacting BEC transition [102]. To remedy the problem in the context of the BCS-BEC crossover, one fixes $T_c$ at a given $v$ by the criterion that the involved jump of the entropy between the normal and superfluid solution is minimal at this temperature. This construction yields indeed a maximum of the $T_c$ curve in the vicinity of $v = 1$, as can be seen in Fig. 2.3. The additional (blue) line gives the critical temperature, below which no solution with vanishing order parameter exists.

Equation (2.49) can also be written in the universal formulation, like eq. (2.48). Using the relations $n_d = g_{\mathrm{dd}}\mu_B$ from the Gross-Pitaevskii equation and $g_{\mathrm{dd}} = 2\pi\hbar^2 a_{\mathrm{dd}}/m$ one obtains with $a_{\mathrm{dd}} = 0.6a$ [60]

$$\bar{T}_c^{\mathrm{BEC}} = \frac{(2\pi)^{1/3}}{\left(0.6\,\zeta(3/2)\right)^{2/3}}\left(\bar{\mu}+1\right)^{2/3}\,, \tag{2.51}$$

which yields physical critical temperatures for $\bar{\mu} \geqslant -1$, due to the energy gain of $-\varepsilon_B/2$ per Fermion upon forming a pair. At even lower values of the dimensionless chemical potential only the vacuum remains.

As mentioned in the introduction to this section, special focus has been given to the unitary limit. Experimentally, the scaling function $f_p(\beta\mu, 0, 0)$ has been measured at MIT by a direct integration of the in-situ density profiles from the non-degenerate regime $\beta\mu \simeq -1.6$ [93] into the superfluid phase [58]. The phase boundary to the superfluid has been observed at $(\beta\mu)_c \simeq 2.5$, which corresponds to the critical temperature $T_c = 0.16\,\varepsilon_F$. Furthermore, the Bertsch parameter has been determined from an extrapolation to zero temperature as $\xi_s = 0.37$ (including the corrected position of the Feshbach resonance in $^6$Li [51]).

From the theoretical perspective several methods have been developed that agree very well with the experimental measurments. The Luttinger-Ward theory by Haussmann et al. [37, 87] finds $\theta_c(v = 0) = 0.16$ and $\xi_s = 0.36$. Regarding the critical temperature, quantum Monte Carlo computations yield $\theta_c = 0.152(7)$ [88] and $\theta_c = 0.171(5)$ [89]. A more recent Monte-Carlo study by Goulko and Wingate [90] also investigated the superfluid regime, where the results are consistent both with the MIT experiment and the Luttinger-Ward approach.

In addition, it turns out to be useful to consider the unitary Fermi gas also in $d = 2$ or $d = 4$ dimensions, where it either becomes equivalent to an ideal Fermi gas or an ideal Bose gas, as has been realized in Ref. [103]. Therefore, it is amenable to an $\epsilon$-expansion around both dimensions, which has been first performed by Nishida and Son [91]. An overview of this method is given in Ref. [104]. A Borel-Padé approximation to match the two expansions in $\epsilon = d - 4$ and $\epsilon = d - 2$ up to next-to-leading order yields for the critical temperature $T_c = 0.183 \pm 0.014$ [92]. Furthermore, the value of the Bertsch parameter has been obtained in a similar manner, after extending the $\epsilon = d - 4$ expansion to third order [105], by a Padé resummation, which finds $\xi_s = 0.365 \pm 0.01$ [106].

The most successful theoretical approach in the sense of both the best agreement with the experimental data and control over the systematic errors has been followed by Van Houcke et al., who performed a bold diagrammatic Monte Carlo simulation (BDMC) for the pressure equation of state of the unitary Fermi gas in the normal regime above $T_c$ [93]. The BDMC results can be further improved by performing a Borel resummation [107] of the underlying asymptotic series. In fact, Rossi even proved for the unitary gas that this series of diagrams, which actually has vanishing convergence radius, is Borel resummable [108].

The phase diagram of the balanced unitary Fermi gas at finite temperatures is depicted in Fig. 2.4, which in this form has first been discussed by Enss [109]. At $T = 0$ and $\mu < 0$ no particles are present and one encounters the vacuum state in accordance with Fig 2.2. The onset of a finite density of Fermions takes place at the quantum critical point at vanishing $\mu$, such that for positive $\mu$ the low-temperature superfluid state forms. Due to the scale invariance, all phase boundaries are straight lines, whose slopes are given by universal numbers. Specifically for the critical

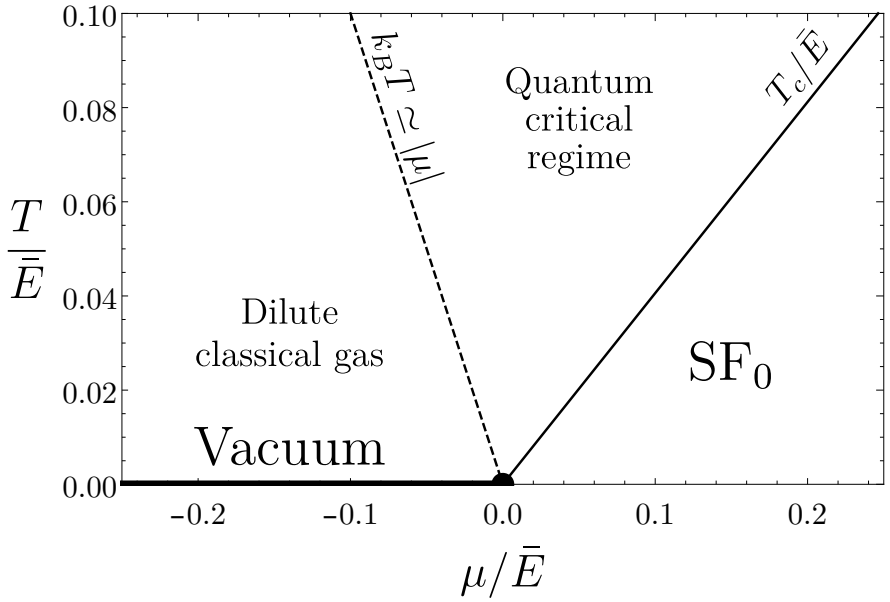


Figure 2.4: Phase diagram of the balanced unitary Fermi gas. The black line indicates the phase transition between the normal and superfluid state, while the dashed line refers to the crossover between the non-degenerate dilute gas and the quantum critical regime, following Ref. [109].

temperature of the superfluid transition one finds the ratio $(T/\mu)_c = 1/(\beta\mu)_c \simeq 0.4$. Furthermore, as discussed by Sachdev [72,73], just above the vacuum in the regime $T \ll |\mu|$ a non-degenerate gas is created from thermal particle fluctuations. When one increases the temperature even further, the system crosses over at $T \simeq |\mu|$ to the quantum critical regime $\mu \ll T$- The latter is theoretically challenging due to the absence of well-defined quasiparticles, which for examples renders the calculation of transport properties difficult. We return to this issue in Chapter 8.

### 2.3.3 BCS-BEC crossover and spin imbalance

In the presence of spin imbalance the phase diagram in the strongly interacting regime of the crossover is much less understood. As a convenient starting point, we therefore briefly review the well-known results of the imbalanced Fermi gas in the weak coupling limit, which historically has been deduced from BCS theory in the context of superconductors, see e.g. the book by Saint-James [110]. This allows us to introduce the necessary concepts for the description of the BCS-BEC crossover at finite Zeeman fields, before summarizing more recent results on ultracold Fermions. Like in the balanced situation, the scaling theory around the fixed-point at unitarity provides a number of theoretical insights for the strong coupling regime. In particular, the phase boundaries in the ground state exhibit a

universal representation, which is detailed in Chap. 3.

The finite-temperature phase boundaries for the weak coupling BCS regime are depicted in Fig. 2.5 in units of the gap $\Delta_0$ at zero temperature, while the projection to the ground state can be found in the universal $\bar{h} - \bar{\mu}$ representation in Fig. 3.1 in the next chapter. Finite temperatures in the connection with a Zeeman field have been studied first by Sarma [26], who found a tricritical point T at $(h/\Delta_0, T/\Delta_0)_T = (0.61, 0.31)$, where the order of the phase transition changes. For critical temperatures larger than $(T/\Delta_0)_T$ the transition is continuous and the endpoint at $h = 0$ is located at the inverse of the universal BCS-ratio $(\pi \exp(-\gamma_E))^{-1} = 0.57$, according to eq. (2.46). For temperatures below $(T/\Delta_0)_T$ the criterion of vanishing order parameter (dashed line), which assumes a second order phase transition between the normal and BCS state, predicts a backbending of the BCS-phase. However, due to the first order character of the transition encountered in this temperature range, the BCS phase remains the global minimum of the free energy and extends further to the blue line, which for $T \to 0$ terminates at the Clogston-Chandrasekhar(CC) limit $h_c = \Delta_0/\sqrt{2}$ [24, 25]. Within the region between these two boundaries a Sarma state [26] may exits as a metastable phase. The latter realizes a spin-imbalanced fermionic superfluid with two Fermi spheres of unequal size $k_\uparrow > k_\downarrow$, but with Cooper pairs with vanishing center-of-mass momentum $\mathbf{Q} = 0$, like in the standard BCS scenario. More specifically, the Sarma phase is characterized by a spectral gap below the Fermi level $\varepsilon_{F\uparrow}$ of the majority component, since pairing affects the states around the smaller Fermi energy $\varepsilon_{F\downarrow} < \varepsilon_{F\uparrow}$ of the minority species in order to form Cooper pairs with $\mathbf{Q} = 0$. As was shown by Fulde and Ferrell [27] and independently by Larkin and Ovchinnikov [28], superfluidity, however, does not immediately break down for fields beyond $h_c$. Instead, Fermions with opposite spin can form Cooper pairs with a finite $\mathbf{Q}_{\mathrm{FFLO}} \neq 0$, which provides a compromise between the tendency to pair and the mismatch of the two Fermi seas, induced by $h$. Larkin and Ovchinnikov furthermore investigated the thermodynamic stability of different spatial modulations of the order parameter. They found that the state which minimizes the free energy exhibits the spatial periodicity $\Delta(\mathbf{x}) \sim \cos(\mathbf{Q}_{\mathrm{FFLO}} \cdot \mathbf{x})$ [28] and therefore is more favorable than the plane-wave state $\Delta(\mathbf{x}) \sim \exp(i\mathbf{Q}_{\mathrm{FFLO}} \cdot \mathbf{x})$, used by Fulde and Ferrell [27]. Moreover, in the ground state the magnitude $|\mathbf{Q}_{\mathrm{FFLO}}|$ satisfies the relation [28]

$$\hbar v_F Q_{\mathrm{FFLO}} = 2.4h\,, \tag{2.52}$$

where $v_F = \hbar k_F/m$ denotes the Fermi velocity obtained from the total density $k_F = (3\pi^2 n)^{1/3}$. At zero temperature the FFLO phase, is located within the range $1/\sqrt{2} < h/\Delta < 0.754$ in the phase diagram 2.5. Solving the gap equation at finite temperatures with the option of a finite pairing vector $\mathbf{Q}$ yields the continuous N-FFLO transition line [110], which is plotted with red color in Fig 2.5. In fact, a later study by Buzdin and Kachkachi [111] and Combescot and Mora [112] revealed that the internal structure of this line is more complicated, since it has a first order part in the vicinity of the tricritical point, too. Furthermore the FFLO-ordered

phase itself may consist of various subphases, which are distinguished by different spatial structures of the order parameter, for details see the review [113].

Let us return to ultracold quantum gases of fermionic atoms. The fact that the individual populations of the trapped hyperfine states can be easily controlled in experiments, in contrast to the superconducting electronic condensed matter systems, motivated the study of the BCS-BEC crossover in the presence of spin imbalance, where the strongly coupled regime near unitarity attracted special interest. The experimental work on trapped Fermions with unequal populations of the hyperfine states was started in 2006 by Patridge et al. [30, 31] and by Zwierlein et al. [32]. Shin et al. [35] focused on the equation of state. Moreover, Shin et. al were also the first to measure the Clogston-Chandraskhar(CC) limit of the unitary gas [33, 34]. Using phase-contrast imaging, they found the universal ratio $(h/\mu)_c = 0.95$ for the transition out of the balanced superfluid in the limit $T \to 0$. This ratio was also investigated by Navon et al. [36], who extracted $(h/\mu)_c = 0.88$ from the experimental data.

On the theoretical side, a qualitative, yet very complete picture of the phase diagram of the imbalanced Fermi gas at zero temperature, including an FFLO phase even at positive scattering lengths, has been obtained by Son and Stephanov [2] from a description based on effective field theory. We will discuss their results in detail in the next chapter, dedicated to the phase diagram in the ground state. Using the expansion around a narrow Feshbach resonance, which allows for a mean-field description within BCS theory, the phase diagram as function of $h$ and $(k_F a)^{-1}$ has been computed by Sheehy and Radzihovsky [69] in the ground state and at finite temperatures by Parish et al. [68]. Moreover, a related large-N expansion has been performed to leading order by Nikolič and Sachdev [1], as well as to next-to-leading order by Veillette et al. [70]. Apart from that, a Quantum Monte Carlo computation by Goulko and Wingate [89] investigated the critical temperature of the unitary gas with small imbalance and a very recent work by Rammelmüller et al. [114] obtained the universal density scaling function $n(\beta\mu, \beta h)/n^{(0)}(\beta\mu, \beta h = 0)$ of the resonant gas from a complex Langevin method. However, so far no quantitatively reliable results for the pressure scaling function $f_p(\mu, h, \lambda_T/a)$ at arbitrary temperatures and scattering lengths have been obtained beyond the mean-field level.

Motivated by the results of the Luttinger-Ward study by Haussmann et al. [37] for the spin-balanced Fermi gas, which agree very well with the measurments by Ku et al. [58], it is the main goal of this thesis to extend this approach to finite Zeeman fields and thereby obtain quantitative results about the phase diagram and the thermodynamic quantities that can be tested experimentally. Another argument in favor of this method, is the possibility to study both resonant and non-resonant interactions at finite $T$, including the possibility to extrapolate towards $T = 0$,

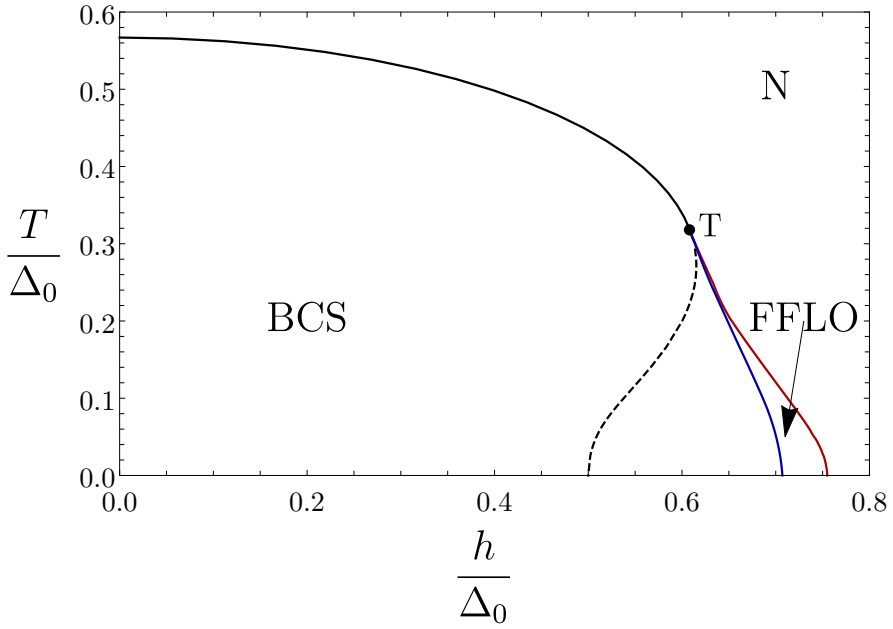


Figure 2.5: Phase diagram of the imbalanced gas in the weak coupling BCS limit. The black line indicates the second order phase transition between the normal and the BCS superfluid that ends at the tricritical point T. Between the black dashed line and the blue line the Sarma solution may exist as a metastable state. The blue line also indicates the first order transition between the homogeneous superfluid and the FFLO state. The red phase boundary marks the continuous transition to the normal state.

## 2.4 Tan relations and their consequences for the thermodynamics of Fermi gases with zero-range interactions

To close this introductory chapter we state the Tan relations in Sec. 2.4.1. First we consider the microscopic definition in the context of the zero-range limit of the interaction potential before we turn to their implications for the thermodynamic properties of the Fermi gas. Afterwards in Sec. 2.4.2, we turn to further thermodynamic quantities, like the specific heat, the compressibility and the Landau-Placzek ratio, which are also influenced by the Tan relations. However, we will concentrate mainly on the unitary gas.

### 2.4.1 Tan relations

Quite remarkably, as discovered by Shina Tan [38–40], fermionic quantum many-body systems with zero-range interactions satisfy a number of exact relations in three dimensions[12]. They involve a central new observable: the extensive Tan contact $C$. Since these relations follow from an operator product expansion [117], they hold irrespective of the state of the system. Therefore, $C$ attains a state-dependent value, while the form of the equations remains invariant. In this section, we will first introduce the contact from a microscopic perspective and then focus on its implications for the laws of thermodynamics. Both points of view will play a role for the implementation of the Luttinger-Ward formalism, later on. Again, we follow the lectures [42] but generalize some of the equations to the situation with finite spin-imbalance. Further details on the Tan relations and their physical consequences, in particular also on nonequilibrium observables, can be found in the review by Braaten [118].

Microscopically, the contact is related to the short-range correlations of the system. In a spatially inhomogeneous system the contact density $\mathcal{C}(\mathbf{x})$ becomes a function of the position $\mathbf{x}$. It is defined via the zero-range limit of the expectation value [42]

$$\frac{\hbar^4}{m^2}\mathcal{C}(\mathbf{x}) = \lim_{\Lambda\to\infty} \bar{g}^2(\Lambda)\langle \hat{O}_c(\mathbf{x})\rangle = \lim_{\Lambda\to\infty} \bar{g}^2(\Lambda)\langle \hat{\Psi}^\dagger_\uparrow(\mathbf{x})\hat{\Psi}^\dagger_\downarrow(\mathbf{x})\hat{\Psi}_\downarrow(\mathbf{x})\hat{\Psi}_\uparrow(\mathbf{x})\rangle\,. \tag{2.53}$$

This product of operators times the squared bare coupling constant $\bar{g}^2(\Lambda)$ turns out to be finite, when the cutoff is sent to infinity. This can be verified from the physical assumption that the total energy density $\varepsilon = \langle \hat{H}\rangle/V = \langle \hat{H}_{\mathrm{kin}} + \hat{H}_{\mathrm{int}}\rangle/V$ must be finite and a smooth function of $1/a$. Hence, taking the derivative of $\varepsilon$ with respect to the scattering length, must yield a well-defined quantity, too. Applying the Hellmann-Feynman theorem gives rise to

$$\frac{\partial\varepsilon}{\partial a} = \frac{\partial}{\partial a}\bar{g}(\Lambda)\langle \hat{O}_c(\mathbf{x})\rangle = \frac{\bar{g}^2(\Lambda)}{ag}\langle \hat{O}_c(\mathbf{x})\rangle\,, \tag{2.54}$$

where we have used (2.31) with $d = 3$ and the relation $g = 4\pi\hbar^2 a/m$. In the following, we restrict our discussion to spatially homogeneous systems, where the contact density becomes a constant $\mathcal{C}(\mathbf{x}) \equiv \mathcal{C}$. This microscopic definition of $\mathcal{C}$ will entail a connection to the vertex function of the Luttinger-Ward formalism, detailed in Section 4.5. Furthermore, we obtain a direct consequence for the thermodynamic properties of a system with zero-range interactions, since we can combine the last two equations, such that

$$\frac{\partial\varepsilon}{\partial a^{-1}} = -\frac{\hbar^2}{4\pi m}\mathcal{C}\,, \tag{2.55}$$

[12] Equivalents of the Tan relations also exist in $d = 1$ [115] and $d = 2$ [116].

which is a special formulation of the Tan adiabatic theorem from eq. (2.59) for homogeneous systems. In particular, knowledge of the contact density as a function of $a$ allows to determine the energy density by integrating the above equation starting from the non-interacting limit. In addition, the total energy density is the sum of the kinetic and interaction energy densities: $\varepsilon = \varepsilon_{\text{kin}} + \varepsilon_{\text{int}}$. Since $\varepsilon_{\text{int}} = \bar{g}(\Lambda)\langle\hat{O}_c(\mathbf{x})\rangle \sim \Lambda\,\mathcal{C}(\mathbf{x})$ diverges in the limit $\Lambda \to \infty$, also $\varepsilon_{\text{kin}}$ does in order to obtain a finite $\varepsilon$. In case of a homogeneous system we have for the complete expression

$$\varepsilon = \sum_{\sigma} \int \frac{d^3k}{(2\pi)^3} \varepsilon_k n_\sigma(\mathbf{k}) + \bar{g}^{-1}(\Lambda) \frac{h^4 \mathcal{C}}{m^2}\,, \tag{2.56}$$

where $n_\sigma(\mathbf{k})$ denotes the momentum distribution of the spin component $\sigma$. We can eliminate the cut-off dependence by replacing the bare coupling constant via (2.29) and find the Tan energy theorem [38].

$$\varepsilon = \sum_{\sigma} \int \frac{d^3k}{(2\pi)^3} \varepsilon_k \left[ n_\sigma(k) - \frac{\mathcal{C}}{k^4} \right]. \tag{2.57}$$

From this relation we immediately conclude that the momentum distribution must acquire an asymptotic tail $\sim \mathcal{C}/k^4$ to render the total energy density finite. When we implement the self-consistent equations of the Luttinger-Ward approach in Chapter 4, we have to keep this interaction-induced asymptotics in mind, because the formalism requires the repeated calculation of Fourier transforms of the single-particle Green's function $\mathcal{G}_{\sigma\sigma}(\mathbf{k}, \tau)$, which is related to the momentum distribution via $n_\sigma(k) = \mathcal{G}_{\sigma\sigma}(\mathbf{k}, 0^-)$. Consequently, the numerical routines must be able to deal with algebraically decaying functions.

Furthermore, equation (2.55) implies that the contact density is also connected to the change of the scaling functions (2.34) and (2.39) upon a variation of the scattering length. To gain further insight concerning this relation, we consider the Tan contact from general thermodynamic grounds. The many-body problem of a dilute fermionic quantum gas, that exhibits an open-channel dominated Feshbach resonance, is quite special, since the interactions depend only on a single observable quantity, namely the scattering length, which in addition can be tuned by varying the external magnetic field strength. Therefore, one can extend the standard dependence of the free energy $F$ on the variables $T$, $V$ and $N_\sigma$ by the new argument $1/a$, which is conjugate to the macroscopic, generalized thermodynamic force $X_{1/a}$ [119], such that the differential $dF$ reads

$$dF(T, V, N_\sigma, 1/a) = -S dT - p dV + \sum_{\sigma} \mu_\sigma dN_\sigma + X_{1/a}\, d\left(\frac{1}{a}\right). \tag{2.58}$$

Performing the Legendre transformation from the microcanonical internal energy $U(S)$, as function of the entropy $S$, to $F(T)$, as function of the temperature, while

keeping the other arguments fixed, reveals that we can identify this force with the contact $C$. This follows from

$$X_{1/a} = \left(\frac{\partial F}{\partial(1/a)}\right)_{T,V,N_\sigma} = \left(\frac{\partial U}{\partial(1/a)}\right)_{S,V,N_\sigma} = -\frac{\hbar^2}{4\pi m}\int d^3x\, \mathcal{C}(\mathbf{x}) = -\frac{\hbar^2 C}{4\pi m}\,, \tag{2.59}$$

where we have inserted the result (2.55) on the right-hand side to be consistent with the microscopic approach. This thermodynamic identity is called the Tan adiabatic theorem [38]. In the grand canonical formulation it reads

$$\left(\frac{\partial \Omega}{\partial(1/a)}\right)_{T,V,\mu,h} = -\frac{\hbar^2}{4\pi m} C \tag{2.60}$$

or expressed in terms of the universal pressure scaling function (2.34) we have

$$\left(\frac{\partial p}{\partial(1/a)}\right)_{T,\mu,h} = p^{(0)}(T,\mu)\left(\frac{\partial f_p}{\partial(\lambda_T/a)}\right)_{\beta\mu,\beta h} = \frac{\hbar^2}{4\pi m}\mathcal{C}\,. \tag{2.61}$$

Another intriguing relation for a uniform system is the Tan pressure relation

$$p = \frac{2}{3}\varepsilon + \frac{\hbar^2}{12\pi m a}\mathcal{C}\,, \tag{2.62}$$

which results from a simple scaling argument. To see this and also for later convenience, we introduce the variables

$$N = N_\uparrow + N_\downarrow \tag{2.63a}$$
$$\delta N = N_\uparrow - N_\downarrow\,. \tag{2.63b}$$

Now, the free energy can be written in terms of a scaling function $f_F$ in a similar manner as $f_p$ in eq. (2.34). Assuming that the quantum many-body problem with attractive zero-range interactions has a well-defined thermodynamic limit, where $F$ is an extensive quantitiy, we define $f_F$ via

$$F(T, N_\sigma, V, 1/a) = N\varepsilon_F f_F(\theta, \delta N/N, v)\,, \tag{2.64}$$

Here we have used the total density $n = n_\uparrow + n_\downarrow$ to set the overall length and energy scales by the inverse Fermi wave vector $k_F$ and the corresponding Fermi energy $\varepsilon_F$

$$k_F = (3\pi^2 n)^{-1/3} \tag{2.65a}$$
$$\varepsilon_F = h^2 k_F^2/(2m) \tag{2.65b}$$

of the corresponding spin-balanced, ideal Fermi gas. We will stick to this notation throughout the remainder of the thesis. In particular, this definition has to be

distinguished carefully from the definition $k_{F\sigma} = (6\pi^2 n_\sigma)^{1/3}$ and $\varepsilon_{F\sigma} = \hbar^2 k_{F\sigma}^2/(2m)$ of a single-component Fermi gas with spin orientation $\sigma$, which is frequently used in the literature, too. Furthermore, on the right-hand side of equation (2.64) we have introduced the reduced temperature

$$\theta = \frac{T}{\varepsilon_F} \tag{2.66}$$

and the dimensionless interaction strength

$$v = \frac{1}{k_F a} \tag{2.67}$$

and for later convenience we also define the dimensionless chemical potential

$$\tilde{\mu} = \frac{\mu}{\varepsilon_F} \tag{2.68}$$

and the Zeeman field

$$\tilde{h} = \frac{h}{\varepsilon_F}\,. \tag{2.69}$$

If we rescale $a \to a/\sqrt{\lambda}, T \to \lambda_T$ and $V \to \lambda^{-3/2}V$, while the particle numbers $N_\sigma$ remain fixed, we obtain from the scaling form of the free energy

$$F(\lambda T, N_\sigma, \lambda^{-3/2}V, \sqrt{\lambda}/a) = \lambda F(T, N_\sigma, V, 1/a)\,. \tag{2.70}$$

Taking the derivative of this equation with respect to $\lambda$ in combination with the standard form of $dF$ in (2.58) yields the Tan pressure relation (2.62) by setting $\lambda = 1$. The latter relation also leads to the conclusion that the unitary gas satisfies the scale-invariance condition $p = 2/3\,\varepsilon$ from eq. (2.42), since $\mathcal{C}$ is finite for all sets of thermodynamic parameters, as discussed in [42], while $1/a = 0$ vanishes at resonance. In Chap. 4.7 we will use the Tan pressure relation to construct a consistency check for the numerical results of the Luttinger-Ward approach.

Physically, the Tan contact originates genuinely from interaction effects. As discussed by Zwerger [42], the zero-range interactions imply the following short-range correlations: The number of $\uparrow$ atoms located within a sphere of radius $b$, with $r_e < b \ll n^{-1/3}$, $\lambda_T$ scales linearly with the radius $N_\uparrow(b \to 0) = C/(4\pi n_\uparrow) \cdot b$, in contrast to a noninteracting gas, where $N_\uparrow$ scales with the volume of the sphere due to the trivial correlations between the spin components. Similarly, the noninteracting Green's functions (4.10) do not show an algebraic tale $\sim \mathcal{C}/k^4$ but an exponential behavior. From a macroscopic perspective the Tan contact measures how the thermodynamic properties of the system change with the scattering length. In particular, in the weakly interacting BCS and BEC limits of the spin-balanced

gas the $C$ can be determined from standard expansion of the of the ground-state energy density in terms of the gas parameter $na^3$. For $a \to 0^-$ this yields [42]

$$\mathcal{C} = k_F^4 \left(\frac{2k_F a}{3\pi}\right)^2 \left(1 + \frac{12(11 - 2\ln 2)}{35\pi} k_F a + ...\right), \tag{2.71}$$

where the leading term arises from the mean-field interaction $\varepsilon_{MF} = gn^2/4 \sim ak_F^6$. In the opposite limit $a \to 0^+$ one finds asymptotically [42]

$$C = k_F^4 \left(\frac{4}{3\pi k_F a} + 0.6 \left(\frac{k_F a}{3\pi}\right)^2 + ...\right), \tag{2.72}$$

whose dominant term arises from the contribution of the two-body bound states $\varepsilon = n/2\varepsilon_B + ...$ to the total energy density. Regarding the strongly interacting regime, the contact density has been computed at arbitrary interaction strengths for the balanced Fermi gas within the Luttinger-Ward approach [37]. At unitarity the numerical result therefrom for the ground state gives rise to a universal number $s_0 = 0.102$, with $\mathcal{C}(1/k_F a = 0) = s_0 k_F^4$. Experimentally, the contact has been measured via Bragg spectroscopy [120, 121]. The obtained result $c_0 = 3\pi s_0 = 3.17 \pm 0.09$, which involves both trap-averaging and the extrapolation to $T = 0$, is close to the theoretical prediction $c_0 = 3.02$.

Taking the opposite, noninteracting limit, the contact density vanishes like $a^2$, as can be seen from eq. (2.71), in agreement with the previous arguments that $\mathcal{C}$ is intrinsically related to the zero-range interactions. Similarly, in a single-component Fermi gas the contact density is also $\mathcal{C}$ zero, since the zero-range interactions affect only atoms of opposite spin. In the limit of extreme imbalance $\mathcal{C}$ scales to zero linearly with the density $n_\downarrow$ of minority atoms, that are immersed in a background of majority atoms with finite density $n_\uparrow$, as noted by Punk et al. [122]. This conclusion follows from the expansion of the total energy density in the presence of a small density of minority atoms $n_\downarrow$

$$\varepsilon = \frac{3}{5} n_\uparrow \varepsilon_{F\uparrow} + \mu_\downarrow n_\downarrow + ... . \tag{2.73}$$

The first term describes the energy of the bare Fermi sea of the majority component, while the second one incorporates the lowest order energy gain by adding a small density of impurities, which is characterized by $\mu_\downarrow$ [80]. Using the definition (2.55) we indeed obtain the linear relation [122]

$$\mathcal{C} = \frac{4\pi m}{\hbar^2} \left(\frac{\partial \mu_\downarrow}{\partial a^{-1}}\right) n_\downarrow . \tag{2.74}$$

The Luttinger-Ward computation presented in the following chapters allows to extract the contact density as function of the temperature, the scattering length and the Zeeman field. In particular, we are able to extend the theoretical predictions

regarding $\mathcal{C}$ in the strong coupling regime to finite spin imbalance. Furthermore, we develop a consistency check for the numerical results, which is based on the Tan pressure relation (2.62). Now we turn to further thermodynamic quantities in connection with the Tan contact, which are also accessible by our computations.

### 2.4.2 Further thermodynamic relations

Apart from the crossover within the superfluid at very low temperatures also the finite temperature phase transition between the normal and the superfluid poses an interesting problem. Since this transition is a continuous one, it is revealed by sharp features appearing in the second derivatives of the thermodynamic potential, which in the context of ultracold Fermions has first been pointed out in Ref. [58]. Examples for such quantities are the specific heat per particle $\tilde{c}_V = C_V/N = T/N\,(\partial S/\partial T)$, which within the formulation (2.64) can be written as

$$\tilde{c}_V = -\frac{1}{N}\left(\frac{\partial^2 F}{\partial T^2}\right)_{N,\delta N,V,1/a} = -\theta\frac{\partial^2 f_F}{\partial\theta^2}\,, \tag{2.75}$$

similarly to the isothermal compressibility $\kappa_T = -V^{-1}(\partial V/\partial p)_T$, which has been measured by Ku et. al [58] in case of the unitary spin-balanced gas. With $p = -\partial F/\partial V$ with $N, \delta N, T, 1/a$ fixed, we obtain from eq. (2.64) at $1/a = 0$ and arbitrary spin imbalance

$$\frac{\kappa_T^{(0)}}{\kappa_T} = \frac{p}{p^{(0)}} + \theta^2\frac{\partial^2 f_F}{\partial\theta^2}\,. \tag{2.76}$$

In order to normalize the pressure and the compressibility we have divided them by their non-interacting counterparts $p^{(0)} = 2/5\,n\varepsilon_F$ and $\kappa_T^{(0)} = 3/(2n\varepsilon_F)$. Comparing the latter two equations gives rise to the simple relation

$$\tilde{c}_V = \frac{3}{2\theta}\left(\frac{p}{p^{(0)}} - \frac{\kappa_T^{(0)}}{\kappa_T}\right)\,, \tag{2.77}$$

which implies an upper bound on the specific heat

$$\tilde{c}_V^{\max} = \frac{3}{2\theta}\frac{p}{p^{(0)}}\,, \tag{2.78}$$

since any stable system requires a non-negative $\kappa_T$. In particular, this relation also holds at the critical temperature below which the unitary gas becomes superfluid. This transition belongs to the universality class of the $d = 3$ XY-model [123], which implies the corresponding specific heat exponent $\alpha \simeq -0.01$ and the universal amplitudes $c_+/c_- \simeq 1.05$, such that the leading, nonanalytic temperature dependence of the specific heat is given by

$$\tilde{c}_V(t) = c_V(T_c) - c_\pm|t|^{-\alpha} + \ldots\,, \tag{2.79}$$

as a function of the dimensionless temperature $t = (T - T_c)/T_c = (\theta - \theta_c)/\theta_c$. The very small and negative value of $\alpha$ yields a finite value $\tilde{c}_V(\theta_c)$, which is very difficult to detect, since the associated peak becomes very narrow. Using the experimental data of the unitary gas [58] $p_c \simeq 0.51 p^{(0)}$ near the critical temperature $\theta_c \simeq 0.16$ of the finite system, we conclude for the bound (2.78) $\tilde{c}_V \leqslant \tilde{c}_V^{\max} = 4.8$. Comparing that result to the largest measured value $\tilde{c}_V \simeq 2.3$ [58], we find that the observed peak roughly exhausts 50% of the allowed bound, probably because of the finite size of the sample and the limited resolution of the experimental devices.

The way to formulate thermodynamic relations in terms of scaling relations has been crucial for the experiment by Ku et al. [58]. As detailed by Zwierlein [124], the high-precision measurement of the equation of state of the unitary balanced gas is based on the representation for the pressure in terms of the density, which we can readily generalize to arbitrary scattering lengths and spin imbalances

$$p(T, n, \delta n, 1/a) = p^{(0)} \tilde{f}_p(\theta, \sigma, v) \,, \tag{2.80}$$

where the spin polarization $\sigma$ is defined in (2.38). Using this definition to compute the isothermal compressibility $\kappa_T$, we find

$$\frac{\kappa_T}{\kappa_T^{(0)}} = \left[ \tilde{f}_p - \frac{2}{5}\theta \left(\partial_\theta \tilde{f}_p\right) - \frac{1}{5} v \left(\partial_v \tilde{f}_p\right) \right]^{-1} \,, \tag{2.81}$$

where no derivative with respect to $\sigma = \delta N/N$ appears, since the compressibility is only sensitive to changes of the volume at fixed particle numbers $N_\sigma$. The last term, which is related to the Tan contact, obviously vanishes at unitary, which was crucial for the experimental procedure. Based on the observed data for the pressure $p$ and $\kappa_T$ as a function of $p$ one can integrate the differential equation for $(\partial_\theta \tilde{f}_p)$ at unitarity and obtain the dimensionless temperature [58]

$$\theta = \theta_i \exp\left( \int_{(p/p^{(0)})_i}^{p/p^{(0)}} dy \left[ y - \frac{\kappa_T^{(0)}}{\kappa_T}(cy) \right]^{-1} \right) , \tag{2.82}$$

where the pair of initial conditions $\{\theta_i, (p/p^{(0)})_i\}$ can be chosen from the nondegenerate regime at high temperatures.

In the more general setting of finite scattering lengths and spin imbalance, however, the gas is not scale invariant and the last term in eq. (2.81) yields a finite contribution. In a trap the function $v\partial_v \tilde{f}_p$ is nontrivial, since even the prefactor $v$ depends on position via the density profile $n(\mathbf{x})$. In particular, this term can be related to the Tan contact. The latter is a function of the thermodynamic variables, such that we can define

$$C(T, N, \delta N, V, 1/a) = V k_F^4 \, \tilde{f}_{\mathcal{C}}(\theta, \sigma, v) \,, \tag{2.83}$$

with an intensive, dimensionless scaling function $\tilde{f}_{\mathcal{C}}$ for the contact density. With this definition we can relate the derivative $\partial_v \tilde{f}_p$ to the contact

$$\begin{aligned}\frac{\partial \tilde{f}_p}{\partial v} &= \frac{k_F}{p^{(0)}} \left(\frac{\partial p}{\partial a^{-1}}\right)_{T,N,\delta N,V} = -\frac{k_F}{p^{(0)}} \frac{\partial}{\partial V} \frac{\partial F}{\partial (a^{-1})} = \frac{k_F}{p^{(0)}} \frac{\partial}{\partial V} \frac{\hbar^2}{4\pi m} V k_F^4 \, \tilde{f}_{\mathcal{C}}(\theta, \sigma, v) \\ &= \frac{5}{4\pi^2} \left[ -\tilde{f}_{\mathcal{C}} + 2\theta \frac{\partial \tilde{f}_{\mathcal{C}}}{\partial \theta} + v \frac{\partial \tilde{f}_{\mathcal{C}}}{\partial v} \right] .\end{aligned} \tag{2.84}$$

However, a direct application of the right-hand side requires to measure the contact and its derivatives locally in the trap, which has not been achieved so far.

Finally, we discuss the Landau-Placzek ratio of the unitary Fermi gas. In general, it is defined as the relative difference of the specific heats at fixed pressure and fixed volume

$$\mathrm{LP} := \frac{C_p}{C_V} - 1 \,, \tag{2.85}$$

which can be rewritten in the form [119]

$$\mathrm{LP} = \frac{T \alpha_p^2}{c_V \kappa_T} \,. \tag{2.86}$$

The thermal expansion coefficient

$$\alpha_p = \frac{1}{V} \left(\frac{\partial V}{\partial T}\right)_p = \kappa_T \gamma \, c_V \tag{2.87}$$

includes the Grüneisen parameter $\gamma$ [125], which for the unitary gas reduces to the universal number $\gamma = 2/3$ due to the scale invariance condition $p = 2/3\varepsilon$ [42]. The thermal pressure coefficient is also related to the Grüneisen parameter via

$$\beta_V = \left(\frac{\partial p}{\partial T}\right)_V = \gamma \, c_V = \frac{\alpha_p}{\kappa_T} \,. \tag{2.88}$$

Furthermore, scale invariance implies the special relation [42]

$$T \beta_V = \frac{5}{2} p - \frac{3}{2} \frac{1}{\kappa_T} \,. \tag{2.89}$$

Based on these considerations we can express the Landau-Placzek ratio of the unitary Fermi gas in the form

$$\mathrm{LP} = \frac{5}{3} p \kappa_T - 1 \,, \tag{2.90}$$

which contains only quantities that are directly accessible in the experimental setup of Ku et al. [58]. To obtain this particular form we have replaced one factor of $\alpha_p$

in equation (2.86) via eq. (2.87) and the other one by the combination of eqs. (2.88) and (2.89). Alternatively, we can use these relations to write

$$\mathrm{LP} = \frac{2}{3}\theta\frac{\kappa_T}{\kappa_T^{(0)}}\tilde{c}_V\,. \tag{2.91}$$

This reveals that $\mathrm{LP}(T \to 0) \sim T^4$ because of the scaling $\tilde{c}_V \sim T^3$ in the limit of very small temperatures where only phonons contribute to the internal energy of the superfluid, while $\kappa_T/\kappa_T^{(0)} \to 1/\xi_s$ approaches a universal constant. In the high temperature regime we can apply the virial expansion to LP. In particular, including the first nontrivial virial coefficient $a_2 = -3/(4\sqrt{2})$ [126] of the unitary gas leads to the asymptotic behavior [42]

$$p = nT(1 - \frac{1}{\sqrt{2\pi}\theta^{3/2}} + ....)\,. \tag{2.92}$$

This implies that the Landau-Plazcek ratio of the unitary gas reads

$$\mathrm{LP} = \frac{2}{3} + \frac{5}{3\sqrt{2\pi}\theta^{3/2}} + ...\,, \tag{2.93}$$

such that the value of the ideal classical gas $\mathrm{LP}_{\mathrm{cl}}^{(0)} = 2/3$ is approached from above. Consequently, LP is a nonmonotonic function. A quantitative comparison between the Luttinger-Ward theory and the experimental data can be found in Fig 5.12.

# Chapter 3

# Universal ground state phase diagram of the imbalanced Fermi gas

In this chapter we present the universal phase diagram in the ground state in the $\bar{h} = 2h/(\varepsilon_B)$ vs. $\bar{\mu} = 2\mu/\varepsilon_B$ representation introduced above the definition of the pressure scaling function $f^{\pm}(\bar{\mu}, \bar{h})$ at $T = 0$, defined in eq. (2.39). The phase boundaries themselves are revealed as nonanalyticities in $f^{\pm}(\bar{\mu}, \bar{h})$. As discussed in Sec. 2.3.1, the latter allows to split the discussion into the cases $1/a < 0$, $1/a = 0$ and $1/a > 0$. We begin with the universal phase diagram in the well-understood weak coupling regime for negative scattering lengths, that we have already discussed at finite temperatures in Sec. 2.3.3 and which allows to draw general conclusions about the structure of the phase diagram beyond the weak coupling limit. Afterwards, we turn to the unitary limit, where $f_p = f(h/\mu)$ (see. eq. (2.40)) depends only on $h/\mu$, and close the chapter with the case of positive scattering lengths. A similar presentation can be found in Ref. [78].

## 3.1 Phase diagram for $1/a < 0$ and general aspects of the $T = 0$ phase diagrams

We begin with the discussion of the ground state phase diagram in the weak coupling limit, shown in Fig. 3.1. To obtain a finite density of particles at least $\mu_\uparrow = \mu + h$ has to be positive, which translates to the condition $h = |\mu|$ for the transition from the vacuum. For $\mu_\uparrow > 0$ and $\mu_\downarrow < 0$ the system forms a fully polarized, non-interacting Fermi sea of $\uparrow$ spins denoted by $N_{\Omega_\uparrow}$. It extends up to the saturation field line $h_s = \mu$, while for $h < h_s$ a finite density of minority atoms accumulates. The given criterion for $h_s$ is equivalent to $\mu_\downarrow = 0$, which marks the onset of a finite density of $\downarrow$-atoms in an ideal Fermi gas. In the BCS limit we have the same criterion for $h_s$, because pairing only gives rise to an exponentially small corrections to the thermodynamic potential and therefore to all thermodynamic functions, as can be seen from eqs. (A.19) and (2.45). The normal phase $N_{\Omega_\uparrow > \Omega_\downarrow}$, which emerges for $\bar{h} < \bar{h}_s$ at $\bar{\mu} > 0$, consequently has two Fermi seas with two different volumes $\Omega_\uparrow$ and $\Omega_\downarrow$. Possibly, this phase is unstable towards p-wave superfluidity in a spin-triplet configuration, where the interactions responsible for the pairing are mediated by the minority component. In the weak coupling limit this

has first been discussed by Kagan. [127], however, for weakly repulsive interactions $k_F a \ll 1$ and more recently by Patton and Sheehy at unitarity [128]. In the following, however, we will neglect this possibility and assume a normal Fermi liquid in this regime, which is consistent with experiments at ENS [129]. For even smaller $h$ we recover the s-wave superfluid order already discussed in Sec. 2.3.3. To find the $T = 0$ phase boundaries of the superfluid states with different orders, expressed in terms of the universal variables, we combine the CC-criterion $h_c = \Delta_0/\sqrt{2}$, as well as the FFLO equivalent $h_{\mathrm{FFLO}} = 0.754\Delta_0$, with the asymptotically exact form of the gap from eq. (2.45). As a result, one finds

$$\bar{h}_c(\bar{\mu} \ll 1) = \frac{(2/e)^{7/3}}{\sqrt{2}} \bar{\mu}\, e^{-\pi/(2\sqrt{\bar{\mu}})} \tag{3.1a}$$

$$\bar{h}_{\mathrm{FFLO}}(\bar{\mu} \ll 1) = 0.754\,(2/e)^{7/3} \bar{\mu}\, e^{-\pi/(2\sqrt{\bar{\mu}})}\,, \tag{3.1b}$$

for the dimensionless fields, where we have again made use of the weak-coupling substitution $\varepsilon_F \to \mu$, which is correct up to terms of order $\Delta^2$. In particular, note that the spin-balanced superfluid $\mathrm{SF}_0$ ceases to exist for Zeeman fields larger than $h_c$. Since the entire phase diagram is described in terms of a single unique scaling function, as we have discussed in the context of eq. (2.40), all phases and their boundaries have to be smoothly connected to the limit $1/a \to 0$. This means that for $\bar{\mu} \gg 1$ all the three functions $\bar{h}_s$, $\bar{h}_c$ and $\bar{h}_{\mathrm{FFLO}}$ must cross over to the linear phase boundaries of the unitary limit, shown in Figure 3.2, unless one would hit another phase transition. The continuation is indicated by the dashed parts of the $\bar{h}_c$ and $\bar{h}_{\mathrm{FFLO}}$ curves in Fig. 3.1. Furthermore, the existence of an FFLO phase at unitary is consistent with the effective field theory picture developed by Son and Stephanov [2] (see Fig 3.4), which will be discussed in more detail below. As will be shown in Chapter 5, the presence of an FFLO instability at $1/a$ is also confirmed by the Luttinger-Ward formalism deployed in this thesis.

Leaving the weak-coupling limit several conclusions from this well-understood regime can be generalized to arbitrary interaction strengths. First of all, strongly negative chemical potentials always entail a vacuum phase. By increasing $\mu_\uparrow$ or equivalently $\mu$, while simultaneously keeping either small $\mu_\downarrow$ or large $h$ enters a fully polarized phase $N_{\Omega_\uparrow}$ from the vacuum. Decreasing $h$ in this situation makes the occupation of the minority component more favorable until its onset is finally encountered at the saturation field line $h_s$. On the other hand the balanced superfluid $\mathrm{SF}_0$ extends from $h = 0$ to its boundary at the critical field line $\bar{h}_c > 0$, since the existence of a finite energy gap for single-fermion excitations stabilizes the superfluid order against finite $h \geqslant 0$.

Another general result for arbitrary interaction strengths has been obtained by Sachdev and Yang [130], who related the population difference to the volumes of the Fermi seas $\Omega_\uparrow, \Omega_\downarrow$ in form of a Luttinger theorem

$$\delta n = \frac{\Omega_\uparrow - \Omega_\downarrow}{(2\pi)^3}\,. \tag{3.2}$$

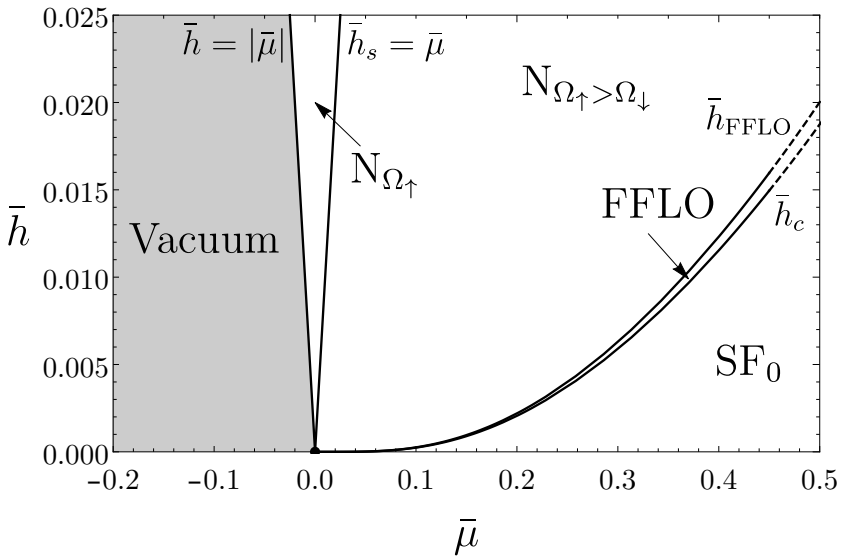


Figure 3.1: Universal phase diagram for negative scattering length. The various phases are denoted as normal phase $\mathrm{N}_{\Omega_\uparrow}$ for the fully polarized ideal gas, $\mathrm{N}_{\Omega_\uparrow > \Omega_\downarrow}$ for the partially polarized normal phase, $\mathrm{SF}_0$ for the balanced superfluid and FFLO for the inhomogenous superfluid. The dashed continuation of $\bar{h}_c$ and $\bar{h}_{\mathrm{FFLO}}$ indicates the crossover toward the unitary regime.

This relation holds for spatially homogeneous phases with or without order. However, in case of a broken translation invariance, like in FFLO phases, one has to take the right-hand side modulo the volume of the first Brilliouin zone connected to the emergent spatial periodicity. As a result, any phase with finite $\delta n$ requires at least on Fermi sea.

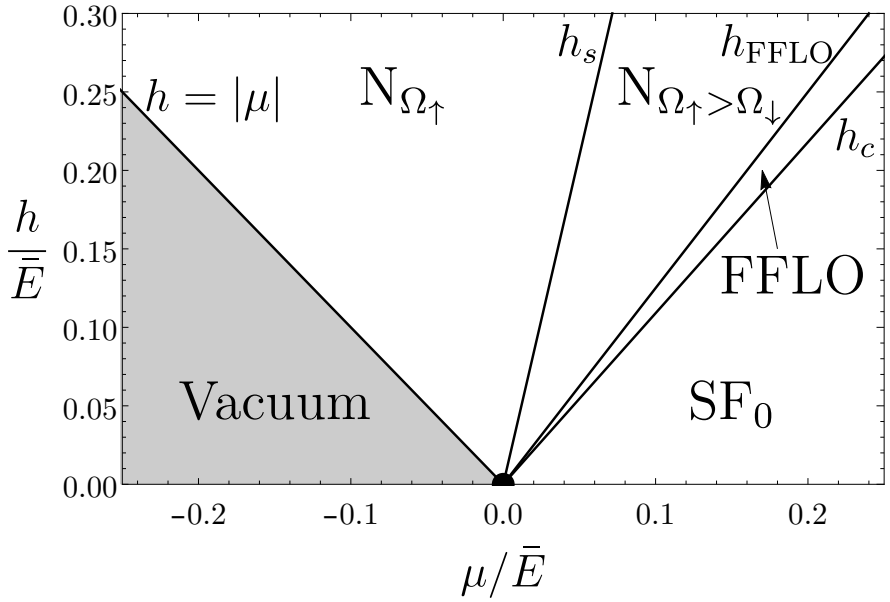


Figure 3.2: Phase diagram for the ground state at resonance. The labeling of the phases is the same as in fig. 3.1.

## 3.2 Phase diagram at $1/a = 0$

After these considerations about the global structure of the phase diagram, we turn now to the unitary case, which is shown in Fig. 3.2. The fact that all phase boundaries are straight lines originates again from the scale invariance. As discussed above eq. (2.40), the pressure scaling form of the unitary gas at zero temperature can be written as $f_p(h/\mu)$, whose arguments are reduced to the single ratio $h/\mu$. Since phase transitions are encoded in $f_p$ as nonanalyticities, universal values of $h/\mu$ exhaust the forms of the phase boundaries in analogy to the finite temperature phase diagram of the balanced unitary gas, represented in Fig. 2.4. Due to the absence of interactions, the emergence of a fully polarized gas from the vacuum takes place at $h = |\mu|$, like on the BCS side. The saturation field line in turn acquires a slope of $(h/\mu)_s \geqslant 1$, because of the strong attractions between a single $\downarrow$-impurity and the Fermi sea of the background $\uparrow$-atoms, which gives rise to the formation of a Fermi polaron. The precise value of this ratio follows from the argument by Chevy [80] that $\mu_\downarrow$ is equal to the ground state energy gain of the polaron. Using the BDMC results from Prokof'ev and Svistunov, who find $(\mu_\downarrow/\mu_\uparrow) = -0.615$ [131] at unitarity, one obtains

$$\left(\frac{h}{\mu}\right)_s = \frac{1 - \mu_\downarrow/\mu_\uparrow}{1 + \mu_\downarrow/\mu_\uparrow} = 4.19\,. \tag{3.3}$$

Regarding the partially polarized normal phase $\mathrm{N}_{\Omega_\uparrow > \Omega_\downarrow}$, located between $\bar{h}_s$ and $\bar{h}_{\mathrm{FFLO}}$, results by Patton and Sheehy [128] from a non-self-consistent diagrammatic theory for the attractive branch of the unitary Fermi gas yield the very low critical temperature $T_c \simeq 0.03\,\varepsilon_{F\uparrow}$ for p-wave pairing. As already mentioned, we will not consider this kind of order any further and assume instead a Fermi liquid.

The CC-limit $(h/\mu)_c$ at unitarity has been addressed in several studies. A comparison of the available results to the Luttinger-Ward value can also be found in Table 5.1 in Section 5.3.1. Lobo et al. [132] determine the ratio $(h/\mu)_c = 0.96$, while the more recent FRG-computation by Boettcher et al. [133] finds $(h/\mu)_c = 0.83$. The leading order $1/N$-expansion yields $(h/\mu)_c = 0.807...$ [1], which, however, becomes substantially changed to $(h/\mu)_c = 1.974...$ [70] by the inclusion of the next-to-leading order. The result from the $\epsilon = 4 - d$ expansion from Nishida and Son yields $(h/\mu)_c = 1.15$ [92], which is obtained from their result $(h_c/\Delta_0) = 0.878$ in leading order, together with $\Delta_0/\mu = 1.31$ [91]. The extrapolation of our Luttinger-Ward data, presented in Chapter 5, to zero temperature yields $(h/\mu)_c = 1.09 \pm 0.05$ in close agreement with the $\epsilon$-expansion, but considerably larger than the quantum Monte Carlo and FRG approaches. From the experimentally side, the Clogston-Chandrasekhar limit of the unitary gas has been determined by Shin et al. [34], who obtained $(h/\mu)_c = 0.95$. However, to determine the chemical potentials of the homogeneous system from the trap, one requires the following conversion formula of the observables $R_c$, denoting the radius of the balanced superfluid in the center of the trap, and the radius $R_\uparrow$, measuring the maximal spatial extent of the majority component in the trap

$$\frac{\mu_\downarrow}{\mu_\uparrow} = \frac{2\left[\xi_s \left(n_s(0)/n_0\right)^{2/3} - 1\right]}{1 - \left(\frac{R_c}{R_\uparrow}\right)^2} + 1\,. \tag{3.4}$$

The right-hand side depends explicitly on the universal value of the Bertsch parameter $\xi_s$, introduced in eq. (2.41). In addition, only the measurable ratio $n_s(0)/n_0$ of the superfluid density in the center of the trap $n_s(0)$ and the density of the fully polarized gas $n_0$, inferred from the outer tails, enters this relation. Inserting the experimental data $n_s(0)/n_0 = 1.72$ and $R_c/R_\uparrow = 0.43$ into the equation above gives the result $(h/\mu)_c = 0.95$ quoted in the paper by Shin et al. [34], provided that one assumes $\xi_s = 0.42$. With the more accurate choice $\xi_s = 0.37$ one finds the appreciably larger value $(h/\mu)_c = 1.35$ for otherwise identical parameters. Similarly, the experiment by Navon et al. [36] estimates a rather small ratio $(h/\mu)_c = 0.88$, which is, however, also based on the assumption $\xi_s = 0.42$.

In addition to the transition to the homogeneous superfluid, our Luttinger-Ward theory furthermore predicts a symmetry-broken phase with FFLO order, whose phase boundary is located at $(h/\mu)_{\mathrm{FFLO}} \simeq 1.28 \pm 0.15$. To determine this number we again have performed an extrapolation of our data to the ground state. Since in this region of the phase diagram the convergence of the self-consistent Green's

functions is rather difficult to achieve, the error bars remain large, but its existence is in agreement with the effective field theory of Son and Stephanov [2]. In contrast, the FRG-study by Roscher et al. [134] indicates that an inhomogeneous unitary superfluid only appears for sufficiently strong mass imbalances $m_\downarrow/m_\uparrow \geqslant 3$. This agrees with works based on mean-field and large $N$ approaches, which predict the FFLO phase to be limited to the fermionic side of the crossover regime, that is for $1/(k_F a) \leqslant -2.86$ [68] or $1/(k_F a) \leqslant -0.46$ [70]. A fully conclusive and quantitative answer for this issue, will certainly require further investigations.

## 3.3 Phase diagram for $1/a > 0$

The most involved phase diagram emerges in the BEC limit of the crossover, presented in Figure 3.3. The transition from the vacuum to a single-component Fermi gas at $\bar{h} = |\bar{\mu}|$ terminates already at $\bar{\mu} = -1$ and $\bar{h} = 1$, where several phases meet. The vertical line at $\bar{\mu} = -1$ and $\bar{h} \leqslant 1$ is the continuation of the vacuum to BEC transition of Fig. 2.2 to finite fields $\bar{h}$. Indeed, for $\bar{\mu} > -1$ a finite density of dimers $n_d$ populates the system, since the condition $2\mu = -\varepsilon_b$ is satisfied (see the discussion below (2.32)), whereas a fully polarized state has a higher energy of $2\mu_\uparrow = 2(\mu + h) > -\varepsilon_B$ . Furthermore, the $\bar{h}_s$ and $\bar{h}_c$ lines terminate in the BEC limit at the common end point $\bar{\mu} = -1$ and $\bar{h} = 1$. Their form can be estimated from the energy density $\varepsilon(n_\uparrow, n_\downarrow)$ of a system consisting of $(n_\uparrow - n_\downarrow)$ excess atoms of the majority component and $n_d = n_\downarrow$ bound pairs in terms of a mean-field approximation

$$\varepsilon(n_\uparrow, n_\downarrow) = \frac{3}{5}\text{const}(n_\uparrow - n_\downarrow)^{5/3} - n_\downarrow \varepsilon_B + g_{\text{ad}} n_\downarrow (n_\uparrow - n_\downarrow) + \frac{1}{2} g_{\text{dd}} n_\downarrow^2 . \tag{3.5}$$

This equation becomes exact in the dilute limit, which indeed is realized around the point $(\bar{\mu} = -1, \bar{h} = 1)$. The prefactor $\text{const} = (6\pi^2)^{2/3}\hbar^2/(2m)$ results from the standard form of a non-interacting, single-component Fermi gas. The interactions among the dimers are quantified by the coupling constant $g_{\text{dd}} = 2\pi\hbar^2 a_{\text{dd}}/m$, with the scattering length $a_{\text{dd}} = 0.6a$ [60], while the mean-field interactions between atoms and dimers are determined by $g_{\text{ad}} = 3\pi\hbar^2 a_{\text{ad}}/m$, with the associated atom-dimer scattering length $a_{\text{ad}} = 1.18a$ [64]. From (3.5), together with the standard relations $\mu_\sigma = \partial\varepsilon/\partial n_\sigma$ and the definitions of the chemical potentials $\mu$ and $h$ (2.30), one can deduce the form of the saturation and critical field lines, $h_s$ and $h_c$, in the vicinity of $\bar{\mu} = -1$ and $\bar{h} = 1$. The first, given by the condition $n_\downarrow = 0$, reads

$$h_s = \text{const}\left(\frac{2\mu + \varepsilon_B}{g_{\text{ad}}}\right)^{2/3} + \frac{\varepsilon_B}{2} - (\mu + \frac{\varepsilon_B}{2}) , \tag{3.6}$$

which is equivalent to the universal form

$$\bar{h}_s = \left(\frac{2\pi}{1.18}\right)^{2/3} (\bar{\mu} + 1)^{2/3} + 1 - (\bar{\mu} + 1) . \tag{3.7}$$

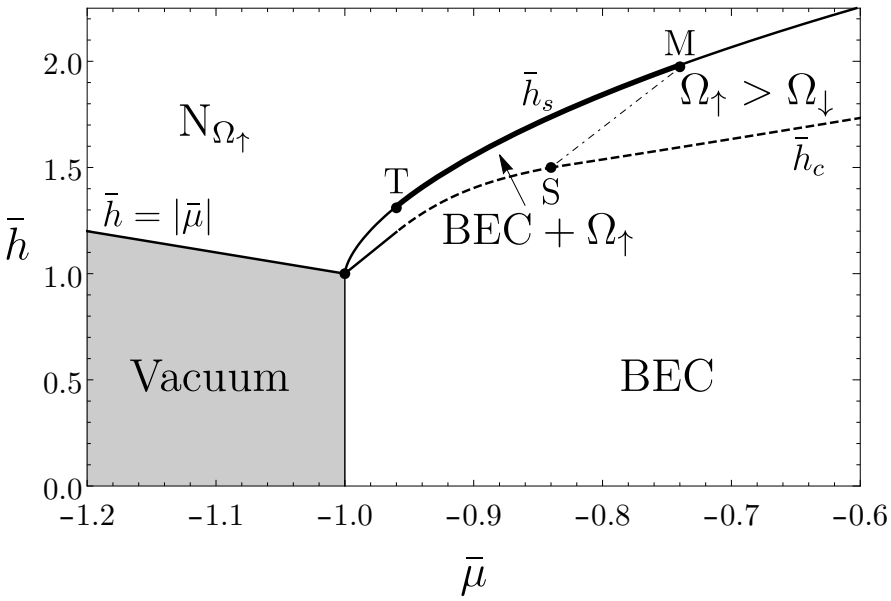


Figure 3.3: Universal phase diagram for positive scattering lengths. BEC refers to a spin balanced Bose-Einstein-Condensate, while BEC + $\Omega_\uparrow$ denominates a BEC in combination with a Fermi sea of excess atoms. $\Omega_\uparrow > \Omega_\downarrow$ is a symmetry-broken phase with two finite, but unequal Fermi seas. The splitting point S, the polaron-to-molecule transition point M and the tricritical point T are discussed in the main text.

Quite surprisingly, the range of validity of this simple ansatz, which entails the relation [122, 131]

$$\mu_\downarrow = -\varepsilon_B - \mu_\uparrow + g_{\mathrm{ad}} n_\uparrow \,, \tag{3.8}$$

for the energy of the a single impurity, extends beyond the point M, that labels the polaron-to-molecule transition. Physically, at this point the state of a single impurity, immersed in a Fermi sea of ↑-atoms, changes from a polaron on the fermionic side $\bar{\mu} > \bar{\mu}_{\mathrm{M}}$ of M to a molecule for $\bar{\mu} < \bar{\mu}_{\mathrm{M}}$. The location of the point M and the nature of the associated many-body ground state have been studied both by a BDMC computation [131] as well as by a variational ansatz for a molecular bound state [122]. Converting their results $1/(k_{F\uparrow}a) = 0.9$ and $\mu_\downarrow = -2.2\,\mu_\uparrow$ to our units, yields for M the coordinates $(\bar{\mu} = -0.74, \bar{h} = 1.97)_{\mathrm{M}}$, which indeed lie on the curve (3.7), as can be seen in Figure 3.3. Due to the change of the impurity character at M, for Zeeman fields just below $\bar{h}_s$ one encounters either a BEC in combination with a finite volume $\Omega_\uparrow$ of the Fermi sea of excess atoms, if $\bar{\mu} \leqslant \bar{\mu}_{\mathrm{M}}$ or a fermionic superfluid $\Omega_\uparrow > \Omega_\downarrow$ with two finite, yet unequal Fermi seas, if $\bar{\mu} \geqslant \bar{\mu}_{\mathrm{M}}$. Possible realizations of the latter are a Sarma or an FFLO phase [2]. Another point of interest on the saturation field line is the tricritical point T, where the transition

from the BEC+$\Omega_\uparrow$ state, becomes first order. In Fig. 3.3 the first-order segment of $h_s$ between T and M is indicated by a thick line. In a canonical formulation with fixed $\delta n$ rather than predefined chemical potentials, the system becomes unstable to phase separation along this first-order line, which implies the coexistence of a less-imbalanced superfluid $\delta n < \delta_{\mathrm{SF}}$ and a normal gas with a spin imbalance [68] larger than $\delta n$. The variational Monte Carlo approach by Pilati and Giorgini [135] determines T at $1/(k_{F\uparrow}a) = 1.7$, which equals $(\bar{\mu} = -0.96, \bar{h} = 1.31)_{\mathrm{T}}$.

Like $\bar{h}_s$, also the critical field line, which satisfies the condition $n_\uparrow = n/2 = n_\downarrow$, can be obtained from eq. (3.5) and we find

$$h_c = \frac{\varepsilon_B}{2} + (3\frac{a_{\mathrm{ad}}}{a_{\mathrm{dd}}} - 1)(\mu + \frac{\varepsilon_B}{2}) \tag{3.9}$$

or

$$\bar{h}_c = 1 + 4.9(\bar{\mu} + 1)\,, \tag{3.10}$$

where the slope follows from inserting the numerical values of the scattering lengths. In fact, this result for $h_c$ is identical to the criterion that a finite polarization appears in the superfluid, when the field strength reaches the minimum of the single-particle excitation energy $\Delta$, i.e. $h_c = \Delta$ as argued by Son and Stephanov [2] and using the result for $\Delta$ by Giorgini et al. [75]. The rather large slope of $\bar{h}_c$ signals that the mean-field expansion for $\bar{h}_c$ is confined to a small convergence radius around $(\bar{\mu} = -1, \bar{h} = 1)$, since otherwise $\bar{h}_c$ and $\bar{h}_s$ cross. Regarding the approach to the unitary regime, $f^{(+)}(\bar{\mu}, \bar{h})$ has to approach the strong coupling-regime $\bar{\mu} \gg 1$ continuously, in analogy to $f^{(-)}(\bar{\mu}, \bar{h})$ on the BCS-side. As a result, $\bar{h}_s$ and $\bar{h}_c$ must converge to straight lines of universal slopes $(h/\mu)_s$ and $(h/\mu)_c$. In Fig. 3.3 we use again dashed lines to indicate the continuation towards the Feshbach resonance. Furthermore, $\bar{h}_c$ must contain the splitting point S, which has been introduced by Son and Stephanov [2] based on a characterization of the minimal energy $\Delta$ of the single-particle excitations in the balanced superfluid. More precisely, for $v \leqslant v_{\mathrm{S}}$ the low-energy part of this spectrum is given by fermionic excitations, that carry a finite momentum $|\mathbf{k}|_0 \leqslant k_F$. In contrast, for $v > v_{\mathrm{S}}$ one encounters bosonic quasi-particles with minimal energy at vanishing $\mathbf{k}_0 = \mathbf{0}$. Punk et al. [136] have obtained $v_{\mathrm{S}} = 0.8$ by evaluating the minimum of the dispersion extracted from the single-particle spectral functions. The latter were obtained from an analytic continuation of the Matsubara-frequency Luttinger-Ward Green's functions to real frequencies. Based on this value, together with the Luttinger-Ward results $\Delta_{\mathrm{S}} = 0.95\varepsilon_F$ and $\mu_{\mathrm{S}} = -0.54\varepsilon_F$ from [37], we can assign the coordinates $(\bar{\mu} = -0.84, \bar{h} = 1.48)_{\mathrm{S}}$ to the splitting point. As becomes apparent in Fig. 3.3, the location of S is not captured by the simple mean-field equation (3.10). Furthermore, it has to be noted, that Pilati and Giorgini [135] obtain $v_{\mathrm{S}} = 0.53$ for an equivalent of S from the thermodynamic criterion that the superfluid undergoes a first-order phase transition to a phase-separated state for $v \leqslant v_{\mathrm{S}}$, while a related approach [137] finds $v_{\mathrm{S}} = 0.66$. Up to now, there is no conclusive explanation for this mismatch.

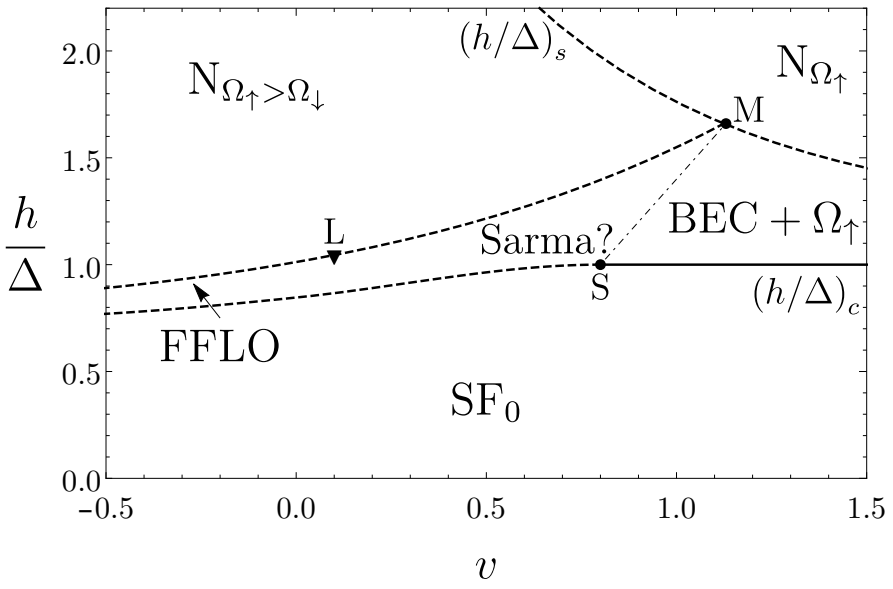


Figure 3.4: Phase diagram according to Ref. [2] around the splitting point. The fermionic imbalanced superfluid contains an FFLO state and possibly also a Sarma phase. The Luttinger-Ward theory predicts the Lifshitz point L close to the unitary limit.

The fact that the minimum of the single-particle dispersion changes character at the splitting point allowed Son and Stephanov to develop an effective field theory, valid in the neighborhood of S [2]. The resulting phase diagram is depicted in Figure 3.4 in terms of the variables $h/\Delta$ and $v = 1/(k_F a)$. Again, $\Delta$ refers to the minimal single-particle excitation energy, which is attained at $|\mathbf{k}_0| \leqslant k_F$ for $v \leqslant v_s$, whereas $\mathbf{k}_0 = \mathbf{0}$ for, $v \geqslant v_s$, such that $h/\Delta \equiv 1$ for $v \geqslant v_S$, where the balanced superfluid $SF_0$ can be continuously polarized. Furthermore, the imbalanced superfluid, which on the fermionic side of S always possesses two Fermi seas, itself likely consists of two phases. Immediately above $h_c$ an inhomogeneous FFLO phase is observed in the effective field theory, while in the triangle SML a homogeneous Sarma phase might be found. Its thermodynamic stability, however, has not yet been conclusively proven. The Lifshitz point L labels the endpoint of the phase boundary between FFLO and the fully polarized phase $N_\uparrow$. Our Luttinger-Ward computations suggest that this point is actually located close to the unitary limit, see the results in Chap 5. In addition, we can translate the point M to the representation in terms of $1/(k_F a)$ and $h/\Delta$. The excitation gap on the bosonic side of the splitting point can be estimated by the mean-field form of the minimum of the single-particle dispersion $\Delta \simeq \sqrt{\mu_M^2 + \Delta_0^2}$, where $\Delta_0$ refers to the anomalous expectation value in the superfluid phase (4.7) at zero temper-

ature. Inserting the Luttinger-Ward result $\Delta_0(v_{\mathrm{M}}) \simeq 1.19\varepsilon_F$ [37], we obtain the coordinates $(v = 1.13, h/\Delta = 1.66)_{\mathrm{M}}$. This agrees very well with the result from our Luttinger-Ward computations $(v = 1.13, h/\Delta = 1.65)_{\mathrm{M}}$, which determines M from the condition that the gas becomes fully polarized at the critical line. Since the transition between $\mathrm{SF}_0$ and the BEC+$\Omega_\uparrow$ is continuous on the bosonic side of S, while the polaron-to-molecule transition of an impurity atom is encountered at M, the line S-M most likely coincides with the boundary for the existence of a finite Fermi sea $\Omega_\downarrow$ at positive interaction strengths. This has also been assumed in Fig 3.3.

# Chapter 4

# Luttinger-Ward theory for BCS-BEC crossover in the presence of spin imbalance

The computation of the scaling function $f_p(\beta\mu, \beta h, \lambda_T/a)$ for arbitrary values of the thermodynamic parameters $T, \mu, h$ and $a$ in the strongly interacting crossover regime around the unitary limit requires a nonperturbative approach. In this work we follow the formalism developed by Luttinger and Ward [138], who represent the grand potential $\Omega[G]$ as functional of the interacting fermionic Green's function $G$. The general properties of the latter are introduced in Sec. 4.1. Next, we summarize the definitions of the Fourier transformations, which will appear quite frequently, in Sec. 4.2. In part 4.3 we discuss the Feynman rules for the single-channel model, before we turn to the Luttinger-Ward formalism itself. Its general properties and the equations of motion for $G$ derived from $\Omega$[G] can be found in Sec. 4.4, together with the ladder approximation for the interactions in the imbalanced Fermi gas. Then we define a suitable vertex function for the ladder approximation in 4.5, which signals the instability towards Cooper pairing. We give the specific form of the self-energy and the corresponding Schwinger-Dyson equation in Sec. 4.6. Finally, we derive expressions for the pressure, internal energy and entropy as functionals of $G$ in Sec. 4.7.

## 4.1 Finite temperature fermionic Green's functions

Green's functions provide a valuable tool to investigate physical questions both in high energy and in condensed matter physics. In thermodynamic problems the single-particle fermionic Green's functions $G$ allow to compute the grand potential $\Omega$, even in the presence of two-body interaction operators [67]. Since $\Omega$ is the central object of the Luttinger-Ward formalism, the Green's functions will play an important role throughout the thesis. Here we give the definitions required for the imbalanced Fermi gas and list the general properties, that will be used in the following chapters. In addition, we introduce the noninteracting Green's functions, which later on provide a starting point for the self-consistent equations.

In the context of thermodynamics one usually works with the imaginary time

formalism, where the Green's functions for the fermionic degrees of freedom are given as thermal expectation values of the field operators $\hat{\Psi}_\sigma(\mathbf{x})$ $\left(\hat{\Psi}_\sigma(\mathbf{x})^\dagger\right)$, that annihilate (create) an atom of spin orientation $\sigma =\uparrow,\downarrow$ along the $z$-axis at position $\mathbf{x}$. As mentioned below eq. (2.6) the spin index actually refers to the hyperfine state that arises from the addition of the nuclear and electronic spins. Due to the fermionic statistics, the field operators obey the canonical anticommutation relations

$$\{\hat{\psi}_\sigma(\mathbf{x}), \hat{\psi}^\dagger_{\sigma'}(\mathbf{y})\} = \delta_{\sigma\sigma'}\delta(\mathbf{x}-\mathbf{y}) \tag{4.1a}$$

$$\{\hat{\psi}_\sigma(\mathbf{x}), \hat{\psi}_{\sigma'}(\mathbf{y})\} = 0 = \{\hat{\psi}^\dagger_\sigma(\mathbf{x}), \hat{\psi}^\dagger_{\sigma'}(\mathbf{y})\}\,. \tag{4.1b}$$

The imaginary time evolution takes place in the imaginary time interval $\tau \in [0, \hbar\beta]$ and is given by $\hat{\Psi}_\sigma(\mathbf{x},\tau) = \exp(\tau K/\hbar)\hat{\Psi}_\sigma(\mathbf{x})\exp(-\tau K/\hbar)$, obtained from the Heisenberg time evolution with the grand-canonical Hamiltonian $K = H - \sum_\sigma \mu_\sigma N_\sigma$ of operators in real time $t$, followed by a Wick rotation $\tau = it$. The normal Green's functions, which are finite both above and below the critical temperature, are defined as [67, 139]

$$\mathcal{G}_{\sigma\sigma}(\mathbf{x}-\mathbf{x}', \tau-\tau') = -\left\langle \mathcal{T}\left[\hat{\Psi}_\sigma(\mathbf{x},\tau)\,\hat{\Psi}^\dagger_\sigma(\mathbf{x}',\tau')\right]\right\rangle, \tag{4.2}$$

where $\mathcal{T}$ denotes the time-ordering operator. Furthermore, we focus only on systems that are both homogeneous in space and imaginary time, which restricts the dependence on the coordinates to the differences $\tau-\tau'$ and $\mathbf{x}-\mathbf{x}'$. Moreover, the fact that the single-channel model (2.26) admits only interactions in the s-wave channel, implies that $\mathcal{G}_{\sigma\sigma}(\mathbf{x},\tau) = \mathcal{G}_{\sigma\sigma}(r,\tau)$ is only a function of the radial coordinate $r = |\mathbf{x}|$. In the presence of a finite Zeeman field $h$ will lead to unequal $\mathcal{G}_{\uparrow\uparrow}(\mathbf{x},\tau) \neq \mathcal{G}_{\downarrow\downarrow}(\mathbf{x},\tau)$, such that we are required to keep track of the spin indices. To simplify the notations it is convenient to introduce the Green's function

$$G(\mathbf{x},\tau) = \{\mathcal{G}_{\uparrow\uparrow}(\mathbf{x},\tau), \mathcal{G}_{\downarrow\downarrow}(\mathbf{x},\tau)\}, \tag{4.3}$$

which gathers the spin components in a vector. Unequal spin populations will also be reflected in the individual spin densities $n_\sigma$, that follow immediately from the normal Green's functions via the standard relation

$$n_\sigma = \mathcal{G}_\sigma\left(\mathbf{x}=\mathbf{0}, \tau=0^-\right). \tag{4.4}$$

In general, a fermionic Green's function obeys antiperiodic boundary conditions with respect to shifts of the imaginary time interval, i.e. it satisfies

$$G(\mathbf{x}, \hbar\beta-\tau) = -G(\mathbf{x},-\tau). \tag{4.5}$$

This property will turn out to be useful in the numerical implementation of the equations of motions for $G$ in Chapter 7.

The normal Green's functions obviously are invariant under the global $U(1)$ transformation $\hat{\Psi}_\sigma(\mathbf{x}) \to \exp(i\varphi)\hat{\Psi}_\sigma(\mathbf{x})$, with $\varphi \in \mathbb{R}$, connected to the particle number conservation. However, below the critical temperature this symmetry is spontaneously broken, which gives rise to anomalous expectation values. These manifest in a mathematical manner the presence of Cooper pairs on the BCS side of the crossover or the appearance of a Bose Einstein condensate of dimers on the BEC side of the crossover. Since we only consider s-wave pairing, which takes place in relative spin-singlet configurations, only Gorkov functions

$$\begin{aligned} \mathcal{F}_{\sigma\bar{\sigma}}(\mathbf{x}-\mathbf{x}',\tau-\tau') &= -\left\langle \mathcal{T}\left[\hat{\Psi}_\sigma(\mathbf{x},\tau)\,\hat{\Psi}_{\bar{\sigma}}\left(\mathbf{x}',\tau'\right)\right]\right\rangle \\ \mathcal{F}^{+}_{\sigma\bar{\sigma}}(\mathbf{x}-\mathbf{x}',\tau-\tau') &= -\left\langle \mathcal{T}\left[\hat{\Psi}^\dagger_\sigma(\mathbf{x},\tau)\,\hat{\Psi}^\dagger_{\bar{\sigma}}\left(\mathbf{x}',\tau'\right)\right]\right\rangle \end{aligned} \tag{4.6}$$

with opposite spin orientations exist, where $\bar{\sigma}$ denotes the spin orientation complementary to $\sigma$. They respect an antiperiodicity condition analogous to eq. (4.5), while the spatial homogeneity and isotropy imply the same restrictions on the position and imaginary time arguments like in the case of the normal Green's function (4.2). From a physical perspective one can extract the superfluid order parameter $\Delta$ from the Gorkov functions via

$$\Delta = \lim_{\Lambda\to\infty} \bar{g}(\Lambda)\mathcal{F}_{\uparrow\downarrow}(\mathbf{x}=\mathbf{0},\tau=0^-) = -\lim_{\Lambda\to\infty} \bar{g}(\Lambda)\mathcal{F}_{\downarrow\uparrow}(\mathbf{x}=\mathbf{0},\tau=0^-)\,. \tag{4.7}$$

The short-time and short-distance limit on the right-hand side, however, is not well defined and requires the renormalization scheme introduced in eq. (2.29), which yields the relation

$$\frac{\Delta}{g} = \int \frac{d^3k}{(2\pi)^3}\left[\mathcal{F}_{\uparrow\downarrow}(\mathbf{k},\tau=0^-) + \frac{\Delta}{2\varepsilon_k}\right] \tag{4.8}$$

in momentum space, with the standard single-particle dispersion relation $\varepsilon_k = \hbar^2k^2/2m$. Note that all quantities involved in the latter equation are well-defined in the zero-range limit. Furthermore, this implies that the anomalous Greens function has a large momentum tail $\mathcal{F}_{\uparrow\downarrow}(\mathbf{k}\to\infty,\tau=0^-) \sim -\Delta/2\varepsilon_k \sim 1/k^2$. In fact, this tail is already observed at the mean field level, as is further discussed in Appendix A.2. For the explicit definitions of the involved Fourier transformation, especially with respect to the sign conventions, see the next section.

To close this discussion about the thermal single-particle Green's functions we return to the normal phase. Setting the bare coupling constant $\bar{g}$ in the Hamiltonian to zero, reduces the problem to the case of a two-component, ideal Fermi gas, which gives rise to the well established form of the noninteracting Green's functions[1] in momentum and frequency space [67, 139]

$$\mathcal{G}^{(0)}_{\sigma\sigma}(\mathbf{k},\omega_n) = \frac{1}{i\hbar\omega_n - \xi_{k,\sigma}}\,, \tag{4.9}$$

[1]Note that in Ref. [37] a different sign convention has been used for $\mathcal{G}^{(0)}_{\sigma\sigma}$.

with the standard short-hand notation $\xi_{k,\sigma} = \varepsilon_k - \mu_\sigma$. The frequencies $\hbar\omega_n = (2n+1)\pi T$, $n \in \mathbb{Z}$ denote the standard fermionic Matsubara frequencies, which guarantee the antiperiodic boundary conditions (4.5). In addition, the Fourier transformation of $\mathcal{G}^{(0)}_{\sigma\sigma}(\mathbf{k}, \omega_n)$ to imaginary time is also known in closed form [67, 139]

$$\mathcal{G}^{(0)}_{\sigma\sigma}(\mathbf{k}, \tau) = \theta(\tau) e^{-\xi_{k,\sigma}\tau}(1 - n_F(\xi_{k,\sigma})) - \theta(-\tau) e^{-\xi_{k,\sigma}\tau} n_F(\xi_{k,\sigma}), \tag{4.10}$$

where $n_F(\xi_k)$ refers to the Fermi-Dirac distribution

$$n_F(\xi_{k,\sigma}) = \frac{1}{\exp(\beta\xi_{k,\sigma}) + 1}. \tag{4.11}$$

As we have seen in eq. (4.4), the density is encoded in the real-space Green's function $\mathcal{G}_{\sigma\sigma}(\mathbf{x}, \tau)$. Unfortunately, there exists no analytic way to perform the Fourier transformation $\mathbf{k} \to \mathbf{x}$ at arbitrary $\tau$. Furthermore, we note the limiting behavior $\mathcal{G}^{(0)}_{\sigma\sigma}(\mathbf{k}, \tau = 0^+) \to 1$, for $k \to \infty$, which renders the function nonintegrable in momentum space, such that the direct application of numerical methods to this Fourier transformation is ruled out. In fact, the necessity to construct a suitable subtraction scheme to solve the self-consistent equations is intimately connected to this particular limit of the Green's function. We also introduce

$$G^{(0)}(\mathbf{k}, \omega_n) = \{\mathcal{G}^{(0)}_{\uparrow\uparrow}(\mathbf{k}, \omega_n), \mathcal{G}^{(0)}_{\downarrow\downarrow}(\mathbf{k}, \omega_n)\} \tag{4.12}$$

in analogy to eq. (4.3). Before we turn to the Luttinger-Ward formalism, that allows to include contributions from the interactions, we will first establish the Fourier transformations and consider the Feynman rules in order to incorporate the interactions.

## 4.2 Notations and Fourier transforms

Since Fourier transformations represent the most frequently encountered, nontrivial mathematical operation in the computations to come, it is useful to state the required definitions in this section and to incorporate the simplifications based on spatial isotropy. We will only deal with fermionic and bosonic correlation functions of the general form $f(\mathbf{x}, \tau)$, which can be distinguished by their boundary conditions on the imaginary time interval $\tau \in [0, \hbar\beta]$

$$f(\mathbf{x}, \hbar\beta - \tau) = \mp f(\mathbf{x}, \tau). \tag{4.13}$$

The upper sign refers to the fermionic case, already encountered in eq. (4.5), whereas the lower one entails the periodicity of bosonic correlators. In particular, due to these boundary conditions, the Fourier transformation from frequency space to $\tau$ actually becomes a Fourier series, that only involves a discrete set of frequencies. For an antiperiodic function $f(\mathbf{x}, \tau)$ these are the fermionic Matsubara

frequencies $\hbar\omega_n = (2n+1)\pi T$, $n \in \mathbb{Z}$ and we define the Fourier transform of $f$ and the corresponding inverse transformation as

$$f(\mathbf{k}, \omega_n) = \int d^3x \int_0^{\hbar\beta} d\tau \; e^{-i(\mathbf{k}\cdot\mathbf{x} - \omega_n\tau)} f(\mathbf{x}, \tau) \tag{4.14a}$$

$$f(\mathbf{x}, \tau) = \int \frac{d^3k}{(2\pi)^3} \frac{1}{\hbar\beta} \sum_n e^{i(\mathbf{k}\cdot\mathbf{x} - \omega_n\tau)} f(\mathbf{k}, \omega_n) \; . \tag{4.14b}$$

Bosonic functions $f(\mathbf{x}, \tau)$ in turn are transformed to the bosonic Matsubara frequencies $\hbar\Omega_n = 2\pi n T$, $n \in \mathbb{Z}$ and the corresponding Fourier transforms read

$$f(\mathbf{Q}, \Omega_n) = \int d^3x \int_0^{\hbar\beta} d\tau \; e^{-i(\mathbf{Q}\cdot\mathbf{x} - \Omega_n\tau)} f(\mathbf{x}, \tau) \tag{4.15a}$$

$$f(\mathbf{x}, \tau) = \int \frac{d^3Q}{(2\pi)^3} \frac{1}{\hbar\beta} \sum_n e^{i(\mathbf{Q}\cdot\mathbf{x} - \Omega_n\tau)} f(\mathbf{Q}, \Omega_n) \; . \tag{4.15b}$$

Note that we use capital letters to distinguish bosonic functions in frequency and momentum space from fermionic ones.

Finally, all the functions $f(\mathbf{x}, \tau)$ discussed in the following chapters only depend on the modulus $r = |\mathbf{x}|$, like the Green's function $G(\mathbf{x}, \tau)$ in eq. (4.3). This implies rotational invariance also in momentum space[2], such that $f(\mathbf{k}, \tau)$ is only a function of $k = |\mathbf{k}|$. In addition, the Fourier transforms effectively become one-dimensional

$$f(\mathbf{k}, \tau) = \int d^3x \, e^{-i\mathbf{k}\cdot\mathbf{x}} f(\mathbf{x}, \tau) = \frac{2\pi i}{k} \int_{-\infty}^{\infty} dr \, r \, e^{-ikr} f(r, \tau) \tag{4.16a}$$

$$f(\mathbf{x}, \tau) = \int \frac{d^3k}{(2\pi)^3} \, e^{i\mathbf{k}\cdot\mathbf{x}} f(\mathbf{k}, \tau) = \frac{1}{(2\pi)^2 ir} \int_{-\infty}^{\infty} dk \, k \, e^{ikx} f(k, \tau) \, , \tag{4.16b}$$

which can easily be verified by introducing standard polar coordinates.

## 4.3 Feynman rules

In the following, we summarize the Feynman rules of the normal phase both in real and momentum space in Figure 4.1. The non-trivial spin structure of the Green's function gives rise to important constraints with respect to the allowed diagrams, when the components of $G$ are combined with interaction lines representing the two-body operator in the Hamiltonian (2.26). As usual, in real space the normal Green's function $\mathcal{G}_{\sigma\sigma}(\mathbf{x}, \tau)$ connects two external points with identical spin indices and has a directed particle flow from the creation (annihilation) to the annihilation (creation) operator, when $\tau$ is positive (negative), corresponding to the propagation of particles (holes). In momentum space one consequently also has to indicate the direction of the momentum. To symbolize the contact interaction $\bar{g}(\Lambda)\delta(\mathbf{x} - \mathbf{x}')$ we

[2] We consider an arbitrary momentum argument $\mathbf{k}$, which can be replaced by any other vector $\mathbf{Q}$, since this step is independent of the quantum statistics.

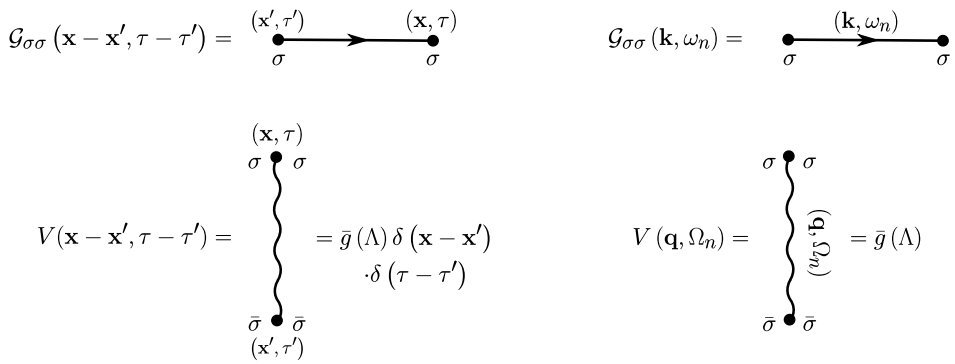


Figure 4.1: The Feynman rules for the various Green's functions and the bare interaction potential, as discussed in the main text. The left column contains the real space and imaginary time representation whereas the right column shows the corresponding lines in momentum and Matsubara frequency space.

use a wavy line, despite the possibility to contract it to a single point by its locality. The reason behind this notation is, that it allows to keep track of the spin indices in a very simple manner. Since the spin is conserved during every collision, we have identical spin indices in the incoming and outgoing Green's function lines at each endpoint of the interaction lines. Moreover, the s-wave nature of the interactions enforces that the fermionic atoms scatter in spin singlet configurations, due to the Pauli principle. This entails opposite spin indices at the endpoints of a single interaction line. Therefore, the particle flow at these endpoints cannot be reversed, as the interatomic potential consists of exactly one annihilation and one creation operator of each spin species, corresponding to one incoming and one outgoing Green's function line per spin index. As discussed in Appendix A, these assignments become more involved once anomalous propagators are included.

## 4.4 Luttinger-Ward formalism for the imbalanced Fermi gas

### 4.4.1 General setup of the Luttinger-Ward formalism

In any problem of equilibrium statistical mechanics the quantity of prime interest is the partition function or the related thermodynamic potential. In the grand-canonical ensemble one considers the grand-potential

$$\Omega(T,\mu_\sigma,V) = -T\log\mathrm{Tr}\,e^{-\beta\left(H-\sum_\sigma\mu_\sigma N_\sigma\right)}, \tag{4.17}$$

with an arbitrary Hamiltonian $H$. In the following, we assume that $H$ admits the standard separation into a sum of a quadratic part $H_0$, which can be diagonalized in a straight-forward manner, and a contribution $H_{\mathrm{int}}$ from the interactions. As

shown by Luttinger and Ward [138] for a fermionic system, $\Omega$ can be expressed as an exact functional of the interacting single-particle Green's function $G$, defined in eq. (4.3), which reads

$$\Omega[G] = \beta^{-1}\big(\mathrm{Tr}\{\ln[G] + [1 - G_0^{-1}G]\} + \Phi[G]\big)\,. \tag{4.18}$$

Here $G_0$ denotes the known, time-ordered Green's function associated with $H_0 - \sum_\sigma \mu_\sigma N_\sigma$ in the imaginary-time formalism, while the Luttinger-Ward functional $\Phi[G]$ contains all the effects of interactions in terms of a sum of all topologically allowed, closed, skeleton diagrams. These are defined as the set of all connected Feynman diagrams without external points, where the interaction vertices are linked directly, that is without further self-energy insertions, by lines representing the dressed $G$. The physical Green's function is determined from the stationarity condition

$$\frac{\delta\Omega}{\delta G} = 0\,, \tag{4.19}$$

which gives rise to a Dyson equation

$$G^{-1} = G_0^{-1} - \Sigma[G]\,. \tag{4.20}$$

The self-energy $\Sigma[G]$ itself depends on the Green's function via the functional derivative

$$\Sigma[G] = \frac{\delta\Phi[G]}{\delta G}\,. \tag{4.21}$$

Therefore, the pair of equations (4.20) and (4.21) has to be solved self-consistently, which allows to include interactions in a non-perturbative manner. Alternatively, one can interpret the Luttinger-Ward formalism as the search for a functional $\Omega[G]$ that is stationary, when $G$ satisfies the exact Dyson equation (4.20). This immediately leads to eqs. (4.18) and (4.21).

A crucial feature of the Luttinger-Ward approach is its conserving nature, that was proven by Kadanoff and Baym [140]: The grand potential $\Omega[G]$ and the derived quantities thereof satisfy all thermodynamic relations, irrespective of the approximations invoked on $\Phi[G]$, provided that the physical $G$ is inserted. Obviously, this property and the non-perturbative treatment of the interactions motivate the application of the method to the imbalanced Fermi gas. Furthermore, the Luttinger-Ward method originally was developed for normal fermionic quantum fluids, yet the extension to superfluid phase, where anomalous propagators are present, has been accomplished by Haussmann et al. [37].

The Luttinger-Ward functional in eq. (4.18) represents a special instance of a 2PI (two-particle irreducible) effective action. 2PI means that one has to cut more than two Green's function lines in any diagram that is part of $\Phi[G]$ to separate it into two disconnected subdiagrams. The self-energy in turn is per definition 1PI [141], which agrees with equation (4.21), since the functional derivative removes exactly

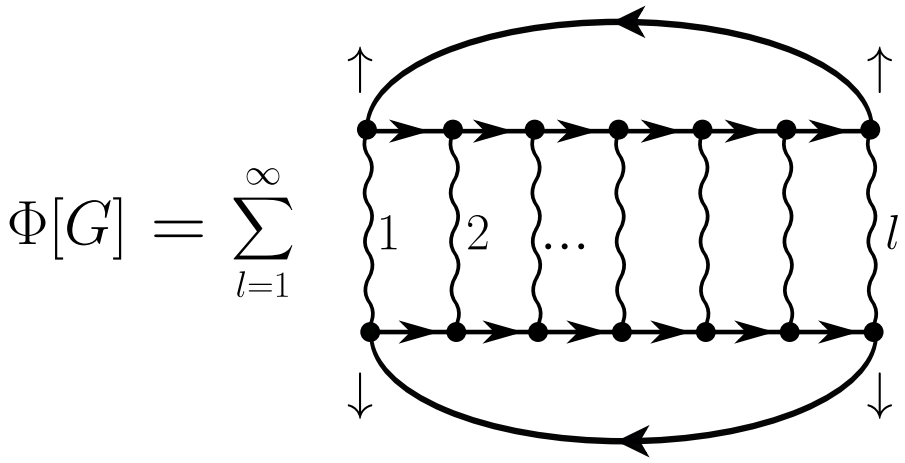


Figure 4.2: The Luttinger-Ward functional in the ladder approximation includes all ladders up to an infinite number of rungs $l$. The spin constraints impose that one of the legs is exclusively formed by $\mathcal{G}_{\uparrow\uparrow}$, while in the other one only $\mathcal{G}_{\downarrow\downarrow}$ appears.

one Green's function line from the 2PI diagrams of $\Phi[G]$. A related equilibrium approach, that works both for bosonic and fermionic statistics, has been developed by De Dominicis and Martin [142,143], who additionally allow for finite field expectation values in case of spontaneously broken symmetries and even for two-particle Green's functions, which have to satisfy stationarity conditions in analogy to (4.19). In case of the BCS-BEC crossover the connection between both methods has been discussed by Haussmann et al. [37] and in the thesis by Cerrito [144].

### 4.4.2 The particle-ladder approximation

Since the exact form of the Luttinger-Ward functional $\Phi[G]$ from eq. (4.18) is not known in closed analytical form, we have to introduce suitable approximations and chose a class of diagrams that fulfills two conditions: On the one hand it must be capable to describe the physically relevant processes and on the other we must be able to find an analytical expression for $\Phi[G]$, which is numerically tractable. The strong interactions in the crossover regime and the fact that pairing even in the weakly coupled BCS-theory is a nonperturbative effect, imply that we have to take into account scattering events of arbitrary order in the dilute gas. An approximation that meets these requests is given by the restriction to the particle-particle ladder, which is also called the T-matrix approximation [67]. The corresponding diagrams are depicted in Fig. 4.2. On the level of the Luttinger-Ward functional the particle-particle ladder contains all ladders with an arbitrarily large number of rungs, that are closed by two backward-propagating Green's functions corresponding to two holes. In the normal phase the particle flows in the upper

and the lower leg run in parallel, while the constraint on the spin indices from the interaction lines in Fig. 4.1 enforces opposite spins in the two legs. Therefore, we only have to take into account the direct ladder diagrams from Fig. 4.2, since exchange ladders, which essentially consist of a single Green's function line with a definite spin orientation, are inconsistent with the condition of spin-singlets at the vertices.

The T-matrix is known to give rise to the BCS instability for arbitrarily weak interactions, where the ladders can be computed with the bare Green's function $G^{(0)}$ and therefore is in agreement with the first request. The system becomes unstable towards the formation of Cooper pair at the critical temperature

$$T_c^{\mathrm{BCS}} = \frac{8e^{\gamma_E}}{\pi e^2}\varepsilon_F\, e^{-\frac{\pi|v|}{2}}\,. \tag{4.22}$$

By construction, this theory does not account for particle-hole fluctuations and thus misses the quantitatively important factor $(4e)^{-1/3}$ from the Gorkov and Melik-Barkhudarov corrections [95] in eq. (2.44). Unfortunately, we are not able to include them in our theory, since the resulting internal momentum structure of the self-energy diagrams is beyond the scope of our current numerical capacities. In the case of a weakly repulsive gas of Fermions the ladder approximation has been used by Galitskii [145] to consider the repeated interactions in the dilute limit, which gives rise to a power series in $k_F a$ for the ground state energy. In the context of ultracold atoms the ladder diagrams or very similar structures frequently appear, for example in the theory of Nozières and Schmitt-Rink [21], in the large-N expansions [70] and in the theory of Gaussian fluctuations developed by Sa de Melo, Randeria and coworkers [146, 147]. Interestingly, the latter approach yields for the ground state energy of the superfluid exactly the same power series in $k_F a$ as one obtains in the repulsive case, in addition to the condensation energy. In the limit of a strongly imbalanced Fermi gas, the Chevy ansatz [80] for Fermi polaron coincides with an impurity Green's function that bears self-energy corrections from the non-self-consistent T-matrix [148]. In case of the BCS-BEC crossover without spin-balance a fully self-consistent T-matrix theory has been established by Haussmann et. al., both for the normal [87, 149] and the superfluid phase [37, 150]. We emphasize the importance of the self-consistency for the quantitative agreement with the experimental results. As discussed already in Section 2.3.2, the result for the critical temperature of the balanced unitary gas $\theta_c \simeq 0.16$ turns out to coincide very well with the measured value in contrast to the non-self-consistent NSR-result of $\theta_c \simeq 0.22$. Therefore, we also maintain the self-consistency in the presence of a finite Zeeman field. Note however, that the particle-particle ladder approximation of Luttinger-Ward functional $\Phi[G]$ is chosen to describe the fermionic pairs in a nonperturbative manner. The repulsive interactions of the bound state molecules at positive scattering lengths in turn are taken into account only approximately. As discussed by Haussmann [149], the lowest order diagrams that effectively describe dimer-dimer scattering processes in terms of the fermionic Green's functions

yield the mean-field result $a_{\mathrm{dd}} = 2a$, instead of the exact result $a_{\mathrm{dd}} = 0.6a$ [60]. By the self-consistent summation of higher order diagrams the effective dimer-dimer scattering length of the Luttinger-Ward formalism might be changed from the mean-field result, but we do not expect to find the physical values of $a_{\mathrm{dd}} = 0.6$ and $a_{\mathrm{ad}} = 1.18$ [64], introduced in Sec. 2.1.3. We will return to this point in Sec. 5.6, where we extrapolate our numerical results to the ground state and compare them to the universal phase boundaries (2.51) and (3.7) at positive $a$.

Regarding the second condition of a tractable form of the approximate Luttinger-Ward functional, we have compute the sum depicted in Fig. 4.2 in closed form. To simplify the expression we first define the the particle-particle bubble $\chi(\mathbf{Q}, \Omega_n)$, that is the convolution of the co-propagating Green's functions, which appears repeatedly in the ladder diagrams

$$\chi(\mathbf{Q}, \Omega_n) = \frac{1}{\beta} \sum_m \int \frac{d^3k}{(2\pi)^3} \mathcal{G}_{\uparrow\uparrow}(\mathbf{k}, \omega_m) \mathcal{G}_{\downarrow\downarrow}(\mathbf{Q} - \mathbf{k}, \Omega_n - \omega_m) . \tag{4.23}$$

At this stage, the definition of this function has to be considered as purely formal, since the integral is UV divergent in the limit of $\Lambda \to \infty$ due to the slow decay of the Green's functions for large momenta. We will rectify this issue in the next section on the vertex function. Based on $\chi(\mathbf{Q}, \Omega_n)$, we can write for the Luttinger-Ward functional

$$\begin{aligned} \frac{\Phi[G]}{V} &= -\sum_{l=1}^{\infty} \frac{(-1)^l}{l} \bar{g}^l(\Lambda) \sum_n \int \frac{d^3Q}{(2\pi)^3} \left[\chi(\mathbf{Q}, \Omega_n)\right]^l \\ &= \sum_n \int \frac{d^3Q}{(2\pi)^3} \log\left[1 + \bar{g}(\Lambda)\chi(\mathbf{Q}, \Omega_n)\right] , \end{aligned} \tag{4.24}$$

where the $1/l$ weight takes into account the symmetry factor of the ladder diagrams. Since $\Phi[G]$ contributes to the pressure via the grand potential $p = -\Omega/V$, it should not contain any divergences, caused by the cutoff-dependence. In fact, the product $\bar{g}(\Lambda)\chi(\mathbf{Q}, \Omega_n)$ turns out to be finite in the zero-range limit $\Lambda \to \infty$, as will be shown below. Surprisingly however, the Hartree diagram, which is given by the $l = 1$ term in Fig. 4.2, vanishes in the zero range limit. This follows from its contribution to the grand potential $\Omega_{\mathrm{H}} = \bar{g}(\Lambda) n_\uparrow n_\downarrow V \to 0$, since $\bar{g} \to 0$ according to the renormalization scheme (2.29) in the zero-range limit. Before we turn to the vertex function in the next section, we state the final form of the grand-potential, that we use to describe the imbalanced Fermi gas in the normal phase

$$\begin{aligned} \frac{\Omega[G]}{V} = &\frac{1}{\beta} \sum_n \sum_{\sigma=\uparrow,\downarrow} \int \frac{d^3k}{(2\pi)^3} \left[\log[\mathcal{G}_{\sigma\sigma}(\mathbf{k}, \omega_n)] + \left(1 - \mathcal{G}^{(0)}_{\sigma\sigma}(\mathbf{k}, \omega_n)^{-1} \mathcal{G}_{\sigma\sigma}(\mathbf{k}, \omega_n)\right)\right] \\ &+ \frac{1}{\beta} \sum_n \int \frac{d^3Q}{(2\pi)^3} \log\left[1 + \bar{g}(\Lambda)\chi(\mathbf{Q}, \Omega_n)\right] . \end{aligned} \tag{4.25}$$

## 4.5 The vertex function $\Gamma$

Strictly speaking the Luttinger-Ward approach (4.18) is built upon the dressed, single-particle Green's function only and no higher order Green's functions are required. However, it will turn out to be very useful to additionally define the bosonic vertex function $\Gamma(\mathbf{x}, \tau)$, too. First of all, it contains physical information, because it both allows to extract the Tan contact parameter, discussed in Section 2.4, and it signals the phase transition by a zero at small momenta in the inverse vertex function $\Gamma^{-1}(\mathbf{Q} \to 0, \Omega_n = 0)$, which indicates the appearance of a Goldstone mode, due to the spontaneously broken $U(1)$ symmetry. In addition, it helps on a formal level to organize the equations of motion for $G$.

### 4.5.1 Definition and physical properties

The vertex function $\Gamma$ is defined as the amputated and connected part of the two-particle Green's function [141], that in general depends on four space-time arguments. In a homogeneous system the arguments can be reduced to one center-of-mass momentum and two relative momenta. The same holds true also for the frequency arguments. Physically a system exhibits a phase transition, when a certain mode becomes infinitely susceptible to an external perturbation, which is signaled by a divergence of $\Gamma$ in the corresponding momentum channel. In the following, we include only the s-wave pairing instability, which is the dominant one in the case of ultracold fermionic quantum gases. In the absence of competing instabilities it suffices to take a very simple dependence of the vertex function $\Gamma(\mathbf{x}, \tau)$ on a single coordinate pair $(\mathbf{x}, \tau)$ into account, which describes the center-of-mass propagation of a $\uparrow\downarrow$-pair of atoms through the medium. The resulting vertex function reads [42]

$$\Gamma(\mathbf{x}, \tau) = \bar{g}(\Lambda)\, \delta(\tau)\delta(\mathbf{x}) - \bar{g}^2(\Lambda)\, \langle \mathcal{T} \left(\hat{\psi}_\downarrow \hat{\psi}_\uparrow\right)(\mathbf{x}, \tau) \left(\hat{\psi}_\uparrow^\dagger \hat{\psi}_\downarrow^\dagger\right)(\mathbf{0}, 0) \rangle \,. \tag{4.26}$$

Its form is compatible with the bare $\delta(\mathbf{x} - \mathbf{x}')$ potential in the single-channel model (2.26), since a perfectly local potential will always give rise to a vertex function that only contains the non-trivial center of mass dynamics of the pairs, as argued in Ref. [150]. More precisely, the vertex can be written as

$$\begin{aligned} \Gamma(\mathbf{x}_1, \tau_1, \mathbf{x}_2, \tau_2, \mathbf{x}_3, \tau_3, \mathbf{x}_4, \tau_4) = \Gamma\left(\frac{\tau_1 + \tau_2}{2} - \frac{\tau_3 + \tau_4}{2}, \frac{\mathbf{x}_1 + \mathbf{x}_2}{2} - \frac{\mathbf{x}_3 + \mathbf{x}_4}{2}\right) \\ \delta(\mathbf{x}_1 - \mathbf{x}_2)\delta(\tau_1 - \tau_2)\delta(\mathbf{x}_3 - \mathbf{x}_4)\delta(\tau_3 - \tau_4)\,, \end{aligned} \tag{4.27}$$

which implies that the physics of the relative degrees of freedom, i.e. the form of the scattering wave function of the pairs has been completely discarded. Consequently, we are not able to describe p-wave pairing within our theory. Furthermore, $\Gamma(\mathbf{x}, \tau)$ is invariant under the exchange of the spin labels $\uparrow \leftrightarrow \downarrow$, which is a consequence of the symmetry of the bare potential. Furthermore, the vertex satisfies periodic boundary conditions in imaginary time $\Gamma(\mathbf{x}, \beta - \tau) = \Gamma(\mathbf{x}, \tau)$, which follows from

the definition of the time ordered-product. Hence, $\Gamma$ describes a bosonic function in agreement with the propagation of pairs.

The short-distance and short-time limit of the vertex is related to the Tan contact density $\mathcal{C}$ (2.53), as was noted in Ref. [151],

$$\frac{\hbar^4}{m^2}\mathcal{C} = |\Delta|^2 - \Gamma(\mathbf{x} = \mathbf{0}, \tau = 0^-)\,. \tag{4.28}$$

$\Gamma$ represents the connected part of the expectation value of the quartic operator in the definition of $\mathcal{C}$, whereas the term with the gap parameter originates from the anomalous, disconnected contraction, which only exists below $T_c$. Note that there is no contribution from the Hartree diagram, which represents the disconnected contraction based on normal Green's functions, since it vanishes in the zero-range limit (see Sec. 4.4.2).

The Fourier transform of the vertex functions yields the pair propagator $\Gamma\left(\mathbf{Q}, \Omega_n\right)$, that only depends on the center-of-mass momentum $\mathbf{Q}$ of the pair and a bosonic Matsubara frequency $\Omega_n$. In the absence of an FFLO-type order parameter the momentum dependence is further simplified to $\Gamma\left(Q, \Omega_n\right)$, due to the isotropy of the system. In any case, for a single momentum argument we can directly obtain the inverse of the vertex function $\Gamma^{-1}\left(\mathbf{Q}, \Omega_n\right) = 1/\Gamma\left(\mathbf{Q}, \Omega_n\right)$, since $\Gamma$ is diagonal in momentum space. The inverse vertex is related to the Thouless criterion [152], which is an example of a general Ward identity [141]. The Thouless criterion ascertains the existence of a gapless Goldstone mode, when the $U(1)$ symmetry is spontaneously broken by Cooper pairing. As discussed in Refs. [37, 150], it can be expressed in the present theory as

$$\sum_{\beta=1,2} \left(\Gamma^{-1}\left(Q, \Omega_n = 0\right)\right)_{\alpha\beta} \begin{pmatrix} \Delta \\ \Delta^* \end{pmatrix}_\beta = \begin{pmatrix} 0 \\ 0 \end{pmatrix} \tag{4.29}$$

for phases without FFLO order, where $\Delta$ refers to the order parameter from eq. (4.7) with trivial momentum dependence. The matrix indices of $\Gamma^{-1}$ account for the Nambu structure in the presence of finite anomalous expectation values in the superfluid phase, see also Appendix A. In the normal phase, where the Nambu structure of all quantities reduces to diagonal elements, this equation is satisfied automatically, since the superfluid order parameter vanishes identically. The approach to the superfluid transition is then indicated by a divergence of the pair propagator $\Gamma(Q, \Omega_n = 0)$. This singularity either emerges in the limit $Q \to 0$, in the case of a standard homogeneous superfluid, or it is encountered at a finite $Q$, corresponding to a finite center-of-mass momentum of the Cooper pairs in an FFLO-phase.

### 4.5.2 The vertex in the ladder approximation

Since the Luttinger-Ward formalism is only based on $G$, we are free to define a vertex function as long as it meets the physical constraints from the previous

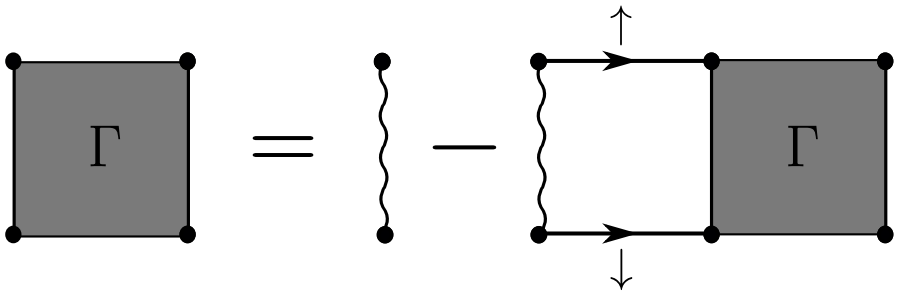


Figure 4.3: Diagrammatic representation of the Bethe-Salpeter equation (4.30) for the vertex $\Gamma(\mathbf{Q}, \Omega_n)$ in the ladder-approximation. The spins indicate the spin-symmetric particle-particle bubble that is inherited by the vertex function.

section. A suitable form for $\Gamma(\mathbf{Q}, \Omega_n)$ is obtained by removing the two hole Green's functions in the ladder diagrams of $\Phi[G]$, depicted in Fig. 4.2. An equivalent result can be obtained by taking out any other pair of Green's functions that connect the *same* rungs. However, if one opened each leg of the ladder between two different pairs of rungs, as would be allowed in a higher effective action formulation like the approach of de Dominics and Martin [142,143], the resulting vertex function would acquire a momentum structure with a non-trivial dependence on relative momenta. Therefore, we stick to the first construction and note that the resulting $\Gamma(\mathbf{Q}, \Omega_n)$ satisfies the Bethe-Salpeter equation shown in Fig. 4.3

$$\Gamma(\mathbf{Q}, \Omega_n) = \bar{g}(\Lambda) - \bar{g}(\Lambda)\chi(\mathbf{Q}, \Omega_n)\,\Gamma(\mathbf{Q}, \Omega_n)\ . \tag{4.30}$$

Its solution can be easily expressed, due to the simple momentum dependence, as

$$\Gamma(\mathbf{Q}, \Omega_n) = \frac{1}{\frac{1}{\bar{g}} + \chi(\mathbf{Q}, \Omega_n)} = \frac{1}{\frac{1}{g} + M(\mathbf{Q}, \Omega_n)}\,. \tag{4.31}$$

Formally, it represents the resummation of the geometric series generated by the particle-particle bubble diagram $\chi(\mathbf{Q}, \Omega_n)$, defined in (4.23). In the zero-range limit $\chi(\mathbf{Q}, \Omega_n)$ is replaced by its renormalized counterpart

$$M(\mathbf{Q}, \Omega_n) = \lim_{\Lambda\to\infty}\left(\chi(\mathbf{Q}, \Omega_n) - \int_{q<\Lambda}\frac{1}{2\varepsilon_q}\right)\,, \tag{4.32}$$

where we have again made use of the connection between the bare and the physical coupling constant from eq. (2.29). The fact, that $\chi(\mathbf{Q}, \Omega_n)$ itself is ill-defined can already be observed at the level of bare Green's functions after performing the

internal Matsubara sum with the techniques outlined in Appendix B

$$\begin{aligned} M^{(0)}(\mathbf{Q},\Omega_n) &= \int \frac{d^3k}{(2\pi)^3}\left[\frac{1}{\beta}\sum_m \mathcal{G}^{(0)}_{\uparrow\uparrow}(\mathbf{k},\omega_m)\,\mathcal{G}^{(0)}_{\downarrow\downarrow}(\mathbf{Q}-\mathbf{k},\Omega_n-\omega_m) - \frac{1}{2\varepsilon_k}\right] \\ &= \int \frac{d^3k}{(2\pi)^3}\left[\frac{1-n_F(\xi_{\mathbf{k}+\mathbf{Q}/2,\uparrow})-n_F(\xi_{\mathbf{k}-\mathbf{Q}/2,\downarrow})}{-i\hbar\Omega_n+\xi_{\mathbf{k}+\mathbf{Q}/2,\uparrow}+\xi_{\mathbf{k}-\mathbf{Q}/2,\downarrow}} - \frac{1}{2\varepsilon_k}\right] \\ &= \int \frac{d^3k}{(2\pi)^3}\left[\frac{1-n_F(\xi_{\mathbf{k}+\mathbf{Q}/2,\uparrow})-n_F(\xi_{\mathbf{k}-\mathbf{Q}/2,\downarrow})}{-i\hbar\Omega_n+2\varepsilon_k+\frac{\varepsilon_Q}{2}-2\mu} - \frac{1}{2\varepsilon_k}\right]. \end{aligned} \tag{4.33}$$

The leading order contribution of the first term for large $k \to \infty$ is canceled identically by the second term, that originates from the renormalization. Fortunately, it will turn out that the complete UV-behavior and the related divergences, that have to be regularized in the limit $\Lambda \to \infty$, actually only arise from the diagrams with noninteracting Green's functions, whereas all interaction contributions to $G$ only give rise to corrections that are finite in the zero-range limit. Similar considerations on the UV-asymptotics can also be found in the review on BDMC-computations in the context of ultracold atoms by van Houcke et al. [153]. As an example, the large $Q$ asymptotics of the renormalized bubble diagram is exclusively determined by the combination of the terms without the Fermi distributions, since the latter vanish exponentially for $Q \to \infty$. More precisely, we can compute this asymptotics for $\Omega_n \neq 0$ exactly via

$$\begin{aligned} \int \frac{d^3k}{(2\pi)^3}\left[\frac{1}{-i\hbar\Omega_n+2\varepsilon_k+\frac{\varepsilon_Q}{2}-2\mu} - \frac{1}{2\varepsilon_k}\right] &= \frac{m^2}{(2\pi\hbar^2)^2}\int dk \frac{(i\hbar\Omega_n-\frac{\varepsilon_Q}{2}+2\mu)}{k^2-\frac{m}{\hbar^2}(i\hbar\Omega_n-\frac{\varepsilon_Q}{2}+2\mu)} \\ &= -\frac{m^{3/2}}{4\pi\hbar^3}\left(\frac{\varepsilon_Q}{2}-2\mu-i\hbar\Omega_n\right)^{1/2}. \end{aligned} \tag{4.34}$$

In the limit of $Q \to \infty$ or $|\Omega_n| \to \infty$ we conclude that the absolute value of $M$ diverges algebraically. Moreover, summing the vertex function in eq. (4.31) directly over all Matsubara frequencies is not well-defined and the same holds true for the momentum integral. Instead, these operations have to be understood as Fourier transforms, which is explained in further detail below. However, the algebraic behavior will require special subtractions before the vertex is amenable to numerical methods, see Chapter 7.

On the contrary, if the dependence on $\Lambda$ is kept manifest in the theory, one finds

$$\int \frac{d^3k}{(2\pi)^3} \frac{1}{-i\hbar\Omega_n + 2\varepsilon_k + \frac{\varepsilon_Q}{2} - 2\mu} = \frac{m}{2\pi^2\hbar^2} \left[ \Lambda + \int_0^\Lambda dk \, \frac{\frac{m}{\hbar^2}(i\hbar\Omega_n - \frac{\varepsilon_Q}{2} + 2\mu)}{k^2 + \frac{m}{\hbar^2}(\frac{\varepsilon_Q}{2} - 2\mu - i\hbar\Omega_n)} \right]$$
$$= \frac{m}{2\pi^2\hbar^2} \left[ \Lambda - \frac{m^{1/2}}{\hbar^2} \sqrt{\frac{\varepsilon_Q}{2} - 2\mu - i\hbar\Omega_n} \arctan \left( \frac{\Lambda}{\frac{m^{1/2}}{\hbar} \sqrt{\frac{\varepsilon_Q}{2} - 2\mu - i\hbar\Omega_n}} \right) \right] . \tag{4.35}$$

After subtracting the term linear in $\Lambda$ in analogy to the renormalization scheme above, this form reproduces eq. 4.34, under the condition that $\Lambda$ is much larger than any other scale. In the opposite limit $|m^{1/2}\sqrt{\varepsilon_Q - 2\mu - i\hbar\Omega_n}/\hbar| \gg \Lambda$, however, the previous asymptotics gets cut off and we have instead the leading order $\Lambda^3/(2\pi^2(\varepsilon_Q/2 - 2\mu - i\hbar\Omega_n)) \to 0$. This result depends explicitly on the cutoff and therefore changes with the renormalization scheme, while the renormalized theory probes the universal low-energy physics in the zero-range limit.

Finally, we note in passing that in the case $\Omega_n = 0$ the zero in the denominator of $M^{(0)}(\mathbf{Q}, \Omega_n)$ in eq. 4.33 gets compensated by the zero in the numerator. As discussed by Pethick and Smith [16], the Fermi edges become sharper with decreasing temperature, which leads to a $\log T/\varepsilon_F$ divergence and ultimately to the exponentially small BCS temperature in eq. (4.22) from the Thouless criterion in the weak coupling limit $1/g + M^{(0)}(Q = 0, \Omega_n = 0) = 0$.

Now, with a concrete form for the vertex available, we can now proceed with the determination of the self-energies, which are the last missing piece, before we can write down the Schwinger-Dyson equation.

## 4.6 Self-energies and the self-consistent equations for $G$

### 4.6.1 Self-energy diagrams

In order to determine the physical Green's functions we have to solve the Dyson equation (4.20), where the self-energy is obtained from $\Sigma[G] = \delta\Phi[G]/\delta G$, see eq. (4.21). This functional derivative can be visualized as taking out one of the Green's functions linking any two of the rungs of the ladders in Fig. 4.2, which yields diagrams of the kind shown in Fig. 4.4. Translating the Feynman diagram into a formula, we have above $T_c$

$$\Sigma_{\sigma\sigma}(\mathbf{k}, \omega_n) = \int \frac{d^3Q}{(2\pi)^3} \frac{1}{\beta} \sum_m \Gamma(\mathbf{Q}, \Omega_m) \, \mathcal{G}_{\bar{\sigma}\bar{\sigma}}(\mathbf{Q} - \mathbf{k}, \Omega_m - \omega_n) , \tag{4.36}$$

where we have utilized the specific diagrammatic form of the vertex, defined in the previous section. Note that the spin indices of the self-energy $\Sigma_{\sigma\sigma}$ coincide with those of the removed Green's function $\mathcal{G}_{\sigma\sigma}$, while the Green's function on the

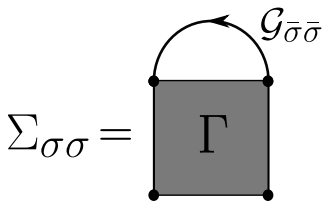


Figure 4.4: Diagrammatic representation of the self-energy $\Sigma[G]_{\sigma\sigma}$ as functional derivative of $\Phi[G]$ in Fig. 4.2. Note that the vertex is closed with a Green's function of opposite spin $\bar{\sigma}$.

right-hand side carries the opposite spin orientation in accordance with the spin structure imprinted by the particle-particle ladder.

### 4.6.2 The self-consistent equations for G

We are now in the position to formulate the self-consistent equations of motion for the Green's function from the previously defined functions. The first step is to compute from a given Green's function $G(\mathbf{k}, \omega_n)$, the particle-particle bubble diagram $M(\mathbf{Q}, \Omega_n)$ defined in eq. (4.32). For the numerical evaluation we Fourier transform the Green's function to real space, where the convolution encountered in the unrenormalized function $\chi$ from eq. (4.23) can be replaced by the product

$$\chi(\mathbf{x}, \tau) = \mathcal{G}_{\uparrow\uparrow}(\mathbf{x}, \tau)\, \mathcal{G}_{\downarrow\downarrow}(\mathbf{x}, \tau) \ . \tag{4.37}$$

This is well defined in real space, except for $\tau \to 0^+$ at $\mathbf{x} = \mathbf{0}$, as can be seen from the dominant part of the $\mathcal{G}_{\sigma\sigma}(\mathbf{x}, \tau)$ in eq. (7.11), which therefore will be treated analytically. To perform the ensuing back transformation to momentum and frequency space, we single out the parts from the bare Green's functions, which require the renormalization. These can be computed with the analytic considerations in (4.35) above, while we treat the remaining terms by numerical means. We detail this procedure for the determination of $M(\mathbf{Q}, \Omega_n)$ in Chapter 7. Next we calculate the vertex function $\Gamma(\mathbf{Q}, \Omega_n)$ according to the geometric series (4.31), before we turn to the computation of the self-energies (4.36), which we carry out again in real space where it attains the product form

$$\Sigma_{\sigma\sigma}(\mathbf{x}, \tau) = \Gamma(\mathbf{x}, \tau)\, \mathcal{G}_{\bar{\sigma}\bar{\sigma}}(-\mathbf{x}, -\tau) \ . \tag{4.38}$$

Then, we Fourier transform the self-energies back to $\Sigma_{\sigma\sigma}(\mathbf{k}, \omega_n)$, which enters the Schwinger-Dyson equation (4.20) and gives rise to an updated Green's function after inverting the equation. With the resulting $G$ the procedure is started over again from equation (4.37) until convergence is reached in the sense that the current $G$ is a fixed point of the self-consistency loop. A pictorial representation of this procedure can be found in Fig. 4.5. In total, we have obtained a closed set of equations that only involve Fourier transformations and component-wise products, for

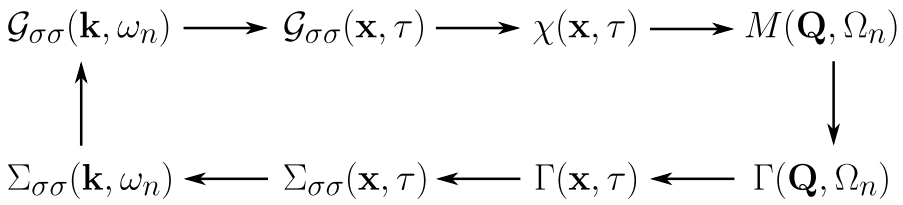


Figure 4.5: Self-consistent loop for the Green's functions. In the horizontal direction either Fourier transforms or multiplications have to be performed. The vertical step on the right is based on the Bethe-Salpeter equation (4.30), while its counterpart on the left represents the Schwinger-Dyson equation (4.20).

which highly optimized algorithms exist. However, due to the specific asymptotics of the functions encountered in the BCS-BEC crossover, we have to use Fourier transformations that are specifically designed to the problem. We introduce these transformations in Chapter 6.

## 4.7 Thermodynamic Quantities

Having solved the self-consistent equations from the previous section, knowledge of the physical Green's function suffices to determine the Luttinger-Ward grand potential $\Omega[G]$ (4.18), which gives access to all thermodynamic quantities. Observables like the spin densities $n_\sigma$ and the contact density $\mathcal{C}$ are easily obtained from $G(\mathbf{x},\tau)$ or $\Gamma(\mathbf{x},\tau)$, respectively, via the short-distance and short-time limits (4.4) and (4.28). In order to determine thermodynamic quantities like the entropy it is in principle possible to directly use relations like $S = -(\partial\Omega/\partial T)_{V,\mu_\sigma}$, which, however, requires to compute derivatives of numerical data. Since these operations are quite sensitive to computational uncertainties, it is preferable to express the entropy $S$and the internal energy $U$ as functionals of $G$ and $\Gamma$, similar to the pressure, which can be directly read-off from $p[G] = -\Omega[G]/V$. To find these functionals, we extend the results used by Haussmann et. al [37] and by Cerrito [144] for the latter observables to a finite spin imbalance, yet only in the normal phase.

Common to $p, U$ and $S$ is that they can be split into two contributions. A simple mean-field term is obtained by both replacing the dressed Green's function $G$ by its bare counterpart $G^{(0)}$ from eq. (4.12), and the full vertex $\Gamma$ by the bare coupling constant $\bar{g}(\Lambda)$. Above $T_c$ these terms will reduce to the noninteracting results. The remainders can be gathered in a functional that includes the interaction effects. This separation turns out to be useful to perform the renormalization in the zero-range limit, which affects only the lowest order interactions. The effects from higher orders have to be treated numerically, but all of them can be interpreted as Fourier transform to $\mathbf{x} = \mathbf{0}$ and $\tau \to 0^-$. Therefore, we can utilize the same methods as in the self-consistent loop, yet, we have to find a form for these terms, which can

be reliably Fourier transformed. This last step involves a new subtraction scheme, which is detailed in Section 7.3 on the numerical implementations.

### 4.7.1 Pressure functional

Let us first focus on the result for the pressure $p = -\Omega/V$, which follows from the ladder approximation to $\Omega[G]$ in eq. (4.25). Applying the identity $\log[\mathcal{G}_{\sigma\sigma}] = \log[\mathcal{G}^{(0)}_{\sigma\sigma}] + \log[(\mathcal{G}^{(0)}_{\sigma\sigma})^{-1}\mathcal{G}_{\sigma\sigma}]$ to the first term and plugging the Bethe-Salpeter equation into the last term, yields

$$\begin{aligned} p[G,\Gamma] = &- \int \frac{d^3k}{(2\pi)^3}\frac{1}{\beta}\sum_{\sigma,n}\log\left[\mathcal{G}^{(0)}_{\sigma\sigma}\left(\mathbf{k},\omega_n\right)\right] \\ &- \int \frac{d^3k}{(2\pi)^3}\frac{1}{\beta}\sum_{\sigma,n}\left\{\log\left[\mathcal{G}^{(0)}_{\sigma\sigma}\left(\mathbf{k},\omega_n\right)^{-1}\mathcal{G}_{\sigma\sigma}\left(\mathbf{k},\omega_n\right)\right] + \left[1 - \mathcal{G}^{(0)}_{\sigma\sigma}\left(\mathbf{k},\omega_n\right)^{-1}\mathcal{G}_{\sigma\sigma}\left(\mathbf{k},\omega_n\right)\right]\right\} \\ &- \int \frac{d^3Q}{(2\pi)^3}\frac{1}{\beta}\sum_{n}\left\{\log\left[\bar{g}\left(\Lambda\right)\,\Gamma^{-1}\left(\mathbf{Q},\Omega_n\right)\right]\right\}. \end{aligned} \tag{4.39}$$

This form singles out the mean-field term in the first line, while the other two lines vanish identically upon the replacements $G \to G^{(0)}$ and $\Gamma \to \bar{g}(\Lambda)$. In particular, the Matsubara sum and the $\mathbf{k}$ integral of $\log[\mathcal{G}^{(0)}_{\sigma\sigma}\left(\mathbf{k},\omega_n\right)]$ are well known and yield the pressure $p^{(0)}(T,\mu_\sigma) = -T/\lambda_T^3\ \mathrm{Li}_{5/2}[-\exp\left(\beta\mu_\sigma\right)]$ [154] of a single-component ideal Fermi gas, in analogy to eq. (2.34) for a balanced two-component gas. Consequently, the first line is equivalent to the pressure $p^{(0)}_{\mathrm{imb}}(T,\mu,h)$ of a noninteracting, spin-imbalanced Fermi gas

$$p^{(0)}_{\mathrm{imb}} = -\frac{T}{\lambda_T^3}\left[\mathrm{Li}_{5/2}\left(-e^{\beta\mu_\uparrow}\right) + \mathrm{Li}_{5/2}\left(-e^{\beta\mu_\downarrow}\right)\right]. \tag{4.40}$$

Physically, the sum can be understood from the fact that in the absence of interactions both spin species form individual Fermi gases within the same volume but without any interspecies correlations. Because of the extensivity of the grand potential both contributions add together $\Omega = \Omega_\uparrow + \Omega_\downarrow$, which immediately leads to the given form of the pressure.

Finally, we consider the second line of eq. (4.39) and note that it scales like $\omega_n^{-3}$ for large Matsubara frequencies. The stated power law can be proven from the universal $1/\omega_n$ behavior for $|\omega_n| \to \infty$ of any Green's function [67], which arises from the contribution of the equal-time anticommutation relations (4.1) to the equation of motion of the Green's functions, irrespective of the presence of interactions. Therefore, we can Taylor expand the logarithm in the limit of large

frequencies, which yields

$$\begin{aligned}\log\left[\mathcal{G}^{(0)}_{\sigma\sigma}\left(\mathbf{k},\omega_n\right)^{-1}\mathcal{G}_{\sigma\sigma}\left(\mathbf{k},\omega_n\right)\right]-\left[1-\mathcal{G}^{(0)}_{\sigma\sigma}\left(\mathbf{k},\omega_n\right)^{-1}\mathcal{G}_{\sigma\sigma}\left(\mathbf{k},\omega_n\right)\right]&\xrightarrow{|\omega_n|\to\infty}\\ \frac{1}{2}(\mathcal{G}^{(0)}_{\sigma\sigma}\left(\mathbf{k},\omega_n\right)^{-1}\mathcal{G}_{\sigma\sigma}\left(\mathbf{k},\omega_n\right)-1)^2+\ldots=\frac{1}{2}\mathcal{G}^2_{\sigma\sigma}\left(\mathbf{k},\omega_n\right)\Sigma^2_{\sigma\sigma}\left(\mathbf{k},\omega_n\right)+\ldots.&\end{aligned}\tag{4.41}$$

In the last step we used the Dyson equation (4.20). With the asymptotics of the self-energy $\Sigma_{\sigma\sigma}\left(\mathbf{k},\omega_n\right)\simeq 1/\sqrt{i\omega_n}$, derived in eq. (7.57), we obtain the desired cubic decrease. We can interpret the sum and the momentum integral of this expression as Fourier transformations to the origin in real space and imaginary time, which, due to the fast decay, can be performed by numerical means. For later convenience we abbreviate this contribution in terms of the auxiliary functional

$$\begin{aligned}H_1[G]=-\int\frac{d^3k}{(2\pi)^3}\frac{1}{\beta}\sum_{\sigma,n}\Big(&\log\left[\mathcal{G}^{(0)}_{\sigma\sigma}\left(\mathbf{k},\omega_n\right)^{-1}\mathcal{G}_{\sigma\sigma}\left(\mathbf{k},\omega_n\right)\right]\\&+\left[1-\mathcal{G}^{(0)}_{\sigma\sigma}\left(\mathbf{k},\omega_n\right)^{-1}\mathcal{G}_{\sigma\sigma}\left(\mathbf{k},\omega_n\right)\right]\Big).\end{aligned}\tag{4.42}$$

Finally, the Matsubara sum of the logarithm in the equation for the pressure (4.39) remains. As the inverse vertex for large $\Omega_n$ is dominated by the leading order bubble diagram from eq. (4.35), that grows like $M^{(0)}\left(\mathbf{Q},\Omega_n\right)\simeq\alpha\left(\frac{\varepsilon_Q}{2}-2\mu-i\hbar\Omega_n\right)^{1/2}$, with $\alpha=-m^{3/2}/(4\pi\hbar^3)$, the sum is mathematically not-well defined, no matter which coupling constant is inserted. To regularize the expression, we first rewrite it in the form

$$\begin{aligned}\log\left[\bar{g}(\Lambda)\Gamma^{-1}\left(\mathbf{Q},\Omega_n\right)\right]=\Bigg(&\log\left[1+\frac{\Gamma^{-1}\left(\mathbf{Q},\Omega_n\right)-\alpha\sqrt{\frac{\varepsilon_Q}{2}+\frac{d}{2}-i\hbar\Omega_n}}{\alpha\sqrt{\frac{\varepsilon_Q}{2}+\frac{d}{2}-i\hbar\Omega_n}}\right]\\&+\log\left[g\alpha\sqrt{\frac{\varepsilon_Q}{2}+\frac{d}{2}-i\hbar\Omega_n}\right]+\log\left[\frac{\bar{g}(\Lambda)}{g}\right]\Bigg),\end{aligned}\tag{4.43}$$

where we have separated the dependence on the bare coupling constant and furthermore have introduced an auxiliary, negative chemical potential[3] $d>0$, which of course does not alter the asymptotics. We will return to this trick, when we construct the subtraction schemes for the numerical implementation in Sec. 7. In practice, we choose the numerical value $d=150\,T$, which drastically simplifies the evaluation of the terms. Computing the Matsubara sum of the constant $\log(\bar{g}(\Lambda)/g)$, yields a Dirac distribution $\delta(\tau)$. Since the convergence factor enforces the evaluation in the limit $\tau\to 0^-$, this contribution vanishes. Therefore, the pressure depends only on physical quantities, as required for any observable. The

[3]Negative in the sense that it appears with the opposite sign compared to standard chemical potentials.

first term now asymptotes as $\Omega_n^{-1/2}$, which decays to zero and thus can formally be summed by introducing an oscillating convergence factor $\exp(i\Omega_n 0^+)$. These convergence factors appear quite often in frequency sums and guarantee finite results in the limit $\tau \to 0^-$, thereby measuring the actual particle excitations that contribute to the thermodynamics rather than the holes [67, 154]. A similar procedure for the grand potential, however with bare ladders, is used by Diener et al. [147]. Yet, this behavior still is not very satisfactory, since it is not amenable to a numerical treatment. Therefore, we will construct a subtraction scheme for this term, that improves its numerical properties, but we postpone the precise definitions to Sec. 7.3, since it requires the explicit form of the decomposition of the vertex function in analytical and numerical parts presented in Sec. 7.2.

Regarding the second term in (4.43), we still encounter a function that asymptotically grows. Yet, we can consider it in terms of a generalized Fourier transform (see App. C or the book by Gel'fand and Shilov [155]), which also exist for algebraically or logarithmically diverging functions. Accepting this interpretation, we can include the standard convergence factor $\exp(i\Omega_n 0^+)$, which allows to rewrite the Matsubara sum as a contour integral (see App. B) in the complex plane by the replacement $i\Omega_n \to z$, while the integrand has to be multiplied by the Bose distribution $n_B(z) = [\exp(\beta z) - 1]^{-1}$. Shifting the arcs of the contour towards infinity, their contributions vanishes exponentially, either due to $n_B(z) \simeq \exp(-\beta z)$ for $\mathrm{Re}(z) \to +\infty$ or because of $\exp(z0^+)$ for $\mathrm{Re}(z) \to -\infty$. Therefore, the only relevant contribution comes from the integral along the branch cut of the square root on the positive real axis, which starts out at $(\varepsilon_Q + d)/2$. Thus, for arbitrary momenta this integral has a uniform suppression of $n_B(d/2) \sim \exp(-\beta d/2)$, even after the integral over momenta has been performed. For our choice of $d$ the term is on the order of $10^{-11}$ and will be neglected in the following. Consequently, we define the second beyond-mean-field contribution to the pressure

$$H_{\log}[\Gamma] = \frac{1}{2}\int \frac{d^3Q}{(2\pi)^3}\frac{1}{\beta}\sum_n e^{i\Omega_n 0^+}\log\left[1 + \frac{\Gamma^{-1}\left(\mathbf{Q},\Omega_n\right) - \alpha\sqrt{\frac{\varepsilon_Q}{2}+\frac{d}{2}-i\Omega_n}}{\alpha\sqrt{\frac{\varepsilon_Q}{2}+\frac{d}{2}-i\Omega_n}}\right]. \tag{4.44}$$

All in all, the pressure finally reads

$$p = p^{(0)}_{\mathrm{imb}} + H_1[G] + H_{\log}\left[\Gamma\right]. \tag{4.45}$$

### 4.7.2 Internal energy

The internal energy is given by the expectation of the Hamiltonian $U = \langle H \rangle$, which consists of a kinetic and potential energy part. As discussed in connection with the Tan relations in Sec. 2.4, the momentum distribution for zero-range interactions exhibits quite generically an algebraic tail $n_\sigma(k) \simeq \mathcal{C}/k^4$, such that the kinetic energy diverges and only the total energy is meaningful. Therefore, we decompose

$U$ in analogy to $p$ in a noninteracting and a higher order part and carefully discuss the limit $\Lambda \to \infty$. Similar arguments can be found in [37, 144]. The energy density $\varepsilon = U/V$ of the single-channel Hamiltonian (2.26) reads

$$\varepsilon = \sum_{\sigma} \int \frac{d^3k}{(2\pi)^3} \varepsilon_k \, \mathcal{G}_{\sigma\sigma}(\mathbf{k}, \tau = 0^-) + \bar{g}(\Lambda) \int d^3x \left\langle \hat{\Psi}_{\uparrow}^{\dagger}(\mathbf{x}) \, \hat{\Psi}_{\downarrow}^{\dagger}(\mathbf{x}) \, \hat{\Psi}_{\downarrow}(\mathbf{x}) \, \hat{\Psi}_{\uparrow}(\mathbf{x}) \right\rangle , \tag{4.46}$$

where $\mathcal{G}_{\sigma\sigma}(\mathbf{k}, \tau = 0^-)$ is identical to the momentum distribution $n_\sigma(k)$, see equation (2.57). The second term actually includes the two-particle Green's function $G_2$, that in general can be written as a sum of disconnected products of single-particle Green's functions plus the connected part, which includes the vertex [141]. In a mathematical form this means

$$\begin{aligned} G_2(1,2,3,4) = {} & G(1,2)G(3,4) - G(1,3)G(2,4) + G(1,4)G(2,3) \\ & - G(1,1')G(2,2')\Gamma(1',2',3',4')G(3',3)G(4',4) , \end{aligned} \tag{4.47}$$

where each argument refers to the set of $(\mathbf{x}, \tau)$ coordinates, as well as to spin orientation and a sum or an integral over the primed indices is understood implicitly. The first line corresponds to the disconnected contributions to $G_2$, which in the energy density give rise to the Hartree, the Fock and the particle-particle bubble diagram $\chi$ of two co-propagating Fermions, according to the definition (4.23). Since the Hartree diagram vanishes in the zero-range limit and the Fock diagram corresponds to an anomalous contraction of opposite spin indices, which does not exist above $T_c$, we obtain the following expression for $\varepsilon$ in momentum space [37]

$$\begin{aligned} \varepsilon = {} & \sum_{\sigma} \int \frac{d^3k}{(2\pi)^3} \varepsilon_k \, \mathcal{G}_{\sigma\sigma}(\mathbf{k}, \tau = 0^-) \\ & + \bar{g}(\Lambda) \int \frac{d^3Q}{(2\pi)^3} \frac{1}{\hbar\beta} \sum_n \left[ \chi(\mathbf{Q}, \Omega_n) - \chi(\mathbf{Q}, \Omega_n) \, \Gamma(\mathbf{Q}, \Omega_n) \, \chi(\mathbf{Q}, \Omega_n) \right] . \end{aligned} \tag{4.48}$$

In the second term the factors of $G$, that connect vertex function in $G_2$ with the external points, have been contracted into $\chi(\mathbf{Q}, \Omega_n)$. Note that at this stage, we use the unrenormalized version of the particle-particle bubble, since the zero-range limit has not been performed yet and the expression still contains $\bar{g}(\Lambda)$.

In fact, it turns out to be more convenient for the numerics to compute the "grand canonical" energy density $\langle H/V - \mu_\uparrow \hat{n}_\uparrow - \mu_\downarrow \hat{n}_\downarrow \rangle$. Obviously $\varepsilon$ can be recovered by adding $\mu_\uparrow n_\uparrow + \mu_\downarrow n_\downarrow = \mu\, n + h\, \delta n$, which is obtained from the self-consistent Green's function directly. Using the momentum-space representation of the bare Green's function (4.9), we find

$$\begin{aligned} \epsilon - \mu\, n - h\, \delta n = {} & - \int \frac{d^3k}{(2\pi)^3} \frac{1}{\beta} \sum_{\sigma,n} \left\{ \left[ \mathcal{G}_{\sigma\sigma}^{(0)}(\mathbf{k}, \omega_n)^{-1} - i\hbar\omega_n \right] \mathcal{G}_{\sigma\sigma}(\mathbf{k}, \omega_n) \right\} \\ & - \int \frac{d^3Q}{(2\pi)^3} \frac{1}{\beta} \sum_n \left[ \frac{\Gamma(\mathbf{Q}, \Omega_n)}{\bar{g}(\Lambda)} - 1 \right] , \end{aligned} \tag{4.49}$$

where the last term results from equation (4.48) by inserting Bethe-Salpeter equation (4.30). From the latter we arrive at the necessary intermediate form $\bar{g}(\chi - \chi\Gamma\chi) = \chi\Gamma$, which yields the above expression by replacing $\chi = \Gamma^{-1} - 1/\bar{g}$. From the last equation we can determine the mean-field contribution in a similar way as in the pressure functional. Here we find

$$\begin{aligned}(\varepsilon - \mu\, n - h\, \delta n)^{(0)} &= -\int \frac{d^3k}{(2\pi)^3}\frac{1}{\beta}\sum_{\sigma,n}\left\{\left[\mathcal{G}^{(0)}_{\sigma\sigma}\left(\mathbf{k},\omega_n\right)^{-1} - i\hbar\omega_n\right]\mathcal{G}^{(0)}_{\sigma\sigma}\left(\mathbf{k},\omega_n\right)\right\} \\ &= \int \frac{d^3k}{(2\pi)^3}\frac{1}{\beta}\sum_{\sigma,n}(\varepsilon_k - \mu_\sigma)\,\mathcal{G}^{(0)}_{\sigma\sigma}\left(\mathbf{k},\omega_n\right)\,,\end{aligned} \tag{4.50}$$

where the Matsubara sum can be solved once more in the presence of a convergence factor $\exp(i\Omega_n 0^+)$. In the symmetric phase we recover again the result for ideal Fermions

$$\begin{aligned}(\varepsilon - \mu_\uparrow n_\uparrow - \mu_\downarrow n_\downarrow)^{(0)} = \frac{2}{3}\frac{T}{\lambda_T^3}&\left[\mathrm{Li}_{5/2}\left(-e^{\beta\mu_\uparrow}\right) + \mathrm{Li}_{5/2}\left(-e^{\beta\mu_\downarrow}\right)\right] \\ &+ \frac{\mu_\uparrow}{\lambda_T^3}\mathrm{Li}_{3/2}\left(-e^{\beta\mu_\uparrow}\right) + \frac{\mu_\downarrow}{\lambda_T^3}\mathrm{Li}_{3/2}\left(-e^{\beta\mu_\downarrow}\right)\,,\end{aligned} \tag{4.51}$$

which follows from the trivial scale invariance $p^{(0)} = 2\varepsilon^{(0)}/3$ in the absence of interactions together with the density of a single-component ideal Fermi gas

$$n^{(0)}(T,\mu_\sigma) = -\frac{1}{\lambda_T^3}\mathrm{Li}_{3/2}(-e^{\beta\mu_\sigma})\,. \tag{4.52}$$

To find the non-trivial term, we first consider the last integral in eq. (4.49) with the vertex. Following the same steps as in equation (2.59) of Ref. [37], it can be rewritten as

$$\begin{aligned}&-\int \frac{d^3Q}{(2\pi)^3}\frac{1}{\beta}\sum_n\left[\frac{\Gamma\left(\mathbf{Q},\Omega_n\right)}{\bar{g}\left(\Lambda\right)} - 1\right] \\ &= \int \frac{d^3Q}{(2\pi)^3}\frac{1}{\beta}\sum_n\left[\Gamma\left(\mathbf{Q},\Omega_n\right)\chi\left(\mathbf{Q},\Omega_n\right)\right] \\ &= \frac{1}{2}\int \frac{d^3k}{(2\pi)^3}\frac{1}{\beta}\sum_{\sigma,n}\left[\Sigma_{\sigma\sigma}\left(\mathbf{k},\omega_n\right)\mathcal{G}_{\sigma\sigma}\left(\mathbf{k},\omega_n\right)\right] \\ &= \frac{1}{2}\int \frac{d^3k}{(2\pi)^3}\frac{1}{\beta}\sum_{\sigma,n}\left\{\mathcal{G}^{(0)}_{\sigma\sigma}\left(\mathbf{k},\omega_n\right)^{-1}\left[\mathcal{G}_{\sigma\sigma}\left(\mathbf{k},\omega_n\right) - \mathcal{G}^{(0)}_{\sigma\sigma}\left(\mathbf{k},\omega_n\right)\right]\right\}\,.\end{aligned} \tag{4.53}$$

To obtain the final result one uses first the Bethe-Salpeter equation (4.30), before exchanging the order of the bosonic and the fermionic integral, where the latter implicitly appears in $\chi\left(\mathbf{k},\omega_n\right)$, given in eq. (4.23). This generates the self-energy from eq. (4.21), which together with the Dyson equation (4.20) last line from the

equation above, where $\bar{g}(\Lambda)$ has dropped out. Combining this intermediate step with (4.49) and (4.50) yields for the higher order contribution to the grand canonical energy density

$$\begin{aligned} H_2[G] &= \varepsilon - \mu n - h\sigma - \left(\varepsilon - \mu n - h\sigma\right)^{(0)} \\ &= -\frac{1}{2}\int \frac{d^3k}{(2\pi)^3}\frac{1}{\beta}\sum_{\sigma,n}\left\{\left[\mathcal{G}^{(0)}_{\sigma\sigma}\left(\mathbf{k},\omega_n\right)^{-1} - 2i\hbar\omega_n\right]\left[\mathcal{G}_{\sigma\sigma}\left(\mathbf{k},\omega_n\right) - \mathcal{G}^{(0)}_{\sigma\sigma}\left(\mathbf{k},\omega_n\right)\right]\right\} \\ &= -\frac{1}{2}\int \frac{d^3k}{(2\pi)^3}\frac{1}{\beta}\sum_{n,\sigma}\left\{\left[\mathcal{G}^{(0)}_{\sigma\sigma}\left(\mathbf{k},-\omega_n\right)^{-1}\right]\left[\mathcal{G}_{\sigma\sigma}\left(\mathbf{k},\omega_n\right) - \mathcal{G}^{(0)}_{\sigma\sigma}\left(\mathbf{k},\omega_n\right)\right]\right\}, \end{aligned} \tag{4.54}$$

where the first bracket has been simplified by noting

$$\mathcal{G}^{(0)}_{\sigma\sigma}(\mathbf{k},-\omega_n)^{-1} = \mathcal{G}^{(0)}_{\sigma\sigma}\left(\mathbf{k},\omega_n\right)^{-1} - 2i\hbar\omega_n\,.$$

This defines a new auxiliary functional $H_2[G]$, where the integrand scales asymptotically like $\omega_n^{-3/2}$ and thus the Matsubara sum exists. One can verify this statement by inserting the Dyson equation with the asymptotics $\mathcal{G}_{\sigma\sigma}\propto 1/\omega_n$ and $\Sigma_{\sigma\sigma} \simeq \sqrt{i\omega_n}^{-1}$ from eq. (7.57). In practice, we will separate further terms, which can be treated by other means to improve the numerical quality, see Sec. 7.3.

Altogether, we have for the combination of internal energy with the pairs of conjugated chemical potentials and spin densities

$$\varepsilon - \mu n - h\sigma = \left(\varepsilon - \mu n - h\sigma\right)^{(0)} + H_2[G]\,. \tag{4.55}$$

### 4.7.3 Entropy

For thermodynamic consistency of the Luttinger-Ward theory within the ladder approximation the entropy $S[G,\Gamma]$ must satisfy the thermodynamic identity[4]

$$\Omega[G,\Gamma] = U[G,\Gamma] - TS[G,\Gamma] - \mu N[G] - h\,\delta N[G]\,. \tag{4.56}$$

Solving for the entropy density yields

$$\frac{S}{V} = \left(\frac{S}{V}\right)^{(0)} + \frac{1}{T}\left(H_{\log}[\Gamma] + H_1[G] + H_2[G]\right), \tag{4.57}$$

where the noninteracting contribution reads

$$\left(\frac{S}{V}\right)^{(0)} = \frac{p^{(0)}_{\mathrm{imb}}}{T} + \frac{\left(\varepsilon - \mu n - h\sigma\right)^{(0)}}{T}\,. \tag{4.58}$$

[4] In the previous work [37] the entropy $S[\Gamma,G]$ was derived from a many-body theory by De-Dominicis and Martin [142,143], where $S$ plays the role of the basic functional equivalent to $\Omega$ in the Luttinger-Ward formalism applied here. However, within the ladder approximation it was shown that the thermodynamic identity is obeyed, at least in the spin balanced case. This result can be generalized to the presence of a finite $h$ as the chemical potentials are added as Lagrange multipliers without affecting the form of the functionals.

### 4.7.4 Consistency check

We close this chapter by discussing a nontrivial consistency check for our thermodynamic functions in the particle-particle ladder approximation. It is based on the Tan pressure relation (2.62). Note that the Tan relations in general are obeyed exactly in a Luttinger-Ward formulation, independent of the detailed form of $\Phi[G]$, as was shown by Enss [109]. With the help of the functionals for the pressure and the internal energy eqs. (4.45) and (4.55) the Tan pressure relation can be written as

$$\begin{aligned} p_2^{(0)} + H_{\log}[\Gamma] + H_1[G] = \frac{2}{3}\Big[(\varepsilon - \mu n - h\delta n)^{(0)} + H_2[G]\Big] \\ + \frac{2}{3}\sum_\sigma \mu_\sigma \mathcal{G}_{\sigma\sigma}(\mathbf{x}=0,\tau=0^-) \\ - \frac{m}{12\pi\hbar^2 a}\Gamma(\mathbf{x}=0,\tau=0^-)\,, \end{aligned} \tag{4.59}$$

where the sum over the Green's functions corrects for the additional terms in $\varepsilon - \mu n - h\delta n$ and the Tan contact is expressed via (4.28). In this way we can relate all the thermodynamic functions, which allows to test the numerical quality of our data.

# Chapter 5

# Numerical results of the Luttinger-Ward theory

In the following, we present the numerical data from the self-consistent solution for the Green's function for the thermodynamic properties of the BCS-BEC crossover in the presence of finite spin imbalance. We first start in Sec. 5.1 with the phase boundary between the normal and either a homogeneous or an FFLO-type superfluid. A first check on our results is provided by the comparison to the known phase diagram in the weak coupling limit, which can be found in Sec. 5.2. Then we focus on the thermodynamics of the unitary Fermi gas in Sec. 5.3, where we discuss the phase diagram as well as the scaling functions for the thermodynamic quantities, before we compare our results for the Landau-Plazcek ratio to the experimental data for the spin-balanced unitary gas. Afterwards, we also show the thermodynamic properties of the system in the strongly interacting regime but away from resonance, where we choose the interaction strengths $v = -0.75$ and $v = 0.75$ as representative values in Sec. 5.4. In Sec. 5.5 we provide a check on the accuracy of our computations, which is based on the Tan pressure relation, see Sec. 4.7.4. In the next Section 5.6 we return to the universal representation of the thermodynamics and show our results for the scaling functions of the phase boundaries discussed in Chapter 2. We close the discussion on the results by studying the FFLO-instability in further detail in Sec. 5.7.

## 5.1 Phase diagram of the BCS-BEC crossover with spin imbalance

One of the primary goals in the context of the thermodynamics of the BCS-BEC crossover is to quantitatively determine the critical temperature for the phase transition to the superfluid. In Sec. 5.1.1 we first state the criterion, which we apply to the vertex function $\Gamma$, to decide whether a set of parameters is located on the phase boundary. Then we present the phase diagram in the form $\tilde{h}_c(v, \theta)$ throughout the crossover. Furthermore, we extract the coordinates of the polaron-to-molecule transition point M, which has been discussed in the context of the universal phase diagram for the ground state at positive $a$, see Fig. 3.3 and the discussion in Sec. 3.3.

### 5.1.1 Determination of the phase transition

As discussed in Section 4.5, the instability to the symmetry-broken phase is indicated by a divergence of the vertex function $\Gamma(\mathbf{Q}, \Omega_n = 0)$ or equivalently by a zero of its inverse $\Gamma(\mathbf{Q}, \Omega_n = 0)^{-1}$. Approaching the low-temperature phase from the normal fluid, we are able to distinguish between two different types of superfluid order. Either the zero in $\Gamma^{-1}$ occurs at $Q = 0$ representing an instability to a homogeneous superfluid or at $Q > 0$, when an FFLO order develops below $T_c$. Typical instances for the inverse vertex in both scenarios are depicted in Fig.5.1. In the numerics, we are not able deal with a genuine divergence of $\Gamma$ and therefore cannot resolve the zero exactly but merely approach it as close as possible. In the case of the homogeneous superfluid we can make use of the scaling $\Gamma^{-1}(\mathbf{Q} \to 0, \Omega_n = 0) \simeq Q^2$, which in the weak coupling limit has been pointed out already by Abrikosov et al. [139]. Since all the terms that are included during the self-consistent loop do not alter this power law notably[1] in the vicinity of the phase transition, we fit the small $Q$-limit of our dimensionless numerical function for[2] $|\hat{\Gamma}^{-1}(\tilde{\mathbf{Q}}, \Omega_n = 0)| = |(2\pi)^{3/2} T \lambda_T^3 \Gamma^{-1}(\mathbf{Q}, \Omega_n = 0)|$ to a simple parabola $a + b\tilde{Q}^2$, with $\tilde{Q} = Q/k_F$ and constant coefficients $a, b > 0$. Physically, the offset $a$ represents the remaining excitation gap and measures the distance to the phase transition. If the fitting routine yields $a < 10^{-7}$, we take the corresponding parameter set as critical. On the other hand for an FFLO instability the range of momenta around the critical $Q_{\mathrm{FFLO}}$ is too small to reliably impose a power-law scaling for the momentum behavior and we can only try to minimize the inverse vertex as far as possible, while a stable convergence of the Green's function is retained. In this situation we accept $|\Gamma^{-1}(\mathbf{Q}_{\mathrm{FFLO}}, \Omega_n = 0)| \leqslant 10^{-5}$ to determine on the phase boundary.

### 5.1.2 Phase diagram

A scan of the dimensionless temperatures $\theta = T/\varepsilon_F$, Zeeman fields $\tilde{h} = h/\varepsilon_F$ and interaction strengths $v$ in combination with the criteria for the inverse vertex from the previous section gives rise to the phase diagram presented in Figure 5.2. The shown surface separates the normal phase, which is encountered for $\tilde{h}$ above the surface, from the symmetry-broken states in the parameter space below it. In particular, the red part of the critical manifold signals the instability to a conventional superfluid, while the phase transition to FFLO-order is colored in blue. In agreement with the physical expectation that pairing becomes more efficiently inhibited with stronger Zeeman fields, we observe for every fixed $v$ a decrease of $\theta_c$ with growing $\tilde{h}$. The further one approaches the BCS limit of the crossover, i.e. for

[1] In a theory, which is capable to describe the critical behavior properly, one should recover the correct scaling $\Gamma(\mathbf{Q}, \Omega_n = 0) \sim 1/Q^{2-\eta}$ with the critical exponent $\eta \simeq 0.038$ [123] of the 3d XY-model. In the Luttinger-Ward theory a finite anomalous dimension might arise from the nonperturbative resummation of diagrams during the self-consistent loop. However, so far our results do not allow to conclusively extract it.

[2] In fact $\Gamma^{-1}(\mathbf{Q}, \Omega_n = 0) < 0$, thus we introduce the following absolute value.

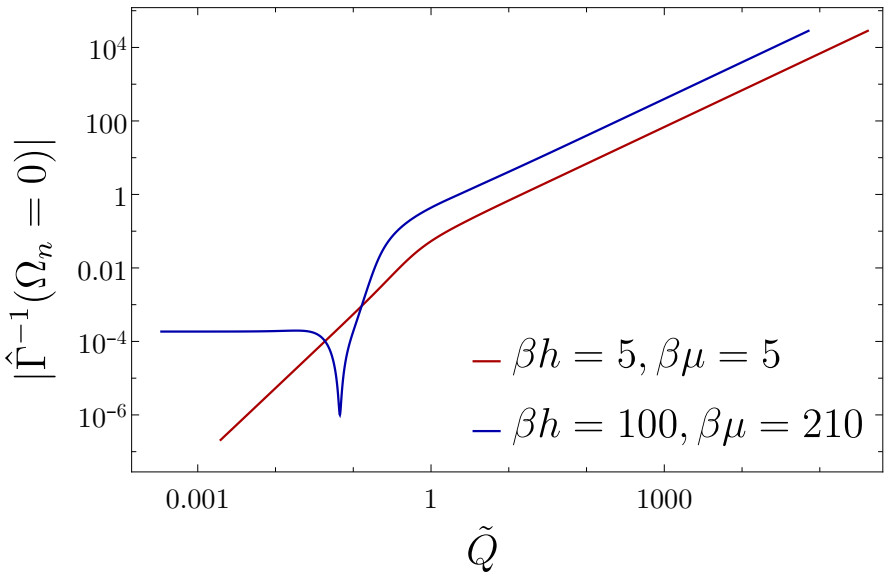


Figure 5.1: Typical examples for the inverse vertex function $\Gamma^{-1}(\mathbf{Q}, \Omega_n = 0)$ at the phase transitions. The $Q^2$ behavior for $Q \to 0$ of the red curve implies the instability towards a homogeneous superfluid. FFLO order is signaled by a zero at a finite $Q_{\mathrm{FFLO}}$ (blue curve). At large momenta we find the linear asymptotics from eq. (4.35).

$v \leqslant -2$, the smaller become the values of $\theta_c$ and $\tilde{h}_c$ up to which the superfluid phase exists, as can be anticipated from the BCS asymptotics $\theta_c \sim \exp(-\pi|v|/2)$ and $h_c, h_{\mathrm{FFLO}} \sim \Delta_0 \sim \exp(-\pi|v|/2)$. On the other hand in the BEC limit, we encounter a superfluid phase also at substantial Zeeman fields $\tilde{h} \geqslant 1$ at all temperatures $0 \leqslant \theta \leqslant \theta_c^{BEC}$, where the upper bound is determined from the ideal BEC condition (2.49) for $a \to 0^+$. In this regime the two-body binding energy $\varepsilon_B \sim 1/a^2$ becomes the dominant energy scale of the system. Since $h$ has to compete with this large energy to break up pairs, the distortion of the superfluid by unpairing the molecules becomes less efficient in this limit, while the depletion of the condensate by thermal fluctuations remains more or less unaffected. Nevertheless, the combination of the Zeeman field with finite temperature effects leads to a reduction of the critical temperature compared to the balanced case also in the BEC limit. In the $\tilde{h} = 0$ plane, we retrieve the critical temperature curve of the balanced gas, known from the previous Luttinger-Ward study by Haussmann et al. [37], who have shown that the limiting behavior in the BCS (4.22) and BEC (2.49) regime is described correctly (apart from the GMB [95] corrections). We will provide arguments that our approach reproduces these well understood limits as well, yet in the universal formulation in terms of $\bar{T}, \bar{\mu}$ and $\bar{h}$, which is postponed to Sec. 5.6. Note, however, that we merely approach the phase transition from the normal fluid. Therefore,

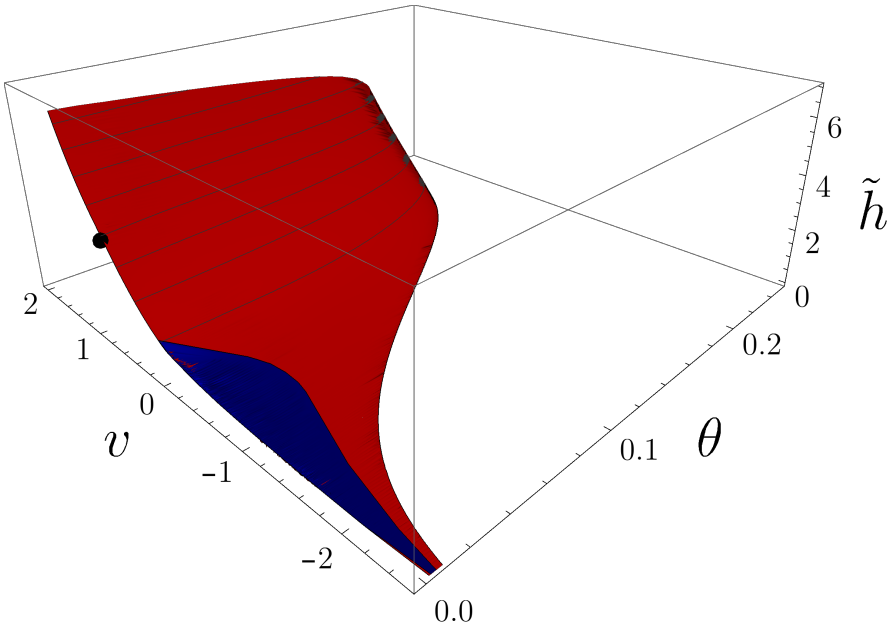


Figure 5.2: Critical temperature throughout the BCS-BEC crossover as function of $v = 1/(k_F a)$ and $\tilde{h} = h/\varepsilon_F$. The red region indicates the transition to a homogeneous superfluid while an FFLO superfluid is found below the blue wedge. The maximal critical temperature $T_c^{(\mathrm{FFLO})} \simeq 0.03\varepsilon_F$ is located on the BCS side at $v \simeq -1$. At unitarity we only detect this order at the very lowest temperatures and it has only minute extent on the bosonic side. The black dot marks the point M, see the next section.

we do not resolve the weak first order character of the phase transition, which is artificially found in the Luttinger-Ward approach along the entire phase boundary, but only recover the monotonous $\theta_{c,lower}$-curve from Fig. 2.3, which in the unitary limit attains the value $\theta_c(v = 0, \tilde{h} = 0) \simeq 0.152$.

The FFLO wedge extends at the lowest achievable temperatures of $\theta \simeq 10^{-3}$ from the extreme BCS limit even beyond unitarity to the bosonic side of the crossover up to interaction strengths of $v \lesssim 0.2$. Unfortunately, for these large interactions strengths the precise location of the FFLO instability depends considerably on the choice for the numerical threshold of a zero in $\Gamma^{-1}(\mathbf{Q}, \Omega_n = 0)$. This is caused by the geometry of the phase diagram in the neighborhood of the Lifshitz point L in Fig. 3.4, which marks the endpoint of the normal-to-FFLO phase boundary at $T = 0$. Around L the phases of different order shrink to very narrow slivers, which leads to a competition between the instabilities of the vertex at finite or zero $Q$ in a rather broad range of interaction strengths. Consequently, locating L precisely by an extrapolation towards $T = 0$ is not possible. Despite these difficulties, the

Luttinger-Ward approach gives strong evidence that L is to be found in the vicinity of the unitary limit, in contrast to mean-field methods that observe the endpoint of the FFLO phase at $1/(k_F a) = -2.86$ [68] or $1/(k_F a) = -0.46$ [70]. Regarding the extent of this unconventional phase to finite temperatures, we first observe that a minimal $\tilde{h}$, whose value depends on $v$, is required to create FFLO-order. This observation is in line with the weak-coupling result that FFLO requires a finite spin imbalance. Once we are above this minimal Zeeman field, there is only the transition towards the nonhomogeneous phase, which is reliably detected. An interesting point with respect to experimental realizations is that we obtain the maximal critical temperature for FFLO at $\theta \simeq 0.03$ on the fermionic side of the crossover for interaction strengths $-0.9 \lesssim v \lesssim -0.4$.

### 5.1.3 Determination of the polaron-to-molecule transition point M

Our Luttinger-Ward data allows to estimate the coordinates of the polaron-to-molecule transition point M from the observation that M is identical to the starting point of the phase boundary between the fully polarized normal and the paritally polarized superfluid, which extends from M to the extreme BEC limit (compare Fig. 3.4). In Fig. 5.3 we show the critical polarization in the regime $0.5 \simeq v \simeq 2.5$ at the lowest available temperatures of $\theta \simeq 0.005$. Indeed, we obtain $\sigma_c = 1$ beyond a certain coupling strength. To determine the location of M, we first note that the $h_s$ curve and the boundary of the partially polarized, normal phase $\mathrm{N}_{\Omega_\uparrow > \Omega_\downarrow}$ with the imbalanced, fermionic superfluid meet at M with different slopes. We assume that this behavior is mapped to a non-differentiable form of the critical polarization at the onset of the constant $\sigma_c = 1$ shown here. Therefore, we linearly continue the branch of the $\sigma_c(v)$ curve, with $\sigma < 1$ towards the crossing with $\sigma = 1$. This determines $v_\mathrm{M} \simeq 1.13 \pm 0.03$, where we have estimated the errors from the $v$-values of the neighboring data points. This procedure is shown in the inset of Fig. 5.3. Furthermore, we obtain for the chemical potentials at this point ($\tilde{\mu} = -1.16, \tilde{h} = 2.73$). Together with the order parameter $\Delta_0(v = 1.13) = 1.19\varepsilon_F$ from [37], we find $h/\Delta = 1.65$, where we use again the mean-field form $\Delta = \sqrt{\mu^2 + \Delta_0^2}$. This result coincides very well with the coordinates $(v = 1.13, h/\Delta = 1.66)_\mathrm{M}$ obtained from the BDMC data [131], as discussed in Sec. 2.3.3. Unfortunately, the results for the universal coordinates $(\bar{\mu}_\mathrm{M}) = -0.91$ and $(\bar{h}_\mathrm{M}) = -2.14$ deviate notably from the BDMC results $(\bar{\mu} = -0.74, \bar{h} = 1.97)_\mathrm{M}$. A similar discrepancy between the formulation based on density units with energy scale $\varepsilon_F$ and the representation in terms of half the binding energy $\varepsilon_B/2$ arises on the BEC side in Sec 5.6, where we discuss the universal representations of the phase boundaries. In general, density units appear more favorable when comparing the results to other methods or known asymptotics. So far, we have not found a conclusive explanation for this fact, except for the trivial observation that $\varepsilon_B \sim v^2$ depends quadratically on the dimensionless coupling strength, which introduces a large rescaling in the BEC limit $v \to \infty$. This can lead to enhanced errors, since our theory accounts for the dimer-dimer and the

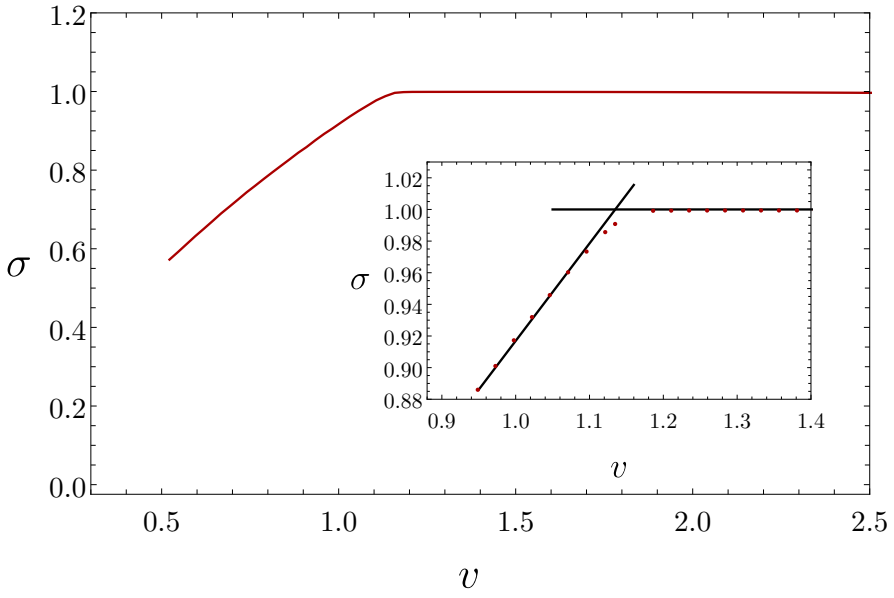


Figure 5.3: Critical polarization $\sigma$ at the lowest available temperatures. The inset shows how we extract the coordinates of the polaron-to-molecule transition point M from the onset the maximal polarization $\sigma = 1$.

atom-dimer interactions only in an approximate manner.

## 5.2 Comparison to weak coupling

In the weak coupling limit $v \ll -1$ the self-consistent theory reduces to diagrams with bare Green's functions $G^{(0)}$. To check whether our approach is consistent with the standard results in this regime, we compare our data to the established form of the phase diagram depicted in Figure 2.5.

The smallest interaction strengths, where we reach temperatures that can be considered as essentially zero, are around $v \gtrsim -2.5$. To obtain a quantitative comparison at these finite couplings, however, we have to take into account the deviations from the pure weak-coupling theory. Figure 5.4 shows both our Luttinger-Ward results for $\tilde{h}_{\mathrm{FFLO}}(T \to 0)$ and $\theta_c(h = 0)$ and their corresponding BCS asymptotics from eqs. (4.22) and

$$\tilde{h}_{\mathrm{FFLO}}(T = 0) = 0.754 \frac{8}{e^2} e^{-\pi|v|/2}\,, \tag{5.1}$$

respectively. While the Zeeman field at $v \simeq -2$ is still described by the BCS asymptotics at the 5%-level, we observe that the critical temperature of the spin-balanced

system already deviates by 23% from the analytic expression. The pronounced difference in the behavior of both quantities can be understood from the fact that the polarization induced by $\tilde{h}$ suppresses interaction effects and therefore brings the system closer to the limit of weak interactions. On the other hand, in the balanced situation, interactions have the largest influence, such that the critical temperature at $h = 0$ is more strongly affected by beyond-mean-field corrections than the critical FFLO field at $T = 0$. To compare our results with the pure weak coupling limit in a $T/\Delta_0$ vs. $h/\Delta_0$ diagram we present our critical data $(\tilde{h}_c(v), \theta_c(v))$ at a given $v$ in the following way

$$\frac{1}{\Delta_0^{(\mathrm{BCS})}(v)} \left( \frac{\tilde{h}(v)}{\delta\tilde{h}_c^{T=0}(v)}, \frac{\theta_c(v)}{\delta\theta_c^{\mathrm{bal}}(v)} \right) . \tag{5.2}$$

Here $\Delta_0^{(\mathrm{BCS})}(v)$ refers to the corresponding BCS gap at zero temperature and vanishing Zeeman field from eq. (2.45). Furthermore, we include two rescaling factors to incorporate the effects of the finite interaction strength from the limit $v \to 0^-$: $\delta\tilde{h}_c^{T=0}(v)$, which describes the deviation of the Zeeman field from the FFLO-asymptotics and its temperature counterpart $\delta\theta_c^{\mathrm{bal}}(v)$ for the spin-balanced BCS-limit. The results of this transformation are depicted in Fig. 5.5 for the interaction strengths $v = -2.5$, $v = -2.3$ and $v = -2.1$, where the values of $\delta\tilde{h}^{T=0}$ and $\delta\theta_c^{\mathrm{bal}}$ can be determined from Fig. 5.4. The used values read

| $v$ | $-2.5$ | $-2.3$ | $-2.1$ |
|---|---|---|---|
| $\delta\theta_c^{\mathrm{bal}}$ | 0.78 | 0.76 | 0.74 |
| $\delta\tilde{h}_c^{T=0}$ | 0.95 | 0.95 | 0.95 |

. (5.3)

Note that we have assumed a constant factor for the Zeeman field, since we cannot achieve low enough temperatures for the corresponding larger values of $\beta h$ of order $10^3$, where $\delta\tilde{h}_c^{T=0}$ must tend to one. Regarding the values of $\delta\theta_c^{\mathrm{bal}}$, we observe a growing deviation towards unitarity, in agreement with the expectation that the BCS asymptotic becomes less precise the larger $v$. Regarding Fig. 5.5, our data collapses for all interaction strengths and shows good agreement with the theory line, in particular for the transition to the homogeneous BCS state. However, in case of the FFLO transition we observe slight noise and the phase boundary appears to be shifted towards the CC-line. Here we encounter the problem that we try to minimize the inverse vertex as far as possible, but we have no sharp criterion for criticality available like the scaling behavior of the vertex function for the transition to the homogeneous superfluid. Furthermore, since the Luttinger-Ward formalism in general gives rise to weak first order transitions it tends to artificially enlarge phases and our approach from the normal fluid leads to critical temperatures below the physical $T_c$. Usually this effect is small in the BCS limit of the crossover, yet, it becomes more pronounced, when one normalizes the results by the gap, which is exponentially sensitive to $v$.

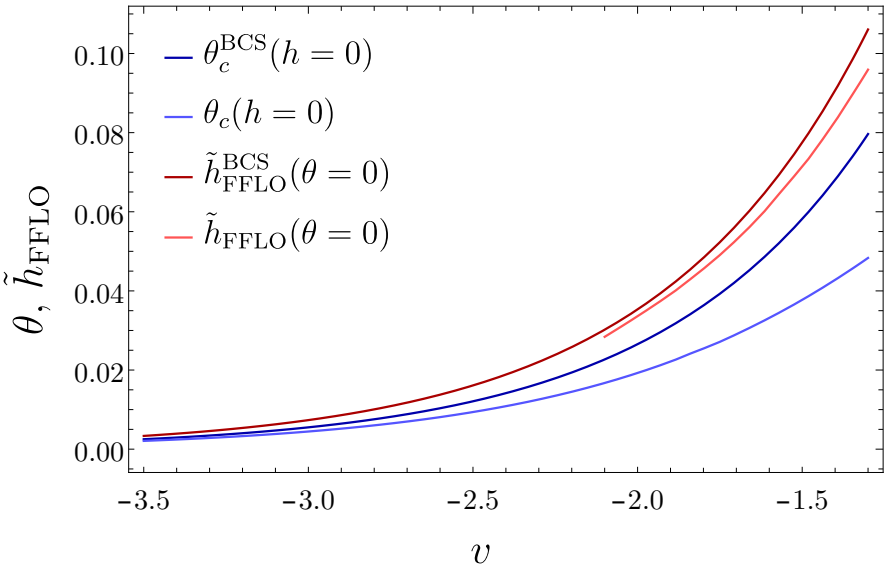


Figure 5.4: Comparison between the BCS asymptotics and the Luttinger-Ward result as function of $v$. Especially the critical temperatures deviate considerably from the weak coupling form in the regime $v \simeq -2$.

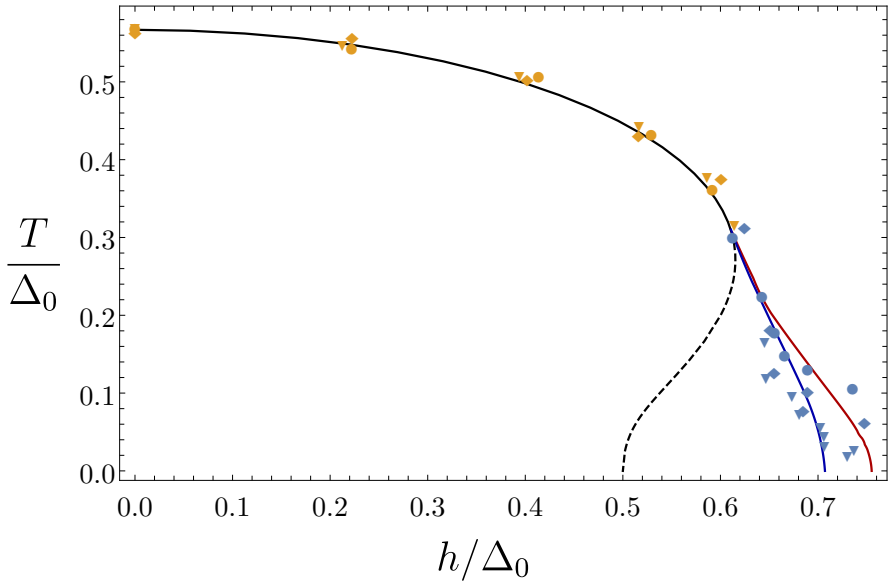


Figure 5.5: Comparison to the weak coupling results from Fig. 2.5: We observe a scaling collapse of our data in the representation (5.2) for different interaction strengths $v = -2.5$ (circles), $v = -2.3$ (diamonds) and $v = -2.1$(triangles). The scaling factors are given in the main text. Yellow symbols: homogeneous superfluid, blue symbols: FFLO.

## 5.3 Thermodynamics of the unitary Fermi gas

After convincing ourselves, that our Luttinger-Ward approach is able to reproduce the weak-coupling limit, we turn now to the strong coupling regime near $\infty$ scattering length. In this chapter we focus on the unitary gas, for which we first show the phase diagram in Sec. 5.3.1, before we discuss the thermodynamic scaling functions in Sec 5.3.2. Finally, we compare the Luttinger-Ward theory in the spin-balanced case to the experimental results by Ku et al. in Sec. 5.3.3, where we present in particular the Landau-Placzek ratio.

### 5.3.1 Phase diagram of the unitary gas

The phase diagram of the resonant gas in the $(h/\mu)$ vs. $(T/\mu)$ plane is presented in Figure 5.6. Once again, we obtain the highest critical temperature for the spin balanced gas, since spin imbalance suppresses pairing. At $h = 0$ the onset of the superfluid phase is encountered at $(T/\mu)_c = 0.38$, which corresponds to the inverse of $(\beta\mu)_c = 2.65$. At lower temperatures the superfluid exists also in the presence of finite Zeeman fields. Moreover, below temperatures of $(T/\mu) \simeq 0.15$ we observe a backbending of the critical field curve, which resembles the dashed line in the weak-coupling limit, shown in Fig 2.5, found originally by Sarma [26]. In fact, by approaching the phase transition from the high-temperature phase without anomalous expectation values we probe the lowest temperature below which the normal phase ceases to exist and thereby we generalize the criterion used by Sarma to the regime of strong interactions. This particular form of the phase boundary indicates a region where the phase transition is of first order and agrees with the existence of a tricritical point along the $(h/\mu)_c$ curve, where the phase transition changes its character. Furthermore a tricritical point at finite $T$ is consistent with the picture, due to Parish et al. [68], who show the evolution of the latter point as function of $v$ from the BCS limit through unitarity to the BEC side. In particular, the tricritical temperature decreases monotonically with the coupling until it reaches $T = 0$ at the endpoint T (see Fig. 3.3) at $v = 1.7$ [135], beyond which the balanced superfluid can always be polarized in a continuous manner. To reliably determine the position of the tricritical point, however, requires the data from the symmetry-broken phase. In the zero-temperature limit we observe the universal ratio $(h/\mu)_c = 1.09 \pm 0.05$ from extrapolating the critical line. An overview of the results on the ratio $(h/\mu)_c$ that have been obtained by various methods can be found in Table 5.1, while a more thorough discussion of the ground state phase diagram has already been given in Sec. 2.3.3. In the regime $T/\mu \leqslant 0.01$ we also detect the FFLO instability, as we have already seen in Fig. 5.2. For the unitary gas we extract $(h/\mu)_{\mathrm{FFLO}} = 1.28 \pm 0.15$. The large error bar in comparison to the CC-field, results from the steep slope of the short FFLO-N boundary. In the frequently used representation based on the Fermi energy we extract the following ground state values $\{\tilde{\mu}_c \simeq 0.395, \tilde{h}_c \simeq 0.430\}$ for the Clogston-Chandrasekhar limit

and $\{\tilde{\mu}_{\mathrm{FFLO}} \simeq 0.400, \tilde{h}_{\mathrm{FFLO}} \simeq 0.500\}$ for the zero-temperature limit of the FFLO phase boundary. These pairs have been obtained from the data point at the smallest available temperature, which are $\theta_{\mathrm{CC}}^{\mathrm{min}} \simeq 0.003$ and $\theta_{\mathrm{FFLO}}^{\mathrm{min}} \simeq 0.001$, respectively, and agree with the universal ratios $(h/\mu)_c$ and $(h/\mu)_{\mathrm{FFLO}}$ within the error of the extrapolation to $T = 0$.

From an experimental point of view, one rather considers fixed densities than chemical potentials. In this picture the first order regime of the phase transition is unstable to phase separation, which means that a superfluid with smaller $\delta n = n_\uparrow - n_\downarrow$ and normal fluid with a higher $\delta n$ coexist. In Figure 5.7 we show the spin polarization $\sigma$ from eq. (2.38) as a function of the critical temperature $T_c$ in units of $T_\uparrow = (6\pi^2 n_\uparrow)^{2/3}$, which we compare to the experimental data by Shin et al. [34]. To perform the change of units we note that we can obtain the individual densities via

$$n_\uparrow = n\frac{1+\sigma}{2} \tag{5.4a}$$

$$n_\downarrow = n\frac{1-\sigma}{2}\,, \tag{5.4b}$$

from $n$ and $\sigma$, which are provided by the numerical evaluation. At $h = 0$, we recover the critical temperature $T_c/T_\uparrow(\delta n = 0) = 0.152... = \theta_c(h = 0)$. For finite imbalances the critical temperature decreases in agreement with the simultaneously growing polarizations, which correspond to increased Zeeman fields in the grand-canonical discussion above. In the temperature regime $T/T_\uparrow \lesssim 0.06$ we observe again a backbending of the phase boundary, like in Fig. 5.6. In fact, this is the region of the phase diagram, where the system is expected to show phase separation. The tricritical point that is identical with the onset of the latter has been experimentally observed at $\delta n/n = 0.20$ and $T/T_\uparrow = 0.07$ by Shin et al. [34]. Incorporating phase separation into the Luttinger-Ward theory will increase the theoretical prediction for the phase with a superfluid fraction towards larger spin polarizations and therefore change the backbending form of the phase boundary. Yet, this procedure requires computations in the presence of anomalous expectation values, which have not been implemented so far. All in all, our theory curve seems to predict critical temperatures that are above those seen in the experiment. Whether these deviations originate from systematic errors of the Luttinger-Ward approach or from experimental uncertainties cannot be answered from the currently available data. Furthermore, we omit the FFLO-data, which in this representation almost collapses to a line at basically zero temperature, where the important effects of phase separation cannot be taken into account by the current approach.

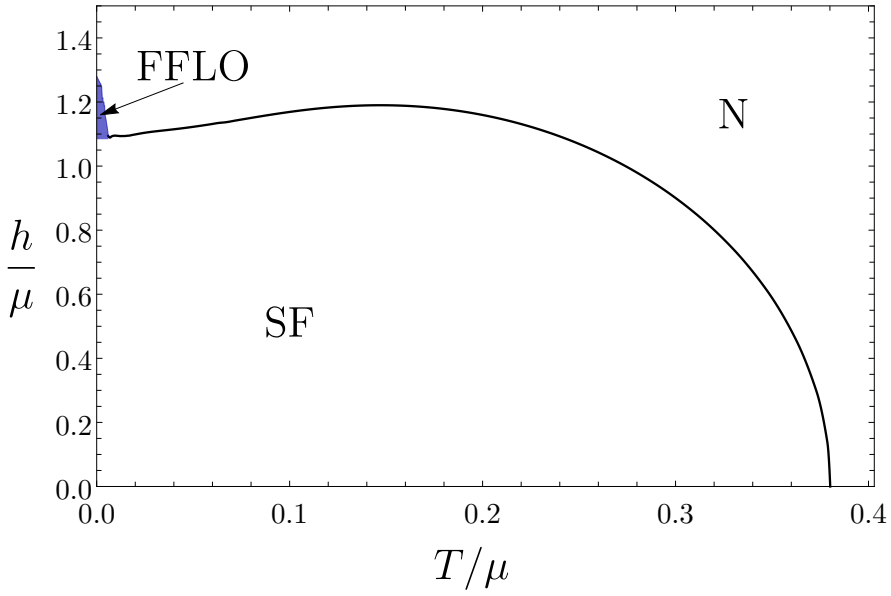


Figure 5.6: Phase diagram of the unitary gas. For temperatures below $T/\mu < 0.38 = (\beta\mu)_c^{-1}$ the gas becomes superfluid, provided the Zeeman field does not exceed the temperature-dependent critical field represented by the black line. Its extrapolation to zero temperature yields $(h/\mu)_c = 1.09 \pm 0.05$. At the very lowest temperatures an FFLO phase appears to emerge, indicated by the blue region. The backbending of the $(h/\mu)_c$ curve for temperatures $T/\mu \lesssim 0.15$ is due to the first order character of the phase transition in this temperature range.

| Method | $(h/\mu)_c$ |
|---|---|
| $1/N$ (LO) [1] | 0.807 |
| $1/N$ (NLO) [70] | 1.947 |
| Lobo [132] | 0.96 |
| Boettcher [133] | 0.83 |
| $\epsilon$-expansion [92] | 1.15 |
| Luttinger-Ward | 1.09 |

Table 5.1: Different theoretical results for $(h/\mu)_c$. See also the detailed discussion in Sec. 3.2.

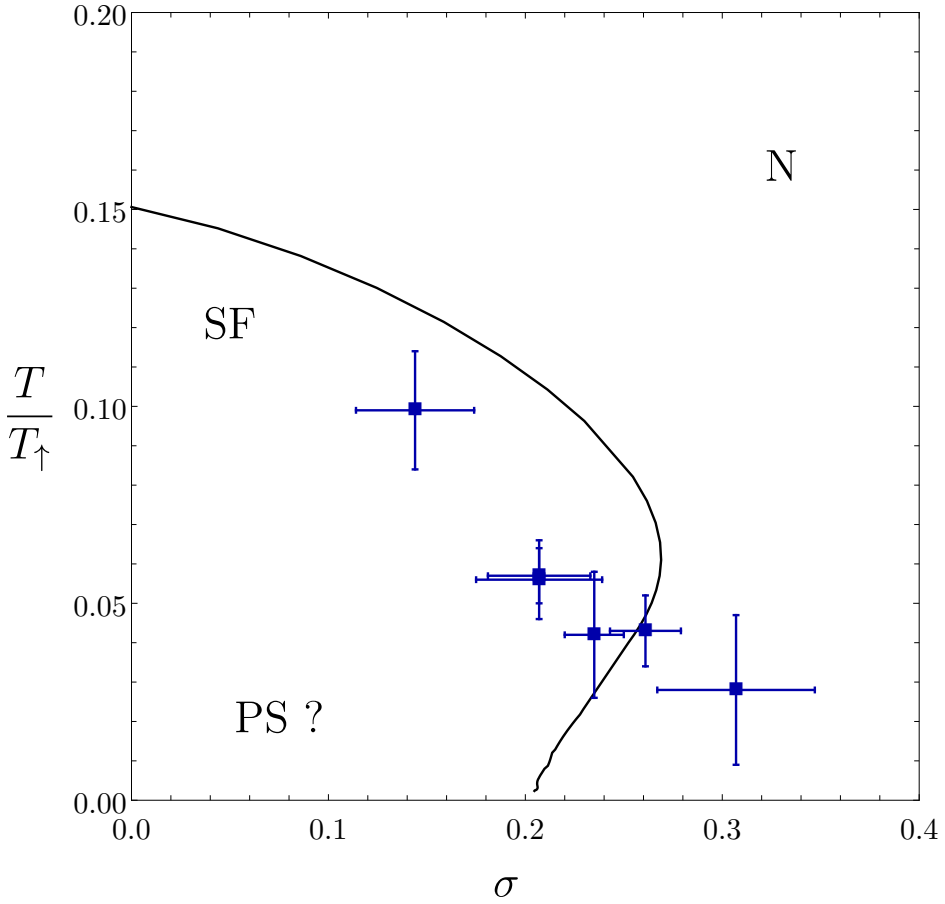


Figure 5.7: Phase diagram of the unitary gas. The black curve represents the Luttinger-Ward data, while the blue points correspond to the experimental data by Shin et. al. [34]. Below the black line one finds a homogeneous superfluid, whereas at lower temperatures the system is unstable to phase separation (PS), which, however, is beyond the scope of the current numerics.

### 5.3.2 Universal scaling functions of the unitary Fermi gas

Apart from the normal-to-superfluid transition, the unitary gas has also attracted particular interest, because it realizes a strongly interacting quantum gas, that exhibits scale invariance. Therefore, we present the Luttinger-Ward results for the thermodynamic properties of the gas at resonance in further detail. In particular, we have derived an expression for the pressure in eq. (4.45) as a functional of the Green's and vertex functions. The results for $p$ are represented in Figure 5.8, where we show the scaling function

$$\hat{p}(\beta\mu, \beta h) = \frac{p(T, \mu, h, 1/a = 0)}{p^{(0)}_{\mathrm{imb}}(T, \mu, h)}\,, \tag{5.5}$$

which is normalized by the pressure of an imbalanced, ideal Fermi gas, see also eq. (4.40). In the special case of a balanced gas at $h = 0$ this function has been determined directly in the experiment by Ku et al. [58, 93]. In particular, we reproduce the result $\hat{p}((\beta\mu)_c \simeq 2.65, 0) \simeq 2.73$ from the Luttinger-Ward study of Haussmann et al. [37]. Following the critical line, colored in black, the dimensionless pressure first decreases until it reaches a very shallow minimum at $\beta\mu \simeq 9$, beyond the plotted range. This minimum has no deeper physical origin but arises from the ratio of two monotonically decreasing functions, which is not necessarily monotonic itself. In the limit of a large Zeeman field $\beta h \to \infty$ the critical pressure converges to $\hat{p} \simeq 1.5$, which is another universal number of the unitary gas. The precise value cannot be estimated in a simple manner, since at the superfluid phase boundary one always finds finite densities of both species (see also Fig. 5.10) and therefore the system remains strongly interacting despite the large value of $\beta h$. Leaving the critical region either by increasing the temperature or the Zeeman field, $\hat{p}$ quickly converges to one, corresponding to the non-interacting limit. This is to be expected, since one approaches either the non-degenerate limit $n\lambda_T^3 \ll 1$ of a dilute classical gas with increasing $T$, or the limit of a single-component ideal Fermi gas with $\delta n \to 1$, when $\beta h$ grows.

A similar picture arises from the study of the densities. In Figures 5.9 and 5.10, we show both the scaling functions of the total density $f_n$, defined via

$$n(T, \mu, h, 1/a = 0) = n^{(0)}_{\mathrm{imb}}(T, \mu, h) f_n(\beta\mu, \beta h) \tag{5.6}$$

and the equivalent $f_{n_\downarrow}$ for the minority component

$$n_\downarrow(T, \mu, h, 1/a = 0) = \frac{n^{(0)}_{\mathrm{imb}}(T, \mu, h)}{2} f_{n_\downarrow}(\beta\mu, \beta h)\,. \tag{5.7}$$

The factor of $1/2$ has been introduced for convenience, such that by definition $f_n(\beta\mu, 0) = f_{n_\downarrow}(\beta\mu, 0)$, which makes comparison of the two functions easier. Here the normalization refers to the density of the noninteracting, imbalanced Fermi gas

$$n^{(0)}_{\mathrm{imb}}(T, \mu, h) = n^{(0)}(T, \mu + h) + n^{(0)}(T, \mu + h)\,, \tag{5.8}$$

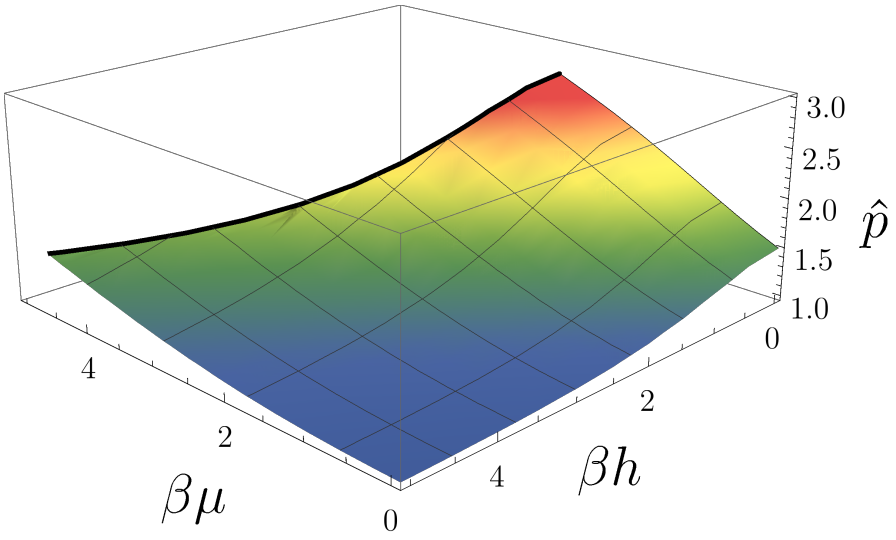


Figure 5.8: Pressure scaling function $\hat{p}$ of the unitary gas defined in eq. (5.5). The black line indicates the phase transition.

where the density of a single component is defined in eq. (4.52). The overall shape of both density functions is similar to the pressure scaling function $\hat{p}$. In general, the density scaling functions decrease away from the critical region either due to an enhanced imbalance associated with by increasing $\beta h$ or due to approaching the non-degenerate limit $\beta\mu \to -\infty$. In particular, under the influence of a growing Zeeman field at fixed $\beta\mu$ the system evolves to a single-component Fermi gas of $\uparrow$ atoms, which is also reflected in the scaling functions: $f_n$ approaches one, while $f_{n_\downarrow}$ vanishes in this regime, which is consistent with the observation that $\hat{p} \to 1$ with increasing $\beta h$. In turn, close to the critical region both the total density and the minority density appear enhanced compared to the non-interacting situation, no matter what $\beta\mu$ and $\beta h$. Obviously, this is caused by the attractive interactions, which play a relevant role at the phase transition. Furthermore, the instability to the superfluid requires a minimal, finite density of minority atoms to form pairs, which implies a finite total density. Similarly, Rammelmüller et al. [114] have observed how the density equation of state of the imbalanced unitary Fermi gas approaches the balanced gas and therby also the phase transition, when $\beta\mu$ is increased at fixed $\beta h$. If one follows the boundary to the superfluid from $h = 0$, one starts out from the absolute maximum of the scaling functions $f_n((\beta\mu)_c, h = 0) = f_{n_\downarrow}((\beta\mu)_c, h = 0) \simeq 3.3$, which agrees with [37]. Leaving the balanced case along the critical line, one first observes a decrease from the maximum, which passes through a very shallow minimum at $\beta h \simeq 8$ (too shallow to be visible in figs. 5.9 and 5.10) and then converges to $f_n \simeq 2.7$ and $f_{n_\downarrow} \simeq 2.1$, respectively, for $\beta h \gg 1$.

Finally, the Tan contact is a quantity of particular interest, since it measures

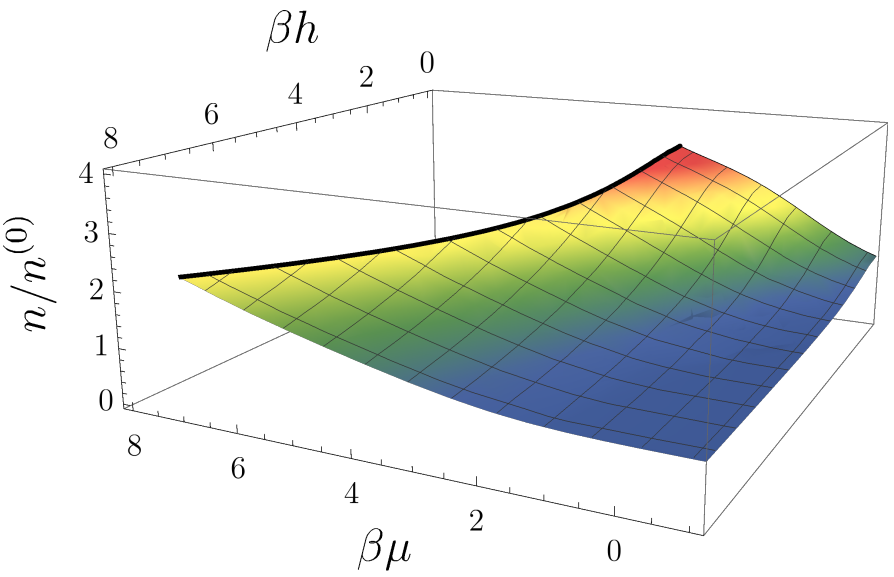


Figure 5.9: Total density of the unitary gas. The black line indicates the boundary to the superfluid phase.

short-distance correlations and contains substantial information both about thermodynamic and dynamic properties, as we have discussed in Sec. 2.4. The dimensionless contact density $\tilde{\mathcal{C}} = \mathcal{C}/k_F^4$ of the resonant gas is shown in Figure 5.11 as a function of $\theta$ and $\tilde{h}$. It attains a maximal value of $\tilde{C} \simeq 0.09$ at the transition to the superfluid at $\tilde{h} = 0$. Remarkably, the value of $\tilde{\mathcal{C}}$ does not vary significantly along the critical line for different values of $\tilde{h}$. In general, the contact remains almost constant upon changes in the temperature at a fixed value of $\tilde{h}$, also away from the critical region. As expected, it quickly approaches zero, when the Zeeman field is increased. In particular, we can extract the behavior of the contact density in the low-temperature and strong polarization limit, given in equation (2.74). In this limit we indeed observe a linear behavior $\mathcal{C} \simeq 6\pi^2 s k_{F\uparrow} n_\downarrow$, with a universal prefactor $s \simeq 0.09$, which agrees very well with the result $s \simeq 0.08$ derived from the polaron ansatz by Punk et al [122].

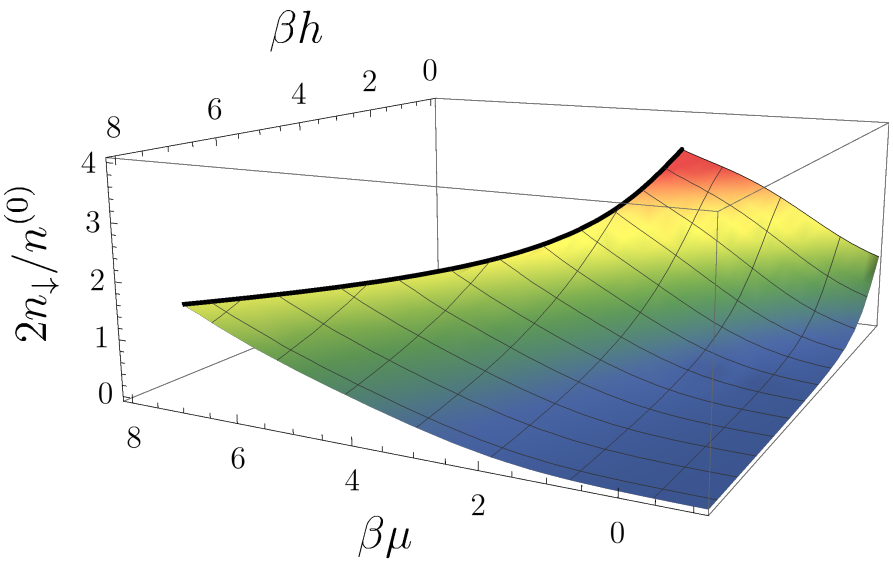


Figure 5.10: Scaling function for the minority component $f_{n_\downarrow} = 2n_\downarrow/n^{(0)}$. The black line indicates the boundary to the superfluid phase.

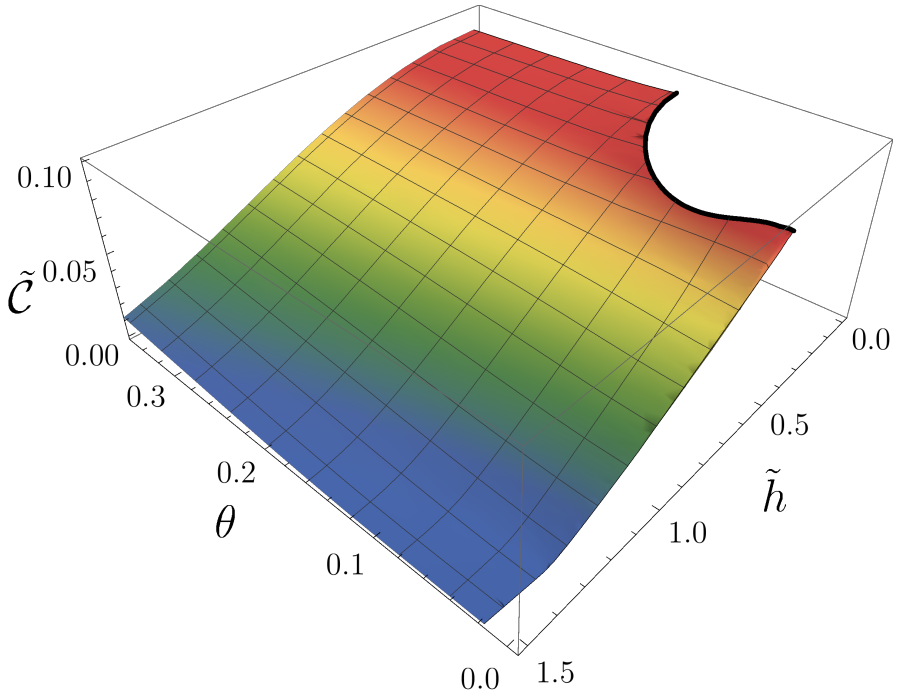


Figure 5.11: Dimensionless contact density $\tilde{\mathcal{C}} = \mathcal{C}/k_F^4$ of the unitary gas. The black line indicates the boundary to the superfluid phase.

### 5.3.3 Comparison of the Luttinger-Ward theory to the experimental results for the balanced, unitary Fermi gas

In this subsection we compare our Luttinger-Ward results to the experimental data for the spin-balanced, unitary gas by Ku et al. [58]. In particular, we focus on the Landau-Placzek ratio LP defined in eq. (2.85) and show our results in Fig 5.12. On the experimental side LP follows from the representation (2.90). Since the latter explicitly involves the isothermal compressibility, we show $\kappa_T$ compared to the experimental observations in Fig. 5.13. While the normal fluid regime is directly accessible from the Luttinger-Ward approach presented here, the data in the symmetry broken phase for the paragraph for equal spin populations are taken from Haussmann et al. [37]. Regarding the Landau-Plazcek ratio, we obtain a very good agreement with the experimental data. Merely, the precise determination of the critical value is not possible due to the sharp features and the multivalued regime in the vicinity of $T_c$, which is an artifact of the first order transition in the Luttinger-Ward theory, see Ref. [37]. The compressibility $\kappa_T = -V^{-1}\partial V/\partial p$ necessarily involves a derivative of the thermodynamic data, which in general leads to an enhancement of numerical errors. However, our data for the disordered phase allows to compute $\kappa_T$ directly from a simple spline interpolation of the pressure. This is possible because of the very small numerical inconsistencies, see Sec. 5.5 on the Tan errors. Therefore, we can also use the equivalent thermodynamic relation $\kappa_T = n^{-2}\partial n/\partial_\mu$ that essentially yields the same curve for the compressibility. To obtain a smooth compressibility below $T_c$, we have used a simple model fit to the data from [37] which both respects the asymptotics $c_V \sim T^3$ and $p \to \xi_s p^{(0)}$ in the limit $T \to 0$ and the critical temperature $\theta_c \simeq 0.16$. Like in the case of LP, we obtain a very good agreement with the experimental observations.

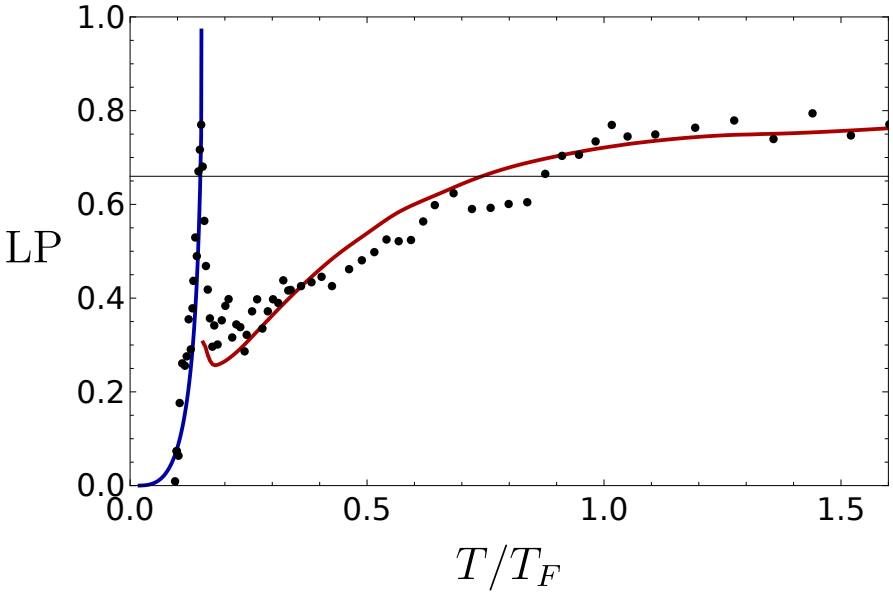


Figure 5.12: Landau-Plazcek ratio of the unitary Fermi gas. Superfluid regime: Blue (from Ref. [37]), Red: Normal phase, Black: Experiment from Ref. [58].

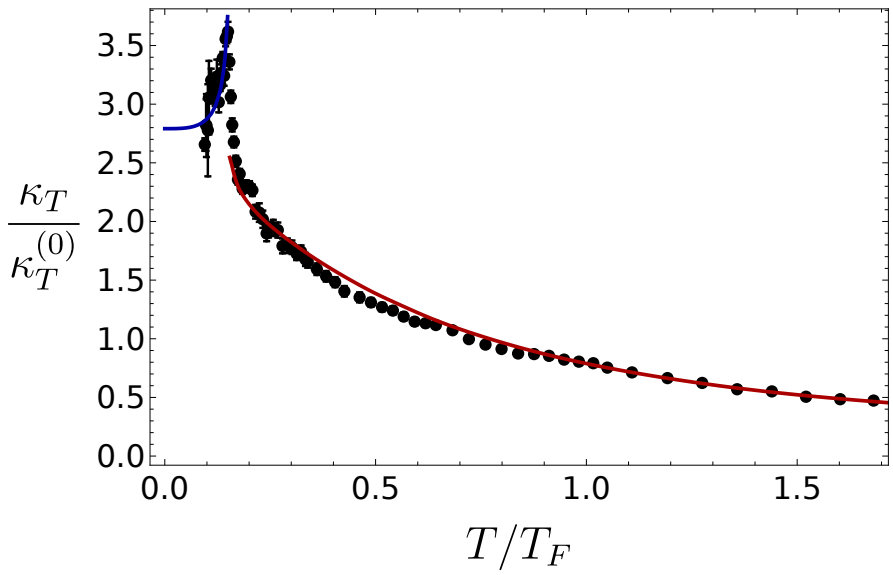


Figure 5.13: Compressibility $\kappa_T/\kappa_T^{(0)}$. Superfluid regime: Blue (from Ref. [37]), Red: Normal phase, Black: Experiment from Ref. [58]

## 5.4 Thermodynamics in the strongly interacting crossover regime

For comparison with the unitary and the weak-coupling case we show our thermodynamic results for two additional coupling strengths: $v = -0.75$, where the FFLO-order been observed at the largest critical temperature $\theta_c \simeq 0.03$ and $v = 0.75$ slightly on the bosonic side of the crossover.

### 5.4.1 Thermodynamic quantities at $v = -0.75$ and $v = 0.75$

We will focus both on the spin polarization $\sigma$ and the internal energy $U/(n\varepsilon_F)$ as functions of the reduced temperature $\theta$ and the Zeeman field $\tilde{h}$. The structure of $\sigma$, which is depicted at $v = -0.75$ in Fig. 5.14 and for $v = 0.75$ in Fig. 5.15, respectively, has a very similar global structure. At $\tilde{h} = 0$ $\sigma$ vanishes, since this corresponds to the spin-balanced gas. At fixed $\theta$ we find an increase of $\sigma$ with growing $\tilde{h}$, which is the expected effect of the Zeeman field, until it saturates at $\sigma = 1$ for large enough $\tilde{h}$. In the ground state the saturation is observed for both interaction strengths for values of $\tilde{h} \gtrsim 2$. At finite temperatures the Zeeman field in case of the positive scattering length has to be slightly larger to fully polarize the system compared to the fermionic regime, since the stronger attractive interactions on the BEC side depolarize the system more effectively. At a given Zeeman field in turn we find for both $v$ only a minor decrease of $\sigma$ with growing $\theta$ due to the enhanced thermal fluctuations.

Regarding the critical region, the phase transition on the fermionic side is only possible for temperatures below $\theta \simeq 0.09$ and we detect the FFLO phase for temperatures smaller than $\theta \simeq 0.03$. The largest critical $\sigma \simeq 0.17$, which is encountered in the ground state at $\tilde{h} = 0.20$, is non-zero, consistent with a transition to FFLO. In addition, the critical curve shows a backbending like at unitarity (see Fig. 5.6), which hints towards a tricritical point. In the bosonic case only a monotonic phase boundary with a homogeneous superfluid exists. The maximal $\theta_c \simeq 0.20$ is reached by the spin-balanced gas. The other endpoint of the critical line at $\theta = 0$ and $\tilde{h}_c \simeq 1.62$ is accompanied by a large polarization $\sigma_c \simeq 0.6$. The nature of the superfluid, and also the order of the transition in the vicinity of this point unfortunately remains open. Since $v \leqslant v_{\mathrm{M}} \simeq 1.13$ and the instability of the vertex is observed at $Q \to 0$ one might find a Sarma phase. Yet, without data about the symmetry-broken phase this issue cannot be answered conclusively.

Like the spin polarization also the global structure of the internal energies, which are presented in Fig. 5.16 for the fermionic and respectively in Fig. 5.17 for the bosonic side, bears many similarities. At fixed $\tilde{h}$ we observe an almost linear growth with $\theta$. This corresponds to the enhanced average energy at fixed density, which is controlled by the temperature. Furthermore $U/(n\varepsilon_F)$ is a monotonically increasing function of the Zeeman field. This can be understood from the growth of the spin imbalance associated with a larger $\tilde{h}$. An enlarged value of $\sigma$ reduces

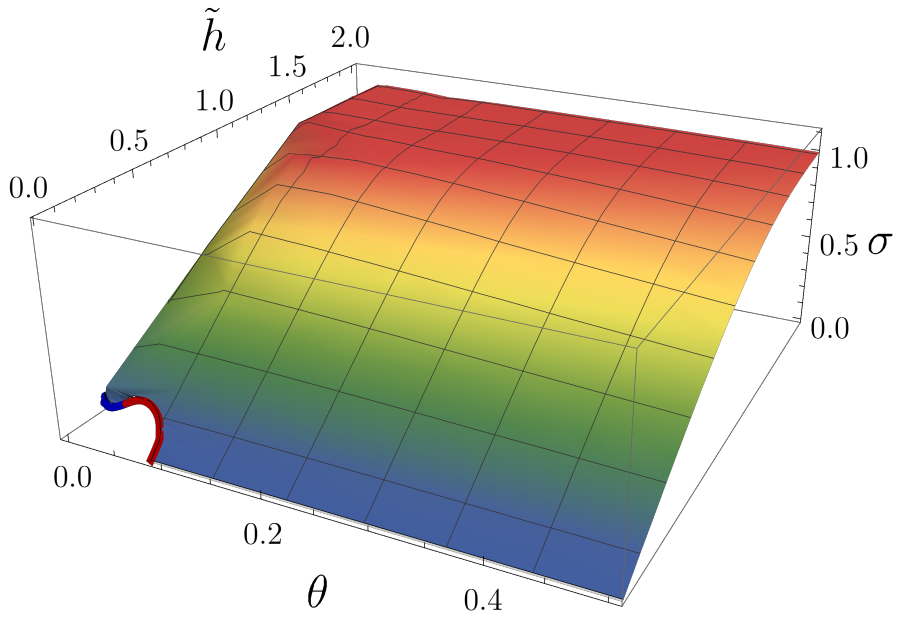


Figure 5.14: Spin polarization $\sigma$ at $v = -0.75$. Along the red line the instability towards a homogeneous superfluid is encountered, while along the red line the transition to an FFLO state has been detected.

the effects of the attractions, such that the internal energy also grows. Whereas the critical value of $U/(n\varepsilon_F) \simeq 0.45$ is nearly independent of the temperature at $v = -0.75$, we observe a smooth evolution from the minimal value $U/(n\varepsilon_F) \simeq 0.21$ in the absence of a finite polarization to the maximum $U/(n\varepsilon_F) \simeq 0.80$ in the ground state on the BEC side at $v = 0.75$. Finally, note that for positive scattering lengths we cannot compute reliably the thermodynamic functions for large $\tilde{h} \gg 1$, while the temperature simultaneously approaches zero. In this regime, which for $v = 0.75$ is encountered at $\theta \lesssim 0.05$ and $\tilde{h} \gtrsim 3$, one actually expects a fully polarized ideal gas. However, our numerics overestimate the minority density, which at large enough attractions and low enough temperatures artificially leads to condensation. Nevertheless, we can determine the asymptotic value of $U/(n\varepsilon_F)(\theta = 0, \tilde{h} \to \infty) = 3/5 \cdot 2^{2/3} + \varepsilon_B/(2\varepsilon_F) \simeq 1.51$, which arises from the energy of $3/5 n_\uparrow \varepsilon_{F,\uparrow}$ of the bare Fermi sea compared to the zero of the energy, which we have chosen as the balanced ground state $n/2\varepsilon_B$. The additional factor $2^{2/3}$ arises from our convention for the Fermi energy (2.65b) in terms of a two-component, balanced gas. As can be seen in Fig. 5.17 our data has converged quite well to this result. In the absence of two-body bound states at the negative $v = -0.75$ we obtain $U/(n\varepsilon_F)(\theta = 0, h \tilde{\to} \infty) = 3/5 \cdot 2^{2/3} \simeq 0.95$, which is also well obeyed by our data.

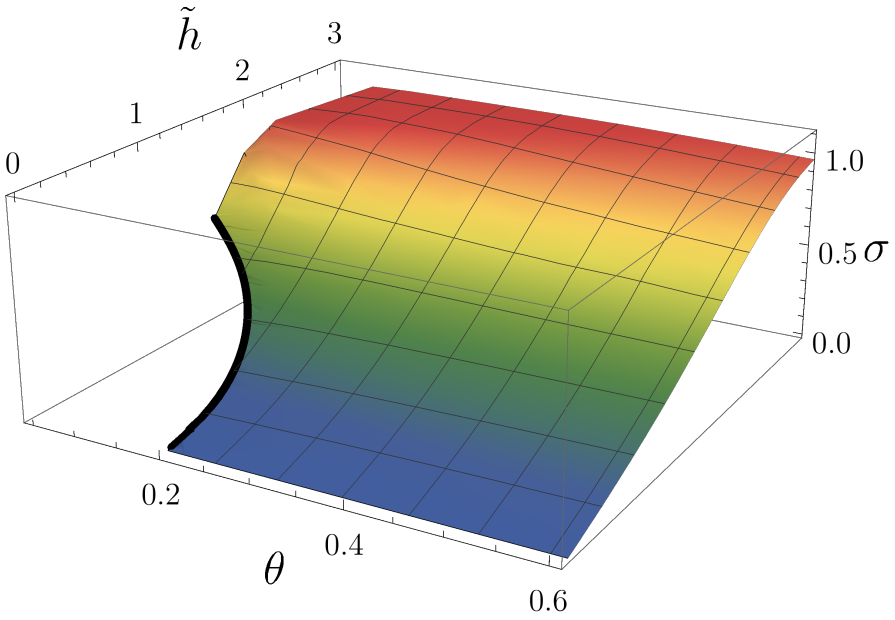


Figure 5.15: Spin polarization $\sigma$ at $v = 0.75$. The black line marks the phase transition to the homogeneous superfluid.

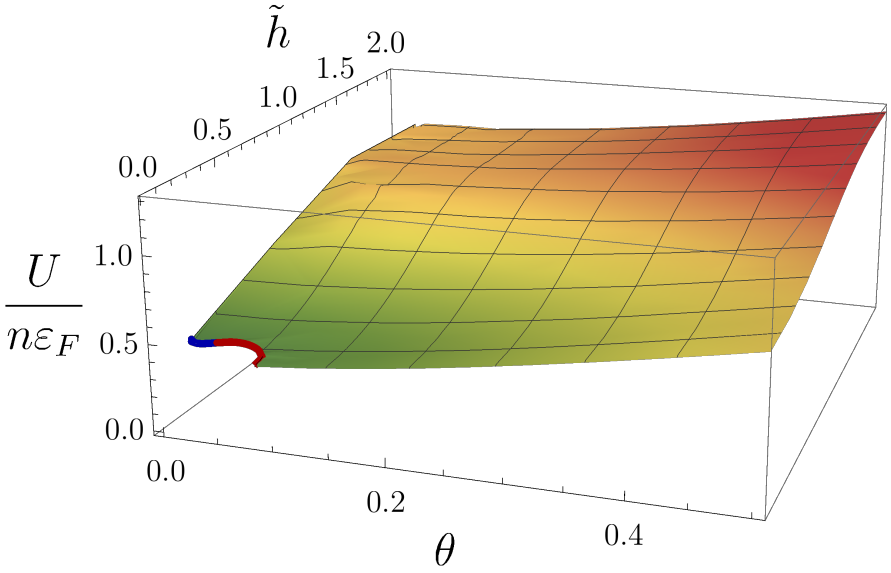


Figure 5.16: Internal energy $U/(n\varepsilon_F)$ at $v = -0.75$. Along the red line the instability towards a homogeneous superfluid is encountered, while along the red line the transition to an FFLO state has been detected.

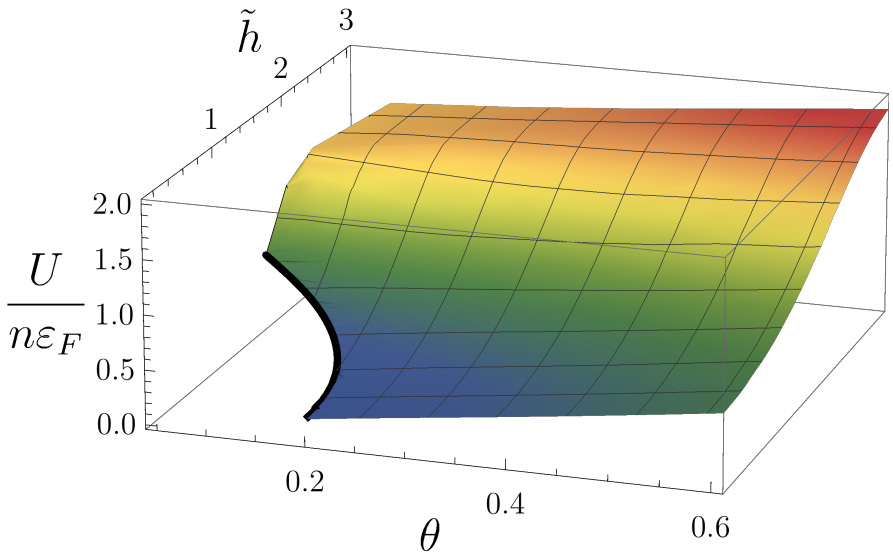


Figure 5.17: Internal energy $U/(n\varepsilon_F)$ at $v = 0.75$. The black line marks the phase transition to the homogeneous superfluid.

### 5.4.2 Phase diagram at $v = -0.75$

To close this section we present the phase diagram at $v = -0.75$ in analogy to the unitary limit, shown in Fig. 5.6. To this end, we rescale the temperature and Zeeman field by the chemical potential[3] $\mu$, which attains an almost constant value $\tilde{\mu}(v = -75) \simeq 0.69$ along the critical line. The corresponding Figure 5.18 can be found below. However, it is to be noted, that this diagram does not represent a genuine scaling function like in the case of unitarity. Here any change away from the critical line would affect the density and therefore alter the coupling strength $v = 1/(k_F a)$. Nevertheless, we can gain further insight from this representation. The superfluid phase at $v = -0.75$ appears only at values below $T/\mu \simeq 0.13$, which is considerably smaller than the unitary value $T/\mu \simeq 0.38$ due to the weaker attractions. As mentioned earlier, the phase boundary also shows a backbending behavior for $T/\mu \lesssim 0.05$. Furthermore, the FFLO phase makes up a substantial part of the phase boundary, which prevents a continuation of the $(h/\mu)_c$ curve towards zero temperature, in contrast to unitarity. Thus the internal structure of the symmetry-broken phase cannot be revealed. Yet, we can extrapolate $(h/\mu)_{\mathrm{FFLO}}$ to its ground state value, which yields $0.32 \pm 0.03$. This results from extrapolating the datapoints at the lowest available temperatures linearly, while we have estimated the error from $(h/\mu)_{\mathrm{FFLO}}$ value of the data point located at the minimal value of $T/\mu$, which would correspond to a sharp turn of the phase boundary towards the $(h/\mu)$ axis.

[3] Since $\mu$ has a zero in the ground state on the bosonic side at $\nu \sim 0.41$ [144], which will strongly affect this representation we only show the fermionic case.

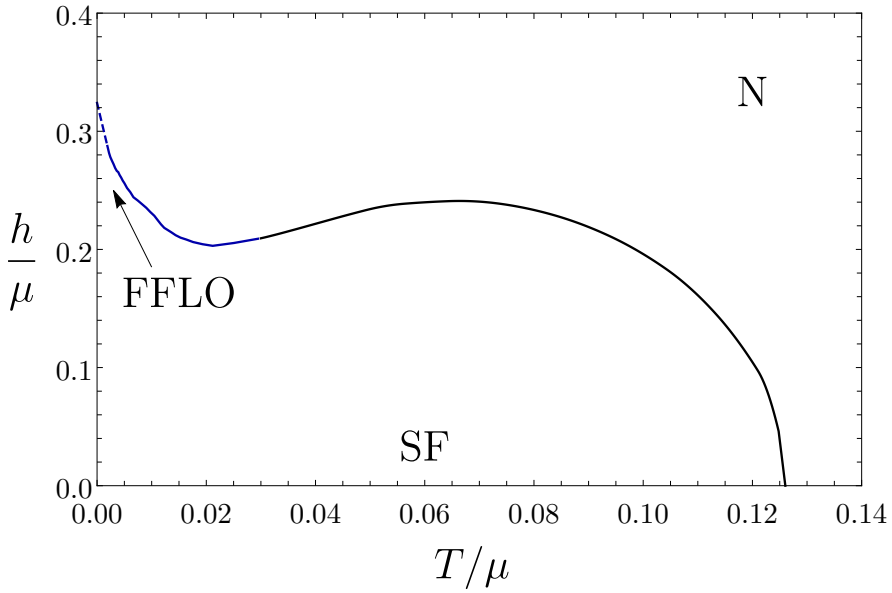


Figure 5.18: Phase diagram at $v = -0.75$. For $h/\mu \lesssim 0.03$ we observe the transition to an FFLO phase (blue). The phase boundaries within the superfluid cannot be determined. Dashed line: extrapolation to $T = 0$.

## 5.5 Tan errors

In Sec. 4.7.4 we have provided a consistency check for our numerics, which is based on the Tan pressure relation (2.62). The relative errors

$$\delta_{\mathrm{Tan}} = \left| \frac{p - \frac{2}{3}\varepsilon - \frac{\hbar^2}{12\pi m a}\mathcal{C}}{p} \right| , \tag{5.9}$$

where the individual terms are evaluated according to eq. (4.59), are depicted for several Zeeman fields in Fig. 5.19. In general, we observe $\delta_{\mathrm{Tan}} \leqslant 0.01$ up to a few exceptions, where the error is of the order of a few percent. Away from the critical region we encounter at most errors on the $10^{-3}$ level, while for the vast majority of data points $\delta_{\mathrm{Tan}}$ is even in the regime of $10^{-4}$. The largest errors appear in the critical region, where the absolute value of vertex function $|\Gamma(\mathbf{Q}, \Omega_n = 0)|$ increases substantially at the unstable center-of-mass momentum $\mathbf{Q}$. In practice we deal with values of the vertex of up to $10^6$, when the transition to a homogenous superfluid is approached, or with the slightly smaller value of $10^{-5}$, which we accept as an FFLO instability. Consequently, sampling the numerical integrals in $H_{\log}[\Gamma]$ close to the phase transition becomes more difficult. However, for most of the $(v, \theta)$ coordinates the deviations remain on the order of $\delta_{\mathrm{Tan}} \simeq 10^{-3}$, even close to the phase transition. Note that the errors at large $\beta h$ increase towards the

BEC side of the crossover. This is related to the opposite regimes of the two chemical potentials, i.e. $\beta\mu_\uparrow \gg 1$, while $\beta\mu_\downarrow \ll -1$. As detailed in Chap. 7, the BCS subtraction scheme for large chemical potentials should therefore be applied to $\mathcal{G}_{\uparrow\uparrow}$, whereas $\mathcal{G}_{\downarrow\downarrow}$ should be treated by the BEC scheme. However, we have not implemented that combination and work within the BCS scheme for both Green's functions, since the error remains below 2%.

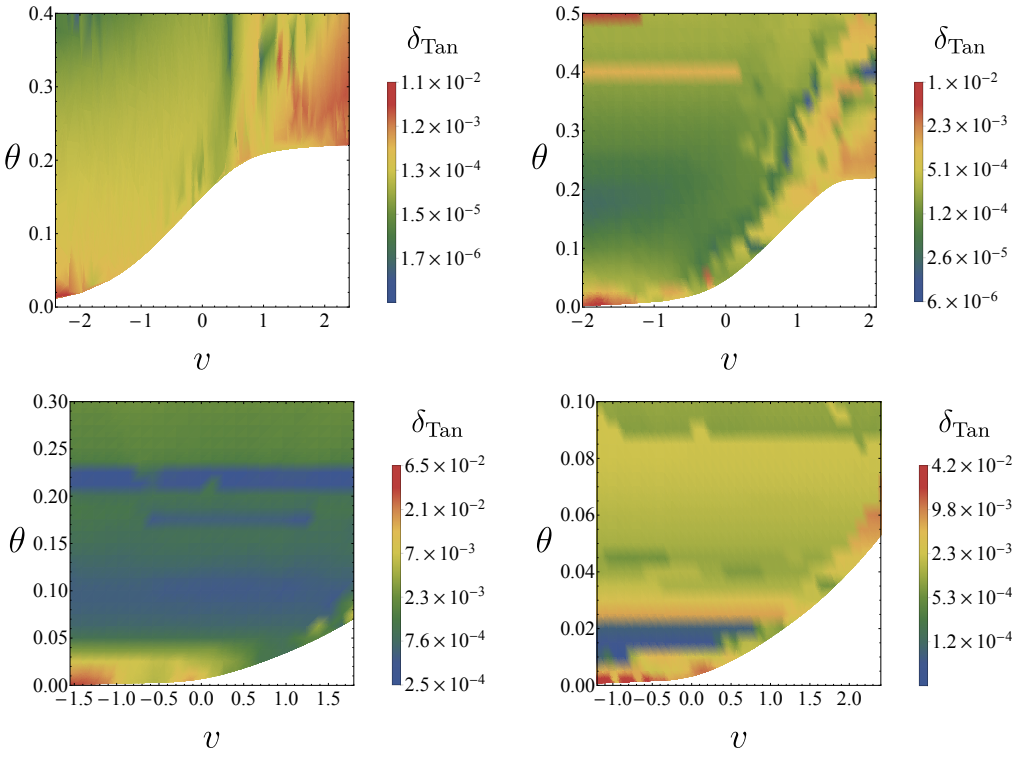


Figure 5.19: Tan errors for fixed $\beta h = 0$ (top left), $\beta h = 5$ (top right), $\beta h = 52$ (bottom left) and $\beta h = 104$ (bottom right). In the white regions the system is in the symmetry-broken state.

## 5.6 Scaling functions for the BCS-BEC crossover

The RG analysis by Nikolić and Sachdev [1] has turned out to yield significant insight into the phase diagram of the BCS-BEC crossover. In particular, it revealed the existence of universal scaling functions like eq. (2.34). One important feature of the Luttinger-Ward formalism is that it provides quantitative results for these scaling functions. In this chapter we discuss the phase boundaries as a function of $\bar{\mu} = \mu/\varepsilon_B$ in an interval that covers several orders of magnitude both at positive and negative values of the scattering length. In the following, we will focus on the

balanced case at finite temperatures as well as on the $T \to 0$ limit in the presence of a Zeeman field. These cases allow to compare our results to the known BCS and BEC asymptotics, while we can also study the crossover towards the strongly interacting regime.

### 5.6.1 Negative scattering lengths

We first consider the fermionic side with $a < 0$, where in the BCS limit $\bar{\mu} \ll 1$ we have for the critical temperature of the balanced gas

$$\bar{T}(\bar{\mu} \ll 1, \bar{h} = 0) = \frac{8e^{\gamma_E}}{\pi e^2}\, \bar{\mu}\, e^{-\pi/(2\sqrt{\bar{\mu}})}\,, \tag{5.10}$$

while in the ground state we encounter the FFLO phase at a critical dimensionless Zeeman field

$$\bar{h}_{\mathrm{FFLO}}(\bar{\mu} \ll 1, \bar{T} = 0) = 0.754 \frac{8}{e^2}\, \bar{\mu}\, e^{-\pi/(2\sqrt{\bar{\mu}})}\,. \tag{5.11}$$

These functions follow from the weak coupling asymptotics (2.48) after eliminating the GMB factor $(4e)^{-1/3}$, since our theory does not take particle-hole fluctuations into account, as discussed in Sec. 4.4.2. In analogy to the universal phase boundaries discussed in Sec. 2.3.3, one replaces $\varepsilon_F \to \mu$, with exponentially small corrections of order $\Delta^2$.

The results for the phase boundaries are depicted in Fig. 5.20 and Fig. 5.21, respectively. The black lines represent our data obtained from the self-consistent Green's functions, whereas the blue and red dashed lines show the limiting asymptotics for $\bar{\mu} \ll 1$ and $\bar{\mu} \gg 1$. In the weak coupling limit $\bar{\mu} \ll 1$, we find excellent agreement with with the equations (5.10) or (5.11), provided we take into account that the substitution $\varepsilon_F = \mu$ only works deep in the BCS-limit, where the corrections from the pairing are exponentially small. Therefore, we replace the chemical potential $\bar{\mu}$ by $\bar{\mu}/0.91$, which corresponds to our result $\tilde{\mu} \simeq 0.91$ at the minimal interaction strength $v \simeq -4$, in the the asymptotic form of $\bar{T}(\mu \ll 1, 0)$ from above. For the ground state we proceed analogously, but with $\bar{\mu} \to \bar{\mu}/0.83$, since we obtain $\tilde{\mu}(v \simeq -2) \simeq 0.83$. In the insets we zoom into the $\bar{\mu} \ll 1$ regime, which reveals that these adjustments of the asymptotics indeed match our data much better than the original forms. Regarding the strongly interacting limit $\bar{\mu} \gg 1$, we encounter a linear behavior as expected from the discussion of the Figures 2.4 and 3.2. For the critical temperature of the balanced gas the slope is given by $(\theta_c/\tilde{\mu})_{1/a=0} \simeq= 0.380$ in agreement with the $\theta_{c,\mathrm{lower}}$ data from Haussmann et al. [37]. The crossover between the weak and the strong coupling regime takes place at a chemical potential $\bar{\mu} \simeq 8$. Regarding the ground state phase diagram, the slope of the critical Zeeman field has been determined by fitting a linear function to the data as $(h_{\mathrm{FFLO}}/\mu)_{1/a=0} \simeq 1.25$, which is consistent with the FFLO-transition encountered in Fig. 5.6. In this case we observe the crossover around $\bar{\mu} \simeq 50$, which takes place at a much larger value

compared to the finite temperature balanced case. This agrees with our previous observation in Sec 5.2 that the Zeeman field follows the weak-coupling asymptotics to up to much larger coupling strength, since the induced imbalance suppresses the effects of the interactions.

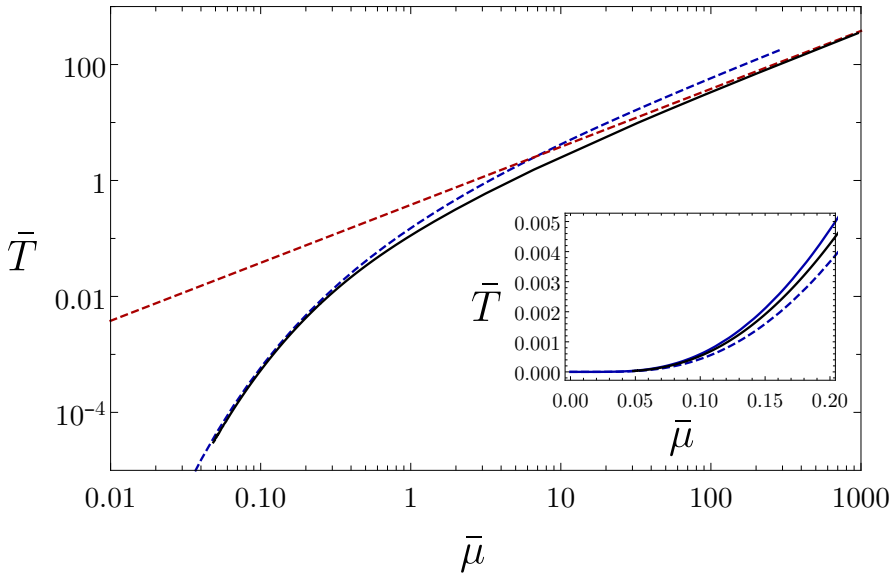


Figure 5.20: Crossover of the Luttinger-Ward $\bar{T}_c$ (black) at $\bar{h} = 0$ from the rescaled BCS asymptotics (5.10) (dashed blue) towards the linear behavior at unitarity with universal slope (dashed red). Inset: Luttinger-Ward data (black) vs. rescaled (blue) and original (dashed blue) BCS result.

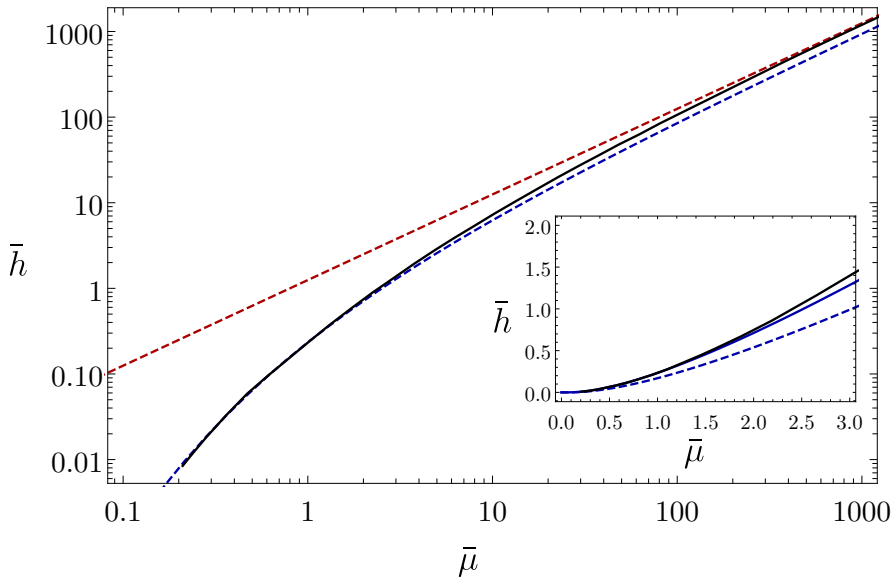


Figure 5.21: Universal phase boundary at $T = 0$ from Luttinger-Ward: $\bar{h}_{\mathrm{FFLO}}$ (black) connects smoothly the rescaled BCS curve (5.11) (blue dashed) to $\bar{\mu} \gg 1$ (red dashed) with universal slope at unitarity. Inset: same color-coding as in Fig. 5.20.

### 5.6.2 Positive scattering lengths

We can perform a similar analysis also for the case of positive $a$, where the weak coupling expansion in the limit $(\bar{\mu} + 1) \ll 1$ for $\bar{T}(\bar{h} = 0)$ is given in eq. (2.51), while the saturation field $\bar{h}_s(\bar{T} = 0)$ follows from eq (3.6). Note that the Luttinger-Ward approach detects $\bar{h}_s$, which corresponds to the normal-to-superfluid phase boundary in the limit $a \to 0^+$, since any admixture of minority atoms gives rise to a superfluid component (see Figs. 3.3, 3.4). Beyond the point M the Luttinger-Ward approach yields the phase boundary between the partially polarized normal and and imbalanced fermionic superfluid, which either realizes a Sarma or an FFLO phase.

However, the asymptotic forms in the BEC limit contain either the scattering length $a_{\mathrm{dd}}$ in the balanced case or $a_{\mathrm{ad}}$ at very strong imbalance, which will not be correctly recovered within the ladder approximation, as we have discussed in Sec. 4.4.2. Therefore, we expect that we have to use a rescaling procedure like on

the fermionic side of the crossover and propose the ansatz

$$\bar{T}_c(\mu \ll 1, \bar{h} = 0) = \frac{(2\pi)^{1/3}}{(\lambda_{\mathrm{dd}}\,\zeta(3/2))^{2/3}}\,(\bar{\mu}+1)^{2/3} \tag{5.12a}$$

$$\bar{h}_s(\mu \ll 1, \bar{T} = 0) = \left(\frac{2\pi}{\lambda_{\mathrm{ad}}}\right)^{2/3}(\bar{\mu}+1)^{2/3} + 1 - (\bar{\mu}+1)\,, \tag{5.12b}$$

where we have introduced two positive fudge parameters $\lambda_{\mathrm{dd}}, \lambda_{\mathrm{ad}}$. They represent the ratios $\lambda_{\mathrm{dd}} = a_{\mathrm{dd}}/a$ and $\lambda_{\mathrm{ad}} = a_{\mathrm{ad}}/a$. In an exact theory they must reproduce the physical results $\lambda_{\mathrm{dd}} = 0.6$ [60] and $\lambda_{\mathrm{ad}} = 1.18$ [64], however, we allow them to deviate from these values in order to determine effective scattering lengths for our theory.

The universal phase diagram at positive $a$ is depicted in Fig. 5.22, where we have determined $\lambda_{\mathrm{dd}} = 2.2$, which is equivalent to a Luttinger-Ward scattering length $a_{\mathrm{dd}}^{\mathrm{LW}} = 2.2a$, by fitting the ansatz for the BEC limit to our data. This result indicates that $a_{\mathrm{dd}}^{\mathrm{LW}}$ deviates even more strongly from the exact result than the mean-field value $a_{\mathrm{dd}}^{\mathrm{MF}} = 2a$. Nevertheless, the modified asymptotics with the given value of $\lambda_{\mathrm{dd}}$ agrees very well with the Luttinger-Ward results. We note that a more reliable estimate for the size of $a_{\mathrm{dd}}$ in the Luttinger-Ward formalism could be obtained both from the inclusion of the higher critical temperature $\theta_{c,\mathrm{upper}}$ that however requires the superfluid phase and from a formulation in terms of density units, which show a less pronounced dependence on $v$. In particular, the deviation between both $\theta_c$ curves in Fig. 2.3 is on the order of 10% around $v \simeq 3$. Increasing the temperature on the left-hand side of eq. (5.12a) will bring the ansatz (5.12a) considerably closer to the exact result, as can be seen in the inset of Fig. 5.22. In the strong coupling limit the scaling function converges to a linear behavior, whose slope matches the unitary result $(\bar{T}/\mu)_c = 0.38$ like in the analogous Fig. 5.20 for negative $a$. Finally, the crossover between the regimes $\bar{\mu}+1 \ll 1$ and $\bar{\mu} \gg 1$ takes place around $\bar{\mu}+1 \simeq 5$.

Let us now turn to the ground state phase diagram of the imbalanced gas, which is presented in Fig. 5.23. Here the situation becomes even more problematic, since we actually obtain datapoints for $\bar{\mu} < -1$, where in an exact theory one encounters the vacuum. In this case the introduction of $\lambda_{\mathrm{ad}}$ does not suffice to reconcile our data with the exact form (3.6). We therefore conclude that our numerics does not determine the energy of the two-particle bound state correctly, which gives rise to an erroneous transformation of the chemical potential. Most likely this is related to the evaluation of $\mathcal{G}_{\downarrow\downarrow}$ within a suboptimal scheme, as discussed in the context of the relatively large Tan errors, which emerge in this regime, see Sec. 4.7.4. The statement, that the binding energy contains errors is supported by the extended ansatz

$$\bar{h}_s(\mp 1\mu \ll 1, \bar{T} = 0) = \left(\frac{2\pi}{\lambda_{\mathrm{ad}}}\right)^{2/3}(\bar{\mu}+1+\delta\bar{\varepsilon}_B)^{2/3} + (1+\delta\bar{\varepsilon}_B) - (\bar{\mu}+1+\delta\bar{\varepsilon}_B)\,, \tag{5.13}$$

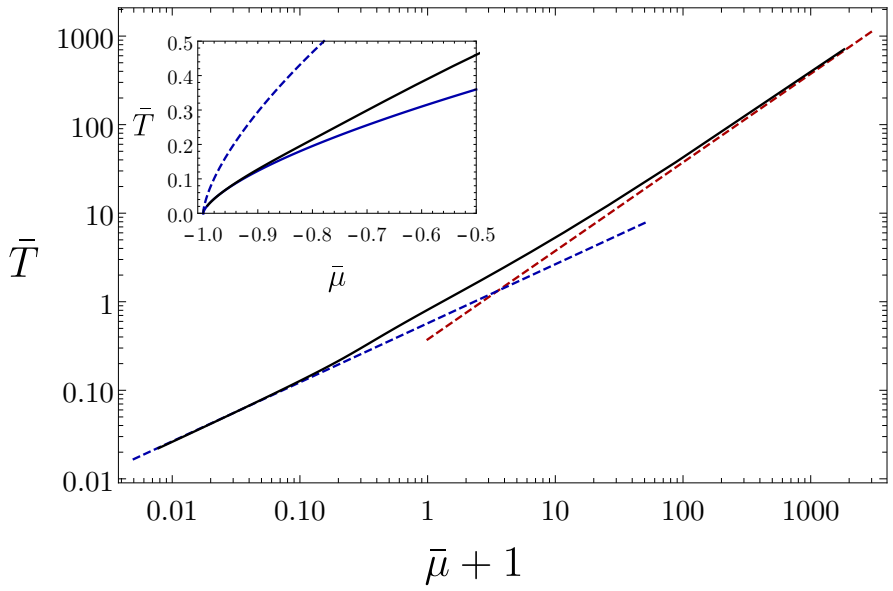


Figure 5.22: Crossover of the universal critical temperature $\bar{T}(\bar{\mu}, \bar{h} = 0)$ (black), that coincides in the regime $\bar{\mu} + 1 \ll 1$ with the rescaled BEC-limit (5.12a) (blue dashed line). For $\bar{\mu} \gg 1$ one encounters the linear behavior at unitarity with the universal value of the slope $(\bar{T}/\bar{\mu}) = 0.38$ (red dashed line). Inset: Weak coupling limit: Luttinger-Ward data (black), rescaled scattering length (blue), exact scattering length $a_{\mathrm{dd}} = 0.6a$ (blue dashed).

which allows a shift of the binding energy by another fudge parameter $\delta\bar{\varepsilon}_B$. Fitting our data to this simple model yields $\lambda_{\mathrm{ad}} = 0.54$ and $\delta\bar{\varepsilon}_B = 0.02$. The small shift of the binding energy about two percent is on the order of the observed $\delta_{\mathrm{Tan}}$, while the effective scattering length becomes $a_{\mathrm{ad}}^{\mathrm{LW}} = 0.54a$. Of course this model is not very rigorous, but we obtain very good agreement between the Luttinger Ward data (black) and this ansatz (dashed blue) even up to $\bar{\mu} \simeq 1$, as can be seen from the inset of Fig. 5.23. In contrast, both the single-parameter ansatz (5.12b) and the exact result with the exact value $\lambda_{\mathrm{ad}} = 1.18$ deviate considerably. Regarding the strongly interacting regime $\bar{\mu} \gg 1$, we again observe a smooth crossover towards a linear behavior, which coincides with the universal ratio $(h/\mu)_{\mathrm{FFLO}} \simeq 1.25$ encountered in the unitary limit. In this case we find the crossover scale between the limiting behaviors at chemical potentials $\bar{\mu}+1 \simeq 10$. At the point M, that belongs to $\bar{h}_s$, we do not detect any sharp change of the scaling function, neither at our Luttinger-Ward result $\bar{\mu}_{\mathrm{M}} = -0.91$ nor at the more accurate BDMC value $\bar{\mu}_{\mathrm{M}} = -0.74$ from Prokof'ev et al. [131]. However, these authors also showed that the energies of the polaron and the molecule cross in an almost perfectly smooth manner at M, which must be reflected in the behavior of $\bar{h}_s$in the vicinity of $\bar{\mu}_{\mathrm{M}}$.

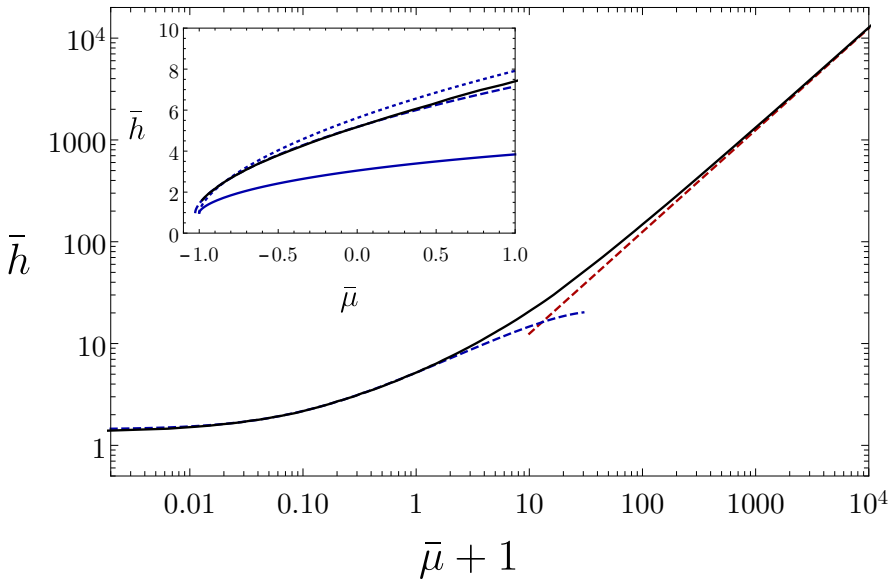


Figure 5.23: Zero temperature projection of the universal normal-to-superfluid phase boundary at positive scattering lengths (black). In the BEC limit this line is equivalent to the saturation field and we observe a smooth crossover from the extended weak coupling ansatz (5.13) in the regime $\bar{\mu}+1 \ll 1$ towards the strongly interacting regime $\bar{\mu} \gg 1$, where the unitary ratio $(\bar{h}/\bar{\mu})_{\mathrm{FFLO}} = 1.25$ is approached.

## 5.7 Properties of the FFLO phase

Within the BCS regime the FFLO phase itself is subdivided into several phases that are distinguished by different geometries of the order parameter [113]. To investigate them in the presence of strong interactions, however, requires to include both anomalous expectation values but also a vertex function $\Gamma(\mathbf{Q}, \Omega_n)$, that does not exhibit rotational invariance in momentum space. Such a non-trivial momentum-dependence currently is far beyond the scope of the numerics, since it requires to perform a genuine matrix inversion to solve the Bethe-Salpeter equation (4.30).

Nevertheless, we are able to analyze the momentum scale, at which the divergence in $\Gamma(Q, \Omega_n)$ occurs, as a function of the other thermodynamic variables. Apart from the overall amplitude of the order parameter, knowledge of the approximate size of the spatial modulation is crucial for experimental detection of a spatially varying order parameter. In particular, if $\Delta(\mathbf{x})$ varies on the typical interparticle distance or even below, it will be impossible to resolve the modulation. A similar problem arises, if the wavelength of the oscillation of $\Delta(\mathbf{x})$ is on the order of several sample sizes. We show the temperature dependence of the critical momentum $\tilde{Q}_{\mathrm{FFLO}} = Q_{\mathrm{FFLO}}/k_F$ in Fig. 5.24 for two different coupling strengths $v = -1.5$ and

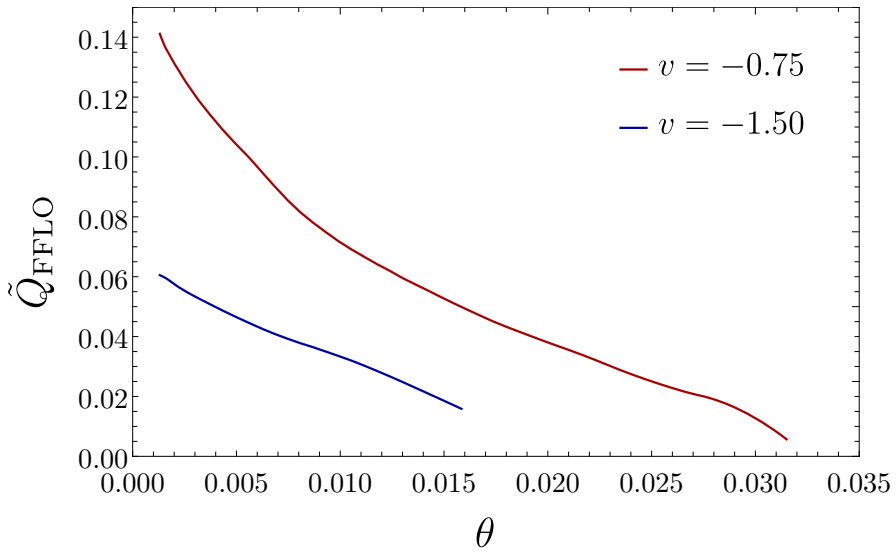


Figure 5.24: Variation of the center of mass momentum $\tilde{Q}_{\mathrm{FFLO}} = Q_{\mathrm{FFLO}}/k_F$ with the reduced temperature at two different interaction strengths.

$v = -0.75$. The critical temperature of the latter coupling strength is close to the maximal $\theta_c \simeq 0.03$ for the FFLO transition. $\tilde{Q}(\theta)$ turns out to be a monotonically decreasing function of $\theta$. We also observe an appreciably larger critical polarization $\sigma$ (not shown) at $v = -0.75$ compared to $v = -1.5$, which in a Fermi liquid picture gives rise to a more pronounced mismatch of the Fermi seas. Based on this representation, we conclude that the stronger attractions at $v = -0.75$ allow for pairing with larger $Q \sim (k_{F\uparrow} - k_{F\downarrow})$. Typical values of the FFLO vector at this coupling are on the order of $\tilde{Q}_{\mathrm{FFLO}} = 0.1$. Together with the standard experimental densities $n \simeq 10^{13}\mathrm{cm}^{-3}$ [63], we infer a spatial variation of $\lambda = 2\pi/Q \simeq 90\ \mu$m. Finally, note that we cannot reliably determine the onset of a finite $\tilde{Q}_{\mathrm{FFLO}}$ at the largest critical temperatures, since we have to use a threshold $\tilde{Q}_0 > 0$ to decide which momenta in our numerical grid really indicate a nonhomogeneous order and which belong to the exponentially dense LFT[4] grid at the origin $Q = 0$.

Apart from the temperature dependence of $\tilde{Q}_{\mathrm{FFLO}}$ also its relation to the Zeeman field at $T = 0$ is of interest. Larkin and Ovchinnikov [28] predicted for the weak coupling limit in the vicinity of the transition point a sinusoidal order parameter $\Delta(\mathbf{x}) = \Delta \cos(\mathbf{Q}_{\mathrm{FFLO}} \cdot \mathbf{x})$, whose wave vector satisfies

$$\hbar Q_{\mathrm{FFLO}} v_F = 2.4h\,, \tag{5.14}$$

with the Fermi velocity $v_F = \hbar k_F/m$. This translates to $\tilde{Q}_{\mathrm{FFLO}} = 1.2\tilde{h}$. We present both $\tilde{h}$ and $\tilde{Q}_{\mathrm{FFLO}}$ in Fig. 5.25. In the weak coupling limit we observe at

[4]For the definition of the logarithmic Fourier transform (LFT) see Sec. 6.1.

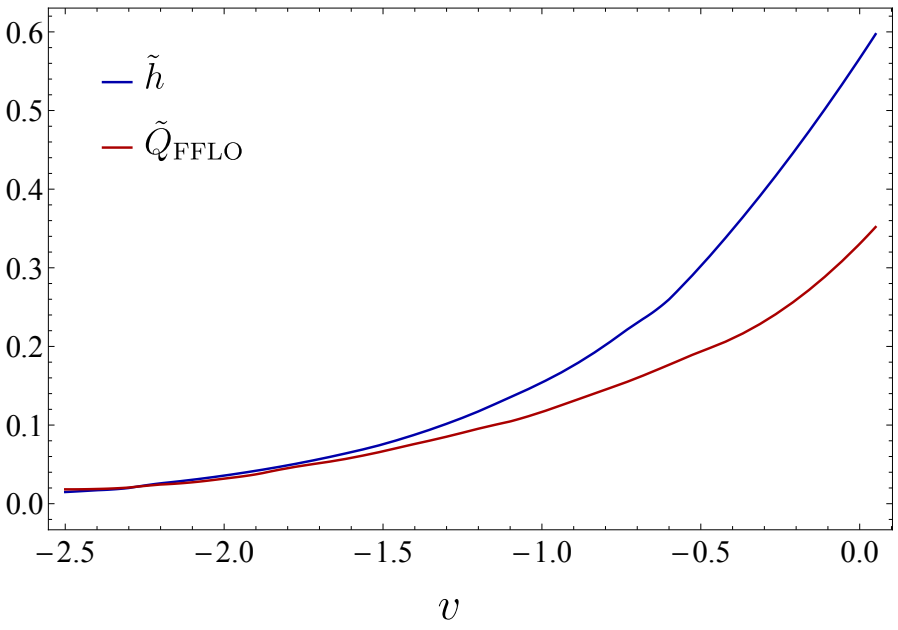


Figure 5.25: Critical field and corresponding center-of-mass-momentum of the pairs in the ground state as function of the interaction strength.

the lowest available temperatures for the smallest available interaction strengths around $v \simeq -2.5$ $\tilde{Q}_{\mathrm{FFLO}}/\tilde{h} \simeq 1.23$ close to the weak-coupling result. An important source for the remaining discrepancy arises from the extrapolation of $\tilde{Q}_{\mathrm{FFLO}}$ to zero temperature, where the considerable slope of the $\tilde{Q}_{\mathrm{FFLO}}(\theta)$ curves at fixed $v$ (see Fig. 5.24) only allows to predict the ground state behavior very with an uncertainty a the percent level. Furthermore, also the finite interaction strength, which implies $\tilde{\mu} \simeq 0.86$ and $\tilde{h}_{\mathrm{FFLO}} \simeq 0.95$ leads to deviations from the genuine weak-coupling limit. Approaching the unitary limit both $\tilde{h}$ and $\tilde{Q}_{\mathrm{FFLO}}$ grow as functions of the coupling strength, however, the latter increases more slowly. The increase is expected from physical arguments, since the stronger the attractions the stronger a Zeeman field is required to destabilize the superfluid state, while FFLO pairing remains favorable for larger spin polarizations, in analogy to the situation a finite temperatures. In addition, $\tilde{h}$ specifies the difference $(\mu_\uparrow - \mu_\downarrow)/2$ of the external parameters, while $\tilde{Q}_{\mathrm{FFLO}}$ is a measure for the mismatch of the Fermi levels of the interacting system, at least as long as a Fermi liquid picture applies. Since this is indeed consistent with experimental observations of the imbalanced unitary gas [129], we conclude that the strong attractions give rise to a renormalization of the spin-dependent $k_{F\sigma}$, thereby diminishing the population imbalance and resulting in a $\tilde{Q}_{\mathrm{FFLO}}$, which is smaller relative to $\tilde{h}$ than in the weak coupling limit (5.14). Note that this implies a crossing of $\tilde{Q}_{\mathrm{FFLO}}(v)$ and $\tilde{h}(v)$ curves, which we indeed observe around $v \simeq -2.3$.

# Chapter 6

# Numerical Fourier Transformations

Fourier transformations between the Matsubara frequencies and momentum space on the one hand to real space and imaginary time on the other constitute the main numerical operation that has to be performed repeatedly for the computation of the Green's functions and the thermodynamic quantities of the imbalanced Fermi gas, see Sec. (4.6.2) on the self-consistent equations. The standard method to deal with this task is the fast Fourier transform (FFT) due to Cooley and Tukey [156]. It reduces the numerical complexity from a grid of $N$ points to $N \log N$ compared to $N^2$, which arises in case of a discrete Fourier transform (DFT) [157] obtained by directly discretizing the Fourier integrals. However, the FFT requires an equidistant grid, which is quite inconvenient for the application to the imbalanced Fermi gas and many other problems where one needs the Fourier transform of functions that exhibit nontrivial variations over several orders of magnitude, e.g. in power law decays. In contrast, the DFT in principle runs on any grid. In the Fermi gas the low-momentum degrees of freedom have to be resolved with sufficient accuracy because they give the major contribution to the thermodynamic properties at ultralow temperatures and furthermore the phase transition to the superfluid is encoded in a zero of $\Gamma^{-1}(\mathbf{Q} \to 0, \Omega_n = 0)$. Concurrently, at momenta much larger than any inverse length scale one expects algebraic tails like in the Green's function $G(\mathbf{k}, \tau = 0^-) \simeq \mathcal{C}/k^4$, see eq. (2.57). Since all thermodynamic quantities can be considered as Fourier transforms to $(\mathbf{x} = \mathbf{0}, \tau = 0^-)$, as discussed in Sec. 4.7, they incorporate a sum over these algebraic tails. Consequently, also the large momentum asymptotics of $G$ and $\Gamma$ have to be sampled with sufficient precision. Using equidistant lattices for an ordinary FFT would imply an immense number of data points, which makes this method unfeasible for the BCS-BEC crossover problem. For example, let us consider a $k^{-4}$ asymptotics and demand that the error from truncating the integral at $k_{\max}$ shall be below the $10^{-8}$-level, which requires $k_{\max} \simeq 10^4$ in for the Fourier transformation in $d = 3$ given in eq. (4.16). Using a step width $\Delta k = 10^{-2}$ yields the huge number $N \simeq 10^6$ of necessary grid points.

One way out is offered by the logarithmic Fourier transformation (LFT), developed first by Haines and Jones [158] in a geophysical context. It combines a logarithmic grid, that covers all relevant short and long length scales, with the efficient $N \log N$ scaling of the FFT algorithm. In Sec. 6.1 we review the major

properties of the LFT. In addition, the Haines and Jones deduced some rather strong conditions on the class of functions to which the method can be applied and on the range of the intrinsic "trade-off parameter" $k_p$ of the transformation. In the present thesis we[1] show that many of these restrictions actually can be lifted, which turns out to be quite important for the application to the imbalanced Fermi gas. Moreover, we prove in Sec. 6.1.2 that the LFT converges exponentially fast towards the exact result in the limit $N \to \infty$. Furthermore, we discuss its capability to also transform non-integrable functions numerically, which from a mathematical point of view have to be interpreted within the framework of generalized functions. These properties make the LFT a useful approach not only for the imbalanced Fermi gas but also for a wider set of problems in theoretical physics that include Fourier transforms of functions varying over many orders of magnitude. Possible examples are generic correlation functions in frequency space, correlators at critical points or glass transitions, where light scattering spectra are measured over ten orders of magnitude, see for example the work by Steffen et al. [159]. Further details and examples can be found in Lang and Frank [160].

Despite being quite powerful, however, it must be emphasized that the LFT cannot be applied to all kinds of functions. For instance, the transformation between Matsubara frequencies and the imaginary time involves the Fourier *sum* evaluated at the *exact* $\omega_n$ or $\Omega_n$. The LFT, which is designed to approximate Fourier integrals, might be extended to converge to a discrete sum[2]. However, the translation of the uniform difference of $2\pi T$ between two successive Matsubara frequencies to the logarithmic grid would involve the combination of several LFTs, each acting on an individual subset of frequencies, which in practice becomes very cumbersome. For the $\omega_n, \Omega_n \leftrightarrow \tau$ transformation we therefore resort to a DFT in combination with a spline interpolation, which has been underlying previous Luttinger-Ward studies of the BCS-BEC-crossover [37, 87]. Originally, this method had been developed to treat the mode-coupling theory of the liquid-glass transition [161]. An overview of this approach can be found in the thesis by Cerrito [144]. We have extended the method from cubic to fifth order splines, which we both utilize and to a more direct cancellation of poles appearing in the course of the computations. The details of the implementation are given in Section 6.2. Furthermore, we apply the spline DFT also to the transformation between momentum and real space in situations, where $1 \ll \beta\mu_\sigma \ll \beta\varepsilon_{Q_{\max}}$, as the LFT in general undersamples functions that show fast variations on an intermediate scale. Since the neighborhood of the Fermi levels is relevant for the fermionic Green's functions, we use in this situation an enhanced density of grid points around $k \simeq \sqrt{\beta\mu_\sigma}$, which can only be treated by a DFT. In the vicinity of the phase transition with a finite FFLO pairing vector $Q_{\mathrm{FFLO}}$ we have implemented a similar method to faithfully resolve the emerging divergence of the vertex function in this regime of momenta. The full procedure

[1] This work was done in collaboration with Johannes Lang.

[2] The DFT, presented in Sec. 6.2, distinguishes in a similar manner between sums and integrals.

regarding the imbalanced Fermi gas is detailed in Section 7.4.

## 6.1 Logarithmic Fourier Transformation (LFT)

### 6.1.1 Definition

To introduce the LFT we will stick to the standard definition used in physics for the Fourier transform of a function $\hat{f}(t)$ from the time domain to the (angular) frequency $\nu$

$$f(\nu) = \mathcal{FT}(\hat{f})(\nu) = \int_{-\infty}^{\infty} dt \hat{f}(t) e^{i\nu t}\,, \tag{6.1}$$

while the inverse transform is given by

$$\hat{f}(t) = \mathcal{FT}^{-1}(f)(t) = \int_{-\infty}^{\infty} \frac{d\nu}{2\pi} f(\nu) e^{-i\nu t}\,. \tag{6.2}$$

At this stage we assume that the functions $f(\nu), \hat{f}(t) \in L^1$ are integrable, such that Riemann-Lebesgue is applicable, while $\delta$ distributions are excluded. Below we discuss an extension to generalized functions. Moreover, one can readily adopt this definition for the effectively one-dimensional Fourier transforms (4.16) arising from the radial symmetry of $G$ and $\Gamma$ in momentum and real space. We define the logarithmic frequency and time coordinates[3] $\omega$, $\tau \in \mathbb{R}$ via

$$\nu = \zeta \nu_0 e^{\omega} \quad \text{and} \quad t = \eta t_0 e^{\tau}\,, \tag{6.3}$$

where $\zeta = \pm 1 = \eta$ keep track of the signs of the original arguments, while the prefactors $\nu_0$ and $t_0$ carry the correct units. In the following, we set them to unity to simplify the notation, however, they can be easily reintroduced. After performing the coordinate transformation to the logarithmic variables the inverse Fourier transformation (6.2) acquires the form of a convolution

$$\hat{f}(t = \eta|t|) = e^{-k_p \tau} \sum_{\zeta=\pm 1} \int \frac{d\omega}{2\pi} \left[ f(\zeta e^{\omega}) e^{(1-k_p)\omega} \right] e^{k_p(\omega+\tau) - i\zeta\eta \exp(\omega+\tau)} \Big|_{\tau = \ln|t|}\,. \tag{6.4}$$

This representation admits to chose a real trade-off parameter $k_p$ [158], which at this point is irrelevant from the perspective of the exact transformation, but will allow us to optimize the numerical properties of the LFT. Upon rewriting the

[3] They must not be confused by the Matsubara frequencies or the imaginary time. In this chapter we explain the general mathematical properties of the LFT independent of a specific physical framework.

convolution as the product of Fourier transforms, we find

$$\hat{f}(\eta|t|) = \frac{e^{-k_p\tau}}{2\pi} \sum_{\zeta=\pm 1} \mathcal{FT}_{s\to\tau}\left[\mathcal{FT}_{\omega\to s}\left(f(\zeta e^{\omega})e^{(1-k_p)\omega}\right)(s)\mathcal{FT}^{-1}_{u\to s}\left(e^{k_p u - i\zeta\eta e^{u}}\right)(s)\right](\ln|t|)\ . \tag{6.5}$$

The $\mathcal{FT}^{-1}_{u\to s}$ transformation does not depend on $f$ and can be computed in closed form as

$$\mathcal{FT}^{-1}_{u\to s}\left(e^{k_p u - i\zeta\eta\exp(u)}\right)(s) = \frac{1}{2\pi}(i\zeta\eta)^{is-k_p}\Gamma(k_p - is)\,, \tag{6.6}$$

where $\Gamma(k_p - is)$ denotes the Gamma function. This identity has to be understood as the analytic continuation of the integral representation of the Gamma function

$$\int \frac{du}{2\pi}\, e^{k_p u - i\zeta\eta\exp(u)} e^{-isu} = \frac{1}{2\pi}(i\zeta\eta)^{is-k_p}\Gamma(k_p - is)\,, \tag{6.7}$$

which is only valid in the limited regime $0 < k_p < 1$, as emphasized in [158], to the set $k_p \in \mathbb{R}\backslash\mathbb{Z}_0^-$. Non-positive integers have to be excluded to avoid the evaluation of the Gamma function at its poles if $s = 0$. Since we are interested in performing the LFT repeatedly, we compute the required values of $\Gamma(k_p - is)$ during the initialization and tabulate them. In any case, modern algorithms, like Spouge's approximation [162], allow to efficiently obtain numerical results for the Gamma function without severe loss of computational efficiency.

Let us return to equation (6.5), which reveals the role of the trade-off parameter: $k_p > 0$ ($k_p < 0$) improves the convergence properties both for $\tau \gg 1$ and $\omega \gg 1$ ($\tau \ll -1$ and $\omega \ll -1$) while the convergence in the opposite limits $\tau \ll -1$ and $\omega \ll -1$ ($\tau \gg 1$ and $\omega \gg 1$) simultaneously deteriorates. In fact, the fundamental request that the Fourier transform $\mathcal{FT}_{\omega\to s}\left(f(\zeta e^{\omega})e^{(1-k_p)\omega}\right)(s)$ exists, which is required to obtain a meaningful LFT, gives rise to a restriction on the range of $k_p$. Suppose the asymptotic exponential behavior $|f(\zeta e^{\omega})| \to \exp(a\omega)$ in the limit $\omega \to -\infty$ and $|f(\zeta e^{\omega})| \to \exp(b\omega)$ for $\omega \to \infty$, with real coefficients $a, b$, which arises from power law tails of $f(\nu)$. Then the trade-off parameter has to satisfy

$$1 + b < k_p < 1 + a \tag{6.8}$$

to render the Fourier transformation well-defined. We immediately conclude that only functions with $b < a$ can be transformed by the LFT. Since the analytic continuation of the $\Gamma$ function in eq. (6.6) merely excludes non-positive integers as possible choices for $k_p$, we are now able to define the Fourier transform of any function $f(\zeta\nu)$ via the LFT, provided $\mathcal{FT}_{\omega\to s}\left(f(\zeta e^{\omega})e^{(1-k_p)\omega}\right)(s)$ can be controlled by an appropriate value of the trade-off parameter. For example, the nonintegrable function $1/(1+\nu)$ has $a = 0$ and $b = -1$, which can be perfectly treated by the

choice $k_p = 1/2$. However, $\delta(t)$-distributions or its derivatives, which originate from monomials like $\nu^c,\ c \in \mathbb{N}_0$ can never be handled by the LFT, as $a = c = b$ contradicts the condition (6.8).

Another way to interpret $k_p$ arises from the point of view of complex analysis. Changing $k_p$ can be understood as shifting the Fourier integral onto a contour running through the complex plane. Deformations of this contour are sensitive to the analytic structure of $f(\nu)$ and offer a large amount of information about the mathematical properties of the LFT. In particular, these considerations allow to estimate the numerical errors of the LFT, see Sec. 6.1.2 below. Inserting eq. (6.6) into eq. (6.5) yields the final form of the LFT

$$\hat{f}(\eta|t|) = \frac{e^{-k_p\tau}}{(2\pi)^2} \sum_{\zeta=\pm1} \mathcal{FT}_{s\to\tau}\left[\mathcal{FT}_{\omega\to s}\left(f(\zeta e^{\omega})e^{(1-k_p)\omega}\right)(i\zeta\eta)^{is-k_p}\Gamma(k_p-is)\right](\ln(|t|)) \ , \tag{6.9}$$

under the condition that a suitable choice of $k_p$ exists. The transformation from $t \to \nu$ can be obtained in the same fashion, however, with an additional factor of $2\pi$ and the replacement $\eta \to -\eta$ on the right-hand side.

Up to now we have considered analytic properties and have seen that one can apply the LFT even to nonintegrable functions. However, the major advantage of the LFT becomes apparent, when one introduces the logarithmic grids

$$\begin{aligned} \nu_{\pm n} &= \pm e^{\omega_n} \quad \text{with} \quad \omega_n = \Delta\omega(n+\bar{\omega}) \\ t_{\pm n} &= \pm e^{\tau_n} \quad \text{with} \quad \tau_n = \Delta\tau(n+\bar{\tau}) \end{aligned} \tag{6.10}$$

of $N$ *equidistant* points labeled by $n \in \{1, 2, ..., N\}$ for the numerical evaluation, since using regular grids allows to perform the Fourier transforms in (6.9) with the widely available, efficient FFT algorithms. The auxiliary space of the variable $s$ is discretized analogously by $s_n = \Delta s(n + \bar{s})$. Furthermore, these grids give rise to a certain degree of flexibility. The step sizes $\Delta\omega$ and $\Delta s$ allow to sample the relevant scales of the function and scale like $1/N$ to recover the exact integral in the limit $N \to \infty$. The shifts $\bar{\omega}$ and $\bar{s}$, which usually are set to $-N/2$ to treat positive and negative exponents symmetrically, can be used to optimally position the center of the grid. The points $\tau_n$ in the image space can be selected such that one resolves the most interesting range of $\tau$ values. We will come to restrictions and optimal parameter choices below, after having discussed the convergence properties. To compute $\hat{f}(\eta|t|)$ for $\eta = \pm1$ completely, we have to execute altogether six FFTs, as well as six componentwise products, which both involve the multiplication of $f$ in auxiliary space with the Gamma function and the final multiplication with $\exp(-k_p\tau_n)$. Since the numerical complexity of these products scales only linearly with the system size, which also is the case for summing the results from $\zeta = \pm1$, the overall cost remains on the order of the FFT algorithm $N \log N$, yet with an enlarged prefactor of $O(1)$ from the additional operations.

One question of great importance for the usefulness of the LFT is, which class of functions can be treated reliably . The necessary equidistant choice of the logarithmic grid implies an exponentially large density of points for $\nu \to 0$ while for $|\nu| \to \infty$ one obtains an exponentially increasing separation between two successive grid points. Regarding the imbalanced Fermi gas, this is the desired behavior to include low-momentum degrees of freedom with high precision, while the slowly varying algebraic tails of the correlation functions are sampled with a sufficient amount of points, too. Severe difficulties arise however, if $f$ varies significantly on intermediate scales, that cannot be assigned to the asymptotics close to the origin, even by exhausting all the freedoms of (6.10). In the case of ultracold Fermions this indeed happens for large $\beta\mu_\sigma$, where a pronounced peak structure due to the Fermi levels appears around $k \simeq k_{F\sigma}$ at weak coupling. We cannot identify $k_{F\sigma}$ with the lowest momentum scale, because then we would cut off the relevant limit $Q \ll k_F$, where the phase transition occurs. An analogous situation appears for the transition to an FFLO state, where $Q_{\mathrm{FFLO}}$ is found on the order of $0.1k_F$, see Fig. 5.24. To keep numerical uncertainties under these conditions as small as possible we switch to a DFT method with an enlarged number of data points in the neighborhood of either $Q_{\mathrm{FFLO}}$ and/or $k_{F\sigma}$.

From a general perspective also oscillating functions, whose characteristic frequency is not damped out in the limit $|\nu| \to \infty$, but remains an important feature of the asymptotics, pose a very difficult task to the LFT: The discrete set of $\omega_n$ will drastically undersample the periodic variations in the regime $|\omega_n \gg 1|$ and consequently give rise to poor numerical results. A reliable approach would require a fine grid on any frequency scale which inevitably leads to inconveniently large $N$ and hampers an efficient evaluation. A prototype example for such a function is given by $f(\nu) = \sin(\nu)g(\nu)$ with an integrable, algebraically decaying function[4] $g(\nu)$. The fact that $f(\nu)$ oscillates with a fixed frequency of order one on all $\nu$ scales downgrades the convergence of the LFT to the exact result from an exponential behavior to an algebraic one. As we will see in the next section, this happens due to the fundamental analytic structure of the LFT.

### 6.1.2 Convergence properties

We can promote the rather qualitative arguments of the last paragraph regarding which classes of function are tractable by the LFT to precise statements about how

[4] In this simple example the Fourier transformation results in $(g(t+1) - g(t-1))/(2i)$, where the algebraic function $g(\nu)$ actually can be treated by the LFT. Note, however, that the uniform shift of the original argument $t \pm 1$ requires an interpolation in $\tau$.

fast the numerical approximation[5]

$$\hat{f}_N(\eta|t_n|) = \\ e^{-k_p\tau_n}\sum_{\zeta=\pm 1}\sum_{l=1}^{N}\frac{\Delta s}{2\pi}e^{is_l\tau_n}(i\zeta\eta)^{is_l-k_p}\Gamma(k_p-is_l)\sum_{m=1}^{N}\frac{\Delta\omega}{2\pi}f(\zeta e^{\omega_m})e^{(1-k_p)\omega_m}e^{i\omega_m s_l} \tag{6.11}$$

converges to the exact Fourier integral in the limit $N\to\infty$. In fact, we can show that the deviation between eq. (6.9) and eq. (6.11) vanishes exponentially with $N$, if $f(\zeta\exp(\omega))\exp((1-k_p)\omega)$ is analytic and integrable in a strip of finite width around the real axis in the complex $\omega$-plane.

Before coming to the proof it is worth studying the implications on $f$ as a function of $\nu$, which helps to understand both the following arguments and the conditions for the application of the LFT. The analyticity of $f(\zeta\exp(\omega))$ implies that we can expand $f$ as a Taylor series around any real $\omega_0$. On a formal level this means

$$\left|\sum_{n=0}^{\infty}\left(\frac{d^n}{d\omega^n}f(\zeta e^{\omega})\right)_{\omega=\omega_0}\frac{(\omega-\omega_0)^n}{n!}\right|<\infty\,, \tag{6.12}$$

for any $\omega\in\mathbb{C}$ that satisfies $R^{\zeta}_{\omega_0}$: $|\omega-\omega_0|<R^{\zeta}_{\omega_0}$, where the existence of a finite convergence radius $R^{\zeta}_{\omega_0}>0$ is guaranteed by the analyticity. The maximal width of the analytic strip is defined as

$$R^{(1)}=\inf_{\substack{\zeta=\pm\\ \omega_0\in\mathbb{R}}}R^{\zeta}_{\omega_0}\,, \tag{6.13}$$

which implies that $R^{\zeta}_{\omega_0}\nrightarrow 0$ in the limits $\omega_0\to\pm\infty$ in order to obtain a nonzero $R^{(1)}>0$. In view of the applicability of the LFT it is useful to translate the analytic properties of $f$ as function of $\omega$ back to the original argument $\nu$. Inverting the variable transformation (6.3) within the disk around $\omega_0=\log(\zeta\nu_0)\in\mathbb{R}$, where the series (6.12) converges, yields:

$$|\log(\zeta\nu)-\log(\zeta\nu_0)|<R^{\zeta}_{\omega_0}\,. \tag{6.14}$$

To estimate the size $R^{\zeta}_{\nu_0}>0$ of the analytic region around $\zeta\nu_0$ we parametrize

$$\zeta\nu=\zeta\nu_0+R^{\zeta}_{\nu_0}e^{i\varphi},\quad\text{if}\quad\zeta\nu_0\to\infty \tag{6.15a}$$

$$\frac{1}{\zeta\nu}=\frac{1}{\zeta\nu_0}+R^{\zeta}_{\nu_0}e^{i\varphi},\quad\text{if}\quad\nu_0\to 0\,, \tag{6.15b}$$

with a real phase $\varphi$ and solve for the value of $R^{\zeta}_{\nu_0}>0$ that satisfies the bound (6.14) as closely as possible. As a result, we find

$$R^{\zeta}_{\nu_0}\lesssim|e^{R^{\zeta}_{\omega_0}}-1|\begin{cases}|\nu_0|\,, & \text{if}\quad\zeta\nu_0\to\infty\\ |\nu_0|^{-1}\,, & \text{if}\quad\nu_0\to 0\end{cases}, \tag{6.16}$$

[5] We assign the factors of $1/(2\pi)$ to the sums over $\omega$ and $s$ for later convenience.

an at least linearly increasing analytical regime in $\nu$. This excludes any nonintegrable divergences of $f(\nu)$ on the real axis, which would render the Fourier transform ill-defined in any case, but also discontinuities or cusps that yield slowly decaying oscillations in the $t$ domain. Note, however that equation (6.16) does not imply that $f(\nu)$ is integrable at $\nu \to 0$ or $\nu \to \pm\infty$. Indeed, as we have already discussed above, $f$ may actually diverge algebraically, as long as a trade-off parameter exists, such that satisfies (6.8).

Now, one may ask what kind of functions are analytic in a strip in the complex $\omega$ plane? Constraints on the width $R^{(1)}$ arise both from the asymptotically larger or small $\omega$, where the behavior of $f(\zeta\omega)$ has to be integrable, but also from nonanalyticities in the complex plane at finite $\mathrm{Re}\,\omega$. We begin with discussing the first scenario and turn to the second case below. First of all, if the asymptotics of the function admits the representation $f(\zeta \exp\omega)\exp((1-k_p)\omega) \simeq \exp((b+1-k_p)\omega)$ for $\omega \to \infty$, introduced above eq. (6.8), $f$ remains exponentially small and analytic, upon continuation to finite $\mathrm{Im}\,\omega \neq 0$. This argument can be analogously repeated for $\omega \to -\infty$, where $b$ has to be replaced by $a$. These kind of functions, which we will call algebraic functions in the following, due to their $\nu$ dependence, are thus ideally suited to be treated with the LFT, since their asymptotics give rise to exponentially fast convergence. A more careful treatment is required in the case of seemingly harmless, exponentially decaying functions. We consider the simple example of a function $f(\zeta\nu) \sim \exp[\alpha(\zeta\nu)^c]$, which is governed by a single, dominant exponent $c \in \mathbb{R}$ in the limit $\zeta\nu \to \infty$ ($\zeta\nu \to 0$). Oscillating functions can be included by $\alpha \in \mathbb{C}\backslash\{0\}$, while the proportionality factor may contain any algebraic function of $\zeta\nu$. Formulated in terms of $\omega = x + iy,\ x, y \in \mathbb{R}$, we have

$$\left|e^{\alpha\nu^c}\right| = \left|e^{\exp(cx)[\mathrm{Re}(\alpha)\cos(cy) - \mathrm{Im}(\alpha)\sin(cy)]}\right| . \tag{6.17}$$

Consider $x \to \infty$ ($x \to -\infty$), then $c \leqslant 0$ ($c \geqslant 0$) reduces the problem to the previously discussed algebraic functions. The most interesting situation is encountered, if $c > 0$ ($c < 0$). In this case a negative $\mathrm{Re}(\alpha)$ is mandatory as otherwise the original function $f(\nu)$ grows exponentially and its Fourier transform does not exist, not even in the sense of generalized functions. Here the trade-off parameter cannot be used to improve the convergence, since it is not able to influence the super-exponential dependence on $x$. Moreover, the latter will inevitably lead to an also super-exponential increase away from the real $\omega$-axis, even if $\mathrm{Re}(\alpha) < 0$. More precisely, this happens once the argument of the square-brackets in (6.17) becomes positive, that is for $|y|$ larger than

$$y_{\max} = \left|\frac{1}{c}\arctan\left(\frac{\mathrm{Re}\,\alpha}{\mathrm{Im}\,\alpha}\right)\right| . \tag{6.18}$$

Note that for $|y| < y_{\max}$ the function $f(\nu)$ still vanishes exponentially fast for $|x| \to \infty$. In case of $|y| = y_{\max}$ the function reduces to the algebraic type, which can possibly be controlled by choosing $k_p$. In accordance with the previous definition,

$y_{\max}$ corresponds to $R^{(1)}$, unless a singularity at finite $\omega$ is encountered closer to the real axis. Therefore, all real, negative $\alpha$ allow for a finite strip of width $\pi/2$. However, recall the simple example $f(\nu) = g(\nu)\sin(\nu)$ from the last paragraph. In this case we have $c = 1$, $\alpha = i$ and thus $R^{(1)} = y_{\max} = 0$, which can only give rise to an algebraic convergence of the discrete approximation to the Fourier transformation as $N \to \infty$.

So far we have estimated the size of the analytic strip from the asymptotic behavior of the function. However, $R^{(1)}$ may also be limited by a nonanalyticity at finite frequencies. In the following, we estimate this width from the directly accessible representation of $f$ as function of the physical variable $\nu$. The resulting criterion can also be used in numerical applications to test the possible convergence of the LFT. Afterwards, we translate the result to $\omega$, which finally determines $R^{(1)}$. First of all, we note that the condition that $f(\zeta\exp(\omega))$ is analytic around the real $\omega$ axis in a strip of finite width rules out any nonanalytic behavior at real $\omega$ and therefore also for real $\nu$. This limitation on $f$ has been expected, since any nonanalyticity, even an integrable one, destroys the point-wise convergence of the Fourier transformation [163]. Let us therefore assume that a pole or the beginning of a branch cut of $f$ is located at $\hat{\nu} = \nu_0 \pm iR^{\zeta}_{\nu_0}$, with $\nu_0 \in \mathbb{R}\backslash\{0\}$, $\zeta = \mathrm{sgn}(\nu_0)$ and $R^{\zeta}_{\nu_0} > 0$, which measures the distance of $\hat{\nu}$ from the real axis. In this case the Laurent series of $f$ around $\hat{\nu}$ can be written as

$$f(\nu) = \frac{\lambda}{(\nu - \nu_0 \mp iR^{\zeta}_{\nu_0})^m} + \ldots , \tag{6.19}$$

where $\lambda$ is a complex parameter and $m > 0$. The ellipsis refers to more regular terms that are not of importance for the determination of the width of the analytic strip. This form gives rise to the $n$-th order derivative

$$\left| f^{(n)}(\nu_0) \right| = \frac{|\lambda|\,(n+m)!}{m!\,(R^{\zeta}_{\nu_0})^{m+n}} \tag{6.20}$$

at $\nu_0$ on the real axis. The latter condition can be used, even in a numerical application, where one computes the finite differences approximating the derivatives, to test the existence of a nonanalyticity and if necessary to extract $R^{\zeta}_{\nu_0}$. To obtain an estimate for the related $R^{\zeta}_{\omega_0}$, which will determine the convergence properties of the LFT, we note that the translation of $\hat{\nu}$ to the logarithmic variable marks exactly the distance from the real $\omega$ axis, where the power series (6.12) around $\omega_0 = \log(\zeta\nu_0)$ ceases to converge. Application of the root criterion yields for the width of the analytic strip

$$\limsup_{n\to\infty} \left| \left( \frac{d^n}{d\omega^n} f(\zeta e^{\omega}) \right)_{\omega_0} \frac{(R^{\zeta}_{\omega_0})^n}{n!} \right|^{1/n} = 1 \,. \tag{6.21}$$

Using the chain rule, the derivative

$$\left(\frac{d^n}{d\omega^n} f(\zeta e^\omega)\right)_{\omega_0} = \sum_{j=1}^{n} a_j f^{(j)}(\nu_0)\nu_0^j$$

can be written in terms of a sum with real coefficients $a_j$ that have a maximum of order $\binom{n}{n/2} \sim 2^n$ around $j \simeq n/2$, due to the derivatives acting on $\nu_0^j$, where we have inserted the Stirling formula $n! \sim (n/e)^n + ...$ for $n \to \infty$. Returning to the root criterion (6.21), we simply estimate $\left(\frac{d^n}{d\omega^n} f(\zeta e^\omega)\right)_{\omega_0} \sim f^{(n)}(\nu_0)\nu_0^n$ with a prefactor of order one due to the factorial growth of the $f^{(j)}$, see eq. (6.20). Note that we could have used any index of order $n$, since the final result will only be influenced by subleading corrections of the Stirling formula, which can only give rise to corrections of $R^\zeta_{\omega_0}$ by factors of order one. All in all, we find for the constraint on the width $R^\zeta_{\omega_0}$, which is caused by the nonanalytic behavior at $\hat{\nu}$,

$$R^\zeta_{\omega_0} \simeq e^{-\omega_0} R^\zeta_{\nu_0} \,. \tag{6.22}$$

The analytic strip and therefore also the speed of convergence with the number of grid points is more severely limited at large $\omega_0$ corresponding to large $\nu_0$, too, while the limit $\omega \to -\infty$ or $\nu \to 0$ does not suffer at all from the pole or branch cut at $\hat{\nu}$. This can be explained from the fact that the origin of $\nu$ is sampled with an exponentially dense grid that is well suited to treat the fast variations around $\nu_0$. In the opposite limit of $\nu_0 \gg 1$, however, the sampling density decreases exponentially and the LFT does not provide very accurate results, if the function $f(\nu)$ is modulated on very short scales around $\nu_0$. Fortunately, in the majority of systems and especially in effective field theories the physically relevant nonanalyticities appear on a low-momentum scale, which has to be sampled with a high density, such that no genuine restriction arises from the previous consideration.

Now we present the proof for the exponential convergence of the LFT.

**Theorem:** Let $f$ be a function that is analytic in a strip of width $R^{(1)} > 0$ in the logarithmic variable $\omega$ and the Fourier transform of $f(\zeta \exp(\omega)) \exp[(1-k_p)\omega]$ exists due to an appropriate choice of the trade-off parameter $k_p$. Then

$$\left| \frac{e^{-k_p\tau_n}}{(2\pi)^2} \sum_{\zeta=\pm 1} \mathcal{FT}_{s\to\tau}\left[\mathcal{FT}_{\omega\to s}\left(f(\zeta e^\omega) e^{(1-k_p)\omega}\right)(i\zeta\eta)^{is-k_p}\Gamma(k_p-is)\right](\tau_n) \right.$$
$$\left. - e^{-k_p\tau_n} \sum_{\zeta=\pm 1}\sum_{l=1}^{N} \frac{\Delta s}{2\pi} e^{is_l\tau_n}(i\zeta\eta)^{is_l-k_p}\Gamma(k_p-is_l) \sum_{m=1}^{N} \frac{\Delta\omega}{2\pi} f(\zeta e^{\omega_m}) e^{(1-k_p)\omega_m} e^{i\omega_m s_l} \right| \to 0 \tag{6.23}$$

vanishes exponentially fast in the limit $N \to \infty$ for all $\tau_n$ of the grid.
To verify this statement we begin by examining the deviation

$$E_1^\zeta(s) = I_1^\zeta(s) - S_1^\zeta(s) \tag{6.24}$$

between the innermost, exact integral of the LFT in eq. (6.9)

$$I_1^\zeta(s) = \int \frac{d\omega}{2\pi} f(\zeta e^\omega) e^{(1-k_p)\omega} e^{is\omega} \tag{6.25}$$

and the numerical approximation in terms of the discrete sum

$$S_1^\zeta(s) = \sum_{m\in\mathbb{Z}} \frac{\Delta\omega}{2\pi} f(\zeta e^{\omega_n}) e^{(1-k_p)\omega_n} e^{is\omega_n} . \tag{6.26}$$

First of all, we note that the product $f(\zeta e^\omega)e^{(1-k_p)\omega}$, apart from being analytic in a strip of width $R^{(1)}$, decays exponentially like $\exp(-R^{(2)}|\omega|)$ with a positive constant $R^{(2)} = \min\left[|a+1-k_p|, |b+1-k_p|\right]$ for $|\omega| \to \infty$ under the conditions stated above. Its Fourier transform $I_1^\zeta(s)$ therefore is also analytic in a strip of width $R^{(2)}$ around the real $s$-axis and the asymptotics is given by $I_1^\zeta(s) \sim \exp(-R^{(1)}|s|)$, see e.g. the book by Titchmarsh [164]. Due to the integrability of $f(\zeta e^\omega)e^{(1-k_p)\omega}$, also the sum $S_1^\zeta(s)$ is finite and the exponential decrease gives rise to exponentially small truncation errors. Therefore, we have extended the sum in eq. (6.26) to all $m \in \mathbb{Z}$. For reasons of notational simplicity, we assume in the following that $\bar{\omega}$ is an integer. Then $S_1^\zeta(s)$ can be treated by the contour integration techniques for bosonic Matsubara sums (see Appendix B)

$$S_1^\zeta(s) = \begin{cases} \oint \frac{dz}{2\pi i} f(\zeta e^{-iz})(1+n_B(z))e^{-iz(1-k_p+is)} & , \mathrm{Re}(s) < 0 \\ \oint \frac{dz}{2\pi i} f(\zeta e^{-iz}) n_B(z) e^{-iz(1-k_p+is)} & , \mathrm{Re}(s) > 0 \end{cases} . \tag{6.27}$$

Here, $\omega = -iz$ and $n_B(z)$ denotes the Bose function with inverse temperature $\beta_\omega = 2\pi/\Delta\omega$. Other values of $\bar{\omega}$ would require to adjust the statistical functions, e.g. half-integers imply a Fermi-Dirac distribution, but the convergence remains unchanged.

For $|s| < \beta_w$ we deform the integration contour in (6.27), such that it runs along two infinitely long, straight lines $B_{R\pm}$ at $\mathrm{Re}\, z = \pm R^{(1)}$, see Fig. 6.1. Because of the holomorphic structure of the integrand $S_1^\zeta(s)$, there are no contributions arsing from nonanalyticities. Regarding the integral $I_1^\zeta(s)$ we shift the integration countour in the same fashion to $B_{R_+^{(1)}}$ or $B_{R_-^{(1)}}$. Thereby we select the half-plane with respect to sign$(s)$, that yields an exponentially small prefactor for the integrand. By combining the expressions for $S_1^\zeta(s)$ and $I_1^\zeta(s)$, we obtain for the error from eq. (6.24)

$$\begin{aligned} E_1^\zeta(s) = & -\int_{B_{R+}} \frac{dz}{2\pi i} f(\zeta e^{-iz}) n_B(z) e^{-(1-k_p+is)iz} \\ & -\int_{B_{R-}} \frac{dz}{2\pi i} f(\zeta e^{-iz})(1+n_B(z)) e^{-(1-k_p+is)iz} . \end{aligned} \tag{6.28}$$

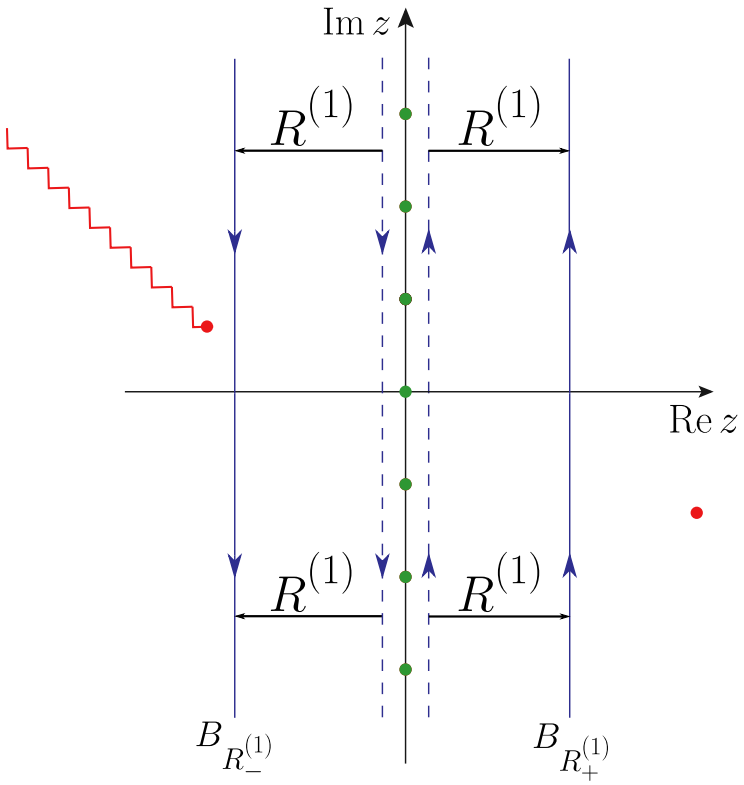


Figure 6.1: The plot shows the shift of the original contours encompass the imaginary axis to $B_{R^{(1)}_\pm}$ at constant, finite real part $\pm R^{(1)}$. The red dot and the red zigzag line symbolize a pole and a branch cut, respectively. $R^{(1)}$ is determined from the real part of closest non-analyticity to the imaginary axis.

Parametrizing the nonvanishing contours by $z = \pm R^{(1)} + iu$, with $u \in \mathbb{R}$, yields the form

$$E_1^\zeta(s) = e^{(-\beta_\omega + |s|)R^{(1)}} F_1^\zeta(s, R^{(1)})\,. \tag{6.29}$$

The exponential prefactor arises from evaluating the integrand at the constant real part of the integration contours, where we have included the uniform exponential prefactor $\exp(-\beta_\omega R^{(1)})$ of the Bose distribution. The function $F_1^\zeta(s, R^{(1)})$ denotes the result of the contour integral from the remainder of the integrand. In particular, $F_1^\zeta(s, R^{(1)})$ can be interpreted as Fourier transformation $u \to s$ of a function that vanishes exponentially fast for $|u| \to \infty$, since the distance of the contours from the imaginary $z$ axis does not exceed $R^{(1)}$, such that $f(\zeta \exp(u \mp iR^{(1)}))$ is located within the analytic region, such that the power series in eq. (6.12) yields finite results and the complete integrand acquires an exponentially small prefactor $\sim \exp(-R^{(2)}|u|)$. Therefore, $F_1^\zeta(s, R^{(1)})$ is well-defined and bounded. In total, we

obtain an exponentially small error $E_1^\zeta$ for all $|s| < \beta_\omega \sim N$. For the practical implementation, we conclude that we can obtain this favorable scaling of the convergence, as long as $\Delta\omega = 2\pi/\beta_\omega$ can be chosen small enough, such that even $\exp[-(\beta_\omega + |s_{\pm N}|)R^{(1)}]$ yields a sufficient suppression of the error to achieve the requested precision. We return to this point, in the next subsection, when we discuss the optimal parameter settings for the LFT.

The next step is to compare the final $s \to \tau$ transformation in (6.9) with its numerical counterpart in (6.11). First, we consider the exact integral

$$I_2^\zeta(\tau) = \int \frac{ds}{2\pi} \Gamma(k_p - is)(i\zeta\eta)^{is-k_p} I_1^\zeta(s) e^{is\tau} \,. \tag{6.30}$$

Due to the exponential decay of $I_1^\zeta(s)$ for real $|s| \to \infty$ and the asymptotic behavior

$$\left|\Gamma(k_p - is)(i\zeta\eta)^{is-k_p}\right| \propto \begin{cases} \sqrt{2\pi}|s|^{k_p-1/2} e^{-\pi|s|} & ,\zeta\eta s \to \infty \\ \sqrt{2\pi}|s|^{k_p-1/2} & ,\zeta\eta s \to -\infty \end{cases} , \tag{6.31}$$

(see e.g. the book Freitag and Busam [165] for the complex form of the Stirling formula) that can only lead to an algebraic growth, $I_2^\zeta(\tau)$ is well-defined. The corresponding deviation reads

$$\begin{aligned} E_2^\zeta(\tau) = &\int \frac{ds}{2\pi} \Gamma(k_p - is) e^{is\tau} (i\zeta\eta)^{is-k_p} I_1^\zeta(s) \\ &- \sum_{l=1}^{N} \frac{\Delta s}{2\pi} \Gamma(k_p - is_l) e^{is_l\tau} (i\zeta\eta)^{is_l-k_p} S_1^\zeta(s_l) \,. \end{aligned} \tag{6.32}$$

In order to treat this error in the same way as $E_1^\zeta(s)$, first note that for sufficiently small $\Delta\omega \sim 1/N$, we can replace $S_1^\zeta(s_l)$ by $I_1^\zeta(s_l)$ at the expense of an exponentially small error. The latter can be estimated via

$$\left|\sum_{l=1}^{N} \frac{\Delta s}{2\pi} \Gamma(k_p - is_l) e^{is_l\tau} (i\zeta\eta)^{is_l-k_p} E_1^\zeta(s_l)\right| \leqslant C N^{k_p+1/2}\, e^{(-2\pi/\Delta\omega + |s_N|)R^{(1)}} \to 0 \,,$$

if $2\pi/\Delta\omega > |s_N|$. Here we have made use of the exponential scaling of $E_1^\zeta(s)$ in eq. (6.29), while we have inserted the worst power law increase from eq. (6.31) times the summation interval and a positive constant $C$ of order one. Once we have substituted $S_1^\zeta(s_l)$ by $I_1^\zeta(s_l)$ in $E_2(\tau)$, we can again extend the sum to all integer values, since $|I_1^\zeta(s)|$ itself becomes exponentially small for $|s| \to \infty$, provided that the maximal value $|s_N|$ already probes this exponential decay. This condition is necessary anyway, in order to keep the truncation errors of the second numerical Fourier transformation in eq. (6.11) under control. Later on, we will derive a condition on $\beta_\omega$ from this observation. Assuming, without loss of generality, that $\bar\tau$

is an integer number, we are in the position to rewrite $E_2^\zeta(\tau)$ as a contour integral in the complex plane[6]

$$\begin{aligned} E_2^\zeta(\tau) = & -\int_{B_{R_+^{(2)}}} \frac{dz}{2\pi i}\, n_B(z)\Gamma(k_p - z)e^{z\tau}(i\zeta\eta)^{z-k_p} I_1^\zeta(-iz) \\ & -\int_{B_{R_-^{(2)}}} \frac{dz}{2\pi i}(1 + n_B(z))\Gamma(k_p - z)e^{z\tau}(i\zeta\eta)^{z-k_p} I_1^\zeta(-iz) \\ & + E_{2,\Gamma}^\zeta(\tau)\,. \end{aligned} \tag{6.33}$$

Here the $B_{R_\pm^{(2)}}$ denote two lines parallel to the imaginary $z$-axis at a distance $R^{(2)}$, marking the boundaries of the region in which $I_1^\zeta(s)$ is analytic, in analogy to the construction for $E_1^\zeta(s)$ (see eq. (6.28) and the discussion below). We have also introduced the Bose-Einstein distribution $n_B(z)$ with inverse temperature $\beta_s = 2\pi/\Delta s$. Furthermore, when one shifts the contour to $B_{R_\pm^{(2)}}$ one has to take the poles of $\Gamma(k_p - z)$ at non-positive integers $-m$ with $m \in \mathbb{N}_0$ that are located between $-R^{(2)} < z < R^{(2)}$ into account. In this regard, one should also forbid combinations of $k_p \pm R^{(2)} \in \mathbb{Z}_0^-$ to avoid a crossing the contours with the poles. This new contribution from the $\Gamma$ function is summarized in the expression

$$\begin{aligned} E_{2,\Gamma}^\zeta(\tau) = & \sum_{\substack{m=\lceil -k_p\rceil \\ \wedge\, m\geqslant 0}}^{\lfloor R^{(2)}-k_p\rfloor} \frac{(-1)^m}{m!} n_B(k_p+m) I_1^\zeta(-i(k_p+m)) e^{(k_p+m)\tau}(i\zeta\eta)^m \\ & + \sum_{\substack{\lceil -R^{(2)}-k_p\rceil \\ \wedge\, m\geqslant 0}}^{\lfloor -k_p\rfloor} \frac{(-1)^m}{m!}\left(1 + n_B(k_p+m)\right) I_1^\zeta(-i(k_p+m)) e^{(k_p+m)\tau}(i\zeta\eta)^m\,, \end{aligned} \tag{6.34}$$

with the residues $\mathrm{Res}_{(-m)}\,\Gamma(z) = (-1)^m/m!$ [165]. The first line arises from the positive real parts $0 < \mathrm{Re}\, z < R^{(2)}$, while the second one originates from the negative ones $-R^{(2)} < \mathrm{Re}\, z < 0$. Therefore, the exponential behavior of the Bose distributions $\sim \exp(-\beta_s(m + k_p))$ overcomes the exponential function in the numerators, provided $\beta_s > |\tau|$. This corresponds to the previous criterion $\beta_\omega > s$ and will not pose a severe restriction. Note that $E_{2,\Gamma}^\zeta$ is known in analytical form except for the function $I_1^\zeta$, which we can compute with exponential precision, as discussed above. As we present in the next subsection, we can improve the total result for the LFT by removing the erroneous contribution $E_{2,\Gamma}^\zeta$ up to the remaining

[6] Note that we have to understand $I_1^\zeta(s \to iz)$ as the analytic continuation of the integral (6.25), which in most cases is only known numerically. Fortunately, we need this expression merely on a formal level to estimate the errors, whereas performing the analytic continuation numerically is not required.

uncertainty on the order of $E_1^\zeta$. Finally, following the same arguments that have led from eq. (6.28) to eq. (6.29), we obtain for the total error

$$E_2^\zeta(\tau) = e^{(-\beta_s+|\tau|)R^{(2)}} F_2^\zeta(\tau, R^{(2)}) + E_{2,\Gamma}^\zeta(\tau)\,, \tag{6.35}$$

where the $F_2^\zeta(\tau, R^{(2)})$ denotes a well-defined, bounded function, that cannot overcome the exponential prefactor. Taking both terms into account we conclude that we again obtain an exponentially small error for $|\tau| < \beta_s$.

Due to the dependence $\beta_\omega, \beta_s \sim N$ the total error $|E_1^\zeta(s) + E_2^\zeta(\tau)|$ vanishes exponentially with $N \to \infty$, provided the relations $\beta_\omega > |s_N|$ and $\beta_s > |\tau_N|$ hold. Furthermore, we determine the overall rate of the exponential convergence as

$$R = \min(R^{(1)}, R^{(2)})\,. \tag{6.36}$$

Moreover, the conditions on $\beta_\omega$ and $\beta_s$ can in principle always be satisfied by an appropriate choice of the grid parameters in eq. (6.10). Finally, we reemphasize that the choice of $k_p$ is quite important, as it also controls the size of the contribution to $E_2^\zeta(\tau)$ from the proximity of the contour to the poles of the Gamma function via the Bose prefactor. We will see in the next section how the numerical results can be improved by subtracting this additional contribution.

### 6.1.3 Optimal parameter settings

Having shown that one can achieve exponentially fast convergence of the numerical approximation of the LFT towards the exact expression, we now address the issue of how the transformation parameters can be optimally chosen and how many grid points are necessary to obtain a predefined precision. We postpone the effect of round-off errors due to a finite floating point precision to the end of the section and focus first on the error sources specific to the LFT. First of all, we have to consider uncertainties arising from discretizing the integrals, which leads to the expressions $E_1^\zeta(s)$ and $E_2^\zeta(\tau)$ in eqs. (6.24) and (6.32). Further errors arise from truncating the resulting sums to a finite interval.

In this section we focus on the class of algebraic functions, whose integrability depends on a suitably choice of the trade-off parameter $k_p$. On the other hand, if the function scales exponentially in any of the limits $\zeta\nu \to 0$ or $\zeta\nu \to \zeta\infty$, its transformation properties cannot be improved by $k_p$ and we will only be able to compute the Fourier transform, if the exponential behavior on its own gives rise to a decreasing function, according to eq. (6.17). In this case we can discard the corresponding limitations on $k_p$ derived in eq. (6.8). However, one should keep in mind that $k_p \gg 1$ will pose problems for the numerics, due to the algebraic growth $\simeq |s|^{k_p}$ in eq. (6.31) and should be avoided. Returning to algebraic functions, the optimal trade-off parameter

$$k_{\text{opt}} = 1 + \frac{a+b}{2} \tag{6.37}$$

renders the tails of $f(\zeta \exp(\omega)) \exp((1-k_p)\omega)$ symmetric for $\omega \to \pm\infty$ and therefore leads to the minimal truncation errors at both ends of the sampled interval. If we demand the truncation errors to be of order $\epsilon \ll 1$, i.e $|f(\zeta \exp(\omega_{1,N})) \exp((1 - k_p)\omega_{1,N})| \leqslant \epsilon$ we find the condition

$$\Delta\omega\, N = \frac{4}{b-a} \log(\epsilon)\,, \tag{6.38}$$

by inserting the asymptotic forms $|f(\zeta e^{\omega})| \simeq \exp(a\omega)$ for $\omega \to -\infty$ and $|f(\zeta e^{\omega})| \simeq \exp(b\omega)$ for $\omega \to \infty$. From the general theory of Fourier transformations [164], it follows that $S_1^{\zeta}(s) \simeq \exp(-R^{(1)}|s|)$, due to the analytic properties of the integrand in eq. (6.25). However, since the difference between sum and integral gives rise to the error $E_1^{\zeta}(s) \simeq \exp(-\beta_\omega R^{(1)} + |s|R^{(1)})$ from eq. (6.24), it only makes sense to include values $|s| < s_{\max} = \beta_\omega/2 = \pi/\Delta\omega$, because for larger $s$ the function $S_1^{\zeta}(s)$ has already fallen below the error. To be consistent, we require the same truncation error of order $\epsilon$ for the sum over $l$ in (6.11), that is $|S_1^{\zeta}(s_{\max})| \simeq \exp(-R^{(1)} s_{\max}) < \epsilon$. With the given value of $s_{\max}$ we eventually obtain the minimally necessary number of points

$$\Delta\omega = -\frac{\pi R^{(1)}}{\log \epsilon} \tag{6.39a}$$

$$N = \frac{4}{(a-b)\pi R^{(1)}} \left(\log \epsilon\right)^2 . \tag{6.39b}$$

Consequently, the number of points and their inverse density grow only logarithmically with increasing precision $\epsilon \to 0$. In the case of a different $k_p \neq k_{\text{opt}}$ the scaling remains unaltered but with larger prefactors. Below, we discuss a scenario, where such a configuration of the transformation, nevertheless, might be useful.

So far we have only considered the transformation from $\omega \to s$. However, one might suspect that an exponentially small error $E_2^{\zeta}(\tau)$ requires a very small $\Delta s \ll 1$, such that $N$ actually becomes larger than the estimate (6.39b). The width of the strip $R^{(2)}$ is determined by the closest nonanalyticity of $S_1^{\zeta}(s)$ in the complex $s$ plane. Using $k_{\text{opt}}$ from eq. (6.37) yields $R^{(2)} = (a-b)/2$, according to the discussion below eq. (6.26). In analogy to the argument for $s_{\max}$, we conclude from the asymptotics of $I_2^{\zeta}(\tau) \sim \exp(-R^{(2)}\tau)$ and the error $E_2^{\zeta}(\tau) \sim \exp((-\beta_s + |\tau|)R^{(2)})$ that the evaluation of the LFT only makes sense for $|\tau| \leqslant \tau_{\max} = \beta_s/2 = \pi/\Delta s$. Demanding that the error $E_2^{\zeta}(\tau)$ does not degrade the overall accuracy $\epsilon$, that is $|E_2^{\zeta}(\tau_{\max})| \simeq \exp(-\beta_s R^{(2)}/2) \leqslant \epsilon$, yields

$$\Delta s = -\frac{\pi R^{(2)}}{\log \epsilon} = \frac{\pi(b-a)}{2\log \epsilon}\,, \tag{6.40}$$

which scales in a similar manner as $\Delta\omega$ in (6.39a) with $1/\log\epsilon$. Note that the restriction on $\tau_{\max}$ does not severely limit the transformation, as $\tau_{\max} \sim |\log \epsilon|$ and thus $t_{\max} \sim 1/\epsilon$ covers a considerable range of times up to the inverse precision.

Furthermore, recall that $R^{(2)}$ only takes into account the analytic properties of $S_1^\zeta(s)$. Apart from them, $E_2^\zeta(\tau)$ in equation (6.32) also contains the contributions arising from the poles of the Gamma function $E_{2,\Gamma}^\zeta(\tau)$ (6.34). After the final multiplication with $\exp(-k_p\tau)$ (see Def. (6.9)), the pole at $-m$ gives rise to the exponential behavior

$$a_m \frac{(-1)^m}{m!} \frac{(i\zeta\eta)^m}{e^{2\pi|k_p+m|/\Delta s}-1} e^{m\tau}\,, \tag{6.41}$$

which is known up to a single numerical prefactor $a_m$. This behavior entails an option to further reduce the numerical uncertainties of the LFT, if some knowledge about the expected asymptotics of $\hat{f}$ is available. In the standard case of a function $\hat{f}(\tau \to \tau_{\max}) \to 0$, we start with the smallest value of $m$, which we fit to the $\tau \to \tau_{\max}$ asymptotics of $\hat{f}(\eta\exp(\tau))$. This is possible, if in the regime of the largest $\tau$-values that have been taken into account, the function has decayed and merely errors remain. Usually this is revealed by a sudden change of $f(\tau \to \tau_{\max})$ to a more slowly decay, which cuts off the mathematically correct behavior. To obtain the latter one needs a better cancellation of the numerical terms, which in turn requires to extend the grid beyond $\omega_{\max}$. Subsequently, we can subtract the fit, before increasing $m$ by one and repeating the procedure. This can continued until either $m$ runs out of the bounds of the sums in $E_{2,\Gamma}^\zeta(\tau)$ or if the result $\sim \exp(-m\tau_{\max})$ has become negligible. If the function carries too much information in the the limit $\tau \to \tau_{\max}$, which can happen in the case of generalized Fourier transformations, one can also try to eliminate the contributions from the $\Gamma$ function from the intermediate stage in eq. (6.9), before multiplying with $\exp(-k_{\text{opt}}\tau)$. At this level one has computed the Fourier transformation of an integrable function, which necessarily satisfies the Riemann-Lebesgue Lemma, and thus approaches zero for large enough $\tau$ values. Our LFT configuration for the imbalanced Fermi gas automatically subtracts the leading two poles from the final result, since the encountered functions always decay sufficiently fast.

Up to now, round-off errors due to finite numerical precision have been entirely ignored in the current discussion. In fact the discussed parameter choices give rise to an accuracy $\hat{f}(\zeta\exp(\tau)) \simeq \epsilon\exp(-k_{\text{opt}}\tau)$, where the exponential factor arises from the final multiplication of the LFT method in eq. (6.9). A simple example, that reveals the influence of round-off errors, is encountered for negative $k_p$ in the limit of large $\tau \gg 1$. In general, we can write the result of the LFT in the form $\hat{f}(\eta\exp(\tau)) = \exp(-k_{\text{opt}}\tau) f_{\text{red}}(\eta,\tau)$, where the reduced function $f_{\text{red}}$ is integrable and vanishes in the limit $\tau \to \infty$, due to the Lemma of Riemann-Lebesgue for Fourier transformations. From a numerical perspective, however, this decay is cut off at $\tau_{\text{cut}}$, independently of the truncation errors, when the asymptotics of $f_{\text{red}}$ hits the threshold of the precision $\delta$ of the internal operations (typically machine precision), i.e. $|f_{\text{red}}(\eta,\tau_{\text{cut}})| = \delta$. For $\tau > \tau_{\text{cut}}$ the correct decrease is replaced by noise on the level of $\delta$. Multiplication with the exponential factor then gives rise to an erroneous exponential growth $\sim \delta\exp(|k_{\text{opt}}\tau|)$. Thus, the LFT can only access

$\tau$-values smaller than $\tau_{\text{cut}}$. As the exact function decays in this limit anyway, no relevant information is contained in the asymptotics and this restriction on the image space does not limit the quality of the results. A more severe problem appears, if the function is not integrable for $\nu \to \infty$ and therefore requires $k_p > 0$. In this case the enhanced round-off errors emerge for $\tau \to -\infty$, which is equivalent to the origin in the time-domain. In fact, the larger $b > -1$, the worse are the integrability properties of $f$. A larger $b$, indeed, automatically yields a more pronounced dynamic compression, which means that the interval of $\tau$ values, where the result can be distinguished from the errors, that is $|\hat{f}(\eta \exp(\tau))| > \epsilon \exp(-k_p \tau)$, shrinks with growing $b$, since $k_p$ necessarily has to be increased to guarantee the existence of the LFT, according to (6.8).

One solution to this problem is to continue the function from the regime of trustworthy $\tau$ values towards $\tau \to -\infty$. This can be achieved either by extrapolating the reliable data directly or if possible by fitting the data to a known analytic form. Another solution, which, however, requires more computational resources, is to repeat the computation with different values of the trade-off parameter. Thereby one resolves a different interval in the time-domain for each value of $k_p$. The complete function $\hat{f}(\eta t)$ is then obtained by combining the results. To keep the truncation errors on the order of $\epsilon$ additional grid points must be included, such that (6.39b) is no longer satisfied. In this situation one can make use of the shifts $\bar{\omega}$ and $\bar{s}$ to rearrange the grids for an optimal sampling of the tails. To estimate the new values of $N$ and $\bar{\omega}$ we take $\Delta\omega$ from eq. (6.39a) in order to obtain the same error estimate from the truncation of $S_1^{\zeta}(s)$ and demand that $|f(\zeta \exp(\omega_{\pm N})) \exp((1-k_p)\omega_{\pm N})| < \epsilon$ for an arbitrary, but allowed $k_p$. Using the most general form of the $\omega_n$ grids from (6.10) together with the asymptotics $f(\zeta e^{\omega}) \sim \exp(a\omega), \exp(b\omega)$ yields

$$\bar{\omega} = \frac{\log \epsilon}{(1 + a - k_p)\Delta\omega} \tag{6.42a}$$

$$N = \frac{b - a}{(1 + b - k_p)(1 + a - k_p)\pi R^{(1)}} \left(\log(\epsilon)\right)^2 . \tag{6.42b}$$

Note that this choice of the parameters reduces to $\bar{\omega} = -N/2$ and $N$ given by eq. (6.39b), if the optimal trade-off parameter $k_{\text{opt}} = 1 + (a + b)/2$ is inserted.

### 6.1.4 Examples

After having discussed the theoretical properties of the LFT, we will now consider two examples of physical interest. Many more examples and the application to convolutions can be found in Ref. [160]. First of all, we study the LFT of a function that mimics the tail of the fermionic Green's function in the problem of the imbalanced Fermi gas $\mathcal{G}_{\sigma\sigma}(|\mathbf{k}| \to \infty, \tau = 0^-) \to \mathcal{C}/k^4$. To this end, we define

$$f_1(\nu) = \frac{1}{1 + \nu^4} , \tag{6.43}$$

which can be Fourier transformed analytically with the three-dimensional transformation (4.16) to

$$\hat{f}_1(t) = \frac{\sin\left(\frac{t}{\sqrt{2}}\right)}{4\pi t} e^{-\frac{t}{\sqrt{2}}} . \tag{6.44}$$

Including the additional factor of $\nu$ from the integration measure, we deduce the coefficients $a = 1$, $b = -3$ for the asymptotics, such that the optimal trade-off parameter reads $k_{\text{opt}} = 0$. To avoid the poles of the $\Gamma$ function, we instead use $k_p = -0.2$. Due to the poles at $\nu = \pm\sqrt{\pm i}$, the analytic region has a width of $R = \pi/4$ in the logarithmic argument $\omega$. Demanding a precision $\epsilon = 10^{-12}$ from the truncation errors, we obtain from the estimates in eq. (6.39) $N = 310$ and $\Delta\omega = 0.09$, which corresponds to $\omega_N = 13.95$. Since these numbers are simple estimates, we choose slightly more conservative values $N = 325$ and $\Delta\omega = 0.08$, to guarantee a sufficient sampling density. Furthermore, we shift the grid of $\omega$ points by $\bar{\omega} = -N/2 + 1.5$, such that the maximal exponent is 14.5. The remaining parameters of the transformation read $\Delta s = 0.22$ and $\Delta\tau = 0.08$, while the other shifts of the grids are set to the standard choice $\bar{s} = -N/2 = \bar{\tau}$. Because of the form of the error $E_2^{\zeta}(\tau)$ given in eq. (6.32) we expect a large contribution from the pole of the $\Gamma$ at $m = 0$, since $k_p = -0.2$ does not give rise to a strong exponential suppression. To improve our result, we subtract the last $\tau$-point, which corresponds to the form of this error after multiplying with $\exp(k_p\tau)$ according to the LFT prescription (6.9). In Fig. 6.2 we compare the LFT result (black) to the exact expression (red) and show the deviation in blue. The latter turns out to be suppressed by at least seven orders of magnitude in comparison to $\hat{f}_1(t)$. The error starts to take over, once $t$ is large enough, such that the exponential factor dominates the exact result of (6.44). However, this happens just when $\hat{f}_1(t)$ has dropped below the $10^{-15}$ level.

To further demonstrate the capability of the LFT, let us also discuss the related example

$$f_2(\nu) = \frac{1}{1+\nu^2} \tag{6.45}$$

in $d = 3$, too, which is nonintegrable but can be Fourier transformed to a Yukawa potential with the decay constant set to one

$$\hat{f}_2(t) = \frac{e^{-t}}{4\pi t} . \tag{6.46}$$

From the three-dimensional asymptotics we have $a = 1$ and $b = -1$. According to the condition (6.8), a trade-off parameter $k_p$ between zero and one makes the function amenable to an application of the LFT. In particular, we conclude the optimal value for the trade-off parameter $k_{\text{opt}} = 1$. Fig. 6.3 shows the result for $N = 800$ points compared to the exact solution. The other parameters are:

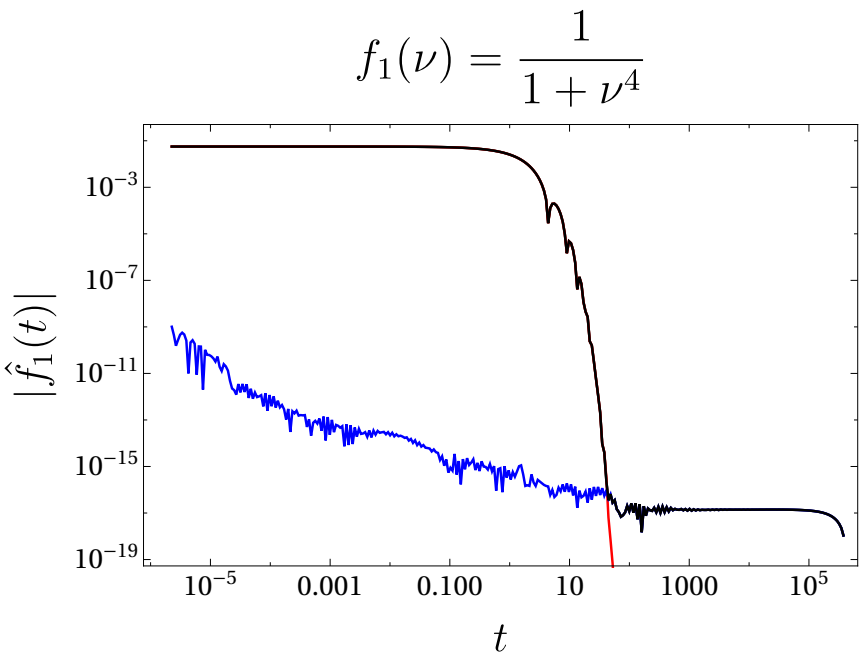


Figure 6.2: Comparison between the LFT output (black) with the exact result (6.44)(red) and the difference between them (blue).

$\Delta\omega = 0.08$, $\Delta\omega = 0.05 = \Delta\tau$, while for the shift variables $\bar{s}$ and $\bar{\tau}$ the value $-N/2$ has been assigned. In this example we have furthermore used two values for the trade-off parameter: $k_p = 1$ with $\bar{\omega} = -N/2$ and $k_p = 0.7$ with $\bar{\omega} = -N/2 + 10$ to reveal the role of $k_p$. The shift in the $\omega$ grid establishes the same truncation errors in order to obtain a valid comparison. In total, we obtain the same features as in the previous example. The $1/t$ decay is very well described by the LFT. The error only dominates for $t \gtrsim 20$, where $\hat{f}_2(t)$ has already decreased below values of $10^{-17}$. The two choices of the trade-off parameter indeed reveal the effect on the convergence properties, that we have discussed earlier: The smaller $k_p$ decreases the error at small $t$, while at large $t$ the error becomes enhanced compared to the optimal choice, as stated earlier. All in all, we conclude that LFT is able to transform also nonintegrable functions with very small errors at a grid size which does not exceed the grid of the previous integrable case by far.

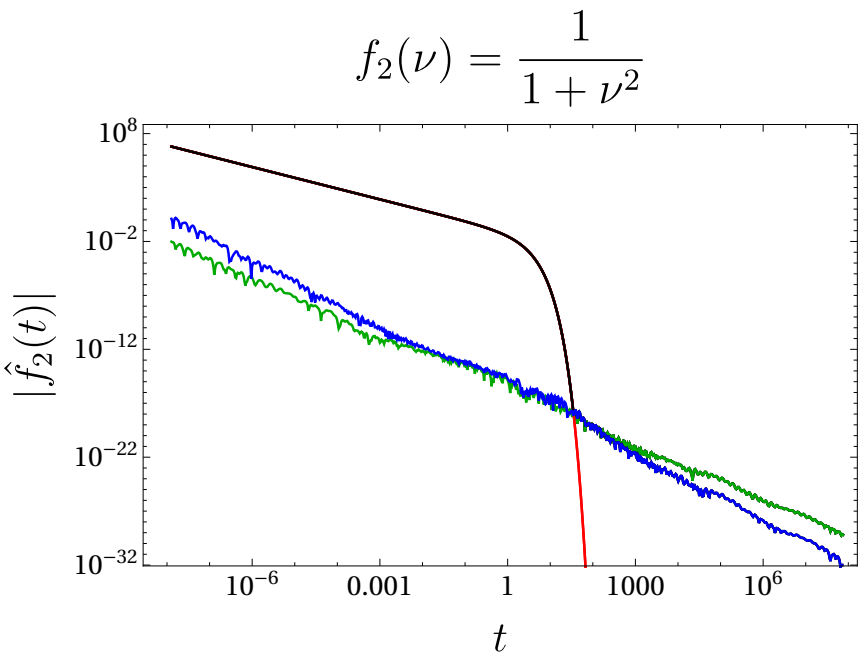


Figure 6.3: Comparison between the LFT output (black) with the exact result (6.46)(red) and the deviations for $k_p = k_{\text{opt}}$ (blue) and $k_p = 0.7$ (green).

## 6.2 Discrete Fourier Transformation (DFT)

As we have discussed in the previous section, we cannot treat every Fourier transformation in the problem of the imbalanced Fermi gas with the LFT. If we have to compute a Fourier series between Matsubara frequencies and imaginary time or a Fourier integral with prominent features on intermediate scales like the Fermi level in the weak coupling limit, that satisfies at low temperatures $1 \ll \beta\mu_\sigma \ll \beta\varepsilon_{k_{\max}}$ or $Q_{\text{FFLO}} \simeq k_F$, we instead apply a DFT in combination with a spline interpolation. We use splines of third and fifth order. In the following, we set up the general construction of a spline interpolation in Sec. 6.2.1, where we focus on quintic splines, before we combine them with the Fourier transformation in Sec. 6.2.2.

The general form of the two cases under consideration read

$$\hat{f}(t) = \sum_{n\in\mathbb{Z}} e^{-it\nu_n} f(\nu_n) \tag{6.47a}$$

$$\hat{f}(t) = \int_{-\infty}^{\infty} \frac{d\nu}{2\pi} e^{-it\nu} f(\nu)\,, \tag{6.47b}$$

where the $\nu_n\,, n \in \mathbb{Z}$ form a set of equidistant frequencies, like the Matsubara

frequencies. Furthermore, we have seen in Chap. 4 that the Green's and the vertex function possess algebraic tails, which arise from the bare Green's function $\mathcal{G}^{(0)}_{\sigma\sigma}(\mathbf{k}, \omega_n)$ in eq. (4.9) and the lowest order pair propagator $M(\mathbf{Q}, \Omega_n)$ in eq. (4.33). Therefore, we again have to consider functions $f(\nu)$ that vary slowly over several orders of magnitude. To sample them properly with a grid of feasible size $N$ we have to choose a subset $\{\nu_j\}_{1\leqslant j\leqslant N} \subset \{\nu_n\}_{n\in\mathbb{Z}}$ with exponentially growing distance $(\nu_{j+1} - \nu_j)$ for $|m| \gg 1$, that sufficiently covers both the limits $\nu_n \to 0$ and $|\nu_n| \to \infty$, in analogy to the LFT. For the Fourier integral the same grid construction applies, yet we can freely select the points in the integration grid as long as we include enough points to sample the asymptotically important scales. To improve the numerical results of the transformations we use the spline interpolation to bridge the gap between the missing $\nu_n$ or equivalently the large distances between neighboring grid points for the integral.

### 6.2.1 Creation of a quintic spline

We state first the general framework of spline interpolations before we focus on fifth order splines. For the construction of cubic splines, we refer the reader to the textbook by Ahlberg et al. [166]. To construct the spline we assume that the pairs of frequencies and function values $(\nu_j, f_j = f(\nu_j))$, with $1 \leqslant j \leqslant N$, are given. The corresponding spline interpolation corresponds to a set of $N-1$ piecewise polynomials $S_{1\leqslant j\leqslant N-1}(\nu)$, where $S_j(\nu)$ is defined on the interval between $\nu_j$ and $\nu_{j+1}$. At the boundaries of these intervals one imposes continuity conditions on the $S_j(\nu)$ to obtain a smooth function. More precisely, one writes

$$S_j(\nu) = \sum_{l=0}^{l_{\max}} a_j^{(l)} (\nu - \nu_j)^l \,, \tag{6.48}$$

where $l_{\max}$ gives the spline order, which in our case is $l_{\max} = 3$ or $l_{\max} = 5$. The $(N-1)(l_{\max}+1)$ spline coefficients $a_j^{(l)}$ can be determined from the continuity conditions. The first of them demands that the spline indeed interpolates the available function values, that means for $1 \leqslant j \leqslant N-1$

$$S_j(\nu_j) = f_j \quad \Rightarrow \quad a_j^{(0)} = f_j \tag{6.49a}$$

$$S_{N-1}(\nu_N) = f_N \,. \tag{6.49b}$$

Furthermore, one requires the spline to be as smooth as possible, which gives rise to boundary conditions for the derivatives at the $\nu_{2\leqslant j\leqslant N}$. In the application to Fourier transformations the smoothness helps to suppress artifacts in $\hat{f}(t)$, which arise from the discontinuities of some higher order derivative at the interpolation points. The corresponding equations for the derivatives read

$$\frac{d^k}{d\nu^k} S_{j+1}(\nu_{j+1}) = \frac{d^k}{d\nu^k} S_j(\nu_{j+1}) \,, \tag{6.50}$$

with $k \in \{0, 1, ..., l_{\max} - 1\}$ and $2 \leqslant j \leqslant N - 1$. These conditions imply for the polynomials (6.48)

$$k!\, a_{j+1}^{(k)} = \sum_{l=k}^{l_{\max}} a_j^{(l)} (\Delta\nu_j)^{l-k} \frac{l!}{(l-k)!}\,, \tag{6.51}$$

where we also have introduced $\Delta\nu_j = \nu_{j+1} - \nu_j$, which is a special instance of the difference operator

$$\Delta(\cdot)_j := (\cdot)_{j+1} - (\cdot)_j\,. \tag{6.52}$$

Altogether, eqs. (6.49a) and (6.50) entail $N + l_{\max}(N-2)$ constraints, such that $l_{\max} - 1$ spline coefficients remain undetermined. To compensate for the missing information one has to add boundary conditions on the spline at $\nu_1$ and $\nu_N$. One possibility are "clamped" splines[7] that are defined by equating the first $(l_{\max}-1)/2$ derivatives of the actual function and the spline at the endpoints $\nu_1$ and $\nu_N$

$$\frac{d^k}{d\nu^k} S_1(\nu_1) = \frac{d^k f}{d\nu^k}(\nu_1) \tag{6.53a}$$

$$\frac{d^k}{d\nu^k} S_{N-1}(\nu_N) = \frac{d^k}{d\nu^k} f(\nu_N)\,, \tag{6.53b}$$

with $1 \leqslant k \leqslant (l_{\max} - 1)/2$. We will come to the special implementation of the boundary conditions for our spline DFT below.

The general strategy to solve for the spline coefficients is to find a linear set of equations for the second highest coefficient $a^{(l_{\max}-1)}$, whose solution allows to determine the remaining coefficients. We present this procedure for quintic splines, which are less frequently applied. First, we use eq. (6.51) with the maximally allowed $k = l_{\max} - 1 = 4$ to eliminate the coefficient of the highest order

$$a_j^{(5)} = \frac{\Delta a_j^{(4)}}{5\Delta\nu_j} = \frac{g_j^{(0)}}{\Delta\nu_j}\,, \tag{6.54}$$

which can be written in this compact way by the help of the difference operator (6.52) and the auxiliary function $g_j^{(0)}$. In the following, we will introduce more of them. They share the common features, which can easily verified in the case of $g_j^{(0)}$, that they all depend *linearly* on the set of variables $\{a_j^{(4)}\}$ and in addition only include the given set of step widths $\{\Delta\nu_j\}$ between adjacent frequencies of the grid.

[7] In fact, the choice of boundary conditions does not matter, if the grid has been chosen appropriately. Either the function becomes negligibly small, which happens e.g. for $|\omega_n| \to \infty$ or we sample the boundary with a high enough density of grid points like at the borders of imaginary time interval $\tau \to 0^+$ or $\beta^-$. In contrast, a dependence on the boundaries indicates that the grid truncates important frequency scales or undersamples the function. Therefore, we are not forced to compute the derivatives of $f$ at $\nu_1$ and $\nu_N$, which are necessary for clamped splines, with a high numerical precision.

Next, we use the continuity equation, equivalent to the $k = 0$ version of eq. (6.51), to solve for the lowest order unknown coefficient

$$a_j^{(1)} = \frac{\Delta a_j^{(0)}}{\Delta \nu_j} - a_j^{(2)} \Delta \nu_j - a_j^{(3)} \Delta \nu_j^2 - g_j^{(1)} \Delta \nu_j^3 \,, \tag{6.55}$$

with the new auxiliary function

$$g_j^{(1)} = a_j^{(4)} + g_j^{(0)} \,. \tag{6.56}$$

Notice that $g_j^{(1)}$ indeed is a linear function of the $\{a_j^{(4)}\}$ and apart from that only depends on the frequency points. Now we can use the smoothness of the first derivative (from eq. (6.51) with $k = 1$) in the form

$$\Delta a_j^{(1)} = 2a_j^{(2)} \Delta \nu_j + 3a_j^{(3)} \Delta \nu_j^2 + 4a_j^{(4)} \Delta \nu_j^3 + 5g_j^{(0)} \Delta \nu_j^3 \tag{6.57}$$

to remove $a_j^{(1)}$ from the equations. To this end, we apply the $\Delta$-operator to the continuity equation (6.55) and insert eq. (6.57), which yields

$$\begin{aligned} a_{j+1}^{(2)} \Delta \nu_{j+1} + a_j^{(2)} \Delta \nu_j = \Delta \left( \frac{\Delta a_j^{(0)}}{\Delta \nu_j} \right) - \Delta (a_j^{(3)} \Delta \nu_j^2) - 3a_j^{(3)} \Delta \nu_j^2 \\ - 4a_j^{(4)} \Delta \nu_j^3 - 5g_j^{(0)} \Delta \nu_j^3 - \Delta \left( g_j^{(1)} \Delta \nu_j^3 \right) \,. \end{aligned} \tag{6.58}$$

Now we have to eliminate $a_j^{(2)}$ in the last equation. To do so, we first replace $a_{j+1}^{(2)}$ with $a_j^{(2)}$ by the help of the relation (6.51) for the second derivative ($k = 2$)

$$a_{j+1}^{(2)} = a_j^{(2)} + 3a_j^{(3)} \Delta \nu_j + 6a_j^{(4)} \Delta \nu_j^2 + 10g_j^{(0)} \Delta \nu_j^2 \tag{6.59}$$

and then solve (6.58) for $a_j^{(2)}$. We obtain

$$a_j^{(2)} = \frac{\Delta \left( \frac{\Delta a_j^{(0)}}{\Delta \nu_j} \right)}{\Delta \nu_{j+1} + \Delta \nu_j} - 3a_j^{(3)} \Delta \nu_j - \frac{\Delta \left( a_j^{(3)} \Delta \nu_j^2 \right)}{\Delta \nu_{j+1} + \Delta \nu_j} - \frac{1}{\Delta \nu_{j+1} + \Delta \nu_j} g_j^{(2)} \,, \tag{6.60}$$

where we have defined

$$g_j^{(2)} = 2a_j^{(4)} \Delta \nu_j^2 \left( 2\Delta \nu_j + 3\Delta \nu_{j+1} \right) + 5g_j^{(0)} \Delta \nu_j^2 \left( \Delta \nu_j + 2\Delta \nu_{j+1} \right) + \Delta \left( g_j^{(1)} \Delta \nu_j^3 \right) \,. \tag{6.61}$$

The next step is to get rid of $a_j^{(3)}$. Using the latter two equations to determine $\Delta a_j^{(2)}$, which we equate with the expression for $\Delta a_j^{(2)}$ from the constraint on the

second derivative (6.59), gives rise to the relation

$$\begin{aligned} 3a_{j+1}^{(3)}\Delta\nu_{j+1} + \Delta\left[\frac{a_{j+1}^{(3)}\Delta\nu_{j+1}^2 - a_j^{(3)}\Delta\nu_j^2}{\Delta\nu_{j+1}+\Delta\nu_j}\right] = \\ = \Delta\left[\frac{\Delta\left(\frac{a_j^{(0)}}{\Delta\nu_j}\right)}{\Delta\nu_{j+1}+\Delta\nu_j}\right] - 6a_j^{(4)}\Delta\nu_j^2 - 10g_j^{(0)}\Delta\nu_j^2 - \Delta\left(\frac{g_j^{(2)}}{\Delta\nu_{j+1}+\Delta\nu_j}\right), \end{aligned} \tag{6.62}$$

that merely depends on the sets of $\{a_j^{(3)}\}$ and $\{a_j^{(4)}\}$. To find an expression for the coefficient $a_j^{(3)}$ of the cubic term in the spline, we shift all the appearing indices to $j$, which can be accomplished with the continuity of the third derivative from eq. (6.51), with $k = 3$

$$a_{j+1}^{(3)} = a_j^{(3)} + 4a_j^{(4)}\Delta\nu_j + 10g_j^{(0)}\Delta\nu_j\,. \tag{6.63}$$

Note that we have to perform this replacement twice for the second term on the left-hand side of eq. (6.62). Finally, we get

$$a_j^{(3)} = \frac{\Delta\left[\frac{\Delta\frac{\Delta a_j^{(0)}}{\Delta\nu_j}}{\Delta\nu_{j+1}+\Delta\nu_j}\right]}{\Delta\nu_{j+2}+\Delta\nu_{j+1}+\Delta\nu_j} - \frac{1}{\Delta\nu_{j+2}+\Delta\nu_{j+1}+\Delta\nu_j}g_j^{(3)}\,, \tag{6.64}$$

where we have introduced one last function

$$\begin{aligned} g_j^{(3)} =& 6a_j^{(4)}\Delta\nu_j(2\Delta\nu_{j+1}+\Delta\nu_j) + 10g_j^{(0)}\Delta\nu_j(3\Delta\nu_{j+1}+\Delta\nu_j) \\ &+ \Delta\left[\frac{1}{\Delta\nu_{j+1}+\Delta\nu_j}\left((4a_j^{(4)}\Delta\nu_j + 10g_j^{(0)}\Delta\nu_j)\Delta\nu_{j+1}^2 + g_j^{(2)}\right)\right]. \end{aligned} \tag{6.65}$$

Having come this far, we are now in the position to formulate the central equation, whose solution determines the $a_j^{(4)}$. To this end, we use eq. (6.64) to compute $\Delta a_j^{(3)}$, which we set equal to same expression obtained from eq. (6.63). This yields

$$4a_j^{(4)}\Delta\nu_j + 10g_j^{(0)}\Delta\nu_j + \Delta\left[\frac{g_j^{(3)}}{\Delta\nu_{j+2}+\Delta\nu_{j+1}+\Delta\nu_j}\right] = \underbrace{\Delta\left[\frac{\Delta\left[\frac{\Delta\frac{\Delta a_j^{(0)}}{\Delta\nu_j}}{\Delta\nu_{j+1}+\Delta\nu_j}\right]}{\Delta\nu_{j+2}+\Delta\nu_{j+1}+\Delta\nu_j}\right]}_{=:b_j}, \tag{6.66}$$

which constitutes a linear set of equations for the $a_j^{(4)}$ in terms of the distances between the grid points and the known function values $a_j^{(0)}$ on the right-hand side. Writing out the recursive definitions of the subsidiary functions gives rise to a lengthy expression, which, however, can be easily handled on a computer. A close inspection additionally reveals that equation (6.66) couples the five indices $j$ to $j+4$. This statement, in fact, holds for an arbitrary $2n+1$ order spline, since one can, at least formally, continue the procedure to use the solution for $a_j^{(l)}$ to determine an equation for the next spline coefficients of order $l+1$. Like in the scheme presented above, one first computes $\Delta a_j^{(l)}$ from the equation for $a_j^{(l)}$, which has to match the the corresponding $l^{\text{th}}$ continuity condition. The subsequent application of the difference operator always increments the number of coupled grid indices by one. From the right-hand side of eq. (6.66) one can estimate the form of the continued fraction generated by this procedure, however, writing down the subsidiary functions $g_j^{(l)}$ for the left-hand side remains a non-trivial task. In contrast, in the simpler case of a cubic spline one has only three coupled coefficients.

We now turn to the boundary conditions, which complete the set of equations required to determine the spline completely. So far, the expression (6.66) constitutes $N-5$ linear equations for the $N-1$ coefficients $a_j^{(4)}$. To obtain the missing four relations we impose the set of convenient conditions on the forth derivative of the spline

$$S_1^{(4)}(\nu_1) = S_2^{(4)}(\nu_2) = 0 = S_{N-1}^{(4)}(\nu_{N-1}) = S_{N-1}^{(4)}(\nu_N)\,. \tag{6.67}$$

We choose these simple constraints, which are easily implemented, since the form of the spline interpolation at the borders of the sampled interval and in particular deviations between the spline and the exact function at the level of the fourth derivative have no notable influence on the Fourier sums or integrals, provided the grid samples the boundaries sufficiently. Therefore, the specific choice of the conditions, is not important. We will return to this issue in Sec 7.4, where we give the concrete numerical grids. Translating the latest equations to the form of eq. (6.66), we have

$$\begin{aligned} 4\Delta\nu_1 a_1^{(4)} &= 0 \\ 4\Delta\nu_2 a_2^{(4)} &= 0 \\ 4\Delta\nu_{N-1} a_{N-1}^{(4)} &= 0 \\ 4\Delta\nu_{N-1} a_N^{(4)} &= 0\,, \end{aligned} \tag{6.68}$$

where the role of the seemingly unnecessary prefactors will be explained in a moment. Furthermore, we have defined the fourth derivative at $\nu_N$ via $a_N^{(4)} = 4!(a_{N-1}^{(4)} + 5g_{N-1}^{(0)}\Delta\nu_{N-1})$, such that we can write the equations (6.66) and (6.68)

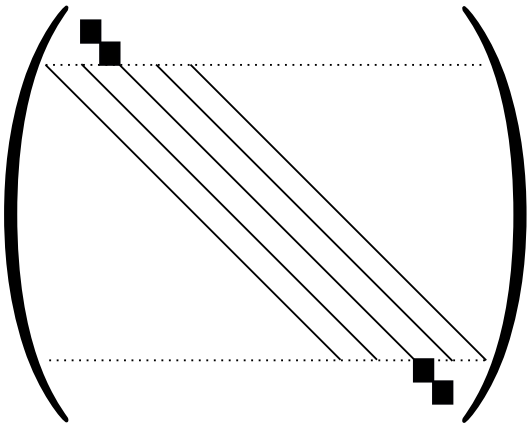

Figure 6.4: Band matrix with five non-zero diagonals. The components between the dotted lines follow from eq. (6.66), while the four black squares on the main diagonal represent the boundary conditions (6.68). Empty spots are zero.

in terms of the standard form of a linear system of equations

$$\sum_{j=1}^{N} (\underline{A})_{i,j}\, a_j^{(4)} = b_j\,. \tag{6.69}$$

The first two equations are given by the two boundary conditions at $\nu_1$ and $\nu_2$, while the last two lines of this system follow from the remaining two boundary conditions. In this form we have to deal with a pentadiagonal matrix, which is pictorially presented in Fig. 6.4. This formulation extends the more-frequently used case of a cubic spline, where the corresponding system can be written in terms of a tridiagonal matrix. To implement the spline in the code for the imbalanced Fermi gas, where we have to recompute the interpolation after every update that $G$ and $\Gamma$ acquire from the self-consistent loop, it is crucial to rewrite the solution to the linear system in the following form

$$a_j^{(4)} = \sum_{i,l=1}^{N} \left(\underline{A}^{-1}\right)_{jl} (\underline{B})_{lk}\, a_k^{(0)}\,. \tag{6.70}$$

Here we have introduced a new matrix $\underline{B}$ via $b_i = \sum_i (\underline{B}_{ij}) a_j^{(0)}$, since the right-hand side of (6.66) depends only linearly on the function values $a_j^{(0)} = f_j$. As $\underline{A}$ and $\underline{B}$ only contain the given distances $\Delta\nu_j$ it suffices to invert $\underline{A}$ only once during the initialization step, provided we use a fixed grid. Subsequently we calculate the matrix product $\underline{A} \cdot \underline{B}$ also just once. Then the computation of the spline coefficient reduces to a matrix times vector operation of standard $\mathcal{O}(N^2)$ complexity, which therefore does not degrade the general scaling of a standard DFT. Apart from

the aspect of efficiency this also allows us to compute the interpolation matrices with an enhanced precision of 40 digits. This is important to obtain the inverse of $\underline{A}$ without large numerical uncertainties, since $\underline{A}$ contains the $\Delta\nu_j$, which cover many orders of magnitude. Once the set of the $a_j^{(4)}$ has been determined, the other coefficients follow from backward insertion into the equations (6.54), (6.64), (6.60) and (6.55). However, as we will see in the next section, the DFT does not even require the entire set of coefficients.

### 6.2.2 Spline-based DFT

With the interpolation described in the previous subsection we can now proceed and compute the Fourier series or integral (6.47). Numerically, we can find a unique expression, which approximates both of them

$$\hat{f}(t) = \sum_{j=1}^{N} \sum_{n=j}^{j+1} \Delta\nu e^{-it\nu_n} f(\nu_n)\,. \tag{6.71}$$

The outer sum runs over the points $\nu_j$ of the predefined grid, where the function values $f_j = f(\nu_j)$ are known, while the inner sums considers a fictitious finer grid in between the $\nu_j$, where $f(\nu)$ is approximated by the spline interpolation. Moreover, note that the inner sums have to be considered as trapezoid sums, that is the first and the last point have to be weighted by 1/2, to avoid double-counting of the boundaries. Furthermore $\Delta\nu$ incorporates the uniform weight of the discretized integration intervals of this artificial grid in case of the Fourier transformation[8]. The exact integral is recovered for $\Delta\nu \to 0$. If one deals instead with a Fourier series, one can simply set $\Delta\nu = 1$. These trapezoid sums can be computed in closed form [37]

$$\hat{f}(t) = \sum_{j=1}^{N-1} \sum_{l=0}^{l_{\max}} a_j^{(l)} I_j^{(l)}(t)\,, \tag{6.72}$$

in terms of the spline coefficients and the functions

$$I_j^{(l)}(t) = e^{-it\nu_j} \left(i\frac{\partial}{\partial t}\right)^l \left[\frac{\Delta\nu}{2i} \cot\left(\frac{\Delta\nu\, t}{2}\right) \left(1 - e^{-it\Delta\nu_j}\right)\right]\,. \tag{6.73}$$

A derivation[9] of the $I_j^{(l)}(t)$ is given in the thesis by Cerrito [144]. Obviously, the second factor cancels the divergence of $\cot(\Delta\nu\, t/2) \simeq 1/t$ for $t \to 0$ such that $\hat{f}(t)$

[8] Since we can evaluate the spline at arbitrary frequencies, we can formally introduce a regular grid in between two adjacent $\nu_j$.

[9] Note the different sign convention of the Fourier transformation.

is analytic in this limit. For numerical purposes it is convenient to rewrite this expression as

$$\begin{aligned}\hat{f}(t) = &\sum_{l=0}^{l_{\max}-1} J^{(l)}(t)\left[a_1^{(l)}e^{-it\nu_1} - a_{N-1}^{(l)}e^{-it\nu_N}\right] \\ &+ J^{(l_{\max})}(t)\sum_{j=1}^{N-1} a_j^{(l_{\max})}\left[e^{-it\nu_j} - e^{-it\nu_{j+1}}\right],\end{aligned} \tag{6.74}$$

with the new definitions

$$J^{(l)}(t) = \left(i\frac{\partial}{\partial t}\right)^l \left[\frac{\Delta\nu}{2i}\cot\left(\frac{t\Delta\nu}{2}\right)\right]. \tag{6.75}$$

Equation (6.74) allows to express $\hat{f}(t)$ exclusively in terms of all highest-order spline coefficients and the coefficients of arbitrary order at the boundary. Thus the backward insertion, discussed at the end of the previous section, becomes unnecessary for the lower order coefficients in the bulk of the splines. Consequently, this representation is to be preferred, since the number of operations is reduced. In fact, the relation between (6.72) and (6.74) can be shown for arbitrary spline orders by first noting

$$I_j^{(l)}(t) = J^{(l)}(t)\left(e^{-it\nu_j} - e^{-it\nu_{j+1}}\right) - \sum_{k=0}^{l-1}\binom{l}{k}J^{(k)}(t)(\Delta\nu_j)^{l-k}e^{-it\nu_{j+1}}. \tag{6.76}$$

According to eq. (6.72) we have to multiply by the $a_j^{(l)}$ and sum over $j$ and $l$ to obtain $\hat{f}(t)$. For the first sum on the right-hand side this yields

$$\begin{aligned}\sum_{j=1}^{N-1}\sum_{l=0}^{l_{\max}} a_j^{(l)}J^{(l)}(t)\left(e^{-it\nu_j} - e^{-it\nu_{j+1}}\right) = &\sum_{j=1}^{N-1} a_j^{(l_{\max})}J^{(l_{\max})}(t)\left(e^{-it\nu_j} - e^{-it\nu_{j+1}}\right) \\ &+ \sum_{l=0}^{l_{\max}-1} J^{(l)}(t)\left(a_1^{(l)}e^{-it\nu_1} - a_{N-1}^{(l)}e^{-it\nu_N}\right) \\ &+ \sum_{j=2}^{N-2}\sum_{l=0}^{l_{\max}-1}\Delta a_j^{(l)}J^{(l)}(t)e^{-it\nu_{j+1}},\end{aligned} \tag{6.77}$$

where the last line results from a shift of the summation index, which allows to introduce the difference operator. The first two sums on the right hand side already correspond to the representation of $\hat{f}(t)$ in (6.74). Therefore, it remains to show that the additional sum in the last line cancels the second contribution of eq. (D.10).

We combine the two terms and use the continuity conditions (6.51) to replace the $\Delta a_j^{(l)}$ and we get

$$\sum_{j=1}^{N-2} e^{-it\nu_{j+1}} \sum_{l=0}^{l_{\max}} \left[ J^{(l)}(t) a_j^{(l)} \sum_{k=0}^{l-1} \binom{l}{k} J^{(k)}(t) (\Delta\nu_j)^{l-k} - \sum_{k=l+1}^{l_{\max}} \binom{k}{l} a_j^{(k)} (\Delta\nu_j)^{k-l} \right] = 0\,, \tag{6.78}$$

The fact that this expression indeed vanishes, can be seen from interchanging the summation order in of one of the terms in eq. (6.78) via

$$\sum_{l=0}^{l_{\max}} \sum_{k=0}^{l-1} g(l,k) = \sum_{k=0}^{l_{\max}} \sum_{l=k+1}^{l_{\max}} g(l,k)\,,$$

which holds for an arbitrary function $g(l,k)$, followed by relabeling $l \leftrightarrow k$. Consequently, we have proven the equivalence of eq. (6.72) and (6.74).

In addition, one should also notice that the functions $J^{(l)}(t)$ from (6.75) involve singularities, when $t$ approaches zero, in contrast to the $I_j^{(l)}(t)$ as mentioned below eq. (6.73). Nevertheless, the complete expression for $\hat{f}(t)$ must be analytic in this limit due to the equivalence of (6.72) and (6.74), which we have just shown. Hence, if one expands $\hat{f}(t)$ around $t = 0$ the negative powers coming from the Laurent series of the individual terms must cancel identically. This implies that we can subtract from $\hat{f}(t)$ a zero in form of the sum of all these poles and and by rearranging the individual terms obtain a regularization term-by-term. The singular behavior of the terms present in (6.74) can always be written as

$$J^{(l)}(t)\, e^{-it\nu_j} \xrightarrow{t\to 0} \left[ \left( i\frac{\partial}{\partial t} \right)^l \left( \frac{1}{it} \right) \right] \sum_{k=0}^{l} \frac{(-i\nu_j t)^k}{k!} = (-i)^{l+1}(l+1)! \sum_{k=0}^{l} \frac{(-i\nu_j)^k}{k!\, t^{l+1-k}}\,. \tag{6.79}$$

Summing this form of the asymptotics over $l$ and $j$ according to eq. (6.74) yields

$$\begin{aligned}
&\hat{f}(t) = \\
&\sum_{l=0}^{l_{\max}-1} \left( J^{(l)}(t) - \frac{(-i)^{l+1}(l+1)!}{t^{l+1}} \right) \left[ a_1^{(l)} e^{-it\nu_N} - a_{N-1}^{(l)} e^{-it\nu_N} \right] \\
&+ \sum_{l=0}^{l_{\max}-1} (-i)^{l+1}(l+1)! \frac{a_1^{(l)}(e^{-it\nu_1} - \sum_{k=0}^{l} \frac{(-it\nu_1)^k}{k!}) - a_{N-1}^{(l)}(e^{-it\nu_N} - \sum_{k=0}^{l} \frac{(-it\nu_1)^k}{k!})}{t^{l+1}} \\
&+ \left( J^{(l_{\max})}(t) - \frac{(-i)^{l_{\max}+1}(l_{\max}+1)!}{t^{l_{\max}}} \right) \sum_{j=1}^{N-1} a_j^{(l_{\max})} \left[ e^{-it\nu_j} - e^{-it\nu_{j+1}} \right] \\
&+ \sum_{j=1}^{N-1} (-i)^{l_{\max}+1}(l_{\max}+1)! \cdot \\
&\qquad \cdot \frac{a_j^{(l_{\max})} \left[ (e^{-it\nu_k} - \sum_{k=0}^{l_{\max}} \frac{(-it\nu_j)^k}{k!}) - (e^{-it\nu_{j+1}} - \sum_{k=0}^{l_{\max}} \frac{(-it\nu_1)^k}{k!}) \right]}{t^{l_{\max}+1}},
\end{aligned} \tag{6.80}$$

where we have rearranged the terms such that all the individual contributions are now finite for $t \to 0$. Therefore, we have achieved a formula that can be applied in the numerical implementation to all ranges of $t$ values and that is based on the efficient evaluation provided by eq. (6.74), which requires only a subset of spline coefficients. In addition, if one considers a Fourier integral the brackets including the $J^{(l)}(t)$ vanish identically, since in the limit $\Delta\nu \to 0$ only the singular terms survive. The above equation thus includes the regularized representation for a continuous transformation, too. Within the computations it is furthermore helpful to replace both the $J^{(l)}(t)$ and the exponential functions by their Taylor series of sufficiently high order, when the arguments become small, to avoid creating errors by the subtractions.

### 6.2.3 Comparison cubic vs. quintic interpolation

As a concrete example, let us consider the function

$$f(\mathbf{k}, \omega_n) = \frac{1}{\hbar^2\omega_n^2 + \varepsilon_k^2 + \mu^2} \tag{6.81}$$

to benchmark the advantages of the quintic spline over the cubic one. Within our numerics we have to transform functions that have similar properties, however, in this case we can find the imaginary time representation analytically with the methods outlined in Appendix B

$$f(\mathbf{k}, \tau) = \frac{1}{2\hbar\sqrt{\varepsilon_k^2 + \mu^2}} \left( \frac{e^{-\tau\sqrt{\varepsilon_k^2+\mu^2}/\hbar}}{e^{-\beta\sqrt{\varepsilon_k^2+\mu^2}} + 1} - \frac{e^{\tau\sqrt{\varepsilon_k^2+\mu^2}/\hbar}}{e^{\beta\sqrt{\varepsilon_k^2+\mu^2}} + 1} \right) \tag{6.82}$$

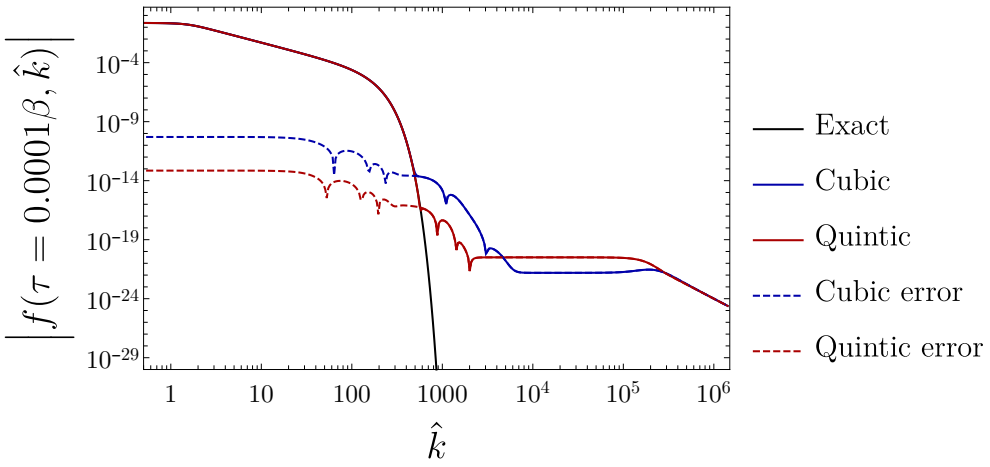


Figure 6.5: Comparison of the DFT based on cubic (blue) and quintic (red) spline interpolation with the exact result from eq. (6.82) (black), with $\beta\mu = 1$.

In particular, in the limit $\tau \to 0^+$, the result will be dominated by the $1/\varepsilon_k$-behavior of the prefactor, which yields an algebraic tail. In Fig. 6.5 we compare this analytic result to our DFT, either computed with a cubic and with a quintic interpolation as a function of[10] $\hat{k} = \hbar k/(2mT)$ at fixed $\tau \simeq 10^{-4}\beta$. For $\hat{k} \lesssim 3000$ the quintic spline yields smaller errors by a factor of approximately $10^{-3}$, while for larger values the situation is reversed and the cubic spline is better, but only by a factor of at most $10^{-2}$. This observation also applies more generically to the functions encountered in the problem of the imbalanced Fermi gas. In particular, we will always observe a fast decrease of the functions at a certain momentum scale, since we include only finite $\tau > 0$ in our grid, such that a Gaussian decay is always present at large enough $k$. The onset of the decay, where the function under consideration starts to vary very quickly, is described much more reliably by the higher order spline. The errors at $\hat{k} \to \infty$ in turn, giving rise to erroneous plateaus, can be more easily identified and removed if necessary, since we know the exponents of the power law tails of all numerical functions exactly.

[10] This normalization, which we use for our internal computations is introduced in more detail in the next chapter.

# Chapter 7

# Numerical implementations of the self-consistent equations

This chapter deals with the specific form of the Green's and vertex functions that we encounter in the imbalanced Fermi gas. We first present a convenient choice for the units in terms of the temperature in Sec. 7.1, before we detail each of the steps for the self-consistent loop in Sec. 7.2 and focus in particular on a suitable subtraction scheme to obtain functions that can be reliably Fourier transformed with numerical methods. As we have already seen in Sec. 4.7 also the thermodynamic quantities show algebraic tails such that we are forced to treat them separately. We present our approach for them in Sec 7.3 and finally we briefly summarize further methods to obtain an efficient code with stable convergence in Sec. 7.4.

## 7.1 Notation and units for the numerical implementation

In this paragraph we show how we conveniently represent the Green's and the vertex functions in dimensionless form for the self-consistent computations. Since both the Matsubara frequencies and the imaginary time interval depend on the temperature, we can reduce the numerical effort by assigning a fixed value of $\beta$ during the initialization stage of the code. Then the matrices required for the DFT from Sec. 6.2 and also the $\beta$-dependent, predefined functions of the subtraction schemes introduced in the next sections have to be generated only once. In practice, we set $\beta = 1$, which is equivalent to expressing the external thermodynamic variables in units of the temperature, like $\hat{\mu} = \beta\mu, \hat{h} = \beta h$. Imaginary frequency arguments reduce to either $\hat{\omega}_n = \beta\omega_n = \pi(2n+1)$ or $\hat{\Omega}_n = 2\pi n$, whereas we measure wave vectors as $\hat{k} = \hbar k/\sqrt{2mT}$, such that the bare dispersion relation becomes $\beta\varepsilon_k = \hat{k}^2$. We abstain from the more standard definition of the unit length in terms of $\lambda_T$ to avoid additional factors of $2\sqrt{\pi}$, which would unnecessarily clutter up our notation below. Moreover, the imaginary time interval is rescaled to $\hat{\tau} \in [0, 1]$ and positions become $\hat{\mathbf{x}} = \sqrt{2mT}\mathbf{x}/\hbar$. Within this notation the dimensionless Green's function reads $\hat{G}(\hat{\mathbf{k}}, \hat{\omega}_n) = TG(\mathbf{k}, \omega_n)$ in momentum and frequency space, which yields for

the bare Green's function from eq. (4.9)

$$\hat{\mathcal{G}}_{\sigma\sigma}\left(\hat{\mathbf{k}},\hat{\omega}_n\right) = \frac{1}{i\hat{\omega}_n - \hat{k}^2 + \hat{\mu}_\sigma}\,. \tag{7.1}$$

The coupling constant $g$ carries units of energy times volume, which are necessary for the correct dimensionality of the bare interaction potential $\bar{g}(\Lambda)\delta(\mathbf{x}-\mathbf{x}')$. In dimensionless form we obtain $\hat{g} = \beta\sqrt{2mT}^3 g/\hbar^3$ and analogously for the vertex function

$$\hat{\Gamma}\left(\hat{\mathbf{Q}},\hat{\Omega}_n\right) = \frac{\beta\hbar^3}{\sqrt{2mT}^3}\,\Gamma\left(\mathbf{Q},\Omega_n\right)\,, \tag{7.2}$$

which follows from writing the Bethe-Salpeter equation (4.30) in these units. In the next paragraphs we will represent all quantities according to these conventions. Therefore, we leave out the caret accents again, as there is no risk of confusion.

## 7.2 Subtraction scheme for the self-consistent loop in the normal phase

In this section we describe in detail the separation of analytical and numerical parts of the Green's and vertex functions as well as the self-energies along the set of self-consistent equations derived in Section 4.6.2. We start out with the single-particle Green's function, which is the central object of the Luttinger-Ward formalism. In fact, it will turn out that we have to implement two different subtraction schemes, one for the case $\mu_\uparrow \gtrsim 1$, realized in the BCS limit and one for values $\mu_\uparrow \lesssim 1$ on the BEC side of the crossover.

### 7.2.1 Green's function

Given a dressed Green's function, we can write it in general as

$$\mathcal{G}_{\sigma\sigma}\left(\mathbf{k},\omega_n\right) = \frac{1}{\mathcal{G}^{(0)}_{\sigma\sigma}\left(\mathbf{k},\omega_n\right)^{-1} - \Sigma_{\sigma\sigma}\left(\mathbf{k},\omega_n\right)}\,, \tag{7.3}$$

due to the Dyson equation. For instance, an expression of this kind results from each of the self-consistent loops. As already discussed in Chap 4 the large-frequency behavior is given by $\mathcal{G}_{\sigma\sigma} \sim 1/\omega_n$, which is already fixed by the equations of motion for the non-interacting Green's function [67], which is defined in dimensionless form in eq. (7.1). Starting out from the dressed Green's function the next step is to compute the particle-particle bubble $\chi\left(\mathbf{x},\tau\right)$, which is the product of the components of $G\left(\mathbf{x},\tau\right)$ (see Fig. 4.5 and eq. (4.37)). Since the algebraic decay of the Green's function renders it nonintegrable, we have to find a decomposition of $\mathcal{G}_{\sigma\sigma}$

such that the problematic terms can be treated analytically, while the remainder can be Fourier transformed by numerical means. We use the following definition

$$\begin{aligned} \mathcal{G}_{\sigma\sigma}\left(\mathbf{k},\omega_n\right) &= \mathcal{G}^{(0)}_{\sigma\sigma}\left(\mathbf{k},\omega_n\right) + \delta\mathcal{G}_{\sigma\sigma}\left(\mathbf{k},\omega_n\right) \\ &= \mathcal{G}^{(0)}_{\sigma\sigma}\left(\mathbf{k},\omega_n\right) + \left[\mathcal{G}_{\sigma\sigma}\left(\mathbf{k},\omega_n\right) - \mathcal{G}^{(0)}_{\sigma\sigma}\left(\mathbf{k},\omega_n\right)\right] , \end{aligned} \tag{7.4}$$

with the quickly decaying, auxiliary Green's function

$$\begin{aligned} \delta\mathcal{G}_{\sigma\sigma}\left(\mathbf{k},\omega_n\right) &= \mathcal{G}_{\sigma\sigma}\left(\mathbf{k},\omega_n\right) - \mathcal{G}^{(0)}_{\sigma\sigma}\left(\mathbf{k},\omega_n\right) \\ &= -\frac{\Sigma_{\sigma\sigma}\left(\mathbf{k},\omega_n\right)}{\mathcal{G}^{(0)}_{\sigma\sigma}\left(\mathbf{k},\omega_n\right)^{-1}\left(\mathcal{G}^{(0)}_{\sigma\sigma}\left(\mathbf{k},\omega_n\right)^{-1} - \Sigma_{\sigma\sigma}\left(\mathbf{k},\omega_n\right)\right)} \sim \left(\omega_n\right)^{-5/2} , \end{aligned} \tag{7.5}$$

where we have inserted the Dyson equation (4.20). The scaling follows from the leading order behavior of the self-energy $\Sigma_{\sigma\sigma}\left(\mathbf{k},\omega_n\right) \sim \left(\omega_n\right)^{-1/2}$ from eq. (7.57) below, together with the asymptotics of the bare Green's function $\mathcal{G}^{(0)}_{\sigma\sigma}\left(\mathbf{k},\omega_n\right) \sim 1/\omega_n$. Consequently we can perform $\mathcal{FT}_{\omega_n\to\tau}(\delta G_{\sigma\sigma})$ with the DFT from Chapter 6. In contrast, the slow asymptotic decay for large Matsubara frequencies of the first term in the decomposition $\mathcal{G}^{(0)}_{\sigma\sigma}\left(\mathbf{k},\omega_n\right) \sim \omega_n^{-1}$ gives rise to the discontinuity in imaginary time, which we have already encountered in eq. (4.10)

$$\mathcal{G}^{(0)}_{\sigma\sigma}\left(\mathbf{k},\tau\right) = \theta(\tau)e^{-(k^2-\mu_\sigma)\tau}\left(1 - n_F(k^2-\mu_\sigma)\right) - \theta(-\tau)e^{-(k^2-\mu_\sigma)\tau}n_F(k^2-\mu_\sigma) . \tag{7.6}$$

Altogether we have in $(\mathbf{k},\tau)$ space

$$\mathcal{G}_{\sigma\sigma}\left(\mathbf{k},\tau\right) = \mathcal{G}^{(0)}_{\sigma\sigma}\left(\mathbf{k},\tau\right) + \delta\mathcal{G}_{\sigma\sigma}\left(\mathbf{k},\tau\right) , \tag{7.7}$$

which now has to be transformed to $(\mathbf{x},\tau)$. Unfortunately, the closed form of the bare Green's function in real space is not known and we have to treat it numerically. However, in the limit $\tau \to 0^+$ the Green's function converges to

$$\mathcal{G}^{(0)}_{\sigma\sigma}\left(|\mathbf{k}| \to \infty, \tau = 0^+\right) \to 1 , \tag{7.8}$$

as the Fermi-Dirac distribution vanishes exponentially at finite temperatures and energies $\varepsilon_k \gg 1$. Therefore, the bare Green's function is also not integrable in momentum space for $\tau \to 0^+$ and we have to find a suitable decomposition of $\mathcal{G}^{(0)}_{\sigma\sigma}\left(\mathbf{k},\tau\right)$ before we can solve the self-consistent equations. This procedure is depicted in Fig. 7.1 to clarify the different steps. Note that we consider the interval $\tau \in [0,1]$ only and use the antiperiodicity (4.5) of the fermionic Green's function, if values of the imaginary time outside of the latter interval are required. We will partition the interacting Green's function in the following way

$$\mathcal{G}_{\sigma\sigma}\left(\mathbf{k},\tau\right) = \mathcal{G}^{\mathrm{ana}}_{\sigma\sigma}\left(\mathbf{k},\tau\right) + \mathcal{G}^{\mathrm{num}}_{\sigma\sigma}\left(\mathbf{k},\tau\right) , \tag{7.9}$$

where $\mathcal{G}^{\mathrm{ana}}_{\sigma\sigma}$ refers to the part that will be treated analytically, while $\mathcal{G}^{\mathrm{num}}_{\sigma\sigma}$ denotes its numerical counterpart. In particular, the latter can be written as

$$\mathcal{G}^{\mathrm{num}}_{\sigma\sigma}\left(\mathbf{k},\tau\right) = \left[\mathcal{G}^{(0)}_{\sigma\sigma}\left(\mathbf{k},\tau\right) - \mathcal{G}^{\mathrm{ana}}_{\sigma\sigma}\left(\mathbf{k},\tau\right)\right] + \delta\mathcal{G}_{\sigma\sigma}\left(\mathbf{k},\tau\right) , \tag{7.10}$$

while we choose for the analytical part $\mathcal{G}^{\mathrm{ana}}_{\sigma\sigma}\left(\mathbf{k},\tau\right) = -\exp(-\tau(k^2-\mu_\sigma))$ that includes the bothersome limit (7.8). Moreover, this function can be transformed in closed form to real space as well as to Matsubara frequencies, due to its Gaussian behavior in $\mathbf{k}$ or its exponential dependence on $\tau$, respectively. The representations of $\mathcal{G}^{\mathrm{ana}}_{\sigma\sigma}$ in the different coordinates read

$$\mathcal{G}^{\mathrm{ana}}_{\sigma\sigma}\left(\mathbf{k},\omega_n\right) = \frac{1+e^{-\left(k^2-\mu_\sigma\right)}}{i\omega_n - k^2 + \mu_\sigma} \tag{7.11a}$$

$$\mathcal{G}^{\mathrm{ana}}_{\sigma\sigma}\left(\mathbf{k},\tau\right) = -e^{-\tau\left(k^2-\mu_\sigma\right)} \tag{7.11b}$$

$$\mathcal{G}^{\mathrm{ana}}_{\sigma\sigma}\left(\mathbf{x},\tau\right) = -\frac{e^{-\frac{r^2}{4\tau}+\mu_\sigma\tau}}{\left(4\pi\tau\right)^{3/2}} , \tag{7.11c}$$

that indeed only depend on $r = |\mathbf{x}|$. Note that a further complication arises from the $\tau \to 1$ limit, where we find $\mathcal{G}^{\mathrm{ana}}_{\sigma\sigma}(\mathbf{k}\to 0, \tau = 1^-) \simeq \exp(\mu_\sigma)$, which becomes exponentially large when $\mu_\sigma \gg 1$. In particular, this happens in the BCS regime, where the chemical potential of at least the majority component is positive and the calculation of the critical temperatures requires to correctly determine exponentially small terms of order $\exp(-T_F/T_c)$. Thus any difference between a numerical function and $\mathcal{G}^{\mathrm{ana}}_{\sigma\sigma}\left(\mathbf{k},\tau\right)$ is prone to severe loss of precision. To circumvent this problem we utilize the definition of (7.11) only in the BEC regime, that is in practice for $\mu_\uparrow < -2$, whereas we retain for $\mu_\uparrow > -2$ solely the first two orders of the Taylor-expanded product[1]

$$e^{-\tau(k^2-\mu_\sigma)\hbar} = e^{-\tau k^2}\left[1 + \mu_\sigma\tau + \mathcal{O}\left(\left(\mu_\sigma\tau\right)^2\right)\right] , \tag{7.12}$$

such that the growth with $\mu_\sigma$ is reduced from an exponential to a linear behavior. We point out that we cannot truncate the Taylor series already after the lowest order $\mathcal{O}(\mu_\sigma^0)$, as the $\mathcal{O}(\tau)$ term will turn out to be connected to a $1/\sqrt{\tau}$ singularity in $\Gamma\left(\mathbf{x},\tau\right)$, which should better not be included in the numerical part. Taking the

[1] As long as $|\mu_\uparrow| \approx 1$, the final results do not depend on the exact criterion that distinguishes between the two regimes and we find a broad interval, where both variants yield identical results within the Tan errors.

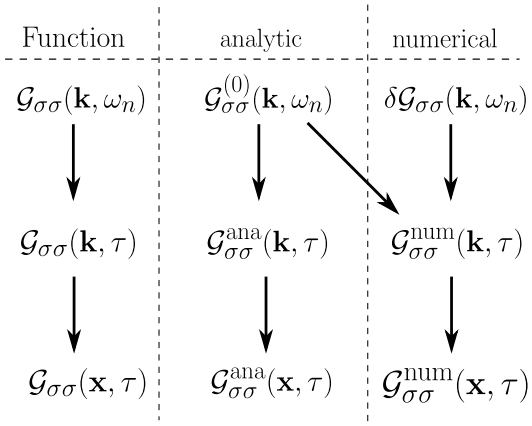


Figure 7.1: Subtraction scheme for the Green's function that is applied both in the BCS and the BEC cases.

form of eq. (7.12), we find the following Fourier transforms

$$\mathcal{G}^{\mathrm{ana}}_{\sigma\sigma}(\mathbf{k},\omega_n) = \frac{1+e^{-k^2}}{i\omega_n - k^2} - \mu_\sigma \frac{1+e^{-k^2}\left(1+k^2-i\omega_n\right)}{\left(i\omega_n-k^2\right)^2} \tag{7.13a}$$

$$\mathcal{G}^{\mathrm{ana}}_{\sigma\sigma}(\mathbf{k},\tau) = -e^{-\tau k^2}\left(1+\mu_\sigma\tau\right) \tag{7.13b}$$

$$\mathcal{G}^{\mathrm{ana}}_{\sigma\sigma}(\mathbf{x},\tau) = -\frac{e^{-\frac{r^2}{4\tau}}}{(4\pi\tau)^{3/2}}(1+\mu_\sigma\tau)\,. \tag{7.13c}$$

We refer to the subtraction scheme based on this modified form for $\mathcal{G}^{\mathrm{ana}}_{\sigma\sigma}(\mathbf{k},\tau)$ as the BCS code, despite the fact that it is in practice also applied at unitarity. The first definition (7.11) in contrast is called the BEC code. Obviously, the explicit form of $\mathcal{G}^{(0)}_{\sigma\sigma}(\mathbf{k},\tau) - \mathcal{G}^{\mathrm{ana}}_{\sigma\sigma}(\mathbf{k},\tau)$, which contributes to $\mathcal{G}^{\mathrm{num}}_{\sigma\sigma}(\mathbf{k},\tau)$ in equation (7.9) depends on whether the BEC or the BCS version is used. Also the particle-bubble, the vertex and the self-energy acquire different decompositions in the two scenarios.

### 7.2.2 Particle-particle bubble

#### BCS case

To present the computations we begin with the BCS case, based on the partition of the Green's function given in eq. (7.13). The first step in the self-consistent loop is to compute the particle-particle bubble diagram, which becomes a product in real space, according to (4.37). After splitting the Green's function in analytical and numerical terms, $\chi(\mathbf{x},\tau)$ reads

$$\begin{aligned}\chi(\mathbf{x},\tau) = {} & \mathcal{G}^{\mathrm{ana}}_{\uparrow\uparrow}(\mathbf{x},\tau)\,\mathcal{G}^{\mathrm{ana}}_{\downarrow\downarrow}(\mathbf{x},\tau) + \sum_\sigma \mathcal{G}^{\mathrm{ana}}_{\sigma\sigma}(\mathbf{x},\tau)\,\mathcal{G}^{\mathrm{num}}_{\bar\sigma\bar\sigma}(\mathbf{x},\tau) \\ & + \mathcal{G}^{\mathrm{num}}_{\uparrow\uparrow}(\mathbf{x},\tau)\,\mathcal{G}^{\mathrm{num}}_{\downarrow\downarrow}(\mathbf{x},\tau)\,.\end{aligned} \tag{7.14}$$

The computation of the vertex function via the Bethe-Salpeter equation (4.30) requires $\chi(\mathbf{Q}, \Omega_n)$ and thus the back transformation first to momentum space and subsequently to Matsubara frequencies. Regarding the $\mathbf{x} \to \mathbf{Q}$ transformation the task is to find a numerically stable partition of the particle-particle bubble, in analogy to the approach for the Green's function from the previous paragraph. The purely analytical term obtained from $\mathcal{G}^{\mathrm{ana}}_{\sigma\sigma}(\mathbf{x}, \tau)\, \mathcal{G}^{\mathrm{ana}}_{\bar{\sigma}\bar{\sigma}}(\mathbf{x}, \tau)$ is a Gaussian, whose Fourier transform to momentum space defines

$$\chi^{\mathrm{ana}}(\mathbf{Q}, \tau) = \left[1 + 2\mu\tau + \left(\mu^2 - h^2\right)\tau^2\right] \frac{e^{-\frac{Q^2\tau}{2}}}{16\sqrt{2}\pi^{3/2}\tau^{3/2}}\,. \tag{7.15}$$

The chemical potential prefactors arise from the spin-symmetric combinations of $\mu_\uparrow$ and $\mu_\downarrow$ in the product of $\mathcal{G}^{\mathrm{ana}}_{\sigma\sigma}(\mathbf{x}, \tau)$ with $\mathcal{G}^{\mathrm{ana}}_{\bar{\sigma}\bar{\sigma}}(\mathbf{x}, \tau)$ according to eqs. (7.13) and (7.14). In the $\tau \to 0^+$ limit the analytical part scales like $\tau^{-3/2}$ due to the $\simeq \tau^{-3}$ singularity of the configuration space function. This divergence is the worst that we will encounter in the following and requires further work, when we compute the transformation to imaginary frequencies.

To improve the numerical transforms of the mixed term of equation (7.14), which also involves $\mathcal{G}^{\mathrm{ana}}_{\sigma\sigma}(\mathbf{x}, \tau) \simeq \tau^{-3/2}$ for $\tau \to 0^+$, we use the identity

$$\begin{aligned}\sum_\sigma \mathcal{G}^{\mathrm{ana}}_{\sigma\sigma}(\mathbf{x}, \tau)\, \mathcal{G}^{\mathrm{num}}_{\bar{\sigma}\bar{\sigma}}(\mathbf{x}, \tau) = \sum_\sigma \Big[ & \mathcal{G}^{\mathrm{ana}}_{\sigma\sigma}(\mathbf{x}, \tau) \left(\mathcal{G}^{\mathrm{num}}_{\bar{\sigma}\bar{\sigma}}(\mathbf{x}, \tau) - \mathcal{G}^{\mathrm{num}}_{\bar{\sigma}\bar{\sigma}}(\mathbf{x} = \mathbf{0}, \tau)\right) \\ & + \mathcal{G}^{\mathrm{ana}}_{\sigma\sigma}(\mathbf{x}, \tau)\, \mathcal{G}^{\mathrm{num}}_{\bar{\sigma}\bar{\sigma}}(\mathbf{0}, \tau) \Big]\,.\end{aligned} \tag{7.16}$$

The last term can be transformed to momentum space analytically and acquires only a constant numerical prefactor, which is why we call expressions of that kind semi-analytic terms, indicated by the index s-a. The usefulness of this rewriting can be motivated by the behavior in the limit of small imaginary times of the first contribution. As already mentioned $\mathcal{G}^{\mathrm{ana}}_{\sigma\sigma}(\mathbf{x}, \tau)$ increases like $\tau^{-3/2}$ for position arguments around $\mathbf{x} = \mathbf{0}$ up to a scale $\mathbf{x}^2/(4\tau) \lesssim 1$. On the other hand for position arguments $|\mathbf{x}| \gtrsim 4\sqrt{\tau}$ the function $\mathcal{G}^{\mathrm{ana}}_{\sigma\sigma}(\mathbf{x}, \tau)$ vanishes quickly due to the Gaussian factor. $\mathcal{G}^{\mathrm{num}}_{\sigma\sigma}(\mathbf{x}, \tau)$, in turn, can be considered constant for small $r \lesssim \sqrt{\tau}$, as it varies on a much larger scale and in particular it is well-defined for $\tau \to 0^+$ for all $\mathbf{x}$. Therefore, the combination $\mathcal{G}^{\mathrm{ana}}_{\sigma\sigma}(\mathbf{x}, \tau) \left(\mathcal{G}^{\mathrm{num}}_{\bar{\sigma}\bar{\sigma}}(\mathbf{x}, \tau) - \mathcal{G}^{\mathrm{num}}_{\bar{\sigma}\bar{\sigma}}(\mathbf{x} = \mathbf{0}, \tau)\right)$ regularizes the $\tau^{-3/2}$ divergence to a $\tau^{-1/2}$ dependence. This is very convenient for the numerical $\mathbf{x} \to \mathbf{Q}$ transformation, because the contribution from the minimal $\tau$ value in the grid becomes much smaller. Furthermore, the position argument appears only in the combination $r^2/\tau$, which gives rise to an additional factor $\tau^{3/2}$ and thus cures the $1/\sqrt{\tau}$ behavior before the transformation to Matsubara frequencies. Moreover, we do not introduce problems in the limit of $|\mathbf{x}| \to \infty$ by this subtraction, since $\mathcal{G}^{\mathrm{ana}}_{\sigma\sigma}(\mathbf{x}, \tau)\, \mathcal{G}^{\mathrm{num}}_{\bar{\sigma}\bar{\sigma}}(\mathbf{x} = \mathbf{0}, \tau)$ is suppressed by the Gaussian form of the first term. Consequently, we can simply add the first term of eq. (7.16) to $\chi^{\mathrm{num}}(\mathbf{k}, \tau)$.

We dub this method "$\delta$-trick", as it amounts to substituting $\mathcal{G}^{\mathrm{num}}_{\bar{\sigma}\bar{\sigma}}(\mathbf{Q}-\mathbf{k},\tau)$ by $\mathcal{G}^{\mathrm{num}}_{\bar{\sigma}\bar{\sigma}}(\mathbf{x}=\mathbf{0},\tau)(2\pi)^3\delta(\mathbf{Q}-\mathbf{k})$ in the convolution

$$\mathcal{G}^{\mathrm{ana}}_{\sigma\sigma}(\mathbf{x},\tau)\,\mathcal{G}^{\mathrm{num}}_{\bar{\sigma}\bar{\sigma}}(\mathbf{x},\tau) = \mathcal{FT}_{\mathbf{Q}\to\mathbf{x}}\left(\int\frac{d^3k}{(2\pi)^3}\mathcal{G}^{\mathrm{ana}}_{\sigma\sigma}(\mathbf{k},\tau)\,\mathcal{G}^{\mathrm{num}}_{\bar{\sigma}\bar{\sigma}}(\mathbf{Q}-\mathbf{k},\tau)\right),$$

in order to obtain the semi-analytic part above and reflects the slow variations of $\mathcal{G}^{\mathrm{num}}_{\sigma\sigma}(\mathbf{x},\tau)$ in real space. In total, we find for the function $\chi(\mathbf{Q},\tau)$

$$\begin{aligned}\chi(\mathbf{Q},\tau) &= \chi^{\mathrm{ana}}(\mathbf{Q},\tau)+\chi^{\text{s-a}}(\mathbf{Q},\tau)+\chi^{\mathrm{num}}(\mathbf{Q},\tau)\\ &= \chi^{\mathrm{ana}}(\mathbf{Q},\tau)+\sum_{\sigma}\mathcal{G}^{\mathrm{ana}}_{\sigma\sigma}(\mathbf{Q},\tau)\,\mathcal{G}^{\mathrm{num}}_{\bar{\sigma}\bar{\sigma}}(\mathbf{x}=\mathbf{0},\tau)+\chi^{\mathrm{num}}(\mathbf{Q},\tau),\end{aligned} \tag{7.17}$$

with $\chi^{\mathrm{ana}}(\mathbf{Q},\tau)$ defined in (7.15), while the total numerical part becomes

$$\begin{aligned}\chi^{\mathrm{num}}(\mathbf{Q},\tau) = \mathcal{FT}_{\mathbf{x}\to\mathbf{Q}}\Bigg[\sum_{\sigma}\mathcal{G}^{\mathrm{ana}}_{\sigma\sigma}(\mathbf{x},\tau)\left\{\mathcal{G}^{\mathrm{num}}_{\bar{\sigma}\bar{\sigma}}(\mathbf{x},\tau)-\mathcal{G}^{\mathrm{num}}_{\bar{\sigma}\bar{\sigma}}(\mathbf{x}=\mathbf{0},\tau)\right\}\\ +\mathcal{G}^{\mathrm{num}}_{\uparrow\uparrow}(\mathbf{x},\tau)\,\mathcal{G}^{\mathrm{num}}_{\downarrow\downarrow}(\mathbf{x},\tau)\Bigg].\end{aligned} \tag{7.18}$$

Now we have to perform the remaining transformation $\chi(\mathbf{Q},\tau)\to\chi(\mathbf{Q},\Omega_n)$, where we consider each of the contributions in eq. (7.17) individually. First of all, the transformation of $\chi^{\mathrm{ana}}(\mathbf{Q},\tau)$, given in eq. (7.15), can be obtained in closed form, however, a representation in terms of an ordinary Fourier integral fails due to the non-integrable $\tau^{-3/2}$ contribution encountered in the $\tau\to 0^+$ limit. Instead one has to apply the theory of Fourier transformations of generalized functions, which is explained e.g. in the book by Gel'fand and Shilov [155]. Within this extended notion of Fourier transforms the authors obtain

$$\mathcal{FT}_{\tau\to\omega}\left(\frac{\theta(\tau)}{\tau^{3/2}}\right) = \sqrt{2\pi}\sqrt{|\omega|}\,[-1+i\,\mathrm{sign}(\omega)] \tag{7.19}$$

for a time argument $\tau$, which covers the complete positive real axis. This result forms the basis for the transformation of $\chi^{\mathrm{ana}}(\mathbf{Q},\tau)\to\chi^{\mathrm{ana}}(\mathbf{Q},\Omega_n)$. Here we only state the final form

$$\begin{aligned}\chi^{\mathrm{ana}}(\mathbf{Q},\Omega_n) &= E_0(\mathbf{Q},\Omega_n)+\mu E_1(\mathbf{Q},\Omega_n)+(\mu^2-h^2)E_2(\mathbf{Q},\Omega_n)\\ &= \frac{-1}{16\sqrt{2}\pi^{3/2}}\left[2e^{-Q^2/2}+\sqrt{2\pi}\sqrt{Q^2-2i\Omega_n}\,\mathrm{erf}\left(\sqrt{\frac{Q^2-2i\Omega_n}{2}}\right)\right]\\ &\quad+\frac{\mu}{8\pi\sqrt{Q^2-2i\Omega_n}}\,\mathrm{erf}\left(\sqrt{\frac{Q^2-2i\Omega_n}{2}}\right)\\ &\quad+(\mu^2-h^2)\left[\frac{-e^{-Q^2/2}}{8\sqrt{2}\pi^{3/2}\left(Q^2-2i\Omega_n\right)}+\frac{\mathrm{erf}\left(\sqrt{\frac{Q^2-2i\Omega_n}{2}}\right)}{16\pi\left(Q^2-2i\Omega_n\right)^{3/2}}\right],\end{aligned} \tag{7.20}$$

where the abbreviation erf denotes the error function and refer the reader to Appendix C for further details on the underlying calculations. The most slowly decaying function $E_0$ reflects the singular $\tau^{-3/2}$ behavior of the leading order $\chi^{\mathrm{ana}}(\mathbf{Q},\tau)$ by the increase $E_0 \sim \sqrt{Q^2 - 2i\Omega_n}$ for large frequencies or momenta, which mathematically originates from (7.19). In fact, this is intimately connected to the large $\Omega_n$ and $Q$ asymptotics of the renormalized pair propagator $M(\mathbf{Q},\Omega_n)$ in the zero range-limit, see Sec. 4.4.2. Taking the $T \to 0$ limit of the finite temperature results discussed here, $M(\mathbf{Q},\Omega_n)$ is exactly recovered as the error functions exponentially converge to one for large absolute values of their arguments. However, it is to be noted, that we have not made use of the renormalization scheme (2.29) here, whose purpose is to render all correlation functions physical and in particular establishes the link $1/g + M(\mathbf{Q},\Omega_n) = 1/\bar{g} + \chi(\mathbf{Q},\Omega_n)$ between the renormalized and bare particle-particle bubble from eq. (4.23). In three dimensions, the bare and the physical coupling constants are related via

$$\frac{1}{g} = \frac{1}{\bar{g}} + \frac{m\Lambda}{2\pi^2\hbar^2}\,,$$

where the constant second term is assigned to the pair propagator. Transforming it to imaginary times yields a contribution $\sim \Lambda\delta(\tau)$. Since $\chi$ can be depicted as a Feynman diagram, it includes all possible imaginary time orderings [67]. However, from the definition of the time ordering operator, which is based on step functions $\theta(\tau)$, we conclude that we always approach $\tau \to 0^{\pm}$ in the sense of a limit. Therefore, the contribution $\sim \Lambda\delta(\tau)$ can never be seen in the formalism based on Fourier transforms, irrespective of the value of $\Lambda$, even in the limit $\Lambda \to \infty$. Effectively, this is equivalent to dimensional regularization, where the scaleless integral $\int d^dq 1/(2\varepsilon_q)$ vanishes. As we will only work with Fourier transforms in the following, we simply set $\bar{g} \to g$ and do not distinguish any more between $\chi$ and $M$, but only use the first notation for the remainder of the thesis.

Another conclusion that is drawn in App. C in relation to the form of these new analytical terms in eq. (7.20), is that including higher orders of $\mu\tau$ in the analytic Green's function $\mathcal{G}^{\mathrm{ana}}_{\sigma\sigma}(\mathbf{k},\tau)$ of equation (7.13) does not improve the asymptotics of $\chi^{\mathrm{ana}}(\mathbf{Q},\Omega_n)$ in eq (7.20) any further, since all of them include the same $(Q^2 - 2i\Omega_n)^{-1}$ terms in Matsubara frequency space as $E_2(\mathbf{Q},\Omega_n)$.

From a computational point of view the error functions cannot be evaluated very efficiently due to the complex arguments. Therefore, we have constructed the terms such that the chemical potentials only appear as prefactors, while the nontrivial error functions are computed once during the initialization and tabulated for the self-consistent loop. After a change of the parameters $\mu, h$ or $g$ it suffices to load the corresponding data arrays and piece together $\chi^{\mathrm{ana}}(\mathbf{Q},\Omega_n)$ according to equation (7.20). We will return to this point when we repeat the procedure for the BEC version.

In the semi-analytic term of eq. (7.17) we can repeat the $\delta$-trick by invoking the

identity

$$\sum_{\sigma} \mathcal{G}^{\mathrm{ana}}_{\sigma\sigma}(\mathbf{Q},\tau)\mathcal{G}^{\mathrm{num}}_{\bar{\sigma}\bar{\sigma}}(\mathbf{x}=\mathbf{0},\tau) = \\ = \sum_{\sigma}\Bigg[\mathcal{G}^{\mathrm{ana}}_{\sigma\sigma}(\mathbf{Q},\tau)\left(\mathcal{G}^{\mathrm{num}}_{\bar{\sigma}\bar{\sigma}}(\mathbf{x}=\mathbf{0},\tau)-\mathcal{G}^{\mathrm{num}}_{\bar{\sigma}\bar{\sigma}}(\mathbf{x}=\mathbf{0},\tau=0^{+})\right) \\ + \mathcal{G}^{\mathrm{ana}}_{\sigma\sigma}(\mathbf{Q},\tau)\,\mathcal{G}^{\mathrm{num}}_{\bar{\sigma}\bar{\sigma}}(\mathbf{x}=\mathbf{0},\tau=0^{+})\Bigg], \tag{7.21}$$

where the last term again can be transformed in closed form to $\Omega_n$. The remainder of eq. (7.17) together with the first line must be transformed by numerical methods. All in all, we obtain

$$\chi(\mathbf{Q},\Omega_n) = \chi^{\mathrm{ana}}_{\mathrm{fin}}(\mathbf{Q},\Omega_n) + \chi^{\text{s-a}}_{\mathrm{fin}}(\mathbf{Q},\Omega_n) + \chi^{\mathrm{num}}_{\mathrm{fin}}(\mathbf{Q},\Omega_n) \\ = \chi^{\mathrm{ana}}(\mathbf{Q},\Omega_n) + \sum_{\sigma}\mathcal{G}^{\mathrm{ana}}_{\sigma\sigma}(\mathbf{Q},\Omega_n)\,\mathcal{G}^{\mathrm{num}}_{\bar{\sigma}\bar{\sigma}}\left(\mathbf{x}=\mathbf{0},\tau=0^{+}\right) + \chi^{\mathrm{num}}_{\mathrm{fin}}(\mathbf{Q},\Omega_n)\,, \tag{7.22}$$

where $\chi^{\mathrm{ana}}_{\mathrm{fin}}(\mathbf{Q},\Omega_n) = \chi^{\mathrm{ana}}(\mathbf{Q},\Omega_n)$ is given in eq. (7.20). Note that the fermionic Green's function in the semi-analytic $\chi^{\text{s-a}}_{\mathrm{fin}}(\mathbf{Q},\Omega_n)$ is transformed to *bosonic* Matsubara frequencies, which yields

$$\mathcal{G}^{\mathrm{ana}}_{\sigma\sigma}(\mathbf{Q},\Omega_n) = \frac{e^{-Q^2}-1}{Q^2-i\Omega_n} + \mu_\sigma \frac{e^{-Q^2}\left[\left(Q^2-i\Omega_n\right)+1\right]-1}{\left(Q^2-i\Omega_n\right)^2}\,, \tag{7.23}$$

in the BCS scheme. Consequently, this term gives rise to a $1/\Omega_n$ asymptotics. The same decay is obtained from the purely numerical term $\chi^{\mathrm{num}}_{\mathrm{fin}}(\mathbf{Q},\Omega_n)$ from the higher orders of the product $\mu_\sigma\tau$ in the single-particle Green's function, as argued above. The final form of the numerical function reads

$$\chi^{\mathrm{num}}_{\mathrm{fin}}(\mathbf{Q},\Omega_n) = \\ \mathcal{FT}_{\tau\to\Omega_n}\Bigg[\sum_{\sigma}\mathcal{G}^{\mathrm{ana}}_{\sigma\sigma}(\mathbf{Q},\tau)\left(\mathcal{G}^{\mathrm{num}}_{\bar{\sigma}\bar{\sigma}}(\mathbf{x}=\mathbf{0},\tau)-\mathcal{G}^{\mathrm{num}}_{\bar{\sigma}\bar{\sigma}}(\mathbf{x}=\mathbf{0},\tau=0^{+})\right)+\chi^{\mathrm{num}}(\mathbf{Q},\tau)\Bigg], \tag{7.24}$$

with $\chi^{\mathrm{num}}(\mathbf{Q},\tau)$ from equation (7.18). The decay for large frequencies can be explained from the finite value that all of these semi-analytic and numerical functions attain at $\tau = 1^{-}$, which yields a discontinuity upon performing the bosonic periodic continuation beyond the imaginary time interval $\tau \in [0,1]$.

### BEC code

We repeat the computation of the particle-particle bubble for the case where $\mathcal{G}^{\mathrm{ana}}_{\sigma\sigma}$ is given by the BEC definition (7.11). The decomposition of $\chi(\mathbf{x},\tau)$ in analytical

and numerical terms (7.14) remains formally unchanged

$$\begin{aligned}\chi(\mathbf{x},\tau) = \mathcal{G}^{\text{ana}}_{\uparrow\uparrow}(\mathbf{x},\tau)\,\mathcal{G}^{\text{ana}}_{\downarrow\downarrow}(\mathbf{x},\tau) + \sum_{\sigma}\mathcal{G}^{\text{ana}}_{\sigma\sigma}(\mathbf{x},\tau)\,\mathcal{G}^{\text{num}}_{\bar{\sigma}\bar{\sigma}}(\mathbf{x},\tau) \\ + \mathcal{G}^{\text{num}}_{\uparrow\uparrow}(\mathbf{x},\tau)\,\mathcal{G}^{\text{num}}_{\downarrow\downarrow}(\mathbf{x},\tau)\ .\end{aligned} \tag{7.25}$$

Like in the BCS regime, we first transform to momentum space. The exclusively analytical term yields

$$\chi^{\text{ana}}(\mathbf{Q},\tau) = \frac{e^{-\frac{Q^2\tau}{2}}}{16\sqrt{2}\pi^{3/2}\tau^{3/2}}\,e^{2\mu\tau}\,, \tag{7.26}$$

due to the Gaussian form. In fact, we can move on and transform the function $\chi^{\text{ana}}(\mathbf{Q},\tau)$ to $(\mathbf{Q},\Omega_n)$ again with the methods explained in App. C. However, the result involves $\text{erf}(\sqrt{(Q^2-2\mu-2i\Omega_n)/2})$, which has to be reevaluated whenever the chemical potential is changed. This consumes too much computation time as discussed above in the BCS case and we are forced to resort to a Taylor expansion of the $\tau$ dependence. To this end, we write equation (7.26) as

$$\begin{aligned}&\chi^{\text{ana}}(\mathbf{Q},\tau) = \chi^{\text{ana}}_{\text{fin}}(\mathbf{Q},\tau) + \chi^{\text{num}}_{(1)}(\mathbf{Q},\tau) = \\ &\frac{e^{-\frac{Q^2\tau}{2}}}{16\sqrt{2}\pi^{3/2}\tau^{3/2}}\left(1+2\mu\tau+2\mu^2\tau^2\right) + \frac{e^{-\frac{Q^2\tau}{2}}}{16\sqrt{2}\pi^{3/2}\tau^{3/2}}\left(e^{2\mu\tau}-1-2\mu\tau-2\mu^2\tau^2\right)\,,\end{aligned} \tag{7.27}$$

where the first term represents the final form of the function that is treated analytically in the $\tau\to\Omega_n$ transformation, while $\chi^{\text{num}}_{(1)}$ is added to the numerical contribution. Comparing $\chi^{\text{ana}}_{\text{fin}}(\mathbf{Q},\tau)$ to the expression for $\chi^{\text{ana}}(\mathbf{Q},\tau)$ in the BCS case, given in equation (7.15), we can immediately write down the result in Matsubara frequencies

$$\chi^{\text{ana}}_{\text{fin}}(\mathbf{Q},\Omega_n) = E_0(\mathbf{Q},\Omega_n) + \mu E_1(\mathbf{Q},\Omega_n) + 2\mu^2 E_2(\mathbf{Q},\Omega_n) \tag{7.28}$$

in analogy to equation (7.20).

Returning to the remaining terms of the decomposition for $\chi(\mathbf{x},\tau)$ we apply the $\delta$-tricks in an identical manner to the mixed products $\mathcal{G}^{\text{ana}}_{\sigma\sigma}(\mathbf{x},\tau)\,\mathcal{G}^{\text{num}}_{\bar{\sigma}\bar{\sigma}}(\mathbf{x},\tau)$ as in eqs. (7.16) and (7.21). The function $\chi(\mathbf{Q},\tau)$ in the BEC code thus acquires the form

$$\begin{aligned}\chi(\mathbf{Q},\tau) &= \chi^{\text{ana}}_{\text{fin}}(\mathbf{Q},\tau) + \chi^{\text{s-a}}(\mathbf{Q},\tau) + \chi^{\text{num}}_{\text{fin}}(\mathbf{Q},\tau) \\ &= \chi^{\text{ana}}_{\text{fin}}(\mathbf{Q},\tau) + \chi^{\text{s-a}}(\mathbf{Q},\tau) + \chi^{\text{num}}(\mathbf{Q},\tau) + \chi^{\text{num}}_{(1)}(\mathbf{Q},\tau)\ ,\end{aligned} \tag{7.29}$$

which is the counterpart to equation (7.17) from the BCS code. Finally, the remaining Fourier transform $\tau\to\Omega_n$ can be executed, which gives rise to

$$\begin{aligned}\chi(\mathbf{Q},\Omega_n) &= \chi^{\text{ana}}_{\text{fin}}(\mathbf{Q},\Omega_n) + \chi^{\text{s-a}}_{\text{fin}}(\mathbf{Q},\Omega_n) + \chi^{\text{num}}_{\text{fin}}(\mathbf{Q},\Omega_n) \\ &= \chi^{\text{ana}}_{\text{fin}}(\mathbf{Q},\Omega_n) + \sum_{\sigma}\mathcal{G}^{\text{ana}}_{\sigma\sigma}(\mathbf{Q},\Omega_n)\,\mathcal{G}^{\text{num}}_{\bar{\sigma}\bar{\sigma}}\left(\mathbf{x}=\mathbf{0},\tau=0^+\right) + \chi^{\text{num}}_{\text{fin}}(\mathbf{Q},\Omega_n)\ .\end{aligned} \tag{7.30}$$

Note that the semi-analytic terms in the BCS and BEC scheme are formally equivalent but differ by the functional form of $\mathcal{G}^{\text{ana}}_{\sigma\sigma}$. In particular, the Green's function evaluated at bosonic arguments reads in the BEC scheme

$$\mathcal{G}^{\text{ana}}_{\sigma\sigma}\left(\mathbf{Q},\Omega_n\right) = \frac{1-e^{-\left(k^2-\mu_\sigma\right)}}{i\Omega_n - Q^2 + \mu_\sigma}\,, \tag{7.31}$$

whereas the numerical function $\chi^{\text{num}}_{\text{fin}}\left(\mathbf{Q},\Omega_n\right)$ is obtained via

$$\begin{aligned}&\chi^{\text{num}}_{\text{fin}}\left(\mathbf{Q},\Omega_n\right) = \\ &\mathcal{FT}_{\tau\to\Omega_n}\Bigg[\sum_\sigma \mathcal{G}^{\text{ana}}_{\sigma\sigma}\left(\mathbf{Q},\tau\right)\left(\mathcal{G}^{\text{num}}_{\bar\sigma\bar\sigma}(\mathbf{x}=\mathbf{0},\tau) - \mathcal{G}^{\text{num}}_{\bar\sigma\bar\sigma}(\mathbf{x}=\mathbf{0},\tau=0^+)\right) \\ &\qquad + \chi^{\text{num}}\left(\mathbf{Q},\tau\right) + \chi^{\text{num}}_{(1)}\left(\mathbf{Q},\tau\right)\Bigg]\end{aligned} \tag{7.32}$$

and contains the additional function $\chi^{\text{num}}_{(1)}$ introduced above.

Within both schemes we have been able to separate the troublesome leading asymptotics of the particle-particle bubble $\chi\left(\mathbf{Q},\Omega_n\right) \sim \sqrt{Q^2 - 2i\Omega_n}$ in the limit of large Matsubara frequencies or momenta from the numerical parts. Note that this is possible, because the latter power law arises from the diagram with bare Green's functions, as discussed in Sec. 4.5.2. Here we even have subtracted the next-to-leading order $\sim 1/\sqrt{Q^2 - 2i\Omega_n}$, such that the numerical terms merely give rise to $1/\Omega_n$ tails, which will be quite convenient for the construction of the vertex.

### 7.2.3 Subtractions for the vertex function

#### BCS code

The vertex function is given by the solution (4.31) to the Bethe-Salpeter equation (4.30) that is a scalar in the normal phase. Using the results for the particle-bubble diagram we can write

$$\Gamma\left(\mathbf{Q},\Omega_n\right) = \frac{1}{\frac{1}{g} + \chi^{\text{ana}}_{\text{fin}}\left(\mathbf{Q},\Omega_n\right) + \chi^{\text{s-a}}_{\text{fin}}\left(\mathbf{Q},\Omega_n\right) + \chi^{\text{num}}_{\text{fin}}\left(\mathbf{Q},\Omega_n\right)}\,. \tag{7.33}$$

From the vertex we have to compute the self-energy, which is accomplished in real space, cf. equation (4.38). We start with the Matsubara-Fourier series to obtain $\Gamma\left(\mathbf{Q},\tau\right)$. Since the vertex scales asymptotically like $\Gamma \sim \sqrt{i\Omega_n}^{-1}$, according to equation (7.20), we are forced to also develop a decomposition for $\Gamma\left(\mathbf{Q},\Omega_n\right)$ that allows to deal with the numerically troublesome terms in an analytical manner. We separate the construction into two steps, where in the first one only terms that scale like $\sim \Omega_n^{-2}$ are transformed numerically. Afterwards, we will see how to extend the approach to compute even terms of order $\mathcal{O}(\Omega_n^{-2})$ exactly, which considerably improves the quality of our results.

Due to the behavior $\chi^{\mathrm{num}}(\mathbf{Q},\Omega_n) \simeq \Omega_n^{-2}$ for large Matsubara frequencies $\Omega_n$, only the analytical part is responsible for the non-integrable asymptotics. Therefore, we consider the following expansion for large Matsubara frequencies based on eq. (7.20)

$$\frac{1}{\frac{1}{g}+\chi^{\mathrm{ana}}_{\mathrm{fin}}(\mathbf{Q},\Omega_n)} = \frac{1}{E_0} - \frac{1}{gE_0^2} - \frac{\mu E_1}{E_0^2} + \frac{1}{g^2E_0^3} + \mathcal{O}(\Omega_n^{-2}), \tag{7.34}$$

where care has to be taken to include all relevant orders. Unfortunately, directly subtracting the terms on the right hand side from $\Gamma$ is impossible, since the Fourier transforms of negative powers of the error functions are not known. Nevertheless, we can separate the dominant asymptotics from these contributions by the help of the definitions

$$E_0^{\mathrm{sub}}(\mathbf{Q},\Omega_n) = \frac{16\pi\,\mathrm{erf}\left[\sqrt{\frac{1}{2}\left(Q^2+d-2i\Omega_n\right)}\right]}{\sqrt{Q^2+d-2i\Omega_n}} \tag{7.35a}$$

$$E_1^{\mathrm{sub}}(\mathbf{Q},\Omega_n) = \frac{(16\pi)^2\,\mathrm{erf}\left[\sqrt{\frac{1}{2}\left(Q^2+d-2i\Omega_n\right)}\right]}{Q^2+d-2i\Omega_n} \tag{7.35b}$$

$$E_2^{\mathrm{sub}}(\mathbf{Q},\Omega_n) = \frac{-8\sqrt{2\pi}}{Q^2+d-2i\Omega_n}e^{-\frac{1}{2}(Q^2+d)} + \frac{8\pi\,\mathrm{erf}\left[\sqrt{\frac{1}{2}\left(Q^2+d-2i\Omega_n\right)}\right]}{\left(Q^2+d-2i\Omega_n\right)^{3/2}}, \tag{7.35c}$$

whose transformations to $(\mathbf{Q},\tau)$ can be obtained by considering the results of Appendix C. Here, we have again made use of the freedom to introduce an auxiliary negative chemical potential $d$, like in Sec. 4.7, whose only effect is to shift the arguments without changing the asymptotics. Choosing $d$ sufficiently large renders many exponential terms effectively irrelevant, like the first one in $E_2^{\mathrm{sub}}$ above, while the error functions simultaneously can be replaced by one. In practice, $d = 150$ provides good results. As before, these additional error functions do not depend on any physical parameter that will change when we scan the whole phase diagram, which is crucial to run the code efficiently, as discussed in the previous section. Combining these functions with the expansion (7.34), yields the asymptotic properties

$$\frac{1}{E_0} + E_0^{\mathrm{sub}} = \frac{d}{\left(Q^2-2i\Omega_n\right)^{3/2}} + \mathcal{O}(\Omega_n^{-2}), \tag{7.36}$$

which actually does not yet fulfill the desired $\mathcal{O}(\Omega_n^{-2})$ behavior. This problem will be solved in combination with $E_2^{\mathrm{sub}}$ in a moment. Furthermore, we have

$$\frac{1}{gE_0^2} - \frac{1}{g}E_1^{\mathrm{sub}} = \mathcal{O}(\Omega_n^{-2}), \tag{7.37}$$

as well as

$$\frac{\mu E_1}{E_0^2} - \frac{1}{g^2 E_0^3} + \frac{d}{\left(Q^2 - 2i\Omega_n\right)^{3/2}} + \left(4\mu + \frac{512\pi^2}{g^2} + d\right) E_2^{\mathrm{sub}}\left(\mathbf{Q}, \Omega_n\right) = \mathcal{O}(\Omega_n^{-2}) \,, \tag{7.38}$$

where the slowly decaying $d/\left(Q^2 - 2i\Omega_n\right)^{3/2}$ term is the remainder of (7.36), which has been canceled now. Therefore, we can finally complete the first stage of the vertex decomposition indicated by the index (1) and bring together the intermediate steps from above. To this end, we partition the vertex in the form

$$\Gamma\left(\mathbf{Q}, \Omega_n\right) = \Gamma_{(1)}^{\mathrm{ana}}\left(\mathbf{Q}, \Omega_n\right) + \Gamma_{(1)}^{\mathrm{num}}\left(\mathbf{Q}, \Omega_n\right) \,, \tag{7.39}$$

where the analytical part becomes

$$\Gamma_{(1)}^{\mathrm{ana}}\left(\mathbf{Q}, \Omega_n\right) = E_0^{\mathrm{sub}}\left(\mathbf{Q}, \Omega_n\right) - \frac{1}{g} E_1^{\mathrm{sub}}\left(\mathbf{Q}, \Omega_n\right) + \left(4\mu + \frac{512\pi^2}{g^2} + d\right) E_2^{\mathrm{sub}}\left(\mathbf{Q}, \Omega_n\right) \,, \tag{7.40}$$

while the numerical function reads

$$\begin{aligned}
&\Gamma_{(1)}^{\mathrm{num}}\left(\mathbf{Q}, \Omega_n\right) = \Gamma\left(\mathbf{Q}, \Omega_n\right) - \Gamma_{(1)}^{\mathrm{ana}}\left(\mathbf{Q}, \Omega_n\right) = \\
&= \left(\frac{1}{\frac{1}{g} + \chi\left(\mathbf{Q}, \Omega_n\right)} - \frac{1}{\frac{1}{g} + \chi_{\mathrm{fin}}^{\mathrm{ana}}\left(\mathbf{Q}, \Omega_n\right)}\right) + \frac{1}{\frac{1}{g} + \chi_{\mathrm{fin}}^{\mathrm{ana}}\left(\mathbf{Q}, \Omega_n\right)} - \Gamma_{(1)}^{\mathrm{ana}}\left(\mathbf{Q}, \Omega_n\right) \\
&= \frac{\left(\mu E_1 + \left(\mu^2 - h^2\right) E_2\right)\left(\frac{1}{g} - E_0\right) + \frac{1}{g^2}}{E_0^2\left(\frac{1}{g} + \chi_{\mathrm{fin}}^{\mathrm{ana}}\left(\mathbf{Q}, \Omega_n\right)\right)} - \frac{\chi_{\mathrm{fin}}^{\text{s-a}}\left(\mathbf{Q}, \Omega_n\right) + \chi_{\mathrm{fin}}^{\mathrm{num}}\left(\mathbf{Q}, \Omega_n\right)}{\frac{1}{g} + \chi\left(\mathbf{Q}, \Omega_n\right)} \\
&\quad - \left(\frac{1}{E_0\left(\mathbf{Q}, \Omega_n\right)} - \frac{1}{g E_0^2\left(\mathbf{Q}, \Omega_n\right)}\right) - \Gamma_{(1)}^{\mathrm{ana}}\left(\mathbf{Q}, \Omega_n\right) \,.
\end{aligned} \tag{7.41}$$

This cumbersome sorting of the terms is necessary because it groups them in a way that avoids large differences in the asymptotics, since the subtractions in the definition of $\Gamma_{(1)}^{\mathrm{num}}$ have to cancel over several orders of magnitude. An additional complication arises from the fact that $1/g + \chi^{\mathrm{ana}}\left(\mathbf{Q}, \Omega_n\right)$ has a zero at $\Omega_n = 0$ around $\mathbf{Q} = \mathcal{O}(1)$. The corresponding divergence is not physical and does not appear in the full expression $1/g + \chi\left(\mathbf{Q}, \Omega_n\right)$. It originates from the used analytic form, which is an expansion for asymptotically large arguments, in the opposite limit. To cure this problem one adds and subtracts an auxiliary functions $\delta\chi\left(\mathbf{Q}, \Omega_n\right)$ via $\chi_{\mathrm{fin}}^{\mathrm{ana}}\left(\mathbf{Q}, \Omega_n\right) \to \chi_{\mathrm{fin}}^{\mathrm{ana}} + \delta\chi\left(\mathbf{Q}, \Omega_n\right)$ and $\chi_{\mathrm{fin}}^{\mathrm{num}}\left(\mathbf{Q}, \Omega_n\right) \to \chi_{\mathrm{fin}}^{\mathrm{num}}\left(\mathbf{Q}, \Omega_n\right) - \delta\chi\left(\mathbf{Q}, \Omega_n\right)$, which leaves the physical vertex invariant but removes the zero. In practice on uses a Gaussian $\delta\chi = \exp\left(-bQ^2\right)$ with a suitable prefactor $b$ of order one that adjusts the width such that the zero is lifted, while the asymptotics remain unchanged.

To keep the notation simple, we will not include $\delta\chi$ explicitly in the following discussion and only emphasize its role when it is necessary.

To achieve the same level of accuracy for the transformation $\Gamma(\mathbf{Q}, \Omega_n) \to \Gamma(\mathbf{Q}, \tau)$ as in the Fourier transform of $\mathcal{G}_{\sigma\sigma}(\mathbf{k}, \omega_n) \to \mathcal{G}_{\sigma\sigma}(\mathbf{k}, \tau)$, where only terms of $\omega_n^{-5/2}$ have been treated numerically, we will now also determine the terms of order $(\Omega_n)^{-2}$ exactly (up to one irrelevant exception). This gives rise to two further subtractions, which can be assigned to the analytic and semi-analytic part of the vertex. The first one

$$\Gamma_a^{\mathrm{sub}}(\mathbf{Q}, \Omega_n) = -\ (16\pi)^4 \left( \frac{1}{g^3} + \frac{d}{256\pi^2 g} + \frac{\mu}{64\pi^2 g} \right) \frac{1}{\left(Q^2 + d - 2i\Omega_n\right)^2}, \tag{7.42}$$

is obtained by extending the expansion (7.34) to the next order[2]

$$\begin{aligned} &\frac{1}{\frac{1}{g} + \chi^{\mathrm{ana}}} = \\ &= \frac{1}{E_0} - \frac{1}{gE_0^2} - \frac{\mu E_1}{E_0^2} - \frac{\left(\mu^2 - h^2\right) E_2}{E_0^2} + \frac{1}{g^2 E_0^3} + \frac{2\mu E_1}{gE_0^3} - \frac{1}{g^3 E_0^4} + \mathcal{O}(\Omega_n^{-5/2}). \end{aligned} \tag{7.43}$$

The first three and the fifth terms already have been captured by the subtractions (7.35). The leading behavior of the last two contributions give rise to the $1/g^3$ and the $\mu/g$ terms of $\Gamma_a^{\mathrm{sub}}$, whereas the $d$ dependent term in (7.42) arises from the $1/\Omega_n^2$ correction of $1/(gE_0^2)$, due to the introduction of the auxiliary chemical potential $d$. In this analysis, we have completely neglected the correction from $E_2/E_0^2$, which actually also shows an $\Omega_n^{-2}$ behavior. However, a careful inspection of the definition (7.35c) reveals that the prefactor of this contribution carries a Gaussian weight in the momentum $\mathbf{Q}$. Since the numerical noise arising from this term in the $\Omega_n \to \tau$ transformation solely emerges at $Q \gg 1$, the uncertainties are strongly suppressed and it suffices to compute the Fourier transform merely numerically.

Besides these exclusively analytical terms we find at this order a contribution originating from the semi-analytical parts of $\chi(\mathbf{Q}, \Omega_n)$ in equation (7.22). Including them in the asymptotic expansion of the vertex function (7.43) gives rise to the leading order combination $-\chi^{\text{s-a}}(\mathbf{Q}, \Omega_n)/E_0^2(\mathbf{Q}, \Omega_n) \sim 1/\Omega_n^2$. Therefore, we treat this dominant term in closed form, which yields the second subtraction

$$\Gamma_b^{\mathrm{sub}}(\mathbf{Q}, \Omega_n) = 256\pi^2 \sum_\sigma \mathcal{G}_{\sigma\sigma}\left(\mathbf{x} = \mathbf{0}, \tau = 0^+\right) \frac{1}{\left(Q^2 + d - 2i\Omega_n\right)\left(Q^2 + d - i\Omega_n\right)}. \tag{7.44}$$

[2]Here the error functions in the highest order terms are expanded themselves, as we only aim for subtracting the dominant asymptotics.

As $\chi^{\mathrm{num}}(\mathbf{Q},\Omega_n) \sim \Omega_n^{-5/2}$ the purely numerical part need not be taken into account at all for the construction of the subtraction scheme, which exemplifies the utility of treating sufficiently many terms analytically. Indeed, the ability to leave only terms of order $\Omega_n^{-5/2}$ to the numerical transformations relies on the precise knowledge of the asymptotic behavior of the semi-analytical and numerical terms.

To begin with actually Fourier transforming the vertex, we summarize its final form

$$\Gamma(\mathbf{Q},\Omega_n) = \Gamma^{\mathrm{ana}}(\mathbf{Q},\Omega_n) + \Gamma^{\mathrm{num}}(\mathbf{Q},\Omega_n) \tag{7.45a}$$

$$\Gamma^{\mathrm{ana}}(\mathbf{Q},\Omega_n) = \Gamma^{\mathrm{ana}}_{(1)}(\mathbf{Q},\Omega_n) + \Gamma^{\mathrm{sub}}_{a}(\mathbf{Q},\Omega_n) + \Gamma^{\mathrm{sub}}_{b} \tag{7.45b}$$

$$\Gamma^{\mathrm{num}}(\mathbf{Q},\Omega_n) = \Gamma^{\mathrm{num}}_{(1)}(\mathbf{Q},\Omega_n) - \Gamma^{\mathrm{sub}}_{a}(\mathbf{Q},\Omega_n) - \Gamma^{\mathrm{sub}}_{b}(\mathbf{Q},\Omega_n)\ . \tag{7.45c}$$

Being equipped with these definitions we can now proceed with the transformation to imaginary time. The $(\mathbf{Q},\tau)$-forms of the various contributions to $\Gamma^{\mathrm{ana}}$ read

$$\Gamma^{\mathrm{ana}}_{(1)}(\mathbf{Q},\tau) = -(2\pi)^{3/2} e^{-\tau\frac{Q^2}{2}-\frac{\tau d}{2}} \left[\frac{4}{\pi\sqrt{\tau}} + \frac{32\sqrt{2\pi}}{g} + \frac{2\sqrt{\tau}}{\pi}\left(4\mu + \frac{512\pi^2}{g^2} + d\right)\right] \tag{7.46a}$$

$$\begin{aligned}\Gamma^{\mathrm{sub}}_{a}(\mathbf{Q},\tau) = (16\pi)^4 &\left(\frac{1}{g^3} + \frac{d}{256\pi^2 g} + \frac{\mu}{64\pi^2 g}\right) \\ &\cdot\left[\tau\left(1 + n_B\left(\frac{Q^2+d}{2}\right)\right)e^{-\tau\frac{Q^2+d}{2}} + \beta\frac{e^{-(\tau+\beta)\frac{Q^2+d}{2}}}{\left(1-e^{-\tau\frac{Q^2+d}{2}}\right)^2}\right]\end{aligned} \tag{7.46b}$$

$$\begin{aligned}\Gamma^{\mathrm{sub}}_{b}(\mathbf{Q},\tau) = 64\pi^2 &\sum_{\sigma}\mathcal{G}^{\mathrm{num}}_{\sigma\sigma}\left(\mathbf{x}=\mathbf{0},\tau=0^+\right) \\ &\cdot\left[\frac{e^{-\frac{Q^2+d}{2}\tau}\left(1+n_B\left(\frac{Q^2+d}{2}\right)\right)}{Q^2+d} - \frac{e^{-\left(Q^2+d\right)\tau}\left(1+n_B\left(Q^2+d\right)\right)}{Q^2+d}\right].\end{aligned} \tag{7.46c}$$

The first equation can be verified by equation (C.16) from Appendix C. The latter two are simple bosonic Matsubara frequency sums, that can be evaluated by the methods outlined in Appendix B. Note that all Bose functions $n_B$ and the second term of (7.46b) are suppressed by at least $\exp(-d/2) \approx 10^{-33}$ and can be neglected in the rest of the computations. Therefore, it also suffices to derive an analytical expression for the simplified functions in configurations space. In turn, since $\Gamma^{\mathrm{num}}(\mathbf{Q},\Omega_n)$ does not exhibit a product structure like the particle-particle bubble, we cannot further improve the properties of its Fourier transform by $\delta$-tricks and directly compute $\Gamma^{\mathrm{num}}(\mathbf{x},\tau)$, instead. To obtain the complete expression for $\Gamma(\mathbf{x},\tau)$, we focus now on the $\mathbf{Q}\to\mathbf{x}$ transformation of the analytical and semi-analytical

contributions summarized in (7.46). We notice that $\Gamma^{\text{ana}}_{(1)}(\mathbf{Q},\tau)$ and $\Gamma^{\text{sub}}_{a}(\mathbf{Q},\tau)$ reduce to simple Gaussians, which are easily transformed to $\mathbf{x}$, after discarding the negligible terms. Furthermore, the more involved transformation of $\Gamma^{\text{sub}}_{b}(\mathbf{Q},\tau)$ is detailed in Appendix D.1. As a result, we find

$$\Gamma^{\text{ana}}_{(1)}(\mathbf{x},\tau) = -\, e^{\frac{-r^2}{2\tau}-\frac{d\tau}{2}}\left[\frac{4}{\pi\tau^2}+\frac{1}{g}\frac{32\sqrt{2\pi}}{\tau^{3/2}}+\frac{2}{\pi\tau}\left(4\mu+\frac{512\pi^2}{g^2}+d\right)\right] \tag{7.47a}$$

$$\Gamma^{\text{sub}}_{a}(\mathbf{x},\tau) = -\;65536\pi^4\left(\frac{1}{g^3}+\frac{d}{256\pi^2 g}+\frac{\mu}{64\pi^2 g}\right)\cdot\left[e^{-\frac{r^2}{2\tau}}\frac{e^{\frac{-d\tau}{2}}}{8\sqrt{2}\pi^{3/2}\sqrt{\tau}}\right] \tag{7.47b}$$

$$\begin{aligned}\Gamma^{\text{sub}}_{b}(\mathbf{x},\tau) =& (256\pi^2)\sum_{\sigma}\mathcal{G}^{\text{num}}_{\sigma\sigma}\left(\mathbf{x}=\mathbf{0},\tau=0^+\right)\frac{-e^{-\sqrt{d}r}}{8\pi r}\\ &\Bigg\{-1+\operatorname{erf}\left(\frac{r-2\sqrt{d}\tau}{2\tau}\right)\\ &+e^{2\sqrt{d}r}\left(\sqrt{\pi}\left(\Gamma\left[\frac{1}{2},\frac{\left(r+\sqrt{d}\tau\right)^2}{2\tau}\right]-\Gamma\left[\frac{1}{2},\frac{\left(r+2\sqrt{d}\tau\right)^2}{4\tau}\right]\right)\right)\\ &\left(1-\operatorname{erf}\left[\frac{r-\sqrt{d}\tau}{\sqrt{2\tau}}\right]\right)\Bigg\}.\end{aligned} \tag{7.47c}$$

Quite importantly, both $\Gamma^{\text{sub}}_{a}(\mathbf{x},\tau)$ and $\Gamma^{\text{sub}}_{b}(\mathbf{x},\tau)$ show a Gaussian decay for $r=|\mathbf{x}|\gg\sqrt{\tau}$. On the other hand, in the short distance regime both functions approach a constant value. In particular, at $\mathbf{x}=\mathbf{0}$ the curly bracket in equation (7.47c) vanishes identically and cancels the prefactor which is proportional to $1/r$. Furthermore, the $1/\sqrt{\tau}$ behavior of equation (7.47b) for $\tau\to 0^+$ is integrable and will be promoted to a function that is linear in $\tau$ by Fourier transformation to momentum space. Hence, both the new subtractions can be transformed to momenta without problems even when they are multiplied by $\mathcal{G}_{\sigma\sigma}(\mathbf{x},\beta-\tau)$, which happens in the computation of the self-energy (cf. equation (4.38)). Therefore, we will assign them to the numerical part of the vertex in real space and imaginary time, despite having the analytical expressions available. They have only been introduced to lower the exponent of the leading frequency asymptotics in $\Gamma^{\text{num}}(\mathbf{Q},\Omega_n)$. Before we finally move on to $\Sigma_{\sigma\sigma}$, we terminate this section on the subtraction scheme for the vertex function with the complete expression for $\Gamma(\mathbf{x},\tau)$

$$\begin{aligned}\Gamma(\mathbf{x},\tau) &= \Gamma^{\text{ana}}_{\text{fin}}(\mathbf{x},\tau)+\Gamma^{\text{num}}_{\text{fin}}(\mathbf{x},\tau)\\ &= \Gamma^{\text{ana}}_{(1)}(\mathbf{x},\tau)+\left[\Gamma^{\text{sub}}_{a}(\mathbf{x},\tau)+\Gamma^{\text{sub}}_{b}(\mathbf{x},\tau)+\Gamma^{\text{num}}(\mathbf{x},\tau)\right],\end{aligned} \tag{7.48}$$

where $\Gamma^{\text{num}}(\mathbf{x},\tau)$ is defined as the Fourier transformation of $\Gamma^{\text{num}}(\mathbf{Q},\Omega_n)$ in equation (7.45) above.

#### BEC code

If $\mu_\uparrow < -2$, we evaluate the BEC code, which means that the form of the analytical Green's function is given by eq. (7.11). However, the computation of $\Gamma(\mathbf{x},\tau)$ does not involve important changes regarding the subtraction scheme. First of all, the form of $\Gamma(\mathbf{Q},\Omega_n)$ in equation (7.33) resulting from the inversion of the Bethe-Salpeter equation remains valid. Of course, when one inserts the particle-particle bubble $\chi(\mathbf{Q},\Omega_n)$ according to equation (7.22), its building blocks follow from eqs. (7.28), (7.31) and (7.32). The distinction between the analytical parts of the particle-particle bubble in the BCS and BEC approaches reduces to merely exchanging the prefactor of the function $E_2(\mathbf{Q},\Omega_n)$ from $\mu^2 - h^2$ in eq. (7.20), valid in the BCS case, to its bosonic counterpart $2\mu^2$, as follows from eq. (7.28). As argued below the extended expansion of $\Gamma(\mathbf{Q},\Omega_n)$ in (7.43), however, the function $E_2(\mathbf{Q},\Omega_n)$ plays no role in the analytic subtractions constructed for the Fourier transformation of the vertex function. Therefore, the BEC versions of $\Gamma^{\mathrm{ana}}_{(1)}(\mathbf{x},\tau), \Gamma^{\mathrm{sub}}_{a}(\mathbf{x},\tau)$ and $\Gamma^{\mathrm{sub}}_{b}(\mathbf{x},\tau)$ are identical to the definitions (7.47) for the BCS scheme. Also the complete function $\Gamma(\mathbf{x},\tau)$ is formally given by equation (7.48) like in the BCS case and one merely has to keep in mind the different form of $\chi$, when one creates the numerical contribution $\Gamma^{\mathrm{num}}_{(1)}(\mathbf{x},\tau)$, given in eq. (7.41).

### 7.2.4 Self-energy

#### BCS code

The self-energy in real space reads in temperature units

$$\Sigma_{\sigma\sigma}(\mathbf{x},\tau) = -\Gamma(\mathbf{x},\tau)\,\mathcal{G}_{\bar{\sigma}\bar{\sigma}}(\mathbf{x},1-\tau)\ , \tag{7.49}$$

according to equation (4.38), where we have also made use of the antiperiodicity of the Green's function. In order to close the self-consistent loop we have to know $\Sigma_{\sigma\sigma}(\mathbf{k},\omega_n)$, which eventually updates the Green's function and we can restart by computing the next particle-particle bubble from the new $\mathcal{G}_{\sigma\sigma}(\mathbf{k},\omega_n)$. The Fourier transformation of the self-energy turns out to be numerically more involved than the functions we have encountered thus far. This is because the vertex has its main contribution coming from the $\tau \to 0^+$ boundary of the imaginary time interval, while the counter-propagating Green's function is peaked at the $\tau \to 1^-$ side. In the previous cases only one of these endpoints played a role in the Fourier transformations, whereas the other one only added negligible contributions. Inserting the decompositions both for $\Gamma$ and $\mathcal{G}_{\bar{\sigma}\bar{\sigma}}$, we obtain

$$\begin{aligned} -\Sigma_{\sigma\sigma}(\mathbf{x},\tau) = {} & \Gamma^{\mathrm{ana}}_{\mathrm{fin}}(\mathbf{x},\tau)\,\mathcal{G}^{\mathrm{ana}}_{\bar{\sigma}\bar{\sigma}}(\mathbf{x},1-\tau) + \Gamma^{\mathrm{num}}_{\mathrm{fin}}(\mathbf{x},\tau)\,\mathcal{G}^{\mathrm{ana}}_{\bar{\sigma}\bar{\sigma}}(\mathbf{x},1-\tau) \\ & + \Gamma^{\mathrm{ana}}_{\mathrm{fin}}(\mathbf{x},\tau)\,\mathcal{G}^{\mathrm{num}}_{\bar{\sigma}\bar{\sigma}}(\mathbf{x},1-\tau) + \Gamma^{\mathrm{num}}_{\mathrm{fin}}(\mathbf{x},\tau)\,\mathcal{G}^{\mathrm{num}}_{\bar{\sigma}\bar{\sigma}}(\mathbf{x},1-\tau)\ . \end{aligned} \tag{7.50}$$

As usual, we first transform back to momenta. The product $\Gamma^{\mathrm{ana}}_{\mathrm{fin}}(\mathbf{x},\tau)\,\mathcal{G}^{\mathrm{ana}}_{\bar{\sigma}\bar{\sigma}}(\mathbf{x},\tau)$ contains six terms, as can be seen from equations (7.11) and (7.47a), together with

the identification $\Gamma^{\text{ana}}_{\text{fin}}(\mathbf{x},\tau) = \Gamma^{\text{ana}}_{(1)}(\mathbf{x},\tau)$ defined in eq. (7.48). However, all of them depend on position only via a common Gaussian prefactor $\exp[-r^2/(2\tau) - r^2/(4-4\tau)]$ and their Fourier transformation yields

$$\begin{aligned} -\Sigma^{\text{ana}}_{\sigma\sigma}(\mathbf{k},\tau) = & \left[\frac{4}{\pi\tau^2} + \frac{32\sqrt{2\pi}}{\tau^{3/2}g} + \frac{2}{\pi\tau}\left(4\mu + \frac{512\pi^2}{g^2} + d\right)\right][1+\mu_{\bar{\sigma}}(1-\tau)] \\ & \cdot e^{k^2\frac{\tau(\tau-1)}{2-\tau} - d\frac{\tau}{2}}\left(\frac{\tau}{2-\tau}\right)^{3/2} . \end{aligned} \tag{7.51}$$

We observe that the worst $\tau$ divergence of $\Sigma^{\text{ana}}_{\sigma\sigma}(\mathbf{k},\tau)$, which we encounter in the limit $\tau \to 0^+$, is a $\tau^{-1/2}$ singularity in the very first term. In contrast, the limit $\tau$ to $1^-$ does not cause any problems.

To transform the semi-analytic terms of the self-energy decomposition (7.50) we again apply the $\delta$-trick introduced in equation (7.16), which relies on the product structure in real space, and write

$$\begin{aligned} &\Gamma^{\text{ana}}_{\text{fin}}(\mathbf{x},\tau)\mathcal{G}^{\text{num}}_{\bar{\sigma}\bar{\sigma}}(\mathbf{x},1-\tau) + \Gamma^{\text{num}}_{\text{fin}}(\mathbf{x},\tau)\,\mathcal{G}^{\text{ana}}_{\bar{\sigma}\bar{\sigma}}(\mathbf{x},1-\tau) = \\ &\quad = \Gamma^{\text{ana}}_{\text{fin}}(\mathbf{x},\tau)\left[\mathcal{G}^{\text{num}}_{\bar{\sigma}\bar{\sigma}}(\mathbf{x},1-\tau) - \mathcal{G}^{\text{num}}_{\bar{\sigma}\bar{\sigma}}(\mathbf{x}=\mathbf{0},1-\tau)\right] \\ &\qquad + \left[\Gamma^{\text{num}}_{\text{fin}}(\mathbf{x},\tau) - \Gamma^{\text{num}}_{\text{fin}}(\mathbf{x}=\mathbf{0},\tau)\right]\mathcal{G}^{\text{ana}}_{\bar{\sigma}\bar{\sigma}}(\mathbf{x},1-\tau) \\ &\qquad + \Gamma^{\text{ana}}_{\text{fin}}(\mathbf{x},\tau)\,\mathcal{G}^{\text{num}}_{\bar{\sigma}\bar{\sigma}}(\mathbf{x}=\mathbf{0},1-\tau) \\ &\qquad + \Gamma^{\text{num}}(\mathbf{x}=\mathbf{0},\tau)\,\mathcal{G}^{\text{ana}}_{\bar{\sigma}\bar{\sigma}}(\mathbf{x},1-\tau)\ . \end{aligned} \tag{7.52}$$

The Fourier transforms of the last two lines can be obtained exactly and the only restriction on their precision arise from the accuracy of the numerical prefactors. In total, we obtain for the self-energy as function of $(\mathbf{k},\tau)$

$$\begin{aligned} \Sigma_{\sigma\sigma}(\mathbf{k},\tau) = & \Sigma^{\text{ana}}_{\sigma\sigma}(\mathbf{k},\tau) - \Gamma^{\text{ana}}_{\text{fin}}(\mathbf{k},\tau)\,\mathcal{G}^{\text{num}}_{\bar{\sigma}\bar{\sigma}}(\mathbf{x}=\mathbf{0},1-\tau) \\ & - \Gamma^{\text{num}}(\mathbf{x}=\mathbf{0},\tau)\,\mathcal{G}^{\text{ana}}_{\bar{\sigma}\bar{\sigma}}(\mathbf{k},1-\tau) + \Sigma^{\text{num}}_{\sigma\sigma}(\mathbf{k},\tau)\ , \end{aligned} \tag{7.53}$$

with the numerical contribution

$$\begin{aligned} -\Sigma^{\text{num}}_{\sigma\sigma}(\mathbf{k},\tau) = & \mathcal{FT}_{r\to k}\left[\Gamma^{\text{ana}}_{\text{fin}}(\mathbf{x},\tau)\left[\mathcal{G}^{\text{num}}_{\bar{\sigma}\bar{\sigma}}(\mathbf{x},1-\tau) - \mathcal{G}^{\text{num}}_{\bar{\sigma}\bar{\sigma}}(\mathbf{x}=\mathbf{0},1-\tau)\right]\right] \\ & + \mathcal{FT}_{r\to k}\left[\left[\Gamma^{\text{num}}_{\text{fin}}(\mathbf{x},\tau) - \Gamma^{\text{num}}_{\text{fin}}(\mathbf{x}=\mathbf{0},\tau)\right]\mathcal{G}^{\text{ana}}_{\bar{\sigma}\bar{\sigma}}(\mathbf{x},1-\tau)\right] \\ & + \mathcal{FT}_{r\to k}\left[\Gamma^{\text{num}}_{\text{fin}}(\mathbf{x},\tau)\,\mathcal{G}^{\text{num}}_{\bar{\sigma}\bar{\sigma}}(\mathbf{x},1-\tau)\right]. \end{aligned} \tag{7.54}$$

Now it remains to transform from imaginary time to Matsubara frequencies, where we first concentrate on the analytic part. Unfortunately, the transformation of the term as a whole in closed form is ruled out due to the complicated form of

the exponential function in $\Sigma^{\text{ana}}_{\sigma\sigma}(\mathbf{k},\tau)$, given in eq. (7.51), which depends in a convoluted manner on the combinations $\tau$, $1-\tau$ and $2-\tau$. Thus, we separate from the entire analytic expression only the leading $1/\sqrt{\tau}$ asymptotics, which would give rise to poor numerical results, despite being integrable from the point of view of standard calculus. More precisely, we write

$$\begin{aligned}\Sigma^{\text{ana}}_{\sigma\sigma}(\mathbf{k},\tau) &= \Sigma^{\text{ana}}_{\text{fin},\,\sigma\sigma}(\mathbf{k},\tau) + \Sigma^{\text{num}}_{(1),\,\sigma\sigma}(\mathbf{k},\tau) \\ &= \Sigma^{\text{ana}}_{\text{fin},\,\sigma\sigma}(\mathbf{k},\tau) + \left[\Sigma^{\text{ana}}_{\sigma\sigma}(\mathbf{k},\tau) - \Sigma^{\text{ana}}_{\text{fin},\,\sigma\sigma}(\mathbf{k},\tau)\right],\end{aligned} \tag{7.55}$$

where the second term approaches a constant value for $\tau \to 0^+$. Therefore, it is tractable by the DFT-routine, while the explicit form of the remaining analytical part reads

$$\Sigma^{\text{ana}}_{\text{fin},\,\sigma\sigma}(\mathbf{k},\tau) = -\frac{\sqrt{2}}{\pi\sqrt{\tau}} e^{-k^2\tau/2}\,. \tag{7.56}$$

For convenience, we have not used a Taylor expansion but kept the leading exponential form in order to avoid introducing an artificial polynomial dependence on $k$, which then would have to cancel perfectly with the numerical parts. The Fourier transform of this new function follows from eq. (C.16). As a result, we have

$$\Sigma^{\text{ana}}_{\text{fin},\,\sigma\sigma}(\mathbf{k},\omega_n) = -\frac{2\,\text{erf}\left(\sqrt{\frac{(k^2-2i\omega_n)}{2}}\right)}{\sqrt{\pi}\sqrt{k^2-2i\omega_n}}\,, \tag{7.57}$$

which confirms, that the self-energy indeed asymptotically behaves like $1/\sqrt{2i\omega_n}$ for $|\omega_n| \to \infty$, as stated previously. Interestingly, the dispersion relation $(k^2/2 - i\omega_n)$ in the self-energy resembles a bosonic pair of twice the Fermion mass, yet evaluated at a fermionic Matsubara frequency. This behavior originates from the product (7.49) of the vertex and the Green's function that determines $\Sigma_{\sigma\sigma}(\mathbf{x},\tau)$ and mixes bosonic and fermionic degrees of freedom. In particular, the mixing can already be observed in the purely analytical term $\Sigma^{\text{ana}}_{\sigma\sigma}(\mathbf{k},\tau)$, given in eq. (7.51). It exhibits a leading exponent $-k^2\tau/2$ which carries an additional factor $1/2$ compared to the bare fermionic Green's function $\mathcal{G}^{(0)}_{\sigma\sigma}(\mathbf{k},\tau)$, see eq. (7.6). Physically, the branch cut from $\sqrt{k^2-2i\omega_n}$ arises from the scattering continuum at sufficiently large energies, which is also encountered in the theory of Gaussian fluctuations, as discussed by Diener et al. [147]. Furthermore, this UV behavior of the self-energy is consistent with the results from the BDMC approach to the unitary Fermi gas [153], too. In addition, the absence of a constant that survives the large-frequency limit reflects the fact that the Hartree diagram vanishes, when the cutoff $\Lambda$ is sent to infinity.

Returning to the decomposition in eq. (7.53), the next step is to determine the dependence of the semi-analytic terms on $\omega_n$. Instead of directly transforming them numerically, we extend the separation between exact and numerical contributions

by adding and subtracting the dominant numerical function values. These are attained at that end point of the imaginary time interval, at which the numerical function is peaked. We find

$$\begin{aligned}\Gamma^{\mathrm{ana}}_{\mathrm{fin}}\left(\mathbf{k},\tau\right)&\mathcal{G}^{\mathrm{num}}_{\bar{\sigma}\bar{\sigma}}\left(\mathbf{x}=\mathbf{0},1-\tau\right)+\Gamma^{\mathrm{num}}\left(\mathbf{x}=\mathbf{0},\tau\right)\mathcal{G}^{\mathrm{ana}}_{\bar{\sigma}\bar{\sigma}}\left(\mathbf{k},1-\tau\right)= \\ &= \Gamma^{\mathrm{ana}}_{\mathrm{fin}}\left(\mathbf{k},\tau\right)\left[\mathcal{G}^{\mathrm{num}}_{\bar{\sigma}\bar{\sigma}}\left(\mathbf{x}=\mathbf{0},1-\tau\right)-\mathcal{G}^{\mathrm{num}}_{\bar{\sigma}\bar{\sigma}}\left(\mathbf{x}=\mathbf{0},1\right)\right] \\ &\quad+\left[\Gamma^{\mathrm{num}}\left(\mathbf{x}=\mathbf{0},\tau\right)-\Gamma^{\mathrm{num}}\left(\mathbf{x}=\mathbf{0},\tau=0\right)\right]\mathcal{G}^{\mathrm{ana}}_{\bar{\sigma}\bar{\sigma}}\left(\mathbf{k},1-\tau\right) \\ &\quad+\Gamma^{\mathrm{ana}}_{\mathrm{fin}}\left(\mathbf{k},\tau\right)\mathcal{G}^{\mathrm{num}}_{\bar{\sigma}\bar{\sigma}}\left(\mathbf{x}=\mathbf{0},1\right)+\Gamma^{\mathrm{num}}\left(\mathbf{x}=\mathbf{0},\tau=0\right)\mathcal{G}^{\mathrm{ana}}_{\bar{\sigma}\bar{\sigma}}\left(\mathbf{k},1-\tau\right)\,,\end{aligned} \tag{7.58}$$

where the second and the third line now contain functions that approach zero at both ends of the $\tau$-interval, which results in a more quickly decaying asymptotics of the numerical functions. Furthermore, the last line is readily Fourier transformed to frequency space by using the analytical expressions (7.42) for $\Gamma^{\mathrm{ana}}_{\mathrm{fin}}\left(\mathbf{k},\omega_n\right)$ and (7.13) for $\mathcal{G}^{\mathrm{ana}}_{\bar{\sigma}\bar{\sigma}}\left(\mathbf{k},\omega_n\right)$, respectively. Note however that the vertex is now evaluated at *fermionic* Matsubara frequencies[3] and that the inverted time argument in $\mathcal{G}_{\bar{\sigma}\bar{\sigma}}\left(\mathbf{k},1-\tau\right)$ yields $-\mathcal{G}^{\mathrm{ana}}_{\bar{\sigma}\bar{\sigma}}(\mathbf{k},-\omega_n)$. The remainder of the self-energy $\Sigma_{\sigma\sigma}\left(\mathbf{k},\tau\right)$ (7.53) has to be transformed by the DFT and we finally obtain

$$\begin{aligned}\Sigma_{\sigma\sigma}\left(\mathbf{k},\omega_n\right)&=\Sigma^{\mathrm{ana}}_{\mathrm{fin},\,\sigma\sigma}\left(\mathbf{k},\omega_n\right)+\Sigma^{\text{s-a}}_{\sigma\sigma}\left(\mathbf{k},\omega_n\right)+\Sigma^{\mathrm{num}}_{\mathrm{fin},\,\sigma\sigma}\left(\mathbf{k},\omega_n\right)= \\ &=\Sigma^{\mathrm{ana}}_{\mathrm{fin},\,\sigma\sigma}\left(\mathbf{k},\omega_n\right)-\Bigg[\Gamma^{\mathrm{ana}}_{\mathrm{fin}}\left(\mathbf{k},\omega_n\right)\mathcal{G}^{\mathrm{num}}_{\bar{\sigma}\bar{\sigma}}\left(\mathbf{x}=\mathbf{0},\beta\right) \\ &\quad-\Gamma^{\mathrm{num}}_{\bar{\sigma}\bar{\sigma}}\left(\mathbf{x}=\mathbf{0},0^{+}\right)\mathcal{G}^{\mathrm{ana}}_{\bar{\sigma}\bar{\sigma}}\left(\mathbf{k},-\omega_n\right)\Bigg]+\Sigma^{\mathrm{num}}_{\mathrm{fin},\,\sigma\sigma}\left(\mathbf{k},\omega_n\right)\,.\end{aligned} \tag{7.59}$$

The analytical part $\Sigma^{\mathrm{ana}}_{\mathrm{fin},\,\sigma\sigma}\left(\mathbf{k},\omega_n\right)$ is defined in (7.57), whereas the semi-analytic part is contained in the square brackets and the remaining terms are gathered in the final numerical contribution

$$\begin{aligned}\Sigma^{\mathrm{num}}_{\sigma\sigma}\left(\mathbf{k},\omega_n\right)&=\mathcal{FT}_{\tau\rightarrow\omega_n}\left[\Sigma^{\mathrm{num}}_{(1),\,\sigma\sigma}\left(\mathbf{k},\tau\right)\right]+\mathcal{FT}_{\tau\rightarrow\omega_n}\left[\Sigma^{\mathrm{num}}_{\sigma\sigma}\left(\mathbf{k},\tau\right)\right] \\ &\quad-\mathcal{FT}_{\tau\rightarrow\omega_n}\left[\Gamma^{\mathrm{ana}}_{\mathrm{fin}}\left(\mathbf{k},\tau\right)\left[\mathcal{G}^{\mathrm{num}}_{\bar{\sigma}\bar{\sigma}}\left(\mathbf{x}=\mathbf{0},1-\tau\right)-\mathcal{G}^{\mathrm{num}}_{\bar{\sigma}\bar{\sigma}}\left(\mathbf{x}=\mathbf{0},1^{-}\right)\right]\right] \\ &\quad-\mathcal{FT}_{\tau\rightarrow\omega_n}\left[\left[\Gamma^{\mathrm{num}}\left(\mathbf{x}=\mathbf{0},\tau\right)-\Gamma^{\mathrm{num}}\left(\mathbf{x}=\mathbf{0},0^{+}\right)\right]\mathcal{G}^{\mathrm{ana}}_{\bar{\sigma}\bar{\sigma}}\left(\mathbf{k},1-\tau\right)\right].\end{aligned} \tag{7.60}$$

The additional function $\Sigma^{\mathrm{num}}_{(1),\,\sigma\sigma}\left(\mathbf{k},\tau\right)$ can be found in eq. (7.55), while all the contributions to the exclusively numerical function $\Sigma^{\mathrm{num}}_{\sigma\sigma}\left(\mathbf{k},\tau\right)$ are listed in equation (7.54). The semi-analytical terms are explained above in eq. (7.58).

[3] The fact that all frequencies in eq. (7.42) come with a prefactor of two gives the fermionic $\omega_n$ effectively a bosonic character.

### BEC-code

We will now recapitulate the computation of the self-energy within the BEC-subtraction scheme. The original real-space product of the vertex and the counter-propagating Green's function (7.49) remains unaltered, however, we have to use the analytical Green's function $\mathcal{G}^{\text{ana}}_{\sigma\sigma}(\mathbf{x}, \beta - \tau)$ defined in eq. (7.11) and construct the vertex according to the rules described in the BEC subsection 7.2.3. With $\Gamma^{\text{ana}}_{\text{fin}}(\mathbf{x}, \tau)$ from equation (7.47a), which is identical to the BCS-definition, the analytical multiplication $\Gamma^{\text{ana}}(\mathbf{x}, \tau)\, \mathcal{G}^{\text{ana}}_{\bar{\sigma}\bar{\sigma}}(\mathbf{x}, \beta - \tau)$ gives rise to a Gaussian that can be easily transformed to momentum space

$$\begin{aligned}\Sigma^{\text{ana}}_{\sigma\sigma}(\mathbf{k}, \tau) = -\ &\left[\frac{4}{\pi\tau^2} + \frac{32\sqrt{2\pi}}{\tau^{3/2} g} + \frac{2}{\pi\tau}\left(4\mu + \frac{512\pi^2}{g^2} + d\right)\right] \\ &\cdot e^{k^2 \frac{\tau(\tau-1)}{2-\tau} - \frac{d}{2}\tau + \mu_{\bar{\sigma}}(1-\tau)} \left(\frac{\tau}{2-\tau}\right)^{3/2} .\end{aligned} \tag{7.61}$$

In comparison to (7.51) in the BCS case, the chemical potential appears now reexponentiated, as expected. Furthermore, the problematic $\tau \to 0^+$ behavior stays the same, because it arises exclusively from $\Gamma^{\text{ana}}_{\text{fin}}(\mathbf{x}, \tau)$. Extracting the $\tau^{-1/2}$ divergence yields

$$\Sigma^{\text{ana}}_{\text{fin},\sigma\sigma}(\mathbf{k}, \tau) = -\frac{\sqrt{2}}{\pi\sqrt{\tau}} e^{-\frac{1}{2}(k^2+d)\tau} , \tag{7.62}$$

where we have included the $d$ dependence, in contrast to eq. (7.50) in the BCS scheme. This also changes the result in Matsubara frequencies to

$$\Sigma^{\text{ana}}_{\text{fin},\sigma\sigma}(\mathbf{k}, \omega_n) = -\frac{2\,\text{erf}\left(\sqrt{\frac{k^2+d-2i\omega_n}{2}}\right)}{\sqrt{\pi}\sqrt{k^2+d-2i\omega_n}} . \tag{7.63}$$

The semi-analytic functions can be treated analogously to the BCS code. However, recall that we have to plug in $\mathcal{G}^{\text{ana}}_{\bar{\sigma}\bar{\sigma}}(\mathbf{k}, \tau)$ from eq. (7.11) both in the semi-analytic and the numerical functions, which still are formally defined via eq. (7.54). Regarding the final Matsubara transformation, we can resort to the form

$$\begin{aligned}\Sigma_{\sigma\sigma}(\mathbf{k}, \omega_n) &= \Sigma^{\text{ana}}_{\text{fin},\sigma\sigma}(\mathbf{k}, \omega_n) + \Sigma^{\text{s-a}}_{\sigma\sigma}(\mathbf{k}, \omega_n) + \Sigma^{\text{num}}_{\text{fin},\sigma\sigma}(\mathbf{k}, \omega_n) = \\ &= \Sigma^{\text{ana}}_{\text{fin},\sigma\sigma}(\mathbf{k}, \omega_n) - \Big[\Gamma^{\text{ana}}_{\text{fin}}(\mathbf{k}, \omega_n)\, \mathcal{G}^{\text{num}}_{\bar{\sigma}\bar{\sigma}}(\mathbf{x} = \mathbf{0}, 1) \\ &\quad - \Gamma^{\text{num}}_{\bar{\sigma}\bar{\sigma}}\left(\mathbf{x} = \mathbf{0}, 0^+\right) \mathcal{G}^{\text{ana}}_{\bar{\sigma}\bar{\sigma}}(\mathbf{k}, -\omega_n)\Big] + \Sigma^{\text{num}}_{\text{fin},\sigma\sigma}(\mathbf{k}, \omega_n)\end{aligned} \tag{7.64}$$

from the BCS case. We also use again the function $\Sigma^{\text{ana}}_{\text{fin},\sigma\sigma}(\mathbf{k}, \tau)$ from equation (7.56) in order to regularize $\Sigma^{\text{ana}}_{\sigma\sigma}(\mathbf{k}, \tau)$, as the small $\tau$-dependence has not changed in the BEC scheme. Therefore, the resulting, additional part $\Sigma^{\text{num}}_{(1),\sigma\sigma}(\mathbf{x}, \tau)$

is still defined as the difference $\Sigma^{\mathrm{num}}_{(1),\,\sigma\sigma}(\mathbf{x},\tau) = \Sigma^{\mathrm{ana}}_{\sigma\sigma}(\mathbf{x},\tau) - \Sigma^{\mathrm{ana}}_{\mathrm{fin},\,\sigma\sigma}(\mathbf{x},\tau)$, however, $\Sigma^{\mathrm{ana}}_{\sigma\sigma}(\mathbf{k},\tau)$ is of course given by eq. (7.61). Finally, in the semi-analytical terms and in the numerical part $\Sigma^{\mathrm{num}}_{\sigma\sigma}(\mathbf{k},\omega_n)$, which is formally equivalent to eq. (7.60), we have to use the BEC expression for the Green's functions from eq. (7.11).

## 7.3 Evaluation of the thermodynamic functions

Once the Green's functions have converged for a given set of thermodynamic parameters $\mu, h, g$, it remains to compute the thermodynamic quantities. Some, like the densities, can be immediately read off from $G$, whereas the pressure, the internal energy and the entropy require the computation of further $G$ dependent-functionals, as described in Section 4.7. The corrections to the ideal gas contributions, unfortunately, require rather involved subtractions to obtain quantitatively reliable results. Similarly to the situation we have encountered during the implementation of the self-consistent loop in the previous section, these originate from the slowly decaying asymptotics of the Green's and vertex functions. Below, we first give the directly accessible quantities converted correctly into density units, before turning to the more complicated functionals $H_1, H_2$ and $H_{\log}$, which require further methods.

### 7.3.1 Directly accessible quantities

From the components of the Green's function $G(\mathbf{x},\tau)$ we infer the densities via the standard limit of short times and distances according to eq. (4.4). Within the unit system explained in Section 7.1 and the decomposition $\mathcal{G}_{\sigma\sigma} = \mathcal{G}^{\mathrm{ana}}_{\sigma\sigma} + \mathcal{G}^{\mathrm{num}}_{\sigma\sigma}$, we obtain

$$n_\sigma = \frac{\hbar^3 \hat{n}_\sigma}{(2mT)^{3/2}} = -\frac{\hbar^3}{(2mT)^{3/2}}\left[\hat{\mathcal{G}}^{\mathrm{ana}}_{\sigma\sigma}(\hat{x}=0,\hat{\tau}=1) + \hat{\mathcal{G}}^{\mathrm{num}}_{\sigma\sigma}(\hat{x}_{\min},\hat{\tau}_{\max})\right], \quad (7.65)$$

where the caret on the density expectation refers to our temperature units. Furthermore, we have used the antiperiodicity (4.5) to project the $\tau \to 0^-$ limit into the available time interval. The analytic part is given in eq. (7.13) or eq. (7.11), depending on whether the BCS or the BEC code is employed. In the numerical part, we have to use the gridpoint with minimal space and maximal time coordinate. With the densities we can immediately determine the dimensionless parameters $\theta, \tilde{\mu}$ and $\tilde{h}$ from eqs. (2.66), (2.68) and (2.69). The dimensionless coupling constant $v = 1/(k_F a)$ acquires the form

$$v = 4\pi\frac{\sqrt{\theta}}{\hat{g}}, \quad (7.66)$$

due to $g = 4\pi\hbar^2 a/m$ and $\hat{g} = \beta(2mT)^{3/2} g/\hbar^3$. The last quantity of this class is the dimensionless contact density $\tilde{\mathcal{C}}$, which follows from the vertex function according

to equation (4.28) where the anomalous contribution above $T_c$ vanishes

$$\tilde{\mathcal{C}} = -\frac{\theta^2}{4}\left[\hat{\Gamma}^{\text{ana}}\left(\bar{x}=0,\hat{\tau}=1\right)+\hat{\Gamma}^{\text{num}}\left(\hat{x}_{\min},\hat{\tau}_{\max}\right)\right]. \tag{7.67}$$

Here we used the bosonic periodicity of $\Gamma$ whose analytic part is defined in equations (7.47a) and (7.48) for both the BCS and the BEC code.

### 7.3.2 General strategies for the auxiliary functionals

To compute the functionals $H_1$, $H_2$ and $H_{\log}$ several conceptual steps are required that we summarize here before tackling each term individually.

First of all, one has to interpret the the Matsubara sums as Fourier transformations to $\tau \to 0^-$, as explained in Sec. 4.7. This renders all the formulas finite, whereas the naive interpretation as sums yields ill-defined results. Furthermore, after the transformation to imaginary time we solve the momentum integrals by performing an LFT or DFT to $\mathbf{x} = \mathbf{0}$. Thus, we can use the same routines as in the self-consistent loop.

Despite the fact that all expressions are physical in terms of Fourier transforms, we are forced to find representations that allow for a numerical treatment. Problematic are functions of the arguments $X^f = i\omega_n - k^2$ or $X^b = Q^2 - 2i\Omega_n$ that asymptotically vanish too slowly. To achieve terms amenable to processing with our DFT and LFT functions, we subtract the corresponding asymptotic behavior, yet as function of $X^f_d = X^f - d$ or $X^b_d = X^b + d$, respectively. Here we utilize again the auxiliary chemical potential $d > 0$, which does not affect the leading asymptotics but renders many terms negligible. Schematically we get for a function $f$ that symbolizes any of the terms in $H_1, H_2$ or $H_{\log}$:

$$f(X^{f,b}) = \left[f(X^{f,b}) - \sum_\alpha (c_\alpha X_d^{f,b})^\alpha\right] + \sum_\alpha (c_\alpha X_d^{f,b})^\alpha, \tag{7.68}$$

where the sum contains all powers of the argument $X^{f,b}$ such that the difference in the brackets decays at least as quickly as $\left(X^{f,b}\right)^{-2}$. Due to the form of the individual functions, we are not able to separate another factor of $1/\sqrt{X^{f,b}}$ like in the previous sections. The remaining sum is known analytically up to the possibly numerical constants $c_\alpha$ and must be evaluated via complex contour integration including a convergence factor $\exp(z0^+)$ where $z$ refers to the complex integration frequency. However, poles and branch cuts only appear for $z \sim d$. Consequently, those terms are suppressed by $\exp(-d)$ and can for large enough $d$ (in practice $d = 150$) safely be neglected.

Another helpful identity is Parseval's theorem, which we apply both to fermionic

and bosonic Matsubara sums

$$\sum_n f(\omega_n)g(\omega_n) = -\int_0^1 d\tau f(\tau)g(1-\tau) \tag{7.69a}$$

$$\sum_n f(\Omega_n)g(\Omega_n) = \int_0^1 d\tau f(\tau)g(1-\tau). \tag{7.69b}$$

We will encounter situations, where either both factors are known analytically and we can find a solution in closed form to the integral on the right (at least in terms of a generalized Fourier transformation) or at most one factor is given by a purely numerical function of imaginary time. In this case the numerical $\tau$ integral will be well-defined due to the integrability of the appearing functions in the compact integration interval. Therefore, the representation in terms of the integration over imaginary times is advantageous compared to the sum over infinitely many Matsubara frequencies, that becomes numerically difficult for slowly algebraically decaying function. Technically, we perform the integral by a *bosonic* DFT to $\Omega_n = 0$.

A last point to mention before going into the details of the evaluation of the auxiliary functionals concerns numerical noise created by the subtraction in eq. (7.68), which originates mostly in the finite precision of the error functions. To get rid of these problems we switch for large arguments $|X^{f,b}| \gg 1$ to an asymptotic expansion of $f(X^{f,b})$, such that the subtracted powers cancel identically and the remainder can be dealt with numerically.

### 7.3.3 Computation of $H_1[G]$

We start with the functional $H_1[G]$, given in (4.42), which we can express in terms of $\delta G_{\sigma\sigma}$ from eq. (7.5)

$$H_1[G] = -\int \frac{d^3k}{(2\pi)^3} \sum_{\sigma,n} \Big[ -\log\left(1 + \mathcal{G}^{(0)}_{\sigma\sigma}\left(\mathbf{k},\omega_n\right)^{-1} \delta\mathcal{G}_{\sigma\sigma}\left(\mathbf{k},\omega_n\right)\right) + \left(\mathcal{G}^{(0)}_{\sigma\sigma}\left(\mathbf{k},\omega_n\right)^{-1} \delta\mathcal{G}_{\sigma\sigma}\left(\mathbf{k},\omega_n\right)\right)\Big] \tag{7.70}$$

For large $|X^f|$ the logarithm may be Taylor expanded revealing the integrand's asymptotic behavior $((\mathcal{G}^{(0)}_{\sigma\sigma})^{-1}\delta\mathcal{G}_{\sigma\sigma})^2 \sim (X^f)^{-3}$, which can be easily transformed numerically. However, to obtain a smooth function we must replace the log by its Taylor series up to tenth order, when $|y| = |((\mathcal{G}^{(0)}_{\sigma\sigma})^{-1}\delta\mathcal{G}_{\sigma\sigma})| < 10^{-3}$. We do this by combining terms of comparable size via

$$\begin{aligned}&\log(1+y) - y \simeq \\ &y^2(1/2 - y(1/3 - y(1/4 - y(1/5 - y(1/6 - y(1/7 - y(1/8 - y(1/9 - y/10)))))))),\end{aligned} \tag{7.71}$$

since otherwise the difference in eq. (7.70) leads to numerical noise.

### 7.3.4 Subtraction scheme for $H_2[G]$

To evaluate $H_2[G]$ from eq. (4.54) we first recall its definition

$$H_2[G] = -\frac{1}{2}\int \frac{d^3k}{(2\pi)^3}\sum_{n,\sigma}\left\{\left[\mathcal{G}^{(0)}_{\sigma\sigma}\left(\mathbf{k},\omega_n\right)^{-1}\right]^* \delta\mathcal{G}_{\sigma\sigma}\left(\mathbf{k},\omega_n\right)\right\}\,, \tag{7.72}$$

where we have made use of the identity $\mathcal{G}^{(0)}_{\sigma\sigma}\left(\mathbf{k},\omega_n\right)^* = \mathcal{G}^{(0)}_{\sigma\sigma}(\mathbf{k},-\omega_n)$ and Definition (7.5) from the previous paragraph. With the latter we find the scaling of the integrand $([\mathcal{G}^{(0)}_{\sigma\sigma}]^*)^{-1}\delta\mathcal{G}_{\sigma\sigma} \sim (X^f)^{-3/2}$, which numerically is quite inconvenient, despite being sumable. To deal with this issue we separate the term in the following way

$$\begin{aligned}
&[\mathcal{G}^{(0)}_{\sigma\sigma}\left(\mathbf{k},\omega_n\right)^{-1}]^*\delta\mathcal{G}_{\sigma\sigma}\left(\mathbf{k},\omega_n\right) = f_{a,\sigma}\left(\mathbf{k},\omega_n\right)\Sigma_{\sigma\sigma}\left(\mathbf{k},\omega_n\right) + f_{b,\sigma}\left(\mathbf{k},\omega_n\right) = \\
&= \left[\frac{[(\mathcal{G}^{(0)}_{\sigma\sigma})^{-1}]^*}{\left(\mathcal{G}^{(0)}_{\sigma\sigma}\right)^{-2}}\right]\left(\mathbf{k},\omega_n\right)\Sigma_{\sigma\sigma}\left(\mathbf{k},\omega_n\right) \\
&\quad + \left[[(\mathcal{G}^{(0)}_{\sigma\sigma})^{-1}]^*\delta\mathcal{G}_{\sigma\sigma} - \frac{[(\mathcal{G}^{(0)}_{\sigma\sigma})^{-1}]^*\Sigma_{\sigma\sigma}}{\left(\mathcal{G}^{(0)}_{\sigma\sigma}\right)^{-2}}\right]\left(\mathbf{k},\omega_n\right)\,.
\end{aligned} \tag{7.73}$$

The function $f_b$ asymptotes like $(X^f)^{-5/2}$ and is therefore directly amenable to our numerical methods. In fact, it contributes

$$\begin{aligned}
H^{\mathrm{num}}_{2,b}[G] &= \sum_\sigma \int \frac{d^3k}{(2\pi)^3}\sum_n f_{b,\sigma}\left(\mathbf{k},\omega_n\right) \\
&= \sum_\sigma \mathcal{F}_{k\to r=0}\left[\mathcal{F}_{\omega_n\to\tau=0}\left[f_{b,\sigma}\left(\mathbf{k},\omega_n\right)\right]\right]
\end{aligned} \tag{7.74}$$

to $H_2[G]$. Regarding the first part including $f_{a,\sigma} = [(\mathcal{G}^{(0)}_{\sigma\sigma})^{-1})]^* / \left(\mathcal{G}^{(0)}_{\sigma\sigma}\right)^{-2}$, we use Parseval's theorem (7.69) to represent it as an integral over imaginary time. The function $f_{a,\sigma}$ can be transformed to imaginary time by standard contour integration, which yields

$$\begin{aligned}
f_{a,\sigma}\left(\mathbf{k},\tau\right) &= \mathcal{FT}_{\omega_n\to\tau}\left[\frac{[(\mathcal{G}^{(0)}_{\sigma\sigma})^{-1})]^*}{(\mathcal{G}^{(0)}_{\sigma\sigma})^{-2}}\right](\mathbf{k},\tau) \\
&= \left[2\xi_{k,\sigma}n_F(\xi_{k,\sigma}) - (2\xi_{k,\sigma}\tau - 1)\right]n_F(-\xi_{k,\sigma})e^{-\tau\xi_{k,\sigma}}\,,
\end{aligned} \tag{7.75}$$

with the dimensionless form of the single-particle energies $\xi_{k,\sigma} = k^2 - \mu_\sigma$. The self-energy acquires different forms with respect to the BCS or BEC scheme. We will

first focus on the BCS version and then briefly state the changes when the BEC code is used. Combining the equations (7.55) and (7.53), we have the following decomposition for the self-energy

$$\begin{aligned}\Sigma_{\sigma\sigma}\left(\mathbf{k},\tau\right) = \Sigma^{\text{ana}}_{\text{fin},\,\sigma\sigma}\left(\mathbf{k},\tau\right) + \Sigma^{\text{num}}_{(1),\,\sigma\sigma}\left(\mathbf{k},\tau\right) \\ + \Sigma^{\text{s-a}}_{\sigma\sigma}\left(\mathbf{k},\tau\right) + \Sigma^{\text{num}}_{\sigma\sigma}\left(\mathbf{k},\tau\right)\,.\end{aligned} \tag{7.76}$$

Now we have to integrate the product of $f_{a,\sigma}(\mathbf{k},1-\tau)$ with all the contributions of the self-energy $\Sigma_{\sigma\sigma}\left(\mathbf{k},\tau\right)$ before the momentum integral will be performed by an efficient one-dimensional LFT. Note that only $\Sigma_{\text{fin},\,\sigma\sigma}\left(\mathbf{k},\tau\right)$ exhibits a singularity $\sim 1/\sqrt{\tau}$ for $\tau\to 0^{+}$, which will be treated analytically anyway. All other contributions to the self-energy are finite within the entire imaginary time interval. Translating them back to $\omega_n$, however, leads to an $\omega_n^{-1}$ asymptotics due to the discontinuous behavior at $\tau=0$ or $\tau=1$. Therefore, also the purely numerical part scales like $f_{a,\sigma}\left(\mathbf{k},\omega_n\right)\Sigma^{\text{num}}_{\sigma\sigma}\left(\mathbf{k},\omega_n\right)\sim\omega_n^{-2}$ and we cannot not improve the asymptotics any further, since we can only subtract analytically known terms.

To show the explicit calculations we begin with the analytic part, which can be written as

$$\begin{aligned}-\int_0^1 d\tau f_{a,\sigma}(\mathbf{k},1-\tau)\Sigma^{\text{ana}}_{\text{fin},\,\sigma\sigma}\left(\mathbf{k},\tau\right) = \left(1+\mu_{\bar{\sigma}}\right)\left[n_F(-\xi_{k,\sigma})h_1^{\text{ana}}(\mu_\sigma,\mathbf{k})\right. \\ \left. - n_F(\xi_{k,\sigma})n_F(-\xi_{k,\sigma})h_2^{\text{ana}}(\mu_\sigma,\mathbf{k}))\right]\end{aligned} \tag{7.77}$$

where the factor $(-1)$ on the left-hand side originates from Parseval's theorem for Fermions and we have introduced the functions

$$\begin{aligned}h_1^{\text{ana}}(\mu_\sigma,\mathbf{k}) = -\frac{\sqrt{2}}{\pi}\left(\frac{4(k^2-\mu_\sigma)}{2\mu_\sigma-k^2}e^{-\frac{k^2}{2}}\right. \\ \left. - e^{-k^2+\mu_\sigma}\frac{\sqrt{2\pi}(2k^4+4\mu_\sigma^2+k^2(1-6\mu_\sigma))\,\text{erf}\left[\sqrt{\mu_\sigma-\frac{k^2}{2}}\right]}{(2\mu_\sigma-k^2)^{3/2}}\right).\end{aligned} \tag{7.78a}$$

$$h_2^{\text{ana}}(\mu_\sigma,\mathbf{k}) = -\frac{4(k^2-\mu_\sigma)}{\sqrt{\pi}\sqrt{2\mu_\sigma-k^2}}e^{-k^2+\mu_\sigma}\,\text{erf}\left[\sqrt{\mu_\sigma-\frac{k^2}{2}}\right]\,. \tag{7.78b}$$

These new functions $h_1^{\text{ana}}$ and $h_2^{\text{ana}}$ can be computed from the methods outlined in App. C, since the integral over the imaginary time can be interpreted as Fourier transform $\tau\to\Omega_n=0$. The zeros in the denominator at $\mu_\sigma=k^2/2$ are canceled identically by the error functions in the numerator, whose Taylor expansion around the origin reads [167]

$$\text{erf}(y) = \frac{2y}{\sqrt{\pi}} - \frac{2y^3}{3\sqrt{\pi}} + \mathcal{O}(y^5)\,.$$

In practice, one must, however, explicitly define a function that resorts to this expansion, when $|2\mu_\sigma - k^2| < 10^{-7}$ to avoid numerical noise. Furthermore, both $h_1^{\text{ana}}$ and $h_2^{\text{ana}}$ carry a Gaussian prefactor that allows to integrate eq. (7.86) numerically over the momentum variable. Hence, we obtain the next contribution to $H_2[G]$

$$\begin{aligned} H_{2a}^{\text{ana}}[G] = \sum_\sigma (1+\mu_{\bar\sigma}) \mathcal{FT}_{k\to r=0} \big[ & n_F(-\xi_{k,\sigma}) h_1^{\text{ana}}(\mu_\sigma, \mathbf{k}) \\ & - n_F(\xi_{k,\sigma}) n_F(-\xi_{k,\sigma}) h_2^{\text{ana}}(\mu_\sigma, \mathbf{k})) \big] \, . \end{aligned} \tag{7.79}$$

Now we have to combine $f_{a,\sigma}$ with the semi-analytic terms $\Sigma^{\text{s-a}}_{\sigma\sigma}$, which we split as (see eq. (7.58))

$$\Sigma^{\text{s-a}}_{(1),\,\sigma\sigma}(\mathbf{k}, \tau) = \mathcal{G}^{\text{num}}_{\bar\sigma\bar\sigma}(\mathbf{x} = \mathbf{0}, 1^-) \Gamma^{\text{ana}}_{\text{fin}}(\mathbf{k}, \tau) \tag{7.80a}$$

$$\Sigma^{\text{s-a}}_{(2),\,\sigma\sigma}(\mathbf{k}, \tau) = \mathcal{G}^{\text{ana}}_{\bar\sigma\bar\sigma}(\mathbf{k}, 1-\tau) \, \Gamma^{\text{num}}(\mathbf{x} = \mathbf{0}, 0^+) \, . \tag{7.80b}$$

Computing the first integral yields the function

$$\begin{aligned} h^{\text{s-a}}_{(1)}(\sigma, \mu, h, g, d, \mathbf{k}) = & - \int_0^1 d\tau f_{a,\sigma}(\mathbf{k}, 1-\tau) \Sigma^{\text{s-a}}_{(1),\,\sigma\sigma}(\mathbf{k}, \tau) = \\ \mathcal{G}^{\text{num}}_{\bar\sigma\bar\sigma}(\mathbf{x} = \mathbf{0}, 1^-) \Bigg\{ & n_F(-\xi_{k,\sigma}) \\ & \cdot \left( h^{\text{s-a}}_{(1),11}(\mu_\sigma, \mathbf{k}) + \frac{h^{\text{s-a}}_{(1),12}(\mu_\sigma, \mathbf{k})}{g} + \left( 4\mu + \frac{512\pi^2}{g} + d \right) h^{\text{s-a}}_{(1),13}(\mu_\sigma, \mathbf{k}) \right) \\ & - n_F(\xi_{k,\sigma}) n_F(-\xi_{k,\sigma}) \\ & \cdot \left[ h^{\text{s-a}}_{(1),21}(\mu_\sigma, \mathbf{k}) + \frac{h^{\text{s-a}}_{(1),22}(\mu_\sigma, \mathbf{k})}{g} + \left( 4\mu + \frac{512\pi^2}{g} + d \right) h^{\text{s-a}}_{(1),23}(\mu_\sigma, \mathbf{k}) \right] \Bigg\} \, . \end{aligned}$$

The explicit expressions for these new functions are given in Appendix D.2. Since the integrals can again be interpreted as Fourier transform to $\Omega_n = 0$ and the integrands consist of products of integer and half-integer powers of $\tau$ with an exponential function of $\tau$, these results can be derived from the general formulas given in App. C. Like in the purely analytic case above, the complete set of $h^{\text{s-a}}_{(1)ij}$ are well-defined and acquire a Gaussian prefactor in $\mathbf{k}$ space. Hence, we integrate numerically over momenta by a one-dimensional Fourier transform to $\mathbf{x} = \mathbf{0}$ and sum over both spin components, which yields

$$H^{\text{s-a}}_{2a1} = \sum_\sigma \mathcal{FT}_{k\to r=0} \left( h^{\text{s-a}}_{(1)}(\sigma, \mu, h, g, d, \mathbf{k}) \right) \, . \tag{7.81}$$

The second semi-analytic term from eq. (7.80b) is treated in the same fashion

$$\begin{aligned} h^{\text{s-a}}_{(2)}(\sigma, \mu, h, g, d, \mathbf{k}) = & - \int_0^1 d\tau f_{a,\sigma}(\mathbf{k}, 1-\tau) \Sigma^{\text{s-a}}_{(2),\,\sigma\sigma}(\mathbf{k}, \tau) = \\ & \Gamma^{\text{num}}_{\text{fin}}(\mathbf{x} = \mathbf{0}, 0^+) \left[ n_F(-\xi_{k,\sigma}) h^{\text{s-a}}_{(2),1}(\mu_{\bar\sigma}, \mathbf{k}) - n_F(\xi_{k,\sigma}) n_F(-\xi_{k,\sigma}) h^{\text{s-a}}_{(2),2}(\mu_{\bar\sigma}, \mathbf{k}) \right] , \end{aligned} \tag{7.82}$$

where the functions $h^{\text{s-a}}_{(2),1}$ and $h^{\text{s-a}}_{(2),2}$ can be found in App. D.2. The latter expression contributes

$$H^{\text{s-a}}_{2,a2} = \sum_{\sigma} \mathcal{FT}_{k\to r=0}\left(h^{\text{s-a}}_{(2)}(\sigma,\mu,h,g,d,\mathbf{k})\right) \tag{7.83}$$

to $H_2[G]$. Finally, we have to consider the self-energies $\Sigma^{\text{num}}_{(1),\,\sigma\sigma}$ and $\Sigma^{\text{num}}_{\sigma\sigma}(\mathbf{k},\tau)$. For the first we actually have an analytic expression available, however, the function is well-behaved enough in $\tau$ that we can directly use our numerical routines like in the self-consistent loop. In this case we obtain

$$\begin{aligned} H^{\text{num}}_{2,a}[G] =& \sum_{\sigma} \int \frac{d^3k}{(2\pi)^3} \int_0^1 d\tau f_{a,\sigma}(\mathbf{k},1-\tau)(\Sigma^{\text{num}}_{(1),\,\sigma\sigma}(\mathbf{k},\tau) + \Sigma^{\text{num}}_{\sigma\sigma}(\mathbf{k},\tau)) \\ =& \sum_{\sigma} \mathcal{F}_{k\to r=0}\left[\mathcal{F}_{\tau\to 0}\left[f_{a,\sigma}(\mathbf{k},1-\tau)(\Sigma^{\text{num}}_{(1),\,\sigma\sigma}(\mathbf{k},\tau) + \Sigma^{\text{num}}_{\sigma\sigma}(\mathbf{k},\tau))\right]\right], \end{aligned} \tag{7.84}$$

with a DFT to the *bosonic* Matsubara frequency $\Omega_n = 0$. Finally, we can piece together the complete expression for the auxiliary functional $H_2[G]$ in the BCS case

$$H_2[G] = H^{\text{ana}}_{2a}[G] + H^{\text{s-a}}_{2a1}[G] + H^{\text{s-a}}_{2a2}[G] + H^{\text{num}}_{2a}[G] + H^{\text{num}}_{2b}[G]\,. \tag{7.85}$$

Now we have to repeat the computation in the BEC scheme. Fortunately, the overall approach remains identical and we merely have to incorporate the changes that arise from the different form of the Green's functions. First of all, the integral

$$\begin{aligned} -\int_0^1 d\tau f_{a,\sigma}(\mathbf{k},1-\tau)\Sigma^{\text{ana}}_{\text{fin},\,\sigma\sigma}(\mathbf{k},\tau) = e^{\mu_{\bar\sigma}}\,[&n_F(-\xi_{k,\sigma})h^{\text{ana}}_1(\mu_\sigma,\mathbf{k}) \\ &- n_F(\xi_{k,\sigma})n_F(-\xi_{k,\sigma})h^{\text{ana}}_2(\mu_\sigma,\mathbf{k}))]\,, \end{aligned} \tag{7.86}$$

acquires a slightly different dependence on the chemical potentials, since they appear in the exponent according to eq. (7.62), when the BEC code is used. Furthermore, the functions $h^{\text{ana}}_1$ and $h^{\text{ana}}_2$ have to be redefined, due to the $d$ dependence of $\Sigma^{\text{ana}}_{\text{fin},\,\sigma\sigma}(\mathbf{k},\tau)$ in contrast to the BCS case. Their new definitions can be found in App. D.2. Similarly, we also have to adjust the definition of the functions $h^{\text{s-a}}_{(2),1}$ and $h^{\text{s-a}}_{(2),2}$, since they include $\mathcal{G}^{\text{ana}}_{\bar\sigma\bar\sigma}(\mathbf{k},\tau)$. Again their BEC definitions are listed in App. D.2. Once all the new BEC forms of the auxialliary functions have been inserted the definitions in eq. (7.85) can be reused to calculate $H_2[G]$.

### 7.3.5 Evaluation of $H_{\log}[\Gamma]$

As we have already discussed in Sec. 4.7, the original form of the functional $H_{\log}[\Gamma]$ in eq. (4.43) was not well-defined and we had to construct a suitable subtraction

scheme. We introduced the parameter $d$, which rendered the unpleasant terms irrelevant and we finally arrived at the representation in eq. (4.44), which in dimensionless units becomes

$$\begin{aligned} H_{\log}[\Gamma] &= \frac{1}{2}\int \frac{d^3Q}{(2\pi)^3}\sum_n e^{i\Omega_n 0^+}\log\left[1+\frac{\Gamma^{-1}\left(\mathbf{Q},\Omega_n\right)-\alpha\sqrt{Q^2+d-2i\Omega_n}}{\alpha\sqrt{Q^2+d-2i\Omega_n}}\right] \\ &= \frac{1}{2}\int \frac{d^3Q}{(2\pi)^3}\sum_n e^{i\Omega_n 0^+}\log\left[1+\frac{\Gamma^{-1}\left(\mathbf{Q},\Omega_n\right)-\alpha\sqrt{X_d^b}}{\alpha\sqrt{X_d^b}}\right]. \end{aligned} \tag{7.87}$$

Note that we have redefined the parameter $\alpha = -m^{3/2}/(4\pi\hbar^3)$ from Sec. (4.7) to the new form $\alpha/\sqrt{2} = -1/(16\pi)$ in dimensionless units, which conveniently absorbs most of the numerical factors in the original expression. The mathematical expression of $H_{\log}$ still requires the convergence factor, since otherwise the Matsubara sum diverges. This can be seen from the asymptotics $\Gamma\left(\mathbf{Q},\Omega_n\right) = \alpha\left(X^b\right)^{-1/2} + \mathcal{O}(1/X^b)$, which follows from the asymptotic form of the analytic terms in the vertex (7.34), that imply a scaling $\sim (X^b)^{-1/2}$ for the logarithm. In this form we cannot utilize our Fourier transform routines and have to develop for one last time a subtraction scheme. Again we will start with the BCS code.

To gain further insight into the asymptotics of $H_{\log}[\Gamma]$ we first expand the full integrand in detail, where we make us of the definitions (7.33) and (7.20)

$$\begin{aligned} &\log\left[1+\frac{\Gamma^{-1}-\alpha\sqrt{X_d^b}}{\alpha\sqrt{X_d^b}}\right] = \log\left[1+\frac{\frac{1}{g}+\chi^{\text{ana}}+\chi^{\text{s-a}}+\chi^{\text{num}}}{\alpha\sqrt{X_d^b}}\right] \\ &= \log\left[1+\frac{\frac{1}{g}+E_0-\alpha\sqrt{X_d^b}+\mu E_1+(\mu+h)(\mu-h)E_2+\chi^{\text{s-a}}+\chi^{\text{num}}}{\alpha\sqrt{X_d^b}}\right]. \end{aligned} \tag{7.88}$$

Listing the asymptotic behavior of all the terms, we have $1/g \sim (X^b)^0$, both $\left(E_0-\alpha(X_d^b)^{1/2}\right)$ and $E_1 \sim (X^b)^{-1/2}$, while finally $E_2$ and $(\chi^{\text{s-a}}+\chi^{\text{num}}) \sim (X^b)^{-1}$. For further details we refer to Section (7.2.2). To achieve a function that is benign enough for a numerical approach we separate all contributions of the logarithm, that asymptotically approach zero at more slowly than $\sim (X^b)^{-5/2}$ and treat them separately. To this end, we make use of the Taylor expansion of the logarithm and

define the new auxiliary function

$$
\begin{aligned}
&h_{\log}\left(\mathbf{Q},\Omega_n\right) = \\
&\log\left[1+\frac{\frac{1}{g}+E_0-\alpha\sqrt{X_d^b}+\mu E_1+\left(\mu+h\right)\left(\mu-h\right)E_2+\chi^{\text{s-a}}+\chi^{\text{num}}}{\alpha\sqrt{X_d^b}}\right] \\
&-\frac{\frac{1}{g}+E_0-\alpha\sqrt{X_d^b}+\mu E_1+\left(\mu+h\right)\left(\mu-h\right)E_2+\chi^{\text{s-a}}+\chi^{\text{num}}}{\alpha\sqrt{X_d^b}} && \text{(7.89a)} \\
&+\frac{\frac{1}{g^2}+\frac{2}{g}\left(E_0-\alpha\sqrt{X_d^b}+\mu E_1+\left(\mu+h\right)\left(\mu-h\right)E_2+\chi^{\text{s-a}}+\chi^{\text{num}}\right)}{2\alpha^2 X_d^b} \\
&+\frac{\left(E_0-\alpha\sqrt{X_d^b}+\mu E_1\right)^2}{2\alpha^2 X_d^b} && \text{(7.89b)} \\
&-\frac{\frac{1}{g^3}+\frac{3}{g}\left(E_0-\alpha\sqrt{X_d^b}+\mu E_1\right)}{3\alpha^3(X_d^b)^{3/2}} && \text{(7.89c)} \\
&+\frac{1}{4g^4\alpha^4(X_d^b)^2}, && \text{(7.89d)}
\end{aligned}
$$

where the labeling of the lines from a to d indicates the order of the Taylor expansion, in which the individual subtractions appear. Including terms up to quartic order is necessary to make $h_{\log}$ scale as $(X^b)^{-5/2}$. Now the latter can be transformed numerically at the expense of solving the Matsubara sums and momentum integrals of the 22 separated terms manually. We will turn to this task now.

First of all, we note that we can simply neglect all powers of $1/(g\alpha X_d^b)$, since rewriting the sum by a contour integration yields an exponential suppression from the Bose function $n_B(d/2)$, that originates from the nonanalyticities in the denominators. In practice, these terms are on the order of $10^{-11}$, if $d = 150$, which is way below the precision of the other computations. Therefore, we immediately get rid of four terms.

All terms linear in the functions $E_i$ can be transformed in closed form up to exponentially small corrections by the help of Parseval's theorem (7.69). We will discuss the procedure on the example of $E_0 - \alpha\sqrt{X_d^b}$, which appears in the first order contribution from line (7.89a). In fact, we always consider the difference $E_0 - \alpha\sqrt{X_d^b}$ as one entity to obtain an asymptotic decrease rather than a growth. In contrast, the other error functions are treated as individual functions for the back transformation to imaginary time. To apply the theorem we have to find the representation of $E_0 - \alpha\sqrt{X_d^b}$ and $1/\sqrt{X_d^b}$ in imaginary time. For the latter we use

the exact Fourier transform

$$\mathcal{F}_{\tau\to\Omega_n}\left[u_1\left(\mathbf{Q},\tau\right)\right]\left(\Omega_n\right) = \mathcal{F}_{\tau\to\Omega_n}\left[\frac{e^{\frac{\tau\left(Q^2+d\right)}{2}}}{\sqrt{2\pi\tau}}\right]$$
$$= \frac{\operatorname{erf}\left(\sqrt{\frac{1}{2}X_d^b}\right)}{\sqrt{X_d^b}} = \frac{1+\left(\operatorname{erf}\left(\sqrt{\frac{1}{2}X_d^b}\right)-1\right)}{\sqrt{X_d^b}}, \tag{7.90}$$

which results from eq. (C.16). The term in the brackets vanishes exponentially with $d \gg 1$, according to eq. (C.2) and will be neglected in the following. Now we have to consider the Fourier transform of $E_0 - \alpha(X_d^b)^{1/2}$ to $\tau$. First we rewrite this function as

$$\left(E_0 - E_0^{\mathrm{sub}}\right) + \left(E_0^{\mathrm{sub}} - \alpha(X_d^b)^{1/2}\right),$$

where the second part behaves like $\exp(-d/2)$ due to the asymptotics of the error function and therefore needs not be taken into account any further. We note that the remainder can be interpreted as the inverse Fourier transform of

$$\mathcal{F}_{\tau\to\Omega_n}\left[\frac{e^{-\frac{\tau}{2}Q^2}\left(1-e^{-\frac{\tau d}{2}}\right)}{16\sqrt{2}\pi^{3/2}\tau^{3/2}}\right] = E_0\left(\mathbf{Q},\Omega_n\right) - E_0^{\mathrm{sub}}\left(\mathbf{Q},\Omega_n\right), \tag{7.91}$$

according to App. C. Plugging both Fourier transforms with the correct prefactors into Parseval's theorem (7.69) results in

$$P_{10}^{\mathrm{ana}} = -\int\frac{d^3Q}{(2\pi)^3}\sum_n\frac{E_0-\alpha\sqrt{X_d^b}}{\alpha\sqrt{X_d^b}} =$$
$$-e^{-\frac{d}{2}}\int\frac{d^3Q}{(2\pi)^3}e^{-\frac{Q^2}{2}}\int_0^1 d\tau\frac{e^{\frac{\tau d}{2}}-1}{2\pi\tau^{3/2}\sqrt{1-\tau}} = -\frac{de^{-\frac{d}{4}}}{8\sqrt{2}\pi^{3/2}}\left[\mathrm{I}_0\left(\frac{d}{4}\right)-\mathrm{I}_1\left(\frac{d}{4}\right)\right], \tag{7.92}$$

where we abbreviate Parseval with the letter $P$, while the index 10 refers to the linear order term that arises from $E_0$. Notice that the integral above factorizes into a simple Gaussian one over all momenta and a well-defined integral over the imaginary time interval because the integrand is integrable both at the $\tau \to 0^+$ and the $\tau \to 1^-$ boundaries. A derivation of this result, where $\mathrm{I}_0$ and $\mathrm{I}_1$ denote modified Bessel functions of the first kind, is given in App. D.3. The other analytic Parseval terms obtained below can be calculated in a similar manner. We reemphasize that the second "=" holds only up to exponentially small corrections. Moreover, the exponential prefactor cancels the exponential growth of the Bessel functions identically, leading to sensible results for the thermodynamic quantities. In the

linear order subtraction in eq. (7.89) also the functions $E_1$ and $E_2$ appear, which can treated in a similar manner by the Parseval trick. They corresponding results read

$$P_{11}^{\text{ana}} = -\frac{1}{(2\pi))^{3/2}} e^{-\frac{d}{4}} \mathrm{I}_0\left(\frac{d}{4}\right) \tag{7.93}$$

$$P_{12}^{\text{ana}} = -\frac{1}{2^{7/2}\pi^{3/2}} e^{-\frac{\beta d}{4}} \left[\mathrm{I}_0\left(\frac{d}{4}\right) + \mathrm{I}_1\left(\frac{d}{4}\right)\right], \tag{7.94}$$

yielding the total analytic contribution of the first order

$$P_1^{\text{ana}} = P_{10}^{\text{ana}} + \mu\, P_{11}^{\text{ana}} + (\mu + h)(\mu - h) P_{12}^{\text{ana}}. \tag{7.95}$$

The quadratic order can be computed analogously, where we first note that

$$\mathcal{FT}_{\tau\to\Omega_n}\left[u_2\left(\mathbf{Q},\tau\right)\right] = \mathcal{FT}_{\tau\to\Omega_n}\left[\frac{1}{2} e^{-\frac{\tau}{2}\left(Q^2+d\right)}\right] = \frac{1 - e^{-\frac{1}{2}X_d^b}}{X_d^b}. \tag{7.96}$$

The exponential in the numerator can again be neglected for all frequencies and momenta thanks to $d$. We repeat the procedure as before and use Parseval's theorem on all the error functions, which gives

$$P_{20}^{\text{ana}} = \frac{2e^{-\frac{d}{2}}}{\pi}\left(2 - 2e^{\frac{d}{2}} + \sqrt{2\pi d}\,\mathrm{erfi}\left(\sqrt{\frac{d}{2}}\right)\right) \tag{7.97}$$

$$P_{21}^{\text{ana}} = \frac{4\sqrt{2}e^{-\frac{d}{2}}}{\sqrt{\pi d}}\mathrm{erfi}\left(\sqrt{\frac{d}{2}}\right) \tag{7.98}$$

$$P_{20}^{\text{ana}} = \frac{4}{\pi d^{3/2}}\left(\sqrt{d} - \sqrt{2}F_D\left(\sqrt{\frac{d}{2}}\right)\right), \tag{7.99}$$

where $\mathrm{erfi}(z) = \mathrm{erf}(iz)/i$ and $F_D$ denotes the Dawson integral

$$F_D(x) = e^{-x^2}\int_0^x dy e^{y^2}.$$

Summing them together yields the analytic Parseval term of the quadratic order

$$P_2^{\text{ana}} = P_{20}^{\text{ana}} + \mu\, P_{21}^{\text{ana}} + (\mu + h)(\mu - h) P_{22}^{\text{ana}}. \tag{7.100}$$

Finally, we deal with the cubic order in line (7.89c) in the same way. For the Parseval trick we first need the Fourier transformation of $(X_d^b)^{-3/2}$, which is

$$\begin{aligned}\mathcal{FT}_{\tau\to\Omega_n}\left[u_3\left(\mathbf{Q},\tau\right)\right] &= \mathcal{FT}_{\tau\to\Omega_n}\left[\frac{\sqrt{\tau}}{\sqrt{2\pi}} e^{-\frac{\tau}{2}}\left(Q^2 + d\right)\right] \\ &= \frac{1 + \left(\mathrm{erf}\left(\sqrt{\frac{X_d^b}{2}}\right) - 1\right)}{(X_d^b)^{3/2}} - \frac{\sqrt{2}e^{-\frac{1}{2}\left(Q^2+d\right)}}{\sqrt{\pi}X_d^b},\end{aligned} \tag{7.101}$$

where only the first term has to be considered, whereas the remainder is exponentially small in $d$. Using this result we go on and compute the two analytical Parseval terms and the total cubic contribution

$$P_{30}^{\text{ana}} = -\frac{32\sqrt{\pi}e^{-\frac{d}{2}}}{\sqrt{2}}\left[2 + e^{\frac{d}{4}}\left((d-2)\mathrm{I}_0\left(\frac{d}{4}\right) - d\mathrm{I}_1\left(\frac{d}{4}\right)\right)\right] \tag{7.102}$$

$$P_{31}^{\text{ana}} = -\frac{64\sqrt{\pi}e^{-\frac{d}{4}}}{\sqrt{2}}\left[\mathrm{I}_0\left(\frac{d}{4}\right) - \mathrm{I}_1\left(\frac{d}{4}\right)\right] \tag{7.103}$$

$$P_{3}^{\text{ana}} = P_{30}^{\text{ana}} + \mu\, P_{31}^{\text{ana}}. \tag{7.104}$$

Taking all analytic Parseval results together, we can solve eleven of the 22 subtraction terms of eq. (7.89) in closed form. Now we will deal with the two $\chi^{\text{s-a}} + \chi^{\text{num}}$ contributions of eq. (7.89a), which we can compute with the numerical analog of the analytical Parseval trick:

$$\begin{aligned} P_1^{\text{num}} =& \int \frac{d^3Q}{(2\pi)^3} \sum_n \frac{\chi^{\text{s-a}}(\mathbf{Q},\Omega_n) + \chi^{\text{num}}(\mathbf{Q},\Omega_n)}{\alpha\sqrt{X_d^b}} \\ =& \mathcal{FT}_{Q\to r=0}\left[\mathcal{FT}_{\tau\to\Omega_n=0}\left[u_1(\mathbf{Q},1-\tau)\frac{\chi^{\text{s-a}}(\mathbf{Q},\tau) + \chi^{\text{num}}(\mathbf{Q},\tau)}{\alpha}\right]\right] \end{aligned} \tag{7.105}$$

$$\begin{aligned} P_2^{\text{num}} =& \int \frac{d^3Q}{(2\pi)^3} \sum_n \frac{\chi^{\text{s-a}}(\mathbf{Q},\Omega_n) + \chi^{\text{num}}(\mathbf{Q},\Omega_n)}{\alpha^2 X_d^b} \\ =& \mathcal{FT}_{Q\to r=0}\left[\mathcal{FT}_{\tau\to\Omega=0}\left[u_2(\mathbf{Q},1-\tau)\frac{\chi^{\text{s-a}}(\mathbf{Q},\tau) + \chi^{\text{num}}(\mathbf{Q},\tau)}{\alpha^2}\right]\right], \end{aligned} \tag{7.106}$$

where the functions $u_1$ and $u_2$ are defined in equations (7.90) and respectively in (7.96).

Now only the single term $(E_0 - \alpha(X_d^b)^{1/2} + \mu E_1^2/(2\alpha^2 X_d^b) \sim (X^b)^{-2}$ from line (7.89b) is left. It cannot be transformed by Parseval's theorem again, since the expressions in imaginary time are unknown in case of the quadratic numerator. Nevertheless, we deal with an analytical expression and we can proceed by subtracting the problematic asymptotics, yet in terms of $X_d^b$:

$$\begin{aligned} h_{\text{last}} :=& \frac{\left(E_0 - \alpha\sqrt{X_d^b} + \mu E_1\right)^2}{(2\alpha^2 X_d^b)} \\ =& \left(\frac{\left(E_0 - \alpha\sqrt{X_d^b} + \mu E_1\right)^2}{(2\alpha^2 X_d^b)} - \frac{\left(\frac{d}{32\pi} + \frac{\mu}{8\pi}\right)^2}{\alpha^2 (X_d^b)^2}\right) - \frac{\left(\frac{d}{32\pi} + \frac{\mu}{8\pi}\right)^2}{\alpha^2 (X_d^b)^2}. \end{aligned} \tag{7.107}$$

With this step we have achieved that the term in brackets asymptotically scales like $(X^b)^{-5/2}$, whereas the additional term can be neglected as its poles are shifted by $d/2$ and thus give rise to exponentially small and therefore negligible contributions.

Now we can perform the Matsubara sum and the momentum integration, which yields

$$H_{\text{last}} = \int \frac{d^3Q}{(2\pi)^3} \sum_n h_{\text{last}}\left(\mathbf{Q}, \Omega_n\right) = \mathcal{FT}_{Q\to r=0} \mathcal{FT}_{\Omega_n \to \tau = 0^+} \left[h_{\text{last}}\left(\mathbf{Q}, \Omega_n\right)\right] \quad (7.108)$$

Now we are done with all parts of the auxilliary functional $H_{\log}[\Gamma]$ and summarize its final form

$$H_{\log}[\Gamma] = H_{\log}^{\text{num}}[\Gamma] + P_1^{\text{ana}} + P_1^{\text{num}} - \frac{1}{2}\left(\frac{2\left(P_2^{\text{ana}} + P_2^{\text{num}}\right)}{g} + H_{\text{last}}\right) + \frac{3}{3g^2} P_3^{\text{ana}} . \quad (7.109)$$

The last issue we have to deal with regards the adjustments required for the BEC code. In this case we have to recall that in the expansion of the analytic part $\chi_{\text{fin}}^{\text{ana}}\left(\mathbf{Q}, \Omega_n\right)$ from eq. (7.28) the prefactor of $E_2$ changes from $\mu^2 - h^2$ to $2\mu^2$, which implies the same replacement for the prefactors of the analytic Parseval terms (7.95) and (7.100). Additionally, one could also use the fact that $\chi_{(1)}^{\text{num}}\left(\mathbf{Q}, \tau\right)$ from eq. (7.27) is known analytically in imaginary time. Then one can treat this contribution in imaginary time by the Parseval trick. However, we have not implemented this additional decomposition, since $\chi_{(1)}^{\text{num}}\left(\mathbf{Q}, \Omega_n\right)$ does not cause numerical problems.

## 7.4 Further specifications on the numerical implementations

In this section we summarize the numerical specifications of the code for the imbalanced Fermi gas. We begin with the grids for Fourier transformations in Sec. 7.4.1 and turn afterwards in Sec. 7.4.2 to the convergence criteria. Special focus is given to the the regime close to the critical temperature, which is the most difficult situation to find a solution for the Green's function due to the vicinity of a divergence in $|\Gamma(\mathbf{Q}, \Omega_n = 0)|$.

### 7.4.1 Grids for the Fourier transformations

In case of the transformations between $\tau \leftrightarrow \omega_n$ or $\tau \leftrightarrow \Omega_n$, respectively, we use a spline DFT described in Sec. 6.2. Starting in imaginary time we use cubic splines, while the for the inverse transformation we have implemented also quintic splines. The additional precision from the higher degree of the interpolation turns out to be useful for the $\Gamma\left(\mathbf{Q}, \Omega_n\right) \to \Gamma\left(\mathbf{Q}, \tau\right)$ transformation, which after transformation to real space is multiplied by the Green's function $\mathcal{G}_{\bar{\sigma}\bar{\sigma}}(-\mathbf{x}, 1-\tau)$ with reversed particle flow to obtain the self-energy. As mentioned previously, this step is particularly sensitive to numerical noise because $\Gamma\left(\mathbf{x}, \tau\right)$ is peaked around $\tau = 0^+$, whereas

$\mathcal{G}_{\bar{\sigma}\bar{\sigma}}(-\mathbf{x}, 1-\tau)$ attains its largest values around the opposite boundary $\tau = 1^-$, such that each factor enhances the errors in the other one.

In frequency space we separate $G$ and $\Gamma$ into real and imaginary parts. Since all real parts are even functions and all imaginary parts are odd functions, we use these symmetries to work exclusively on positive Matsubara frequencies. In case of the bosonic frequencies our grid of in total $N = 512$ points contains all the eighty smallest $\Omega_n$. Larger frequencies are joined with an exponential scaling, such that $\Omega_{\max} \simeq 2\pi 10^{10}$. Since the slowest asymptotics in frequency space that we have to treat numerically in the self-consistent loop scales like $\Omega_n^{-5/2}$, we estimate the truncation errors from the finite interval as $\Omega_{\max}^{-3/2} \lesssim 10^{-16}$ just below machine precision. With this maximal frequency, faster asymptotics, as would appear in higher order derivatives, are irrelevant. On the other hand, we describe the limit of small Matsubara frequencies exactly, anyway. Therefore, the choice of boundary conditions for the spline interpolation does not matter, as already stated in Sec. 6.2. For the fermionic frequencies we use the same grid shifted by $\pi$.

To sample the imaginary time interval we define the auxiliary function

$$f(n) = 1 - \frac{2}{\pi} \arctan(e^{-(n+N/2+1/2)\alpha}) \,, \tag{7.110}$$

where we choose the parameter $\alpha = 10/(55\pi) \simeq 0.058$, which is responsible for distances between adjacent $\tau$ points close to the boundaries. The $\tau$ points are then calculated via

$$\tau_n = \frac{f(n) - f(1)}{(f(N) - f(1))\,(1 + 2\delta)} + \delta \,, \tag{7.111}$$

where $n \in \{1, 2, ..., 512\}$. This construction samples the imaginary time interval symmetrically up to exponentially small corrections below the floating point precision. Furthermore, we obtain an exponentially dense grid at the boundaries, where the major contributions of the $G$ and $\Gamma$ are located. The additional variable $\delta = 10^{-9}$ directly controls the smallest $\tau$ point. Note that the exponentially dense points at the boundaries $\tau \to 0^+$ and $\tau \to 1^-$ entail exponentially small weights for the Fourier integrals, such that the boundary conditions again do not matter for the spline DFT. Unfortunately, one encounters numerical errors from the phase factors $\exp(i\tau_{\max}\Omega_n) \simeq 1$ in the limit of large Matsubara frequencies due to the limited numerical precision. To improve the results of the Fourier transform we use instead the shifted interval $\tau_n \in [-0.5, 0.5]$, since in the DFT the problematic boundary terms are now multiplied with the smallest function values from the center of the original interval.

Regarding the transformation between real and momentum space, the standard routine is an LFT on a grid of $N = 512$ points both in $\mathbf{x}$ or $\mathbf{k}$. Since we use the same grid for bosonic and fermionic functions, we do not distinguish between the letters $\mathbf{k}$ and $\mathbf{Q}$ in the following. The grid parameters in the formulation of

eq. (6.10) read

$$\Delta k = \frac{3}{80}\,, \qquad \bar{k} = -\frac{N}{2} - 1 + \frac{\log(100)}{\Delta k} \simeq -134.2 \tag{7.112a}$$

$$\Delta s = \frac{5\pi}{48}\,, \qquad \bar{s} = -\frac{N+1}{2} \tag{7.112b}$$

$$\Delta x = \frac{3}{80}\,, \qquad \bar{x} = -\frac{N}{2} - 1 - \frac{\log(3)}{\Delta x} \simeq -286.3\,. \tag{7.112c}$$

The smallest momentum $k_{\min} \simeq 0.0068$ resolves the low-momentum degrees of freedom. On the other hand, the largest momentum $k_{\max} = 1.4 \cdot 10^6$ gives rise to $k_{\max}^2 \tau_{\min}/2 \simeq 1000$, such that also in the bosonic functions the Gaussian decay at large momenta is resolved. See for example the analytical the particle-particle bubble (7.15), whose Gaussian behavior is inherited by the numerical functions. Choosing $k_{\max}$ too small, in turn, yields an almost constant function in case of the smallest $\tau \to 0$, which cannot be transformed by the LFT due to the restriction eq. (6.8). In real space we have the contribution $x_{\min}^2/(4\tau_{\min}) \simeq 0.13$ from fermionic functions, which samples the typical behavior $\exp(-x^2/(4\tau))$ densely enough to obtain smooth plateaus in the numerical functions at the smallest $x$ and $\tau$ values. To improve the results from the LFT, we extrapolate the height of these plateaus to $x = 0$ and add the corresponding term to the Fourier transform. The used trade-off parameters are $k_p = -0.1$ for $k \to x$ and $k_p = -0.5$ for $x \to k$, respectively. For the computations of the thermodynamic quantities that can be considered as a transformation to $\mathbf{x} = 0$ we use $k_p = -0.8$ to improve the results at the origin.

On these grids the code runs with about ten loops per second on a modern desktop computer.

However, in the weak coupling limit the critical temperature $\theta_c = \exp(-\pi|v|/2)$ becomes exponentially small and conversely we have to deal with large chemical potentials, especially of the majority component $\hat{\mu}_\uparrow = \mu + h$. This leads to a sharp variation of $\mathcal{G}_{\sigma\sigma}(\mathbf{k}, \tau)$ around $k^2 \simeq \mu_\sigma$, which causes problems for the LFT, see Sec. 6.1.2. Therefore, we switch to a DFT with an increased number of grid points around the dressed Fermi energy. Technically, we define an extra grid with 2100 $k$ points between 6.4 and 60. In the interval $6.4 \leqslant k \leqslant 11$, we distribute 240 points according to the square-root scaling $k^{1/2}/3$ to obtain a sampling with an approximately constant step width in the quadratic $k^2$ argument of the Green's and vertex functions. The remaining 1960 points between $11 < k < 60$ follow the power law $k^{2/3.2}/3$ to reach larger momenta. Nevertheless, even this choice keeps the sampling density below 1, in contrast to the exponentially growing steps of the LFT grid. Note that, we have to compute all the analytical functions on this very large grid during the initialization. To determine the spin-dependent, dressed Fermi levels, we search for the sign change of $\mathrm{Re}\,\mathcal{G}_{\sigma\sigma}(\mathbf{k}, \omega_n = \pi)^{(-1)}$ as function of $k$ for both spin components. If the obtained $k_{0\sigma} \geqslant 6.4$, which corresponds to the onset of the denser grid, we increase the sampling density by up to 200 extra points around the corresponding Fermi edge. In case of an overlap of the dense

intervals around both Fermi levels or an overlap with a region where the LFT grid has the higher sampling density, we reduce the number of points correspondingly for the sake of computational effort. Moreover, we use cubic splines here, since the required DFT matrices (see (6.70)) have to be created during the loop and the resulting tridiagonal matrix can be solved more quickly. In practice, this allows to treat $\hat{\mu}_\uparrow \lesssim 2000$. In case of an FFLO instability we use a similar construction with another grid of 400 extra points between $k = 1$ and $k = 5$ with equidistant spacings of $1/100$. If the dominant value of $|\Gamma(\mathbf{Q}, \Omega_n = 0)|$ appears at a finite $Q$, where the differences between neighboring points of the LFT grid are larger than $1/100$ we use up to 200 points of the FFLO grid to sample the vertex functions sufficiently well around its maximum. Of course the larger number of grid points slows the evaluation down, but we still achieve a few loops per second.

### 7.4.2 Stabilization of the convergence

As we have seen in Sec. 7.2, all the analytic functions that appear in the subtraction schemes depend on the variables $\mu, h$ and $g$ only via a prefactor that in turn does not vary with momentum and frequency or position and time, respectively. Therefore, the parts that are genuine functions of the latter arguments are static with respect to $\mu, h$ and $g$ and can be computed once during the initialization and stored for the self-consistent loop. We will return to that issue below, since it is also quite important for the convergence in the critical regime. The main step of the self-consistent loop is to compute from the current Green's function $G_{\text{curr}}$ the next Green's function $G_{\text{next}}$. Close to the phase transition, where $|\Gamma(\mathbf{Q}, \Omega_n = 0)|$ becomes increasingly large at the unstable momentum $Q$, however, the Green's function becomes very sensitive and the convergence very unstable, since the large value of the vertex influences $G$ via the self-energy. Therefore, it can be necessary to reduce the rate with which the Green's function is updated via

$$G_{\text{next}} = \delta G[G_{\text{curr}}] + (1 - \delta) G_{\text{curr}} \,, \tag{7.113}$$

where the update parameter $\delta$ has to be chosen in $(0, 1]$ and $G[G_{\text{curr}}]$ denotes the Green's function that would be obtained from the self-energy after a single iteration with $G_{\text{curr}}$. With this prescription we accept a Green's as the self-consistent solution to the Schwinger-Dyson equation, if the criterion

$$\frac{1}{\delta} \sum_{k,\omega_n} |G_{\text{next}} - G_{\text{curr}}| \leqslant 10^{-8} \,. \tag{7.114}$$

Here the sum runs over all grid points and the prefactor takes into account for the reduced updates. Away from the critical region, where we can always work with $\delta = 1$, we achieve convergence within ten to 50 iterations. When one approaches the critical temperature and the update parameter has to be reduced it turns out

to be very helpful to fix the inverse vertex at a certain value $\Gamma_0^{-1}$

$$\Gamma^{-1}(\mathbf{Q}, \Omega_n = 0) = \Gamma_0^{-1} = \frac{1}{g} + \chi(\mathbf{Q}, \Omega_n = 0)\,, \tag{7.115}$$

instead of directly iterating the computations for the loop. To satisfy the equation with the current particle-particle bubble $\chi(\mathbf{Q}, \Omega_n = 0)$ one adjusts the coupling constant $g$. This criterion is of course applied to the momentum, where $|\Gamma(\mathbf{Q}, \Omega_n = 0)|$ exhibits its maximum, which can change during with the iterations. Typically, the variations of $g$ are small and since we are interested in phase diagram the entire BCS-BEC crossover, we can scan the entire phase diagram without any extra cost. Here we make again use of the fact that $g$ appears as simple prefactor in the analytical parts, which can be updated very efficiently. Much more importantly, this way reduces the number of required iterations from several hundred down to around 50 for the transition to the homogeneous superfluid. In case of the FFLO instability still 500-1000 iterations are needed. Yet, without fixing the vertex the code would run on the order of $10^4$ times, since the convergence is very unstable and the update parameter $\delta$ has to be chosen very small. In this not only the large vertex makes the Green's function very sensitive, but also the fact that the momentum $Q$ at which the maximum of $|\Gamma^{-1}(\mathbf{Q}, \Omega_n = 0)|$ is detected changes with the iterations, which worsens the convergence. In particular, this becomes problematic in the vicinity of the Lifshitz point L (see Figure 3.4), where superfluid phases with $Q = 0$ and finite $Q_{\mathrm{FFLO}}$ neighbor each other and the unstable momentum can jump between both types of order. Therefore, we use a reduced update also for the vertex function in analogy to eq. (7.113) and distinguish between the current vertex function $\Gamma_{\mathrm{curr}}$, the vertex that is obtained from the current Green's function $\Gamma[G_{\mathrm{curr}}]$ and finally the vertex that shall be used in the next loop $\Gamma_{\mathrm{next}}$. In this case we use a local version

$$\Gamma_{\mathrm{next}}\left(\mathbf{Q}, \Omega_n\right) = \Gamma_{\mathrm{curr}}\left(\mathbf{Q}, \Omega_n\right) + \left(\frac{\Gamma[G_{\mathrm{curr}}] - \Gamma_{\mathrm{curr}}}{1 + \alpha\Gamma_{\mathrm{curr}}^{1/4}}\right)\left(\mathbf{Q}, \Omega_n\right)\,, \tag{7.116}$$

where $\alpha = 10$. This model leads to large updates of the small parts of the vertex, while the region of the emergent singularity that signals the phase transition changes much more slowly. As a result, the convergence is improved. To avoid stabilizing a wrong solution with an unphysical type of order for the given set of parameters one has to test the obtained preliminary Green's function by relaxing the above condition on the vertex and check that it remains a solution of the unbiased loop. Unfortunately, it is very difficult to find a model for the update that works for all set of thermodynamic variables and for example it can be helpful to increase the parameter $\alpha$ or use $\Gamma_{\mathrm{curr}}^{1/2}$ in the denominator.

For the transition to the homogenous superfluid we can determine the critical point very precisely. First we find a physical Green's function at a fixed value of the inverse vertex that is already close to zero, i.e. $\Gamma_0^{-1} \simeq -10^{-4}$. The corresponding

physical inverse vertex satisfies $\Gamma^{-1}(\mathbf{Q}_{\min}, \Omega_n = 0) = \Gamma_0^{-1}$, where $\mathbf{Q}_{\min}$ is the minimal momentum in the numerical grid. Then we fit the curve $(a + bQ^2)$, with fit parameters $a, b$ to the low-momentum behavior of $\Gamma^{-1}(\mathbf{Q}_{\min}, \Omega_n = 0)$ and set the critical inverse vertex to $\Gamma_c^{-1} = bQ_{\min}^2$. Finally, we run the code with $\Gamma_c^{-1}$ inserted into the fixing criterion for the vertex (7.115). This yields the quadratic scaling of the vertex function at the critical point, shown in Fig. 5.1. If $|bQ_{\min}^2| \leqslant 10^{-7}$, we choose $\Gamma_c^{-1} = -10^{-7}$, since the numerical Fourier transforms cannot produce cancellations below that level. Nevertheless, we have guaranteed a critical vertex of at least $|\Gamma_c(\mathbf{Q} \to 0, \Omega_n = 0)| = 10^7$ even in this situation. In case of an FFLO instability, we unfortunately do not resolve the momentum regime around $Q_{\mathrm{FFLO}}$ well enough to apply an equivalent fitting routine, since it is located outside of the exponentially dense region of the LFT grid. Therefore, we try maximize $|\Gamma_c(\mathbf{Q}_{\mathrm{FFLO}} \to 0, \Omega_n = 0)|$ as good as possible. Due to the worse convergence (see the discussion above) we accept in the FFLO case $|\Gamma_c(\mathbf{Q}_{\mathrm{FFLO}} \to 0, \Omega_n = 0)| > 10^5$ as critical.

# Chapter 8

# Transport properties of the unitary Fermi gas

The high degree of control over the external parameters and the isolation from the environment of trapped ultracold Fermi gases allows to extend the investigation of the physical properties beyond the static, thermodynamic quantities to dynamical aspects. In this regard, the spectral functions and the response to an RF field have been investigated both experimentally and theoretically[1]. For details on this rich field we refer the reader to the lectures by Zwerger [42]. In the following, we will focus on transport properties of the balanced unitary Fermi gas, which is the most interesting case in the strongly interacting regime of the BCS-BEC crossover. Further details can again be found in Ref. [42]. Like in any fluid, the long-wavelength excitations at small frequencies can be described by hydrodynamics both in the normal and in the superfluid phase. The crucial input to this theory are the transport coefficients, which describe the dissipation of local currents that transport the conserved quantities particle number, momentum and energy. In a normal fluid one has the heat conductivity $\kappa$, the shear viscosity $\eta$ and the bulk viscosity $\zeta$. In a superfluid the latter has to be replaced by three independent variables $\zeta_{1,2,3}$ [169], since below $T_c$ both the normal and the superfluid current are involved in transport processes, which gives rise to a richer hydrodynamic behavior.

In addition, the spin degree of freedom entails a spin conductivity $\sigma_s$ and a spin diffusion constant $D_s$ related by an Einstein relation $D_s = \sigma_s/\chi_s$, where $\chi_s$ is the equilibrium spin susceptibility. A recent review on spin transport has been provided by Enss and Thywissen [170]. In this thesis, however, we will consider mainly the first class of transport coefficients from above.

In the following, we give a short overview over known results regarding the transport properties of the unitary Fermi gas in Sec 8.1. Then we discuss Luttinger-Ward results for the scaling functions of the shear viscosity in Sec. 8.2, which allows to study the ratios $\eta/s$ and $\eta/(\hbar n)$ and in particular their universal quantum bounds, where $s$ denotes the entropy density. In Sec. 8.3 we calculate the heat conductivity in the quantum critical regime within a large-N expansion.

[1] Quite recently also the out-of-time-order-correlations of the unitary Fermi gas have been studied by a Boltzmann equation [168].

## 8.1 General results for the hydrodynamic behavior of the unitary gas

The hydrodynamic properties of the Fermi gas at infinite scattering length are strongly influenced by the enhanced symmetry. In particular, the scale invariance of the unitary gas implies the operator identity $\mathrm{Tr}\,\hat{\Pi} = \sum_{i=1}^{3} \hat{\Pi}_{ii} = 2\hat{\varepsilon}$, where $\hat{\Pi}$ is the stress tensor and $\hat{\varepsilon}$ is the operator for the energy density, see Ref. [42]. In a general system in thermal equilibrium the expectation value $\langle\hat{\Pi}\rangle = p\delta_{ij}$ is identical to the pressure $p$, which in the case of the unitary gas immediately leads to the relation $p = 2/3\varepsilon$ of a non-relativistic, scale invariant system. As has been shown by Son [81], in a nonequilibrium context the conformal symmetry of the resonant gas gives rise to the remarkable fact that the bulk viscosities $\zeta \equiv 0$ in the normal fluid or $\zeta_{1,2} \equiv 0$ in the superfluid vanish identically. Note that $\zeta_2$ determines the change of the pressure in an isotropic compression of the normal fluid via $\delta p = -\zeta_2 \mathrm{div}\mathbf{v}_n$, where $\mathbf{v}_n$ denotes the velocity of the normal component of the superfluid. Therefore, $\zeta_2$ corresponds to the single bulk viscosity $\zeta$ of the symmetric phase. Furthermore, below $T_c$ a change of pressure can be created by a counterflow of the normal and superfluid component that is described by $\zeta_1$ via $\delta p = -\zeta \mathrm{div}[\rho_s(\mathbf{v}_s - \mathbf{v}_n)]$, where $\rho_s$ and $\mathbf{v}_s$ are the superfluid mass density and velocity, respectively [171]. Experimentally this has been confirmed above $T_c$ by Elliot et al. [172] from the ballistic growth of the mean-squared radius of a trapped cloud of unitary Fermions after releasing them from a strongly anisotropic trap.

Microscopically, the frequency-dependent viscosities follow from the Kubo formula, which involves the retarded correlation function of the stress tensor $\hat{\Pi}_{ij}$ [173]

$$\chi_{ij,kl}(\mathbf{q} = 0, \omega) = \frac{i}{\hbar} \int dt \int d^3x\, e^{i\omega t}\theta(t) \left\langle \left[\hat{\Pi}_{ij}(\mathbf{x}, t), \hat{\Pi}_{jk}(\mathbf{0}, 0)\right]\right\rangle . \tag{8.1}$$

In particular, from the odd imaginary parts one can extract the shear viscosity as function of $\omega$

$$\mathrm{Re}\,\eta(\omega) = \frac{\mathrm{Im}\,\chi_{xy,xy}(\mathbf{q} = 0, \omega)}{\omega} , \tag{8.2}$$

while the transport coefficient follows from the well-defined dc-limit

$$\eta = \lim_{\omega \to 0} \mathrm{Re}\,\eta(\omega) . \tag{8.3}$$

As has been observed by Taylor and Randeria [76], the shear viscosity has an algebraic tail in the high-frequency limit $\eta(\omega) \sim \mathcal{C}/\sqrt{\omega}$, that depends on the Tan contact density $\mathcal{C}$ introduced in Sec. 2.4. Furthermore, $\eta(\omega)$ satisfies a subtracted f-sum rule at arbitrary scattering lengths [76, 173, 174]

$$\frac{2}{\pi} \int_0^\infty d\omega \left[\mathrm{Re}\,\eta(\omega) - \frac{\hbar^{3/2}\mathcal{C}}{15\pi\sqrt{m\omega}}\right] = p - \frac{\hbar^2\mathcal{C}}{4\pi m a} , \tag{8.4}$$

where the subtraction regularizes the algebraic high-frequency tail, while on the right-hand side the equilibrium values of the pressure and the Tan contact density appear. The function $\eta(\omega)$ has been obtained in the normal phase from a Luttinger-Ward computation of the response functions (8.1) by Enss et al. [173], which at least within this formalism is finite in the zero-range limit. Furthermore, the Fourier-transformed linear response functions $\chi_{ij,kl}(\mathbf{q}=0,t)$ are retarded, thermal correlations functions in real time, which exhibit a scaling behavior in the vicinity of the quantum critical point at $\mu = 0 = 1/a = h$ (see Sec. 2.3.1) like their static thermodynamic counterparts. However, in the case of linear response scaling is encountered in the time argument, too. Thus the shear viscosity can be written in terms of a scaling function, whose prefactor follows from dimensional analysis, provided that $\eta$ indeed is finite in the limit $\Lambda \to \infty$, which rules out an anomalous dimension [42]. In general, a scaling form for the transport coefficient $\eta$ can be given also away from resonance and at finite Zeeman fields, in analogy to the thermodynamic functions in Chapter 2. However, since we focus here on the unitary, spin-balanced gas, we omit the variables $1/a = 0$ and $h = 0$ and write

$$\eta(T,\mu) = \frac{\hbar}{\lambda_T^3} f_\eta(\beta\mu)\,. \tag{8.5}$$

Both the high and the low temperature limits of $f_\eta$ can be deduced from general arguments. In the limit of a nondegenerate gas one finds [173, 175]

$$\eta^{\mathrm{cl}} = \frac{15}{8\sqrt{2}}\frac{\hbar}{\lambda_T^3}\,, \tag{8.6}$$

The scaling $T^{3/2}$ follows from the surprising observation that the shear viscosity of a classical gas does not depend on its density [176]. Representing $\eta$ at unitarity in terms of temperature and density, enforces the following functional dependence on dimensional grounds [81]

$$\eta(T,n) = \hbar n \alpha(\theta)\,. \tag{8.7}$$

This reveals the scaling $\alpha \sim \theta^{3/2} = (T/\varepsilon_F)^{3/2}$, in the high-temperature limit in order to cancel the prefactor $n \sim \varepsilon_F^{3/2}$. The classical temperature dependence has been experimentally confirmed by Joseph et al. [177].

In the contrary limit of low temperatures the unitary gas becomes superfluid. In the case of $^4$He Landau and Khalatnikov [178] have shown that phonon-phonon interactions in the normal fraction give rise to a shear viscosity that actually diverges in the zero-temperature limit $\eta(T \to 0) \sim T^{-5}$

$$\eta(T\to 0) = \rho_n(T)\frac{m^2 n^2 c_s^3}{\hbar^2}\frac{2^{13}(2\pi)^7}{13!\cdot 9(u+1)^4}\left(\frac{\hbar c_s}{k_B T}\right)^9\,, \tag{8.8}$$

where the normal fluid component arises from the phonon contribution $\rho_n(T) = 2\pi^2\hbar/(45c_s)(k_BT/\hbar c_s)^4$. The dimensionless coupling constant $u = d\log c_s/d\log n$

arises from the nonlinear corrections to the hydrodynamic equations, which entail phonon-phonon scattering. In case of the unitary gas, where in analogy to $^4$He at the lowest temperatures only phonon-like Goldstone modes with linear dispersion exist, Rupak and Schäfer [179] have found a similar result. In the Fermi gas with infinite scattering length the sound velocity $c_s = v_F\sqrt{\xi_s/3}$ depends on the density and the Bertsch parameter[2]. Due to $v_F \sim n^{1/3}$, we have $u = 1/3$, which is a universal constant in contrast to the case of superfluid $^4$He. From the high- and low- temperature limits (8.6) and (8.8), respectively, it is possible to deduce the asymptotic behavior of the viscosity scaling function $f_\eta$, defined in eq. (8.5). Using in the latter limit $\mu = \xi_s\varepsilon_F$, one finds [42]

$$f_\eta(\beta\mu) \to \begin{cases} \frac{3}{8\sqrt{2}}\,, & \beta\mu \to -\infty \\ 0.005(\beta\mu)^{13/2}\,, & \beta\mu \to \infty \end{cases} . \tag{8.9}$$

Below in Fig. 8.1 we present Luttinger-Ward results for the viscosity scaling function. Before coming to that we emphasize that the stated asymptotics imply a non-monotonic behavior of the ratios

$$\frac{\eta}{s} = \frac{\hbar}{k_B}\frac{f_\eta(\beta\mu)}{f_s(\beta\mu)} \quad \text{and} \quad \frac{\eta}{\hbar n} = \frac{f_\eta(\beta\mu)}{f_n(\beta\mu)} = \alpha(\beta\mu)\,, \tag{8.10}$$

upon varying the chemical potential at a fixed temperature $T \ll \bar{E}$ from the non-degenerate limit $\beta\mu \ll -1$ through the quantum critical regime $\mu \ll T$ into the superfluid regime $\beta\mu \gg 1$. The corresponding scaling functions for the thermodynamic variables entropy density $s = S/V$ and the total density $n$ are defined via[3]

$$s(T,\mu) = \frac{k_B}{\lambda_T^3} f_s(\beta\mu) \tag{8.11a}$$

$$n(T,\mu) = \frac{1}{\lambda_T^3} f_n(\beta\mu)\,. \tag{8.11b}$$

The resulting functions from the Luttinger-Ward theory can again be found in the next subsection. Before discussing them we give general arguments why the two ratios from above individually attain a minimum, whose value scales linear with $\hbar$ and therefore contains information about the quantum nature of the system. In the non-degenerate regime one recovers the results from the virial expansion of the classical gas, where the identification $n\lambda_T^3 = 2z$, with the fugacity $z = \exp(\beta\mu)$ becomes valid. Using the equation of state of an ideal classical gas, one finds the asymptotic behavior $f_s(\beta\mu \ll -1) \sim |\beta\mu|\exp(-|\beta\mu|)$ and $f_n(\beta\mu \ll -1) \sim$

[2]The relation between the speed of sound and $\xi_s$ can be verified from the general hydrodynamic relation $mc_s^2 = (n\kappa_T)^{-1}$ and the scale invariance of the unitary gas that implies for the compressibility $\kappa_T = \kappa^{(0)}/\xi_s$.

[3]In this section we we have reintroduced $k_B$.

$\exp(-|\beta\mu|)$, such that the ratios of the shear viscosity (8.10) grow exponentially, since $f_\eta$ approaches a constant. In the opposite limit of $T \to 0$ the density of the fermionic system scales as $n \simeq (\xi_s \mu)^{3/2}$, which entails $f_n(\beta\mu \gg 1) \sim (\beta\mu)^{3/2}$. The entropy density in turn scales like $s \sim k_B (k_B T/\hbar c_s)^3$ due to the phonon contribution of the normal component and we find $f_s(\beta\mu \gg 1) \sim (\beta\mu)^{-3/2}$, which follows from $c_s \sim v_F \sim \mu^{1/2}$. Consequently, we obtain the power laws $\eta/s \sim (\beta\mu)^8$ and $\eta/(\hbar n) \sim (\beta\mu)^5$ upon approaching the ground state at fixed chemical potential. As both ratios diverge in both the limits $\beta\mu \ll -1$ and $\beta\mu \gg 1$ $\eta/s$ and $\eta/\hbar n$ must attain a minimum at finite $\beta\mu$. From the Luttinger-Ward results [173] for the shear viscosity one finds a minimum $(\eta/s)_{\min} \simeq 0.6\hbar/k_B$ at $\beta\mu \simeq 1.13 < (\beta\mu)_c \simeq 2.65$ above $T_c$. In contrast, the minimum of $\eta/n$ in turn seems to be located in the superfluid regime, which is also indicated by experiments [177]. We will provide plots of the universal ratios in Sec. 8.2 below and estimate the position of the extremum in the latter ratio.

In fact, such minima as function of the temperature are expected quite generically, as was pointed out by Schäfer and Teany [180]. However, the result $(\eta/s)_{\min} \simeq 0.6\hbar/k_B$ [173] found for the unitary gas is only about a factor seven larger than the smallest value $\eta/s = \hbar/(4\pi k_B)$ ever obtained. The latter is encountered in the conformally invariant, relativistic $\mathcal{N} = 4$ supersymmetric Yang-Mills theory [181], while any perturbation away from this particular model entails a growth of $\eta/s$. Therefore, Kovtun, Son and Starinets (KSS) [182] have conjectured this value to be the minimal possible ratio for $\eta/s$ in any physical system. Regarding Galilean invariant systems the unitary Fermi gas has the smallest $\eta/s$-ratio so far observed, which makes it the most perfect nonrelativistic fluid presently known[4].

In the quantum critical regime $\mu \ll T$ the shear viscosity can be accessed by a Boltzmann approach within a large-N expansion, as is discussed by Enss [109]. Setting $N = 1$ one finds $\eta/s \simeq \hbar/k_B f_\eta(0)/f_s(0) \simeq 0.74\hbar/k_B$, which is close to the minimal ratio obtained from the Luttinger-Ward computation. Since the heat conductivity $\kappa$ has not been studied very thoroughly we provide in Sec.  a similar computation in a $1/N$ expansion in the most interesting quantum critical regime. The results allow to determine the Prandtl number within the large-N formalism, which is connected to the question whether the scale-invariant unitary gas with Galilean symmetry can be mapped to a gravity theory in the sense of the AdS-CFT correspondence (for a review see the book by Ammon and Erdmenger [183]). But let us first turn to the Luttinger-Ward results for the scaling functions introduced above.

[4] Water, whose hydrodynamics properties can be described by classical physics has a minimal $\eta/s$ ratio of only about 25 times the (KSS) value [173].

## 8.2 Viscosity scaling functions

We come now to the Luttinger-Ward results for the scaling functions relevant for the shear viscosity. First of all, we present in Fig. 8.1 the scaling function $f_\eta$ defined in eq. (8.5). The data for this monotonically growing function has been taken from the Luttinger-Ward computation in the normal phase by Enss et al. [173], who checked the correct asymptotics (8.6) in the case of large temperatures. Unfortunately, so far there is no data for the symmetry-broken phase available, such that the known asymptotics $f_\eta \simeq 0.005(\beta\mu)^{13/2}$ (see eq. (8.9)) in the opposite limit $T \to 0$ cannot be seen. Interestingly, the slope of $f_\eta$ becomes very small in the vicinity of the critical point. However, whether $d(f_\eta)(d\beta\mu)_c = 0$ is satisfied exactly remains an open question. Next we show the thermodynamic scaling functions $f_s(\beta\mu)$ and

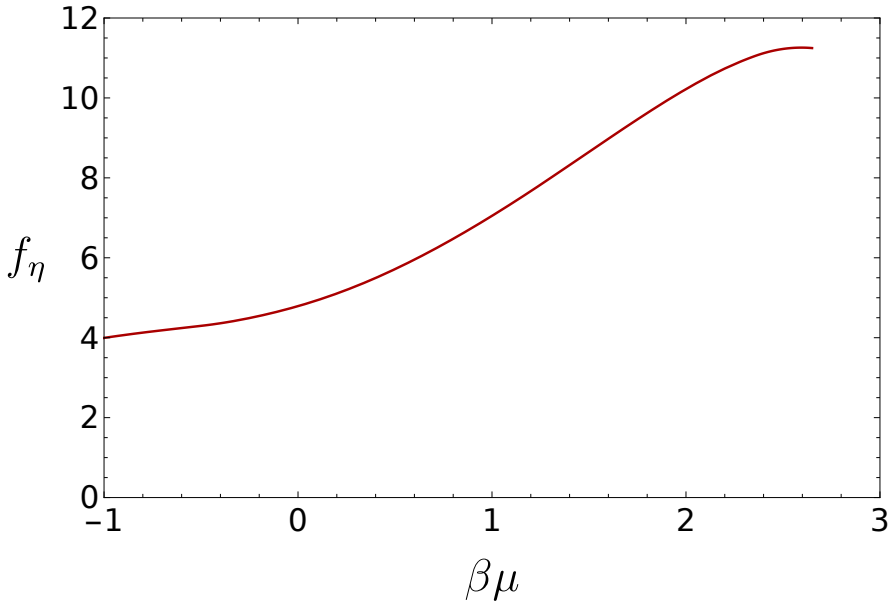


Figure 8.1: The scaling function of the shear viscosity $f_\eta$ of the unitary gas in the normal phase as function of $\beta\mu$. The data for $\eta$ is taken from Ref. [173].

$f_n(\beta\mu)$ in Figs. 8.2 and 8.3, respectively. In both cases the symmetric phase is depicted in red and obtained from the Luttinger-Ward computations presented in the previous chapters of this thesis. The data for the ordered phase has been taken from Ref. [37] and is shown in blue. We observe a maximum in $f_s$ close to the critical value $(\beta\mu)_c \simeq 2.65$, which automatically favors a minimum in the ratio $\eta/s = \hbar f_\eta/(k_B f_s)$. On the other hand $f_n$ shows a monotonous growth with $\beta\mu$. Note that the multi-valued regime in the vicinity of the phase transition is an artifact of the Luttinger-Ward theory [37].

Based on the above results we present the ratio $\eta/s$ in dimensionless form in

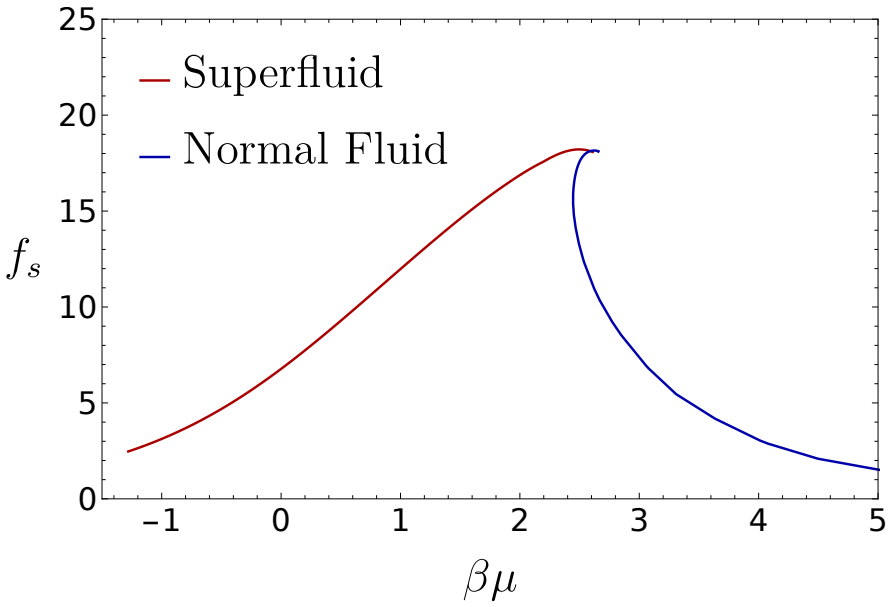


Figure 8.2: Scaling function $f_s(\beta\mu)$ for the entropy density. Red: Normal fluid regime from the Luttinger-Ward approach presented in this thesis, Blue: Superfluid from Ref. [37].

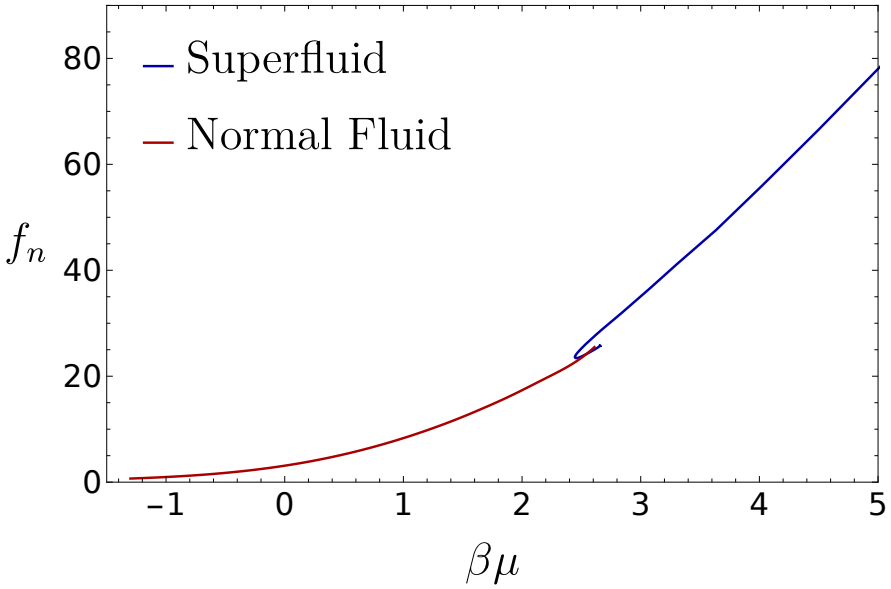


Figure 8.3: Scaling function $f_n(\beta\mu)$ for the density. Red: Normal fluid regime from the Luttinger-Ward approach presented in this thesis, Blue: Superfluid from Ref. [37].

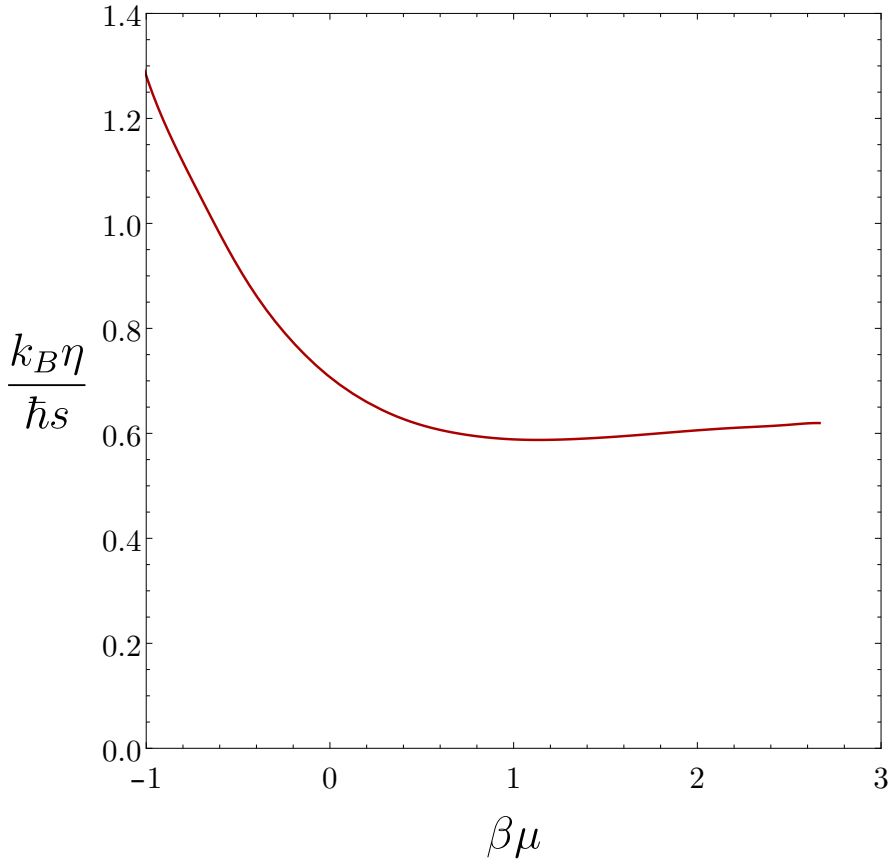


Figure 8.4: Shear viscosity to entropy density ratio $f_\eta/f_s = k_B\eta/(\hbar s)$ above $T_c$. The data for $\eta$ has been taken from Ref. [173]. The curve attains a minimal value of 0.6 at $\beta\mu \simeq 1.13$.

Fig. 8.4. We indeed observe a minimum of $(\eta/s)_{\min} \simeq 0.6\hbar/k_B$ located at $\beta\mu \simeq 1.13$.

Regarding the ratio $\alpha = \eta/(\hbar n)$, where the minimum is found in the superfluid regime, as can be seen in Fig. 8.5, we use a simple ansatz to extrapolate the known normal fluid regime to temperature regimes below $T_c$. This can be most easily be done as function of $\theta = T/T_F$, for which we write the ansatz

$$\alpha(\theta \leqslant \theta_c) = \frac{0.005 \cdot 3\sqrt{\pi}}{8}\xi_s^{13/2}\theta^{-5} + A + B\theta\,, \tag{8.12}$$

in agreement with the scaling relation $\eta/(\hbar n) \sim (\beta\mu)^5$ given in the previous section. The prefactor of the leading term is fixed by the asymptotics $f_\eta \simeq 0.005(\beta\mu)^{13/2} = 0.005\xi_s^{13/2}\theta^{-13/2}$, which follows from the ground state relation of the unitary gas

$\mu = \xi_s \varepsilon_F$ and from rewriting the density scaling function

$$f_n = n\lambda_T^3 = \frac{8}{3\sqrt{\pi}}\theta^{-3/2}\,. \tag{8.13}$$

The additional parameters are adjusted from imposing continuity conditions on both $\alpha(\theta_c)$ and its derivative $\alpha'|_{\theta_c}$ without affecting the known dominant behavior for $T \to 0$. These two conditions seem to be reasonable, since $f_\eta$ does not indicate any singular behavior in the vicinity of the phase transition and furthermore both $\partial n/\partial T$ and $\partial n/\partial \mu = n^2 \kappa_T$ are continuous at the critical temperature. This follows from the representation $n = \lambda_T^{-3} f_n$ and the fact that the compressibility itself shows the same critical behavior (2.79) at $T_c$ as $C_V/N$ [42]. The density itself is of course finite at a continuous transition. The result from this ansatz can be found in Fig. 8.5. Indeed, we observe a minimum $\alpha_{\min} \simeq 0.35$ at $\theta_{\min} \simeq 0.12$. Using the Luttinger-Ward data from Haussmann et al. [37] the latter value translates to $(\beta\mu)_{\min} \simeq 3.01$. These numbers of course depend on the form of the ansatz (8.12) and serve only as a first estimate.

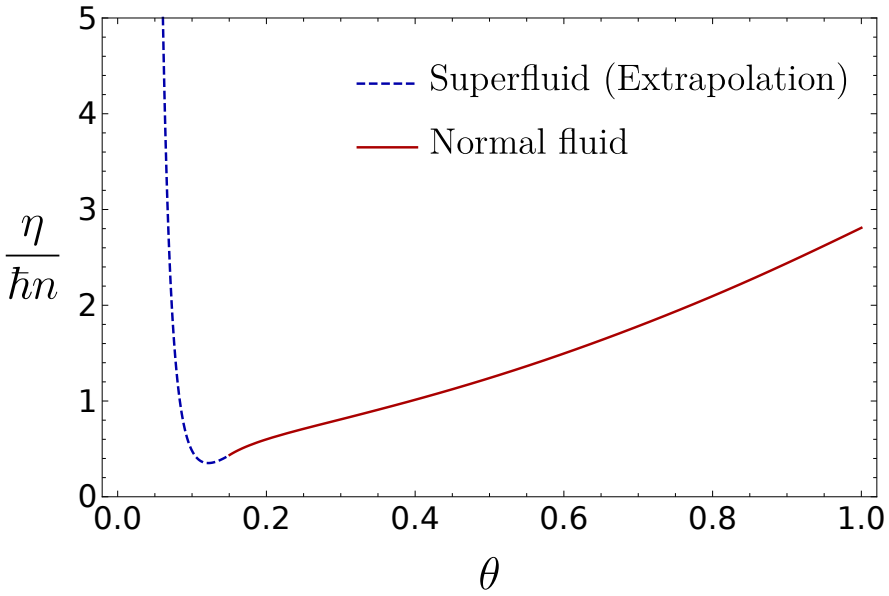


Figure 8.5: The shear viscosity to density ratio $\alpha = \eta/\hbar n$ of the unitary gas in the normal phase as function of $T/T_F$. The data for $\eta$ is taken from [173].

## 8.3 Heat conductivity of the unitary Fermi gas

In this section we present a large-N computation to determine the heat conductivity of the spin balanced, unitary Fermi gas in the quantum critical regime $\mu \ll T$,

where the lack of well-defined quasiparticles renders the determination of transport properties difficult [42]. The large-N approach, which has been previously used on the shear viscosity by Enss [109], however, allows to formulate the problem in terms of a Boltzmann equation. To obtain a description of the interaction effects at next-to-leading order in N we first review the corresponding representation of the thermodynamic partition function in Sec. 8.3.1, before we describe the solution of the Boltzmann equation, that eventually yields the heat conductivity, in Sec. 8.3.2. We close the chapter by considering the Prandtl number in Sec. 8.3.3.

### 8.3.1 Large-N expansion of the action

Before we actually turn to transport properties, it is useful to consider thermodynamic quantities in the large-N formalism, because we can obtain an expression for the scattering cross section that will enter the Boltzmann equation in the next section. Usually, in a large-N approach one introduces $N_f$ copies[5] or "flavors" of the physical degrees of freedom of the system. In our case this extends the fermionic field operators $\hat{\Psi}_\sigma \to \hat{\Psi}_{\sigma,a}$ by an additional flavor index $a \in \{1, 2, \dots, N_f\}$. In particular, this procedure assigns to every Feynman diagram an inverse power of $N_f$, which in the limit $N_f \to \infty$ allows to organize the expansion for the correlation functions according to these $N_f$ prefactors. Of course all diagrams with the leading power of $N_f$ have to be resummed. A convenient starting point for large-N computations is provided by the coherent state path integral representation of the grand-canonical partition function $\mathcal{Z}(\beta, \mu)$ (see the book by Altland and Simons [154]). For the Fermi gas with $N_f$ flavors it reads

$$\mathcal{Z}(\beta, \mu) = \int \prod_{\sigma,a} \mathcal{D}\bar{\psi}_{\sigma,a} \mathcal{D}\psi_{\sigma,a} e^{-\frac{1}{\hbar} S\left[\bar{\psi}_{\sigma,a}, \psi_{\sigma,a}\right]}, \tag{8.14}$$

where the $\psi_{\sigma,a}$ denote the corresponding Grassmann variables of the fermionic quantum fields. After promoting the action $S$ for the single-channel model (2.26) to a large-N version, it becomes

$$\begin{aligned} S = S_0 + S_{\text{int}} = \int_0^{\beta\hbar} d\tau \int d^3x \Big\{ & \sum_{\sigma,a} \bar{\psi}_{\sigma,a}(\mathbf{x}, \tau) \left( \hbar\partial_\tau - \frac{\hbar^2 \nabla^2}{2m} - \mu_\sigma \right) \psi_{\sigma,a}(\mathbf{x}, \tau) \\ & + \frac{\bar{g}(\Lambda)}{N_f} \sum_{a,b} \bar{\psi}_{\uparrow,a}(\mathbf{x}, \tau) \bar{\psi}_{\downarrow,a}(\mathbf{x}, \tau) \psi_{\downarrow,b}(\mathbf{x}, \tau) \psi_{\uparrow,b}(\mathbf{x}, \tau) \Big\}. \end{aligned} \tag{8.15}$$

Note that we have rescaled the coupling constant by a factor $1/N_f$ to keep the ratio between kinetic and interaction terms of the action fixed. Regarding transformations in the new flavor space, the action is invariant under $\mathrm{Sp}(2N_f)$ transformations, which generalizes the SU(2)-symmetry of the fermionic spin 1/2 degree of

[5] We reserve the variable $N$ for the total particle number, which is proportional but not identical to $N_f$.

freedom [1]. The original physical action without additional flavors is recovered by setting $N_f = 1$.

We proceed by decoupling the quartic interaction term via a Hubbard-Stratonovich transformation in the Cooper channel that in turn introduces the complex bosonic field $\phi$. Although we have not used any approximations so far, this channel will certainly include the kind of ladder diagrams that have turned out to be important in the Luttinger-Ward computations discussed in the previous chapters of this thesis. From a technical perspective, we interpret the Fermion-Fermion interaction of the original action $S$ as the standard solution of bosonic Gaussian integrals

$$\frac{1}{\mathcal{N}} \int \mathcal{D}\phi^* \mathcal{D}\phi \, \exp\left( \int dx \, \left[ \frac{N_f}{\bar{g}(\Lambda)} \phi^*(x)\phi(x) + \sum_a \left( \phi(x) \bar{\psi}_{\uparrow,a}(x) \bar{\psi}_{\downarrow,a}(x) + h.c. \right) \right] \right) = \\ = \exp\left[ -\frac{\bar{g}(\Lambda)}{N_f} \sum_{a,b} \int dx \, \bar{\psi}_{\uparrow,a}(x) \bar{\psi}_{\downarrow,a}(x) \psi_{\downarrow,b}(x) \psi_{\uparrow,b}(x) \right]. \tag{8.16}$$

Recall that for large enough values of the cutoff $\Lambda$ the bare coupling constant $\bar{g}(\Lambda)$ is negative according to the renormalization scheme eq. (2.29) and therefore the integral over $\phi$ and $\phi^*$ is convergent. Furthermore, we have defined the shorthand notation $x \equiv (\mathbf{x}, \tau)$ and $\int dx \equiv \int_0^{\hbar\beta} d\tau \int d^3x$. $\mathcal{N}$ symbolizes the unimportant normalization and will be omitted again in the following. Inserting this identity in the combination of equations (8.14) and (8.15) only quadratic terms in the Fermion fields $\psi_{\sigma,a}$ and $\bar{\psi}_{\sigma,a}$ remain in the partition function

$$\mathcal{Z} = \int \mathcal{D}\bar{\psi}_{\sigma,a} \mathcal{D}\psi_{\sigma,a} \mathcal{D}\phi^* \mathcal{D}\phi \, e^{-\frac{1}{\hbar} S_{\mathrm{BF}}[\bar{\psi},\psi,\phi^*,\phi]} \tag{8.17a}$$

$$S_{\mathrm{BF}}[\bar{\psi},\psi,\phi^*,\phi] = \int dx \left[ -\frac{N_f}{\bar{g}(\Lambda)} \phi^*(x)\phi(x) + \int dx' \sum_a \bar{\Psi}_a(x) G^{-1}(x-x') \Psi_a(x') \right], \tag{8.17b}$$

where the action now appears invariant under $\mathrm{O}(N_f)$ transformations in flavor space. Here $\Psi_a(x) = (\psi_{\uparrow,a}(x), \bar{\psi}_{\downarrow,a}(x))$ collects the fermionic variables within a Nambu spinor and

$$G^{-1}(x-x') = \delta(x-x') \begin{pmatrix} \hbar\partial_\tau - \frac{\hbar^2\nabla^2}{2m} - \mu_\uparrow & -\phi(x) \\ -\phi^*(x) & +\hbar\partial_\tau + \frac{\hbar^2\nabla^2}{2m} + \mu_\downarrow \end{pmatrix} \tag{8.18}$$

denotes the matrix-valued, inverse Gorkov Green's function. The signs in the $G_{22}^{-1}$ element can be easily checked by using the anticommutation relations of Grassmann variables $\{\psi_{\sigma,a}, \bar{\psi}_{\sigma',b}\} = 0 = \{\psi_{\sigma,a}, \psi_{\sigma',b}\}$ and the fermionic antiperiodicity $\psi_{\sigma,a}(\tau = 0) = -\psi_{\sigma,a}(\tau = \beta)$, together with partial integration. Apart from being Gaussian the path integral over the Grassmann fields factorizes in the flavor index and can

thus be evaluated in closed form. The resulting purely bosonic partition function reads

$$\mathcal{Z} = \int \mathcal{D}\phi^* \mathcal{D}\phi \, e^{-\frac{1}{\hbar} S_{\mathrm{B}}[\phi^*,\phi]} \tag{8.19a}$$

$$S_{\mathrm{B}} = -N_f \int dx \left[ \frac{|\phi(x)|^2}{\bar{g}(\Lambda)} + \frac{T}{V} \operatorname{Tr} \log G^{-1}[\phi^*(x), \phi(x)] \right], \tag{8.19b}$$

where Tr indicates a trace over the Nambu index. The number of flavors now only occurs in the prefactor of the bosonic action, which in the limit of large $N_f \gg 1$ allows for a controlled stationary phase expansion around the saddle point of $S_{\mathrm{B}}$. The saddle point value $\langle\phi\rangle$ follows from $\delta S_{\mathrm{B}}/\delta\phi = 0$ and describes the physical order-parameter configuration. In the quantum critical regime $T/\mu \gg 1$ the expectation value of the Hubbard-Stratonovich field vanishes identically, since we are deep in the symmetric phase in agreement with the critical threshold $(T/\mu)_c \simeq 0.38$ from Fig. 3.2. Expanding the action to quadratic order in the fluctuations $\phi$ around $\langle\phi\rangle = 0$ yields

$$\begin{aligned}
\frac{S_{\mathrm{B}}}{N_f} =& \hbar V \int \frac{d^3k}{(2\pi)^3} \sum_{\sigma,n} \log\left[-\mathcal{G}^{(0)}_{\sigma\sigma}(\mathbf{k},\omega_n)\right] - \int \frac{d^3Q}{(2\pi)^3} \frac{1}{\beta\hbar} \sum_n |\phi(\mathbf{Q},\Omega_n)|^2 \frac{1}{\bar{g}(\Lambda)} \\
&- \int \frac{d^3Q}{(2\pi)^3} \frac{1}{\beta\hbar} \sum_n |\phi(\mathbf{Q},\Omega_n)|^2 \int \frac{d^3k}{(2\pi)^3} \frac{1}{\beta} \sum_m \mathcal{G}^{(0)}_{\uparrow\uparrow}(\mathbf{k},\omega_m) \, \mathcal{G}^{(0)}_{\downarrow\downarrow}(\mathbf{Q}-\mathbf{k}, \Omega_n - \omega_m) \\
=& \hbar V \int \frac{d^3k}{(2\pi)^3} \sum_{\sigma,n} \log\left[-\mathcal{G}^{(0)}_{\sigma\sigma}(\mathbf{k},\omega_n)\right] - \int \frac{d^3Q}{(2\pi)^3} \frac{1}{\beta\hbar} \sum_n |\phi(\mathbf{Q},\Omega_n)|^2 \left[\frac{1}{g} + M^{(0)}(\mathbf{Q},\Omega_n)\right],
\end{aligned} \tag{8.20}$$

up to corrections of order $\mathcal{O}(\phi^4)$. Note that we have replaced the bare coupling constant by the renormalized one via eq. (2.29), and we recognize the particle-particle diagram $M^{(0)}(\mathbf{Q},\Omega_n)$ with bare Green's function lines from eq. (4.33). Therefore, we obtain for the propagator of the Hubbard-Stratonovich field the vertex $\Gamma^{(0)}(\mathbf{Q},\Omega_n) = (1/g + M^{(0)})$, that is the geometric series of all particle ladder diagrams, whose legs are formed by $\mathcal{G}^{(0)}_{\sigma\sigma}$. Furthermore, the two bare Green's functions in the saddle-point contribution $\mathcal{O}(\phi^0)$, which originate from the diagonal elements of the Gorkov Green's function in the absence of a superfluid order parameter can both be written in terms of the forward propagating $\mathcal{G}^{(0)}_{\sigma\sigma}(\mathbf{k},\omega_n)$. The technical procedure based on the correct choice of convergence parameters is explained in detail in App. A of Ref. [147]. Here we argue that from a physical point of view this term is to be expected in the given from, since the $N_f = \infty$ contributions represents an ideal two-component Fermi gas, while interaction effects only appear at finite $N_f$. With this Gaussian form of $S_{\mathrm{B}}$ and the fact that away from the critical region we have $\operatorname{Re}\Gamma^{(0)}(\mathbf{Q},\Omega_n) < 0$, we can perform the remaining path integral

from eq. (8.19a) and find for the grand potential $\Omega(\mu, T) = -T \log \mathcal{Z}$

$$\frac{\Omega}{N_f} = 2\,\Omega^{(0)} - \frac{TV}{N_f} \int \frac{d^3Q}{(2\pi)^3} \sum_n \log \Gamma^{(0)}\left(\mathbf{Q}, \Omega_n\right) + \mathcal{O}(N_f^{-2})\,. \tag{8.21}$$

Here $\Omega^{(0)} = -p^{(0)}V$ denotes the noninteracting contribution from evaluating the action at the trivial saddle point configuration, while the pressure of an ideal Fermi gas is given in eq. (2.35). For the computation of the related standard Matsubara sum and the momentum integral for $\Omega^{(0)}$ we refer the reader to the book of Altland and Simons [154].

The inclusion of higher order monomials of $\phi$ beyond the quadratic order in the expansion of the action $S_\mathrm{B}$ around the saddle point gives rise to contributions that are suppressed by higher inverse powers of $N_f$. Diagrammatically, this can be most easily verified by considering the exact Bose-Fermi theory from eq. (8.17), as has been discussed also by Enss [109]. Since in this particular formulation of the model the Bose propagator scales like $N_f^{-1}$, while each closed Fermion loop introduces a factor $N_f$, only the closed RPA loop diagrams (see Fetter and Walecka [67]) add a contribution of $\mathcal{O}(1)$ to the partition function. The resummation of all these fermionic loops is identical to the sum of particle-particle ladders $\Gamma^{(0)}$ that appears in the bosonic action $S_\mathrm{B}$.

Finally, let us return to $M^{(0)}\left(\mathbf{Q}, \Omega_n\right)$ from equation (4.33). Simplifying also the finite temperature parts will be quite helpful for the next chapter. In particular, we can perform the angular integrals analytically, which gives rise to [109]

$$\begin{aligned}\Gamma^{(0)}\left(\mathbf{Q}, \Omega_n\right)^{-1} = {} & \frac{m}{4\pi\hbar^2 a} - \frac{m^{3/2}}{4\pi\hbar^3}\sqrt{\frac{\varepsilon_Q}{2} - i\Omega_n - 2\mu} \\ & + \frac{m}{2\pi\hbar^2 Q}\int_0^\infty dp\, \frac{p}{e^{\beta(\varepsilon_p - \mu)} + 1} \log\left[\frac{i\Omega_n + 2\mu - \varepsilon_p - \varepsilon_{Q-p}}{i\Omega_n + 2\mu - \varepsilon_p - \varepsilon_{Q+p}}\right].\end{aligned} \tag{8.22}$$

For the scattering processes that influence the transport properties in the next chapter, we need the vertex also in real frequencies $i\Omega_n \to \Omega + i0^+$, where the choice of the infinitesimal imaginary part ensures retarded scattering processes and therefore causality. Since we have an analytical expression available, the analytic continuation can be easily accomplished. In the following, the real frequency counterpart of the vertex function is denoted by the T-matrix

$$\mathcal{T}(\mathbf{Q}, \Omega) = \Gamma^{(0)}(\mathbf{Q}, i\Omega_n \to \Omega + i0^+)\,. \tag{8.23}$$

Now we have gathered all the prerequisites from the large-N approach that are necessary for the computation of the heat conductivity of the balanced unitary Fermi gas in the quantum critical regime.

### 8.3.2 Heat conductivity from Boltzmann equation

If we expose a physical system to a stationary temperature gradient $\nabla_{\mathbf{x}} T$, it will respond with a heat current density $\mathbf{j}_Q$. In a linearized description, applicable to situations close to thermal equilibrium, the heat conductivity $\kappa$ relates $\mathbf{j}_Q$ and $\nabla_{\mathbf{x}} T$ via Fourier's law

$$\mathbf{j}_Q = -\kappa \nabla_{\mathbf{x}} T \,, \tag{8.24}$$

provided that simultaneously the particle current vanishes $\mathbf{j}_N = 0$ [169,184], i.e. one excludes convection. The goal of this paragraph is to determine $\kappa$ in the quantum critical regime for the unitary gas, which is not directly amenable to kinetic theory because of the absence of well-defined quasiparticle excitations. In contrast, both in the regimes $\beta\mu \ll -1$ and $\beta\mu \gg 1$ one does not encounter this problem. In the first case of a nondegenerate, dilute gas one can apply classical transport theory, while deep in the superfluid regime transport can be described in terms of the phonon modes [179]. In the case of $\beta\mu \simeq 0$, in turn, the large-N expansion justifies the treatment with a Boltzmann equation, as we will discuss below.

In the standard statistical mechanics formulation the local particle and heat current densities are given by

$$\mathbf{j}_N(\mathbf{x}, t) = \int \frac{d^3p}{(2\pi\hbar)^3} \frac{\mathbf{p}}{m} f(\mathbf{x}, \mathbf{p}, t) \tag{8.25a}$$

$$\mathbf{j}_Q(\mathbf{x}, t) = \int \frac{d^3p}{(2\pi\hbar)^3} \frac{\mathbf{p}}{m} \varepsilon_p f(\mathbf{x}, \mathbf{p}, t) \,, \tag{8.25b}$$

with the single-particle distribution function $f(\mathbf{x}, \mathbf{p}, t)$. Of course this formulation for a quantum mechanical problem is only possible if the gradients and currents vary on macroscopic length scale rather than on a microscopic one, where the simultaneous measurement of position and momentum contradicts the Heisenberg uncertainty principle [169]. In case of the unitary Fermi gas this does not really imply a severe restriction, since we are interested in currents that vary on scales that are large compared to the interparticle spacing. In a homogeneous, unitary gas in thermal equilibrium the distribution function reduces to the isotropic momentum distribution $f(\mathbf{x}, \mathbf{p}, t) = f_{\mathrm{eq}}(p) \neq n_F(p)$, such that both currents vanish. However, this function differs from the Fermi-Dirac distribution due to the strong interaction effects that have to be taken into account nonperturbatively. As we have discussed in detail in the previous chapters, one can treat the thermodynamic properties with the Luttinger-Ward formalism. However, to obtain a simple estimate for the heat conductivity, which requires to include at least weak nonequilbrium effects, we use the large-N expansion from the preceding subsection. In this formulation interactions are suppressed by inverse powers of $N_f$. In particular, the leading interaction contribution from the NSR-like $\mathcal{T}$-matrix acquires already a factor $1/N_f$, see eq. (8.21). Therefore, also the self-energies, which still follow from (4.36), are of order $\mathcal{O}(1/N_f)$. This justifies the application of a Boltzmann equation to

compute the distribution function $f$, as has first been argued by Enss [109], since the lifetime of the excitations is of order $\tau_\sigma \sim N_f \sim 1/\operatorname{Im}\Sigma_{\sigma\sigma}$. Moreover, the excitations propagate freely between two subsequent scattering events (with $1/N_f$ corrections to the bare dispersion from $\operatorname{Re}\Sigma_{\sigma\sigma}$) and finally only particle-particle scattering has to be taken into account, since particle-hole diagrams are further suppressed in $1/N_f$. The Boltzmann equation that considers the time evolution of the distribution function $f_1 \equiv f(\mathbf{x}_1, \mathbf{p}_1, t)$ reads [169, 184]

$$\frac{\partial f_1}{\partial t} + \dot{\mathbf{x}}_1 \cdot \nabla_{\mathbf{x}} f_1 + \dot{\mathbf{p}}_1 \cdot \nabla_{\mathbf{p}} f_1 = -\frac{1}{N} I\left[f_1\right] . \tag{8.26}$$

The collision term on the right-hand side

$$\begin{aligned} &-\frac{1}{N_f} I[f_1] = \\ &-\frac{1}{N_f} \int \frac{d^3 p_2}{(2\pi\hbar)^3} \frac{|\mathbf{p_1} - \mathbf{p_2}|}{m} \int d\Omega \, \frac{d\sigma}{d\Omega} \left[ f_1 f_2 (1 - f_{1'})(1 - f_{2'}) - (1 - f_1)(1 - f_2) f_{1'} f_{2'} \right] \end{aligned} \tag{8.27}$$

describes the averaged gains and losses from scattering events $1 + 2 \leftrightarrow 1' + 2'$ with other excitations in the presence of the Pauli blockade of occupied quasiparticle states, where the indices refer to the position and momentum arguments of the individiual excitations. Physically, the Pauli suppression is weakened considerably by the attractive interactions of the unitary Fermi gas, because already $f_{\mathrm{eq}}(p)$ is no longer a free Fermi Dirac distribution $n_F(p)$.

The differential cross section is related to the on-shell T-matrix from eq. (8.23)

$$\frac{d\sigma}{d\Omega} = \left| \frac{m}{4\pi\hbar^2} \mathcal{T}\left(\mathbf{Q} = \mathbf{p}_1 + \mathbf{p_2}, \omega = \varepsilon_{p_1} + \varepsilon_{p_2}\right) \right|^2 , \tag{8.28}$$

which only depends on the center-of-mass variables, as we have discussed in Sec. (4.5). Note that the non-trivial dependence on the center-of-mass momentum and energy already signals the presence of a background medium. The effect of the Pauli blockade from the ladder diagrams can be found in Ref. [67]. This situation has to be contrasted to an expansion around the nondegenerate limit, where the fugacity $z = \exp(\beta\mu)$ vanishes. In this case one recovers the vacuum scattering amplitude $f_0(k) = (-1/a - ik)^{-1}$ in the T-matrix $\mathcal{T}(Q = 0, \omega = \hbar^2 k^2/m, \mu = 0) \sim f_0(k)$, where the implicit limit $i0^+$ ensures the correct poles structure with bound states in the upper complex half plane.

In the following, we present a solution to the Boltzmann equation in the quantum critical regime, which allows to determine $\kappa$. First, we make use of a very simple ansatz for the distribution function, which gives rise to a first value of $\kappa$. Afterwards we will include corrections to the approximation in order to obtain a better result for the heat conductivity.

Since the linear regime of eq. (8.24) exists only close to equilibrium, one expects the local Fermi-Dirac function

$$n_F^{\mathrm{loc}}(\mathbf{x},\mathbf{p},t) = \frac{1}{e^{\beta(\mathbf{x})(\varepsilon_p-\mu(\mathbf{x}))}+1}\,, \tag{8.29}$$

with position-dependent temperature $T(\mathbf{x})$ and chemical potential $\mu(\mathbf{x})$, that vary slowly in space, to be a suitable ansatz for the distribution function. In a situation without convection the pressure has to be spatially uniform, because otherwise a mechanical net force acts on the particles, which creates a finite $\mathbf{j}_N$. Hence, we also have omitted an average velocity of the Fermions that would appear in the form $\mathbf{u}(\mathbf{x})\cdot\mathbf{p}$ in the local Fermi-Dirac distribution. Furthermore, to really guarantee $\mathbf{j}_N = 0$ we will choose $\nabla_{\mathbf{x}}\mu$ appropriately below. To describe dissipation it is not sufficient, however, to merely take a local equilibrium into account, because of the fundamental property $I[n_F^{\mathrm{loc}}] \equiv 0$ of the collision term in the Boltzmann equation [169,184], which implies the absence of dissipation and therefore no well-defined transport coefficients. Instead, we use the ansatz

$$f(\mathbf{x},\mathbf{p},t) = n_F^{\mathrm{loc}}(\mathbf{x},\mathbf{p},t) + n_F(p)(1-n_F(p))\phi(\mathbf{p})\,, \tag{8.30}$$

where $\phi(\mathbf{p})$ describes the deviations from local equilibrium, while the prefactor has been chosen for later convenience. In particular, it vanishes exponentially in the limits $\mathbf{p}\to 0$ and $\mathbf{p}\to\infty$. Now we insert this ansatz into the Boltzmann equation and use the semi-classical approximations $\dot{\mathbf{x}} = \mathbf{p}/m$ and $\dot{\mathbf{p}} \sim -\nabla_{\mathbf{x}}\, p(T,\mu) = 0$ for the motion of the phase space elements of size $(\Delta\mathbf{x},\Delta\mathbf{p})$ centered around $(\mathbf{x},\mathbf{p})$. This yields

$$n_F(p_1)\,(1-n_F(p_1))\,\frac{\mathbf{p}_1}{m}\left(\frac{\varepsilon_{p_1}-\mu}{T^2}\nabla_{\mathbf{x}}T - \frac{1}{T}\nabla_{\mathbf{x}}\mu\right) = -\frac{1}{N_f}I[\phi_1]\,, \tag{8.31}$$

where we have expanded the left-hand side to linear order in the gradients of the temperature $\nabla_{\mathbf{x}}T$ and the chemical potential $\nabla_{\mathbf{x}}\mu$. Within this order we can replace $T(\mathbf{x})$ and $\mu(\mathbf{x})$ by their averages $T$ and $\mu$ taken over the entire sample. Furthermore, we consider both the gradients and the $1/N_f$ terms as small in the sense that to first order no further interaction corrections to the Fermi distribution appear in the streaming terms, while on the right-hand side we have replaced $T(\mathbf{x})$ and $\mu(\mathbf{x})$ by $T$ and $\mu$. The linearized collision term reads

$$I[\phi_1] = \int\frac{d^3p_2}{(2\pi)^3}\frac{|\mathbf{p}_1-\mathbf{p}_2|}{m}\int d\Omega\,\frac{d\sigma}{d\Omega}n_F(p_1)n_F(p_2)\left(1-n_F(p_1')\right)\left(1-n_F(p_2')\right) \cdot\Big\{\phi_1+\phi_2-\phi_{1'}-\phi_{2'}\Big\}\,, \tag{8.32}$$

where $\phi_1 = \phi(\mathbf{p}_1)$ etc. The linearized collision operator has several general properties, which we state here without proof. The derivations are detailed in the books

by Jäckle [184] and by Smith and Jensen [169]. In the space of deviation functions $\{\phi\}$ $I$ is a linear, positive semi-definite and symmetric integral operator, i.e $\int_{\mathbf{p}} \phi I[\phi] \geqslant 0$ and $\int_{\mathbf{p}} \psi I[\phi] = \int_{\mathbf{p}} I[\psi]\phi$. In addition, the five collision invariants $\psi_i$: the particle number ($i = 0$), the three momentum components ($i = 1, 2, 3$) and the energy ($i = 4$), which are guaranteed by the exact collision term, remain collision invariants of the linearized operator. Technically, this means $I[\psi_i] = 0$ for all $i$.

Let us now turn to the streaming terms on the left-hand side of the linearized Boltzmann equation. Since we have fixed the pressure $p = \text{const}$ and the temperature profile $T(\mathbf{x})$, it is convenient to express thermodynamic quantities in terms of a local Gibb's free enthalpy $G(T(\mathbf{x}), N, p) = \mu(T(\mathbf{x}), p)N$. Consequently, we can write for the gradient of the chemical potential to first order in the thermal gradient

$$\nabla_{\mathbf{x}}\mu(\mathbf{x}) = \left(\frac{\partial\mu}{\partial T}\right)_p \nabla_{\mathbf{x}} T = -\tilde{s}\nabla_{\mathbf{x}} T\,, \tag{8.33}$$

where $\tilde{s} = S/N$ is the entropy per particle in global equilibrium. We can express $\tilde{s}$ by the help of the grand potential $\Omega(T, \mu, V)$ from the previous section. In particular, it is sufficient to consider only the noninteracting $N_f = \infty$ limit, where $\Omega \to \Omega^{(0)} = -p^{(0)}V$, since at next-to-leading order in $N_f$ the effects of interactions merely appear in the collision terms on the right-hand side of the Boltzmann equation. Using the form of the pressure $p^{(0)}(\mu, T)$ from eq. (2.35) and the definition of the polylogarithm (2.36) we find in the quantum critical regime $\mu \ll T$

$$\tilde{s} = -\frac{-\left(\frac{\partial\Omega^{(0)}}{\partial T}\right)_{\mu,V}}{\left(\frac{\partial\Omega^{(0)}}{\partial\mu}\right)_{T,V}} = \frac{5\mathrm{Li}_{5/2}(-1)}{2\mathrm{Li}_{3/2}(-1)} = \frac{5(4-\sqrt{2})\zeta(5/2)}{2(4-2\sqrt{2})\zeta(3/2)} = 2.83344\,. \tag{8.34}$$

This is a pure number because in the quantum critical regime one has $n(\mu = 0, T) = 2.67\lambda_T^{-3}$ and $S/V = 2.32nk_B \sim T^{3/2}$ [109]. Therefore, the total entropy vanishes also at $\mu = 0$ in the limit $T \to 0$, since the particle number $N(T \to 0)$ approaches zero in the vacuum state, in agreement with Fig. 2.3. Note that the scaling with temperature follows quite generally from the scaling arguments of the previous sections, while the given numerical prefactors follow from the leading order $N_f = \infty$. Without loss of generality we choose the temperature gradient to point along the $z$-axis, such that the linearized Boltzmann equation (8.31) reads

$$n_F(p_1)\left(1 - n_F(p_1)\right)\left(\frac{\varepsilon_{p_1} - T\tilde{s}}{T}\right)\frac{p_{1,z}}{m}\frac{\partial_z T}{T} = -\frac{1}{N_f} I[\phi_1]\,, \tag{8.35}$$

where we have put $\mu = 0$, which corresponds to the quantum critical regime.

A standard procedure in the context of the Boltzmann equation is to choose the deviation $\phi(\mathbf{p})$ from local equilibrium proportional to the inhomogeneity on the left-hand side. In fact, if one considers just a single ansatz function for $\phi$, the

determination of the transport coefficient from the Boltzmann equation reduces to the computation of a single number instead of the solution of an integral equation, as is discussed by Jäckle [184] based on the maximum principle for transport coefficients. First, we will follow this simple approach here, too, but later on allow for a more general form of $\phi$, which gives corrections on the order of 10% to this first solution. For now we set

$$\phi(\hat{\mathbf{p}}) = (\hat{p}^2 - \tilde{s})\hat{p}_z \,, \tag{8.36}$$

since the prefactor is irrelevant, as will become clear below. Moreover, we have defined the dimensionless momentum

$$\hat{\mathbf{p}} = \frac{1}{\sqrt{2mT}}\,\mathbf{p} \,, \tag{8.37}$$

which implies[6] $\beta\varepsilon_p = \beta p^2/2m = \hat{p}^2$. In this formulation the Fermi-Dirac distribution in the quantum critical regime automatically reads $n_F(\hat{p}) = (\exp(\hat{p}^2)+1)^{-1}$, while the Boltzmann equation becomes

$$n_F(\hat{p}_1)\,(1-n_F(\hat{p}_1))\,\phi(\hat{\mathbf{p}}_1)\frac{\sqrt{2mT}}{m}\frac{\partial_z T}{T} = -\frac{1}{N_f} I[\phi(\hat{\mathbf{p}}_1)] \,. \tag{8.38}$$

First of all, with the ansatz for $\phi$ from above, the particle current $\mathbf{j}_N$ indeed vanishes due to the given value of $\tilde{s}$ from eq. (8.34). This can be easily proven by inserting $\phi$ into the definition (8.25a) and introducing standard polar coordinates. The radial integral can be solved analytically by noting $n_F(\hat{p}^2)[1-n_F(\hat{p}^2)] = -\partial_{\hat{p}^2} n_F(\hat{p}^2)$ and the identity [67]

$$\int_0^\infty d\hat{p}\,\hat{p}^n\, n_F(\hat{p}^2) = \frac{1}{2}\left(1-2^{(1-n)/2}\right)\Gamma\left(\frac{1+n}{2}\right)\zeta\left(\frac{1+n}{2}\right) \,, \quad n>-1 \,, \tag{8.39}$$

which is closely related to the $\mu = 0$ case of the standard Fermi-Dirac integrals, which yield polylogarithms [77]. The heat current in turn becomes

$$\begin{aligned}
\mathbf{j}_Q &= 2N_f \int \frac{d^3p}{(2\pi\hbar)^3}\varepsilon_p \frac{\mathbf{p}}{m} n_F(p)[1-n_F(p)]\phi(\hat{p}) \\
&= \frac{N_f}{3\pi^2}\left\{7\,\Gamma(\tfrac{5}{2})\zeta(\tfrac{5}{2})(1-2^{-3/2}) - 5\,\Gamma(\tfrac{3}{2})\zeta(\tfrac{3}{2})(1-2^{-1/2})\right\}\frac{mT^3}{\hbar^3}\hat{\mathbf{e}}_z \\
&= \hat{j}^{(0)}\cdot 2N_f\frac{mT^3}{\hbar^3}\hat{\mathbf{e}}_z = 0.17718\cdot 2N_f\frac{mT^3}{\hbar^3}\hat{\mathbf{e}}_z \\
&= 1.11325\cdot 2N_f\frac{T^2}{\hbar\lambda_T^2}\hat{\mathbf{e}}_z \,,
\end{aligned} \tag{8.40}$$

[6] In this chapter we consider momenta rather than wave vectors, which is the typical notation in the context of distribution functions. This explains the differences with respect to the appearance of $\hbar$ compared to Chap. 7.

where $\hat{\mathbf{e}}_z$ is the unit vector along the $z$-axis. Consequently, the heat current and the temperature gradient are aligned in parallel, as expected in an isotropic medium. To determine $\kappa$ we first multiply both sides of the Boltzmann equation (8.35) by $2N_f\phi(\hat{\mathbf{p}}_1)/(2\pi\hbar)^3$ and integrate over $\mathbf{p}_1$. Due to the vanishing particle current we find

$$\mathbf{j}_Q \cdot (\partial_z T)\hat{\mathbf{e}}_z = -2T^2 \int \frac{d^3p_1}{(2\pi\hbar)^3}\phi(\hat{\mathbf{p}}_1)I[\phi(\mathbf{p}_1)]\,, \tag{8.41}$$

which we rewrite by the help of Fourier's law (8.24) as

$$\kappa = \frac{\mathbf{j}_Q^2}{2T^2\int \frac{d^3p_1}{(2\pi\hbar)^3}\phi(\hat{\mathbf{p}}_1)I[\phi(\mathbf{p}_1)]}\,. \tag{8.42}$$

Now it remains to solve the integral in the denominator, where the collision integral is given in eq (8.32). Since the momentum component $p_z$ is a collision invariant, $I[p_z] = 0$ and we can simplify the integral

$$\int \frac{d^3p_1}{(2\pi\hbar)^3}\phi(\hat{\mathbf{p}}_1)I[\phi(\hat{p}_1)] = \int \frac{d^3p_1}{(2\pi\hbar)^3}\,\hat{p}_1^2\,\hat{p}_{1,z}I[\phi(\hat{p}_1)]\,. \tag{8.43}$$

The calculation of this integral is most easily accomplished in the center-of-mass system, where the momenta of the four excitations read $\mathbf{p}_1 = \mathbf{k} + \mathbf{Q}/2$, $\mathbf{p}_2 = -\mathbf{k} + \mathbf{Q}/2$, $\mathbf{p}_1' = \mathbf{k}' + \mathbf{Q}/2$ and $\mathbf{p}_2' = -\mathbf{k}' + \mathbf{Q}/2$. Since the scattering processes are elastic and the single-particle dispersion is isotropic the magnitude of the relative momenta is conserved $|\mathbf{p}_1 - \mathbf{p}_2| = |\mathbf{p}_1' - \mathbf{p}_2'|$, such that $k' = k$. Furthermore, we define the short-hand notations $x = \cos[\angle(\mathbf{Q}, \mathbf{k})]$ and $x' = \cos[\angle(\mathbf{Q}, \mathbf{k}')]$. Then we have for combination of the deviations from local equilibrium

$$\phi(\hat{\mathbf{p}}_1) + \phi(\hat{\mathbf{p}}_2) - \phi(\hat{\mathbf{p}}_1') - \phi(\hat{\mathbf{p}}_2') = \hat{k}\hat{Q}(x\hat{k}_z - x'\hat{k}_z')\,, \tag{8.44}$$

while the prefactor formed by the Fermi-Dirac distributions can be conveniently written as [109]

$$n_F(p_1)n_F(p_2)(1 - n_F(p_1'))(1 - n_F(p_2')) = \frac{1}{4g(\hat{Q}, \hat{k}, x)g(\hat{Q}, \hat{k}, x')} \tag{8.45}$$

with

$$g(\hat{Q}, \hat{k}, x) = \cosh\left(\hat{k}^2 + \frac{\hat{Q}^2}{4}\right) + \cosh\left(\hat{k}\hat{Q}x\right)\,. \tag{8.46}$$

To compute the denominator we first represent it in dimensionless form

$$\int \frac{d^3p_1}{(2\pi\hbar)^3}\,\phi(\hat{p}_1)I[\phi(\hat{p}_1)] = \frac{\sqrt{mT}}{\hbar^3}\frac{T}{\hbar}\int \frac{d^3\hat{p}_1}{(2\pi)^3}\,\phi(\hat{p}_1)\hat{I}[\phi(\hat{p}_1)]\,, \tag{8.47}$$

which entails the dimensionless T-matrix

$$\mathcal{T}(Q,k) = \frac{\hbar^3}{m^{3/2}T^{1/2}}\hat{\mathcal{T}}(\hat{Q},\hat{k})\,. \tag{8.48}$$

The integral over the dimensionless collision term can now be written in terms of the transformed momenta

$$\begin{aligned}\int \frac{d^3\hat{p}_1}{(2\pi)^3}\,\phi(\hat{p}_1)\hat{I}[\phi(\hat{p}_1)] = 2^{7/2}\int_0^\infty \frac{d\hat{k}}{(2\pi)^3}2\hat{k}^4\int_0^\infty \frac{d\hat{Q}}{(2\pi)^3}\hat{Q}^3\left|\hat{\mathcal{T}}\left(\hat{Q},2\hat{k}^2+\frac{\hat{Q}^2}{2}\right)\right|^2 \\ \cdot\int d\Omega_Q\int d\Omega_k\int d\Omega_{k'}\left(\hat{k}^2+\hat{k}\hat{Q}x+\frac{\hat{Q}^2}{4}\right)\left(\hat{k}_z+\frac{\hat{Q}_z}{2}\right)\frac{x\hat{k}_z-x'\hat{k}'_z}{4g(\hat{Q},\hat{k},x)g(\hat{Q},\hat{k},x')}\,,\end{aligned} \tag{8.49}$$

where the additional factor of $2^{7/2}$ originates from the definition of the momenta $\hat{p} = p/\sqrt{2mT}$. Next we consider the integrals over solid angles related to the three vector variables $\mathbf{Q}$, $\mathbf{k}$ and $\mathbf{k}'$ in the second line. Most conveniently, one first integrates over the angles of the relative momenta. To this end, one introduces the unit vector $\hat{\mathbf{e}}_Q = \mathbf{Q}/Q$ parallel to the center-of-mass momentum to measure the polar angles of the relative momenta. Afterwards, the final integration over the angular degrees of freedom of $\mathbf{Q}$ is performed in the coordinate system $\hat{\mathbf{e}}_x, \hat{\mathbf{e}}_y, \hat{\mathbf{e}}_z$, defined by $\nabla T \sim \hat{\mathbf{e}}_z$. For the first integration we create a new orthonormal system $\hat{\mathbf{e}}_1, \hat{\mathbf{e}}_2, \hat{\mathbf{e}}_Q$, where the exact definition of the first two vectors turns out to be irrelevant. In this basis the relative momenta become

$$\mathbf{k} = k\left(\sqrt{1-x^2}\cos(\varphi_{kQ})\hat{\mathbf{e}}_1 + \sqrt{1-x^2}\sin(\varphi_{kQ})\hat{\mathbf{e}}_2 + x\hat{\mathbf{e}}_Q\right) \tag{8.50a}$$

$$\mathbf{k}' = k\left(\sqrt{1-x^2}\cos(\varphi_{k'Q})\hat{\mathbf{e}}_1 + \sqrt{1-x^2}\sin(\varphi_{k'Q})\hat{\mathbf{e}}_2 + x\hat{\mathbf{e}}_Q\right)\,, \tag{8.50b}$$

where $\varphi_{kQ}$ and $\varphi_{k'Q}$ denote the azimuthal angles of $\mathbf{k}$ and $\mathbf{k}'$ in the coordinate system $\hat{\mathbf{e}}_1, \hat{\mathbf{e}}_2, \hat{\mathbf{e}}_Q$. Their $z$-components $k_z = \mathbf{k}\cdot\hat{\mathbf{e}}_z = k\cos\theta$ and $k'_z = \mathbf{k}'\cdot\hat{\mathbf{e}}_z = k\cos\theta'$ in the original coordinate system can be written as

$$\cos\theta = \cos(\varphi_Q - \varphi_{kQ})\sin\theta_Q\sqrt{1-x^2} + \cos\theta_Q\, x \tag{8.51a}$$

$$\cos\theta' = \cos(\varphi_Q - \varphi_{k'Q})\sin\theta_Q\sqrt{1-(x')^2} + \cos\theta_Q\, x'\,, \tag{8.51b}$$

which is the cosine relation of spherical trigonometry [169]. Here $\varphi_Q$ and $\theta_Q$ refer to the azimuthal and the polar angle of $\mathbf{Q}$ with respect the coordinate system $\hat{\mathbf{e}}_x, \hat{\mathbf{e}}_y, \hat{\mathbf{e}}_z$, such that we have for the vector component $Q_z = Q\cos\theta_Q$. Now we insert these definitions into eq. (8.49). Fortunately, many terms vanish either due to the azimuthal integrations or because of the symmetry of the function $g(\hat{Q},\hat{k},x)$,

defined in eq. (8.46). We arrive at the much shorter expression

$$\int \frac{d^3p_1}{(2\pi\hbar)^3}\,\phi(\hat{p}_1)I[\phi(\hat{p}_1)] = \frac{1}{(2\pi)^3}\int_0^\infty d\hat{k}\,\hat{k}^7\int_0^\infty d\hat{Q}\,\hat{Q}^4 \cdot\left|\hat{\mathcal{T}}\left(\hat{Q},2\hat{k}^2+\frac{\hat{Q}^2}{2}\right)\right|^2\left[\mathcal{W}(\hat{Q},\hat{k},2)\mathcal{W}(\hat{Q},\hat{k},0)-\mathcal{W}(\hat{Q},\hat{k},2)^2\right], \tag{8.52}$$

where we have introduced the functions

$$\mathcal{W}(\hat{Q},\hat{k},n) = \int_{-1}^{1}\frac{dx\,x^n}{g(\hat{Q},\hat{k},x)} \tag{8.53}$$

for the averages over the polar angles. In particular, $\mathcal{W}(\hat{Q},\hat{k},n)\equiv 0$, if $n$ odd, while the results for $n=0$ and $n=2$ can be given in analytic form. With the abbreviations $a=2\hat{k}^2+\hat{Q}^2/2$ and $b=\hat{k}\hat{Q}$, we have [109]

$$\mathcal{W}(\hat{Q},\hat{k},0) = -\frac{2\log\left[\cosh\left(\frac{a-b}{2}\right)\cosh^{-1}\left(\frac{a+b}{2}\right)\right]}{\sinh(a)b} \tag{8.54a}$$

$$\mathcal{W}(\hat{Q},\hat{k},2) = -\frac{2e^a(\coth(a)-1)\left(a^3-3ab^2+a\pi^2+3b^2\log\left[\frac{e^a+e^b}{1+e^{a+b}}\right]\right)}{3b^3} - 4e^a(\coth(a)-1)\frac{\left(b\mathrm{Li}_2(-e^{b-a})-b\mathrm{Li}_2(-e^{a+b})-\mathrm{Li}_3(-e^{b-a})+\mathrm{Li}_3(-e^{a+b})\right)}{b^3}. \tag{8.54b}$$

Now the remaining radial integrals in eq. (8.52) have to be solved numerically. Fortunately, we can directly use standard integration routines, since the hyperbolic functions in the $\mathcal{W}(\hat{Q},\hat{k},n)$ give rise to a Gaussian suppression at large momenta, which cannot be overcome by the residual terms and the T-matrix, that at most diverge algebraically. Regarding the limit $i0^+$ in the latter, one can use a finite imaginary part $\epsilon$ and decrease its size until convergence is reached. In practice, we obtain a precision of $10^{-7}$ with $\epsilon=10^{-8}$. All in all, we find

$$\int \frac{d^3p_1}{(2\pi\hbar)^3}\,\phi(\hat{p}_1)I[\phi(\hat{p}_1)] = 0.016316\,, \tag{8.55}$$

which implies for the heat conductivity of the unitary Fermi gas in the quantum critical regime

$$\kappa = 1.70514N_f^2\frac{T}{\hbar\lambda_T}+\mathcal{O}(N_f)\,. \tag{8.56}$$

This follows from inserting the integrated collision term into eq. (8.42), with the current $\mathbf{j}_Q$ given in eq. (8.40). Note that the leading order of $\kappa$ carries a factor $N_f^2$, which indicates the ill-defined notion of a transport coefficient in the absence of

any interactions. In case of the shear viscosity, that has been obtained in a similar approach by Enss [109], one finds in analogy

$$\eta = 3.214917 \frac{N_f^2 \hbar}{\lambda_T^3} + \mathcal{O}(N_f)\,. \tag{8.57}$$

We reemphasize that the large-N expansion includes corrections from the finite density of the medium, that are included even by the bare particle ladders in the leading order T-matrix from eq. (8.23). For the high-temperature regime a computation of $\kappa$, based on the Boltzmann equation with the vacuum scattering cross section, yields at unitarity [185]

$$\kappa^{\mathrm{cl}} = \frac{225}{64\sqrt{2}} \frac{T}{\hbar \lambda_T} = 2.485... \frac{T}{\hbar \lambda_T}\,, \tag{8.58}$$

which differs from the result in the quantum critical regime obtained here.

Recall that we have simply set the deviation from the local equilibrium $\phi$ proportional to the inhomogeneity of the Boltzmann equation and the question arises how strongly the value of the heat conductivity depends on this particular choice. To improve the result we extend the ansatz for $\phi$ by further functions. To this end, we introduce the scalar product

$$\langle \chi | \psi \rangle := \int \frac{d^3 \hat{p}}{(2\pi)^3}\, \chi(\hat{\mathbf{p}})\, \left[ n_F(\hat{p})\,(1 - n_F(\hat{p})) \right]\, \psi(\hat{\mathbf{p}}), \tag{8.59}$$

for dimensionless functions of the variable $\hat{\mathbf{p}}$. An expansion of $\phi$ is most conveniently performed in an orthonormal basis with respect to this particular bilinear form. In other words, we have to find a set of polynomials $\chi^{(i)}(\hat{\mathbf{p}})$, $i \in \mathbb{N}_0$ of arbitrary degree that satisfy

$$\langle \chi^{(i)} | \chi^{(j)} \rangle = \delta_{ij} \qquad \forall \quad i, j\,. \tag{8.60}$$

Since the temperature gradient is the only term that breaks the rotational invariance of the system, we will only consider basis functions of the form

$$\chi^{(i)}(\hat{\mathbf{p}}) = \mathcal{N}_i\, \hat{p}_z \left( d_0^{(i)} + d_1^{(i)}\, \hat{p}^2 + d_2^{(i)}\, \hat{p}^4 + ... + d_i^{(i)}\, \hat{p}^{2i} \right)\,, \tag{8.61}$$

with real coefficients that describe currents along the $z$ axis. Here $\mathcal{N}_i$ denotes the normalization, while the function is analytic in $\hat{\mathbf{p}}$, apart from the factor $\hat{p}_z$, and we have the freedom to set the coefficient of the highest power to unity, i.e $d_i^{(i)} = 1$ in every $\chi^{(i)}$. This enables us to compare the results more directly to the previous computation. Note that these functions by construction have vanishing overlap with the collision invariants $\phi = 1$ for the particle number conservation, the momentum components $\phi = \hat{p}_{x,y}$ and the isotropic energy $\phi = \hat{p}^2$. Therefore, also the components of the particle current $j_{N,\,x}$ and $j_{N,\,y}$ vanish. The remaining

current $j_{N,z}$ will be considered below. To compute the coefficients $d_j^{(i)}$ one first calculates the scalar products of the $\chi^{(i)}$, which can be done analytically by the help of eq. (8.39). Subsequently, one demands the orthogonality of the basis functions, which results in a system of linear equations for the coefficients. In practice, we can take into account only a finite number of the $\chi^{(i)}$, however, when one extends the truncated set the previously determined coefficients do not change, due to the mutual orthogonality of the $\chi^{(i)}$. We use the five polynomials of smallest degree

$$\begin{aligned}
\chi^{(0)}(\hat{\mathbf{p}}) &= 10.7907\hat{p}_z \\
\chi^{(1)}(\hat{\mathbf{p}}) &= 6.71951\hat{p}_z\left(-\tilde{s}+\hat{p}^2\right) \\
\chi^{(2)}(\hat{\mathbf{p}}) &= 2.50655\hat{p}_z\left(10.734-7.53193\hat{p}^2+\hat{p}^4\right) \\
\chi^{(3)}(\hat{\mathbf{p}}) &= 0.675374\hat{p}_z\left(-51.0212+53.6366\hat{p}^2-14.1822\hat{p}^4+\hat{p}^6\right) \\
\chi^{(4)}(\hat{\mathbf{p}}) &= 0.142871\hat{p}_z\left(292.171-409.854\hat{p}^2+162.174\hat{p}^4-22.8065\hat{p}^6+\hat{p}^8\right)\,,
\end{aligned} \tag{8.62}$$

which entails a very good convergence of the heat conductivity. Quite importantly, the function $\chi^{(0)}$ represents the collision invariant $\hat{p}_z$. The exact solution to the Boltzmann equation, which includes arbitrarily many basis functions can therefore be written as a unique linear combination

$$\phi(\hat{\mathbf{p}}) = \sum_{j=1}^{\infty} c_j\,\chi^{(j)}(\hat{\mathbf{p}})\,, \tag{8.63}$$

which excludes $\chi^{(0)}$, because the orthogonality of the basis vectors will ensure $j_{N,z}=0$. Consequently, the particle current vanishes, as requested by the definition below eq. (8.24).

Within this formulation for the function space the Boltzmann equation itself can be written as

$$\left[n_F(\hat{p}_1^2)\left(1-n_F(\hat{p}_1^2)\right)\right]\frac{\chi^{(1)}(\hat{\mathbf{p}}_1)}{\mathcal{N}_1}\frac{\sqrt{2mT}}{m}\frac{\partial_z T}{T} = -\frac{1}{N_f}\sum_j c_j I[\chi^{(j)}(\hat{\mathbf{p}}_1)]\,. \tag{8.64}$$

Multiplying both sides of the equation with $\chi^{(i)}$ for $i\geqslant 1$ ($i=0$ yields only a trivial statement about the momentum conservation) and integrating over $\int d^3\hat{\mathbf{p}}_1/(2\pi)^3$ transforms the Boltzmann equation into a linear equation for the vector $\mathbf{c} = (c_1, c_2, c_3, ....)$, which reads

$$\frac{\sqrt{2}\partial_z T}{\mathcal{N}_1\sqrt{mT}}\hat{\mathbf{e}}_1 = -\frac{1}{N_f}\frac{4T}{\hbar}\underline{A}\cdot\mathbf{c}\,. \tag{8.65}$$

On the left-hand side, where only the first entry yields a nonvanishing contribution, we have profited again from the orthogonality of the basis functions. The components of the dimensionless matrix $\underline{A}$, where the prefactor arises from making the

internal momentum integral over $\mathbf{p}_2$ dimensionless, contain the integrals

$$A_{i,j} = \int \frac{d^3\hat{p}}{(2\pi)^3}\, \chi^{(i)}(\hat{\mathbf{p}}_1)\, \hat{I}\left[\chi^{(j)}(\hat{\mathbf{p}}_1)\right]. \tag{8.66}$$

These can be computed like above, in the center-of-mass frame. Due to the higher degree of the polynomials they now also include higher order angular averages $\mathcal{W}(\hat{Q}, \hat{k}, 2n)$ with $n > 1$. The latter can be calculated analytically, for example with *Mathematica*. The remaining integrals over the $\hat{Q}$ and $\hat{k}$ require a numerical evaluation, however, the integrands still decay exponentially and can be integrated with standard routines. Since the collision term of the linearized Boltzmann equation is in general a positive, symmetric operator [169, 184] also the matrix $\underline{A}$ is symmetric with positive diagonal components. If one truncates the basis at a maximal index $i_{\max}$, $\underline{A}$ reduces to an $i_{\max} \times i_{\max}$ matrix. Including the indices $1 \leqslant i \leqslant 4$ and $1 \leqslant j \leqslant 4$, we find

$$\underline{A} = \begin{pmatrix} 0.736699 & -0.279182 & 0.158146 & -0.0969151 \\ -0.279182 & 1.09841 & -0.472149 & 0.274414 \\ 0.158146 & -0.472149 & 393.907 & -0.572904 \\ -0.0969151 & 0.274414 & -0.572904 & 231.815 \end{pmatrix}. \tag{8.67}$$

To check the dependence of $\kappa$ on $i_{\max} \leqslant 4$, we can solve the system of equations for a basis of up to four functions by taking out the corresponding square matrix from the left upper corner of $\underline{A}$. For convenience, we absorb all the dimensionful quantities in a redefinition of the coefficients

$$\mathbf{c} = N_f \frac{\lambda_T\, \partial_z T}{4\sqrt{\pi} T} \hat{\mathbf{c}}\,, \tag{8.68}$$

for which we find

$$\begin{aligned} i_{\max} = 1: &\qquad \hat{\mathbf{c}} = (-0.202010) \\ i_{\max} = 2: &\qquad \hat{\mathbf{c}} = (-0.223541, -0.056817) \\ i_{\max} = 3: &\qquad \hat{\mathbf{c}} = (-0.223543, -0.056808, 0.000022) \\ i_{\max} = 4: &\qquad \hat{\mathbf{c}} = (-0.223544, -0.056802, 0.000022, -0.000026)\,. \end{aligned} \tag{8.69}$$

By comparing the coefficients for different $i_{\max}$, we observe that the leading order coefficients $\hat{c}_{1,2,3}$ are well converged. Furthermore, $\hat{c}_1$ is the dominant index, while the higher components decrease quickly. Nevertheless, taking more than one basis vector into account changes $\hat{c}_1$ by an amount of 10%, which will affect the heat conductivity in a similar manner. Since the result for $\hat{c}_1$ appears to be well converged, we do not continue to consider polynomials with higher powers, because this coefficient completely determines the heat current

$$j_{Q,z} = 2N_f \int \frac{d^3p}{(2\pi\hbar)^3} \varepsilon_p \frac{p_z}{m} n_F(p)\,(1 - n_F(p))\, c_1 \chi^{(1)}(\hat{\mathbf{p}}) = N_f^2 4\sqrt{\pi}\hat{c}_1 \hat{j}_Q^{(0)} \frac{T}{\hbar\lambda_T} \partial_z T\,. \tag{8.70}$$

Fourier's law (8.24) allows us to read off the heat conductivity from the prefactor. While we recover the result (8.56) in case of $i_{\max} = 1$, the inclusion of higher order polynomials entails the heat conductivity

$$\kappa = 1.8869 N_f^2 \frac{T}{\hbar \lambda_T} + \mathcal{O}(N_f)\,, \tag{8.71}$$

which mirrors the growth of the coefficient $\hat{c}_1$. The fact that $\kappa$ increases within this larger basis space is consistent with the maximum principle for the transport coefficients [169, 184].

### 8.3.3 The Prandtl number of the unitary gas in the quantum critical regime

The Prandtl number Pr is quite generally defined as the ratio of the shear viscosity and the heat conductivity [169, 184]

$$\mathrm{Pr} = \frac{\nu}{D_T} = \frac{\eta c_p}{\kappa n m}\,, \tag{8.72}$$

where $\nu$ is the kinematic viscosity $\nu = \eta/(nm)$ and $D_T = \kappa/(nmc_p)$ is the thermal diffusion constant that appears in the heat diffusion equation $\partial_t T(\mathbf{x}, t) = D_T \nabla^2 T(\mathbf{x}, t)$. The specific heat $c_p$ per volume at constant pressure is given by

$$c_p = \frac{T}{V}\left(\frac{\partial S}{\partial T}\right)_{T,N}\,. \tag{8.73}$$

Using the scale invariance of the resonant gas $p = 2/3\epsilon$ we have $S = 5pV/2T - \mu N/T$, which follows from $\Omega = U - TS - \mu N = -pV$. Then we can calculate the specific heat at fixed $p$, which yields

$$c_p = -\frac{S}{VT} + \frac{5p}{2V}\left(\frac{\partial V}{\partial T}\right)_{N,p} - \left(\frac{\partial \mu}{\partial T}\right)_p n = -\frac{5p}{2n}\left(\frac{\partial n}{\partial T}\right)_p\,, \tag{8.74}$$

after setting $\mu = 0$. Notice, that one should not discard the $\mu$ term in the expression for the entropy above directly, since its derivative $(\partial\mu/\partial T)_p = -S/N$ does not vanish but reduces instead to eq. (8.34). With this identity we obtain as the final result to leading order in $N_f$

$$\begin{aligned} c_p &= -\frac{5p}{2n}\left[\left(\frac{\partial n}{\partial T}\right)_\mu + \left(\frac{\partial n}{\partial \mu}\right)_T \left(\frac{\partial \mu}{\partial T}\right)_p\right] = -\frac{5p}{2n}\left[\left(\frac{\partial n}{\partial T}\right)_\mu + \left(\frac{\partial n}{\partial \mu}\right)_T \tilde{s}\right] \\ &= 3.20873 \frac{N_f}{\lambda_T^3}\,. \end{aligned} \tag{8.75}$$

To obtain the numerical value one uses the pressure and the density of the ideal Fermi gas with $h = 0$ from eqs. (2.35) and (5.8), which represent the $N_f \to \infty$

limit, where the system consists of $N_f$ identical copies of noninteracting Fermions according to eq. (8.21) for the large-N grand potential. With the result for the shear viscosity by Enss [109], given in eq. (8.57), we find for the Prandtl number of the unitary gas in the quantum critical regime

$$\mathrm{Pr} \simeq 0.5686 + \mathcal{O}(N_f^{-1})\,, \tag{8.76}$$

where we have inserted the value for $\kappa$ from eq. (8.71) derived from the extended ansatz for the distribution function. Note that the leading order contribution is independent of the number of flavors, since both transport coefficients scale quadratically with $N_f$, while the density in the denominator of the Defintion (8.72) cancels the factor of $N_f$ in $c_p$. In case of the simpler ansatz with a single polynomial, that led to eq. (8.56), one obtains $\mathrm{Pr} \simeq 0.6292 + \mathcal{O}(N_f^{-1})$, which is closer to the value of the nondegenerate gas $\mathrm{Pr}^{\mathrm{cl}} = 2/3$ [169, 184]. Since the shear viscosity has been computed with a single ansatz function, the large-N Boltzmann result will increase, if one includes also higher order polynomials for $\eta$. However, the estimated growth is about 2% -3% such that the result remains below $\mathrm{Pr}^{\mathrm{cl}}$ [175]. In fact, the large-N approach does take into account finite-density corrections, as discussed above, and we therefore do not expect to recover the result from the regime of small fugacities $z = \exp(\beta\mu) \to 0$, where a virial expansion is possible. Braby et al. [185] indeed obtain $\mathrm{Pr} = 2/3$ in the high-temperature limit from the Boltzmann approach with the vacuum cross section. They also compute the Prandtl number at smaller $T$ and for arbitrary scattering lengths, where they obtain values larger than $\mathrm{Pr}^{\mathrm{cl}}$ for all parameters in the absence of the medium.

Quite remarkably, the Prandtl number is also connected to the question whether a gravity dual in the sense of an AdS-CFT correspondence can be constructed for the unitary Fermi gas, which is symmetric under conformal transformations. However, the mapping to a gravitational description so far has only been established for Lorentz-invariant, conformal field theories. As argued by Rangamani et al. [186] the construction of a gravity dual for a nonrelativistic conformal field theory, like the unitary gas, entails $\mathrm{Pr} \equiv 1$. Due to the discrepancy with the result $\mathrm{Pr} \simeq 0.57$ obtained here, the existence of a gravity dual for the unitary gas seems to be rather unlikely, but of course it cannot be ruled out as long as higher order corrections remain unknown.

# Chapter 9

# Conclusion

In this thesis we have studied the thermodynamics of a spin-imbalanced Fermi gas in the vicinity of an open-channel dominated Feshbach resonance. Based on a Luttinger-Ward formalism we have obtained quantitative results for the universal scaling functions of the thermodynamic quantities in the symmetric phase $T \geqslant T_c$ both for finite and infinite scattering length $a$, which arise from the strongly-coupled quantum critical point at $1/a = 0$ and vanishing chemical potentials [1]. Furthermore, we have determined the phase boundary to the symmetry-broken phase, where we have detected either an instability to a homogeneous superfluid or to a spatially periodic FFLO superfluid, depending on the temperature, the scattering length and the Zeeman field $h$. Regarding the first, the extrapolation to zero temperature yields the universal value $(h/\mu)_c = 1.09 \pm 0.05$ for the Clogston-Chandrasekhar limit of the unitary gas. The phase boundary of the normal-FFLO transition extends for sufficiently strong $h$ and low enough temperatures beyond the unitary limit also to positive scattering lengths in agreement with the qualitative predictions by Son and Stephanov [2]. At unitary we obtain the universal ratio $(h/\mu)_{\mathrm{FFLO}} = 1.28 \pm 0.15$ the ground state phase transition. The largest critical temperatures of $T_c \simeq 0.03\varepsilon_F$ are encountered on the fermionic side of the crossover in the regime $v \gtrsim -1$, where the order-parameter varies typically on the scale $Q_{\mathrm{FFLO}} \simeq 0.1k_F$.

The Luttinger-Ward formalism allows to include the strong interactions close to infinite scattering length to all orders, which gives rise to a Schwinger-Dyson equation for the spin-dependent single-fermion Green's function $\mathcal{G}_{\sigma\sigma}$ that we have solved fully self-consistently. For the numerical computations we both have developed a discrete Fourier transform that uses a spline interpolation of up to quintic order and moreover have also applied a logarithmic Fourier transformation. The mathematical properties of the latter have been investigated in further detail in this thesis. We have proven that the LFT convergences to the exact result exponentially fast in the number of grid points, provided that the function under consideration is analytic in a strip of finite width around the real axis of the logarithmic variable. Furthermore, the choice of the trade-off parameter $k_p$ allows to treat also Fourier transforms numerically that are only defined in the sense of generalized functions.

Apart from thermodynamic quantities, we have considered transport properties of the balanced unitary gas. We present Luttinger-Ward results for the scaling

functions of the shear viscosity $f_\eta$. Afterwards, we compute the heat conductivity $\kappa$ in the quantum critical regime $T \gg \mu$ within a large-N expansion. The latter allows to apply a Boltzmann equation, which takes the presence of a finite density into account. Within a suitable set of basis functions we obtain to leading order in the number of flavors $N_f$ $\kappa = 1.8869 N_f^2 T/(\hbar\lambda_T)$ and for the Prandtl number $\mathrm{Pr} = 0.5686$, which is below the classical result $\mathrm{Pr}^{\mathrm{cl}} = 2/3$.

# Appendix A

# Outlook on the implementation of Luttinger-Ward formalism in the symmetry-broken phase

In this appendix we summarize the general properties of the anomalous Green's functions of the spin-imbalanced Fermi gas that appear below $T_c$. Then we briefly derive their mean-field forms both in $(\mathbf{k}, \omega_n)$ and $(\mathbf{k}, \tau)$ space, which provide a starting point for the self-consistent Luttinger-Ward computations in the symmetry-broken phase, discussed afterwards. In particular, their asymptotic behavior will require an extension of the subtraction schemes discussed in Chap. 7. To close the appendix we give a short outlook on the self-consistent loop.

## A.1 General properties of the anomalous propagators

Recall the Definition (4.6) of the anomalous Green's functions

$$\begin{aligned} \mathcal{F}_{\sigma\bar{\sigma}}(\mathbf{x}-\mathbf{x}', \tau-\tau') &= -\left\langle \mathcal{T}\left[\hat{\Psi}_\sigma(\mathbf{x},\tau)\,\hat{\Psi}_{\bar{\sigma}}(\mathbf{x}',\tau')\right]\right\rangle \\ \mathcal{F}^+_{\sigma\bar{\sigma}}(\mathbf{x}-\mathbf{x}', \tau-\tau') &= -\left\langle \mathcal{T}\left[\hat{\Psi}^\dagger_\sigma(\mathbf{x},\tau)\,\hat{\Psi}^\dagger_{\bar{\sigma}}(\mathbf{x}',\tau')\right]\right\rangle , \end{aligned} \tag{A.1}$$

which suggests that there are four new components of the single-particle Green's function $G$. Fortunately, not all of them are independent, but can be expressed instead in terms of a single Gorkov Green's function

$$\mathcal{F}(\mathbf{x},\tau) \equiv \mathcal{F}_{\uparrow\downarrow}(\mathbf{x},\tau) , \tag{A.2}$$

whereas for the remaining spin combinations the following identities hold

$$\mathcal{F}^+_{\downarrow\uparrow}(\mathbf{x},\tau) = (\mathcal{F}(-\mathbf{x},\tau))^* \tag{A.3a}$$

$$\mathcal{F}_{\downarrow\uparrow}(\mathbf{x},\tau) = -\mathcal{F}(-\mathbf{x},-\tau) \tag{A.3b}$$

$$\mathcal{F}^+_{\uparrow\downarrow}(\mathbf{x},\tau) = -(\mathcal{F}(\mathbf{x},-\tau))^* . \tag{A.3c}$$

Regarding the first and last equation, it will turn out that within our approximations all anomalous functions can be chosen real, such that the complex conjugate

is inconsequential. Note however, that in the presence of finite spin imbalance the identification $\mathcal{F}_{\downarrow\uparrow}(\mathbf{x},\tau) = -\mathcal{F}(\mathbf{x},\tau)$ due to spin-singlet pairing, which has been used in the previous work on the Luttinger-Ward theory for the balanced BCS-BEC crossover [37,144,150] does *not* hold and we have to stick to the more general equations given above. These identities can be derived easily from the definitions (A.1). Here we prove the general relation between $\mathcal{F}_{\downarrow\uparrow}$ and $\mathcal{F}$ in equation (A.3b), since the spin-imbalanced case usually is not discussed in standard textbooks like Fetter and Walecka [67] or Abrikosov, Gorkov and Dzyaloshinsky [139]. To this end, we first make use of the spatial homogeneity and shift the position argument, before we use the cyclic properties of the trace:

$$\begin{aligned}
\mathcal{F}_{\downarrow\uparrow}(\mathbf{x},\tau) =& \frac{-1}{Z}\Big\{\theta(\tau)\,\mathrm{Tr}\left[e^{-\beta H}e^{\frac{\tau}{\hbar}H}\hat{\Psi}_{\downarrow}(\mathbf{x})e^{-\frac{\tau}{\hbar}H}\hat{\Psi}_{\uparrow}(\mathbf{0})\right] \\
&\qquad - \theta(-\tau)\,\mathrm{Tr}\left[e^{-\beta H}\hat{\Psi}_{\uparrow}(\mathbf{0})e^{\frac{\tau}{\hbar}H}\hat{\Psi}_{\downarrow}(\mathbf{x})e^{-\frac{\tau}{\hbar}H}\right]\Big\} \\
=& \frac{-1}{Z}\Big\{\theta(\tau)\,\mathrm{Tr}\left[e^{-\beta H}e^{\frac{\tau}{\hbar}H}\hat{\Psi}_{\downarrow}(\mathbf{0})e^{-\frac{\tau}{\hbar}H}\hat{\Psi}_{\uparrow}(-\mathbf{x})\right] \\
&\qquad - \theta(-\tau)\,\mathrm{Tr}\left[e^{-\beta H}\hat{\Psi}_{\uparrow}(-\mathbf{x})e^{\frac{\tau}{\hbar}H}\hat{\Psi}_{\downarrow}(\mathbf{0})e^{-\frac{\tau}{\hbar}H}\right]\Big\} \\
=& \frac{-1}{Z}\Big\{\theta(\tau)\,\mathrm{Tr}\left[e^{-\beta H}\hat{\Psi}_{\downarrow}(\mathbf{0})e^{-\frac{\tau}{\hbar}H}\hat{\Psi}_{\uparrow}(-\mathbf{x})e^{\frac{\tau}{\hbar}H}\right] \\
&\qquad - \theta(-\tau)\,\mathrm{Tr}\left[e^{-\beta H}e^{-\frac{\tau}{\hbar}H}\hat{\Psi}_{\uparrow}(-\mathbf{x})e^{\frac{\tau}{\hbar}H}\hat{\Psi}_{\downarrow}(\mathbf{0})\right]\Big\} \\
=& -\mathcal{F}_{\uparrow\downarrow}(-\mathbf{x},-\tau) = \mathcal{F}(r,\beta-\tau)\,.
\end{aligned} \tag{A.4}$$

In the very last step we have make use of the rotational invariance and have replaced $-\mathbf{x}$ by $r = |\mathbf{x}|$. The remaining two identities follow analogously. A convenient way to summarize all components of the Green's function $\underline{G}$ is to arrange them in a Nambu structure, which is indicated by the line below the symbol. Here the Nambu spinor $\Phi = \left(\hat{\Psi}_{\uparrow}, \hat{\Psi}^{\dagger}_{\downarrow}, \hat{\Psi}_{\downarrow}, \hat{\Psi}^{\dagger}_{\uparrow}\right)$ contains all four field operators, in contrast to the spinor with two components that we have used for the large-N expansion of the action of the spin-balanced system, see Sec. 8.3.1. In this extended basis $\underline{G}$

reads

$$\begin{aligned}\underline{G}\left(\mathbf{x},\tau\right) &= -\left\langle \mathcal{T}\left[\Phi\left(\mathbf{x},\tau\right)\Phi^{\dagger}\left(\mathbf{0},0\right)\right]\right\rangle \\ &= \begin{pmatrix} \mathcal{G}_{\uparrow\uparrow}\left(\mathbf{x},\tau\right) & \mathcal{F}\left(\mathbf{x},\tau\right) & 0 & 0 \\ \left(\mathcal{F}(-\mathbf{x},\tau)\right)^{*} & -\mathcal{G}_{\downarrow\downarrow}(-\mathbf{x},-\tau) & 0 & 0 \\ 0 & 0 & \mathcal{G}_{\downarrow\downarrow}\left(\mathbf{x},\tau\right) & -\mathcal{F}(-\mathbf{x},-\tau) \\ 0 & 0 & -\left(\mathcal{F}(\mathbf{x},-\tau)\right)^{*} & -\mathcal{G}_{\uparrow\uparrow}(-\mathbf{x},-\tau) \end{pmatrix}.\end{aligned} \tag{A.5}$$

The upper and lower block-diagonal submatrices can be exchanged by flipping all spin indices with the help of eq. (A.3c). After transforming $G\left(\mathbf{x},\tau\right)$ from equation (A.5) to momentum and Matsubara frequeny space, we obtain

$$\underline{G}\left(\mathbf{k},\omega_n\right) = \begin{pmatrix} \mathcal{G}_{\uparrow\uparrow}\left(\mathbf{k},\omega_n\right) & \mathcal{F}\left(\mathbf{k},\omega_n\right) & 0 & 0 \\ \left(\mathcal{F}(\mathbf{k},-\omega_n)\right)^{*} & -\mathcal{G}_{\downarrow\downarrow}(-\mathbf{k},-\omega_n) & 0 & 0 \\ 0 & 0 & \mathcal{G}_{\uparrow\uparrow}\left(\mathbf{k},\omega_n\right) & -\mathcal{F}(-\mathbf{k},-\omega_n) \\ 0 & 0 & -\left(\mathcal{F}(-\mathbf{k},\omega_n)\right)^{*} & -\mathcal{G}_{\downarrow\downarrow}(-\mathbf{k},-\omega_n) \end{pmatrix}. \tag{A.6}$$

Retaining the spin indices, we extract the following exact relations between the interacting anomalous Green's in momentum and Matsubara frequency space from the Nambu Green's function $\underline{G}\left(\mathbf{k},\omega_n\right)$

$$\mathcal{F}^{+}_{\bar{\sigma}\sigma}\left(\mathbf{k},\omega_n\right) = \left(\mathcal{F}_{\sigma\bar{\sigma}}(\mathbf{k},-\omega_n)\right)^{*} \tag{A.7a}$$

$$\mathcal{F}_{\bar{\sigma}\sigma}\left(\mathbf{k},\omega_n\right) = -\mathcal{F}_{\sigma\bar{\sigma}}(-\mathbf{k},-\omega_n)\,. \tag{A.7b}$$

As a short-hand notation we introduce furthermore

$$\underline{G} = \begin{pmatrix} G^{(1)} & 0 \\ 0 & G^{(2)} \end{pmatrix}. \tag{A.8}$$

Explicit expressions for $\underline{G}$, that satisfy all these general properties, arise within BCS-mean-field theory. Since the latter provides a starting point for the self-consistent Luttinger-Ward computations in the symmetry-broken phase, we will in the following derive explicitly the mean-field form of $\underline{G}$ in the presence of a finite Zeeman field.

## A.2 Green's functions at the mean-field level

To obtain the equations of motion for $\underline{G}$ on the mean-field level, we follow the derivation given in Ref. [67]. First, we factorize the quartic interaction operator $\hat{V}$

of the single-channel Hamiltonian (2.26) via

$$\begin{aligned}\hat{V} &= \bar{g}\int d^3x\ \hat{\Psi}^\dagger_\uparrow(\mathbf{x})\hat{\Psi}^\dagger_\downarrow(\mathbf{x})\hat{\Psi}_\downarrow(\mathbf{x})\hat{\Psi}_\uparrow(\mathbf{x}) \\ &\simeq \bar{g}\int d^3x\ \langle\hat{\Psi}^\dagger_\uparrow(\mathbf{x})\hat{\Psi}^\dagger_\downarrow(\mathbf{x})\rangle\hat{\Psi}_\downarrow(\mathbf{x})\hat{\Psi}_\uparrow(\mathbf{x}) + \bar{g}\int d^3x\ \hat{\Psi}^\dagger_\uparrow(\mathbf{x})\hat{\Psi}^\dagger_\downarrow(\mathbf{x})\langle\hat{\Psi}_\downarrow(\mathbf{x})\hat{\Psi}_\uparrow(\mathbf{x})\rangle \\ &\quad - \bar{g}\int d^3x\langle\hat{\Psi}^\dagger_\uparrow(\mathbf{x})\hat{\Psi}^\dagger_\downarrow(\mathbf{x})\rangle\langle\hat{\Psi}_\downarrow(\mathbf{x})\hat{\Psi}_\uparrow(\mathbf{x})\rangle \\ &= \Delta^*\int d^3x\ \hat{\Psi}_\downarrow(\mathbf{x})\hat{\Psi}_\uparrow(\mathbf{x}) + \Delta\int d^3x\ \hat{\Psi}^\dagger_\uparrow(\mathbf{x})\hat{\Psi}^\dagger_\downarrow(\mathbf{x}) - \frac{|\Delta|^2}{\bar{g}} \\ &=: \hat{V}_{\rm MF}\,,\end{aligned} \tag{A.9}$$

where we have inserted the definition of the superfluid gap $\Delta = \bar{g}\langle\hat{\Psi}_\downarrow(x)\hat{\Psi}_\uparrow(x)\rangle = -\bar{g}\langle\hat{\Psi}_\uparrow(x)\hat{\Psi}_\downarrow(x)\rangle$ from eq. (4.7). The final form of the mean-field operator has then been obtained by making use of the spatial homogeneity of the system, which leads to a position-independent expectation value $\Delta$. Note that this simplification discards any FFLO-type order. Like in the study of the normal phase, our theory will only be able to detect an instability of the homogenous superfluid towards an inhomogeneous superfluid phase by a divergence at finite $Q \neq 0$ for $\Omega_n = 0$ in one of the eigenvalues of matrix-valued vertex function $\underline{\Gamma}(\mathbf{Q}, \Omega_n = 0)$ in Nambu space, see eq. (A.25) below. The spatial structure of the order parameter, which requires to determine the anomalous propagator $\mathcal{F}(\mathbf{k}, \omega_n)$ as a function of a general momentum variable $\mathbf{k}$, including the angular coordinates (see the paper by Larkin and Ovchinnikov [28] from 1964) remains beyond the scope of our Luttinger-Ward approach. In the construction of $V_{\rm MF}$ we have only taken into account quadratic terms proportional to the anomalous expectation values, since the Hartree contributions, formed by the diagonal parts of the Green's function, vanish anyway in the zero-range limit $\Lambda \to \infty$, as discussed in Sec. 4.4.2.

Substituting $\hat{V}$ by $\hat{V}_{\rm MF}$ yields the quadratic Hamiltonian[1]

$$\begin{aligned}H_{\rm MF} = &\sum_\sigma\int d^3x\ \hat{\Psi}^\dagger_\sigma(\mathbf{x})\left(-\frac{\hbar^2\nabla^2}{2m} - \mu_\sigma\right)\hat{\Psi}_\sigma(\mathbf{x}) \\ &+ \Delta^*\int d^3x\ \hat{\Psi}_\downarrow(\mathbf{x})\hat{\Psi}_\uparrow(\mathbf{x}) + \Delta\int d^3x\ \hat{\Psi}^\dagger_\uparrow(\mathbf{x})\hat{\Psi}^\dagger_\downarrow(\mathbf{x}) - \frac{|\Delta|^2}{\bar{g}}\,,\end{aligned} \tag{A.10}$$

that determines the linear mean-field equations of motion for the fermionic field operators. They are obtained from the Heisenberg equations in imaginary time

[1] The electronic problem may also include the minimal coupling of the motional degrees of freedom to a magnetic vector potential $\mathbf{A}(\mathbf{x})$, that is responsible for the Meissner effect and the formation of vortex lattice in type II superconductors, see Ref. [67].

$\hbar\,\partial_\tau \hat{\Psi}_\sigma = [H_{\mathrm{MF}}, \hat{\Psi}_\sigma]$ or $\hbar\,\partial_\tau \hat{\Psi}^\dagger_\sigma = [H_{\mathrm{MF}}, \hat{\Psi}^\dagger_\sigma]$, respectively, and read

$$\hbar\frac{\partial}{\partial\tau}\hat{\Psi}_\sigma(\mathbf{x},\tau) = +\left(\frac{\hbar^2\nabla^2}{2m} + \mu_\sigma\right)\hat{\Psi}_\sigma(\mathbf{x},\tau) - \Delta\,\sigma\hat{\Psi}^\dagger_{\bar{\sigma}}(\mathbf{x},\tau) \tag{A.11a}$$

$$\hbar\frac{\partial}{\partial\tau}\hat{\Psi}^\dagger_\sigma(\mathbf{x},\tau) = -\left(\frac{\hbar^2\nabla^2}{2m} + \mu_\sigma\right)\hat{\Psi}^\dagger_\sigma(\mathbf{x},\tau) - \Delta^*\bar{\sigma}\hat{\Psi}_{\bar{\sigma}}(\mathbf{x},\tau)\,, \tag{A.11b}$$

where we have identified $\uparrow$ with $+1$ and $\downarrow$ with $-1$. The equations of motion for all the components $\mathcal{G}^{\mathrm{MF}}_{\sigma\sigma}(\mathbf{x},\tau)$, $\mathcal{F}^{\mathrm{MF}}_{\sigma\bar{\sigma}}(\mathbf{x},\tau)$ and $\mathcal{F}^{+\mathrm{MF}}_{\sigma\bar{\sigma}}(\mathbf{x},\tau)$ of the Green's function at the mean-field level can now be calculated by taking the $\tau$ derivative of the definitions (4.2) and (4.6), while the time-derivative of the operators is replaced by the set of equations (A.11). This results in

$$\left[-\hbar\frac{\partial}{\partial\tau} + \left(\frac{\hbar^2\nabla^2}{2m} + \mu_\sigma\right)\right]\mathcal{G}^{\mathrm{MF}}_{\sigma\sigma}(\mathbf{x},\tau) - \Delta\,\sigma\mathcal{F}^{+\mathrm{MF}}_{\bar{\sigma}\sigma}(\mathbf{x},\tau) = \hbar\,\delta(\tau)\delta(\mathbf{x}) \tag{A.12a}$$

$$\left[\hbar\frac{\partial}{\partial\tau} + \left(\frac{\hbar^2\nabla^2}{2m} + \mu_{\bar{\sigma}}\right)\right]\mathcal{F}^{+\ \mathrm{MF}}_{\bar{\sigma}\sigma}(\mathbf{x},\tau) + \Delta^*\sigma\,\mathcal{G}^{\mathrm{MF}}_{\sigma\sigma}(\mathbf{x},\tau) = 0\,. \tag{A.12b}$$

The Dirac $\delta$ distributions originate, as usual in equations of motions for Green's functions, from the $\tau$ derivative and the equal-time anticommutation relations (4.1). Note that our order parameter carries an additional factor $(-1)$ in comparision to Ref. [67], where the Hamiltonian is defined with the coupling constant $-\bar{g}$. The time evolution of $\mathcal{F}^{\mathrm{MF}}_{\sigma\bar{\sigma}}(\mathbf{x},\tau)$ in turn is related to the reversed normal Green's functions $\mathcal{G}^{\mathrm{MF}}_{\sigma\sigma}(-\mathbf{x},-\tau)$

$$\left[\hbar\frac{\partial}{\partial\tau} - \left(\frac{\hbar^2\nabla^2}{2m} + \mu_{\bar{\sigma}}\right)\right]\mathcal{F}^{\mathrm{MF}}_{\sigma\bar{\sigma}}(\mathbf{x},\tau) - \Delta\sigma\,\mathcal{G}^{\mathrm{MF}}_{\bar{\sigma}\bar{\sigma}}(-\mathbf{x},-\tau) = 0\,. \tag{A.13}$$

To solve these coupled, linear differential equations, we Fourier transform them to momentum and frequency space, which yields algebraic equations that allow to extract the final mean-field Green's functions. As a result, we find

$$\begin{aligned}\mathcal{G}^{\mathrm{MF}}_{\sigma\sigma}(\mathbf{k},\omega_n) &= \frac{(i\hbar\omega_n + \xi_{k,\bar{\sigma}})}{(i\hbar\omega_n - \xi_{k,\sigma})\,(i\hbar\omega_n + \xi_{k,\bar{\sigma}}) - |\Delta|^2} \\ &= \frac{-(i\hbar\omega_n + \xi_{k,\bar{\sigma}})}{\hbar^2\omega_n^2 - 2h\sigma i\hbar\omega_n + E_k^2 - h^2}\end{aligned} \tag{A.14a}$$

$$\begin{aligned}\mathcal{F}^{+\mathrm{MF}}_{\bar{\sigma}\sigma}(\mathbf{k},\omega_n) &= \frac{\sigma\Delta^*}{(i\hbar\omega_n - \xi_{k,\sigma})\,(i\hbar\omega_n + \xi_{k,\bar{\sigma}}) - |\Delta|^2} \\ &= \frac{-\sigma\Delta^*}{\hbar^2\omega_n^2 - 2h\sigma i\hbar\omega_n + E_k^2 - h^2}\end{aligned} \tag{A.14b}$$

$$\begin{aligned}\mathcal{F}^{\mathrm{MF}}_{\sigma\bar{\sigma}}(\mathbf{k},\omega_n) &= \frac{\sigma\Delta}{(i\hbar\omega_n - \xi_{k,\sigma})\,(i\hbar\omega_n + \xi_{k,\bar{\sigma}}) - |\Delta|^2} \\ &= \frac{-\sigma\Delta}{\hbar^2\omega_n^2 - 2h\sigma i\hbar\omega_n + E_k^2 - h^2}\,,\end{aligned} \tag{A.14c}$$

with the additional definitions $\xi_k = \varepsilon_k - \mu$ and $E_k = \sqrt{\xi_k^2 + |\Delta|^2}$, which is the standard dispersion relation of Bogoliubov quasiparticles in BCS theory. In the case of vanishing Zeeman field these results agree with the Nambu-Gorkov Green's functions in Ref. [67], up to the additional phase $\exp(i\pi) = -1$ assigned to the order-parameter. Furthermore, the anomalous Green's functions are only even in $\omega_n$, if $h = 0$, but they satisfy the exact relations in eq. (A.7b). Consequently, only for $h = 0$, where $\xi_{k,\sigma} = \xi_k = \xi_{k,\bar{\sigma}}$, the simplified relation $\mathcal{F}_{\bar{\sigma}\sigma}(\mathbf{k}, \omega_n) = -\mathcal{F}_{\sigma\bar{\sigma}}(\mathbf{k}, \omega_n)$ holds, as mentioned above.

Recall the subtraction scheme for the normal phase from Chap 7, where the bare Green's function $\mathcal{G}^{(0)}_{\sigma\sigma}$ gives rise to the problematic UV behavior, which has to be separated to solve the self-consistent loop numerically. In the symmetry-broken phase the mean-field Green's functions are the equivalent of $\mathcal{G}^{(0)}_{\sigma\sigma}(\mathbf{k}, \omega_n)$, since the latter is exactly recovered within BCS theory in the case $\Delta = 0$. We note the asymptotics $\mathcal{G}^{\mathrm{MF}}_{\sigma\sigma}(\mathbf{k}, \omega_n) \sim 1/\omega_n$ for $|\omega_n| \to \infty$, which is identical to the scaling of $\mathcal{G}^{(0)}_{\sigma\sigma}$, while $\mathcal{F}^{\mathrm{MF}}_{\sigma\bar{\sigma}}(\mathbf{k}, \omega_n) \sim 1/\omega_n^2$ and $\mathcal{F}^{\mathrm{MF}}_{\sigma\bar{\sigma}}(\mathbf{k}, \omega_n) \sim 1/\omega_n^2$. Regarding the self-consistent computation of the Green's function $\underline{G}$ below $T_c$, the fact that the diagonal parts show the same power-law behavior for large Matsubara frequencies allows to reuse large parts of the subtraction scheme developed for the normal phase, whereas the faster decay of the anomalous Green's function poses a much easier problem with merely two additional subtractions (see below).

Moreover, we can express these functions in terms of a Dyson equation at the mean-field level

$$\underline{G}^{\mathrm{MF}}(\mathbf{k}, \omega_n)^{-1} = \underline{G}^{(0)}(\mathbf{k}, \omega_n)^{-1} - \underline{\Sigma}^{\mathrm{MF}}(\mathbf{k}, \omega_n) \tag{A.15}$$

with the bare Green's function in Nambu space

$$\underline{G}^{(0)}(\mathbf{k}, \omega_n) = \mathrm{diag}\left[\mathcal{G}^{(0)}_{\uparrow\uparrow}(\mathbf{k}, \omega_n), -\mathcal{G}^{(0)}_{\downarrow\downarrow}(-\mathbf{k}, -\omega_n), \mathcal{G}^{(0)}_{\downarrow\downarrow}(\mathbf{k}, \omega_n), -G^{(0)}_{\uparrow\uparrow}(-\mathbf{k}, -\omega_n)\right]. \tag{A.16}$$

and the constant mean-field self-energy

$$\underline{\Sigma}^{\mathrm{MF}}(\mathbf{k}, \omega_n) = \begin{pmatrix} 0 & \Delta & 0 & 0 \\ \Delta^* & 0 & 0 & 0 \\ 0 & 0 & 0 & -\Delta \\ 0 & 0 & -\Delta^* & 0 \end{pmatrix}. \tag{A.17}$$

Like in the normal phase, also in the case of finite $\Delta$ the Fourier transformation to imaginary time can be performed in closed form by using Matsubara sums and contour integrals. A concrete example of the calculation is provided in Appendix B.

The mean-field Green's functions in imaginary time read for $\tau > 0$

$$\mathcal{G}^{\mathrm{MF}}_{\sigma\sigma}(\mathbf{k},\tau) = -\frac{1}{2}\left(1+\frac{\xi_k}{E_k}\right)e^{-(E_k-\sigma h)\tau/\hbar}\big(1-n_F(E_k-\sigma h)\big) - \frac{1}{2}\left(1-\frac{\xi_k}{E_k}\right)e^{(E_k+\sigma h)\tau/\hbar}n_F(E_k+\sigma h) \tag{A.18a}$$

$$\mathcal{F}^{\mathrm{MF}}_{\sigma\bar{\sigma}}(\mathbf{k},\tau) = -\frac{\sigma\Delta}{2E_k}\left[e^{-(E_k-\sigma h)\tau/\hbar}\big(1-n_F(E_k-\sigma h)\big) - e^{(E_k+\sigma h)\tau/\hbar}n_F(E_k+\sigma h)\right] \tag{A.18b}$$

$$\mathcal{F}^{+\mathrm{MF}}_{\bar{\sigma}\sigma}(\mathbf{k},\tau) = -\frac{\sigma\Delta^*}{2E_k}\left[e^{-(E_k-\sigma h)\tau/\hbar}\big(1-n_F(E_k-\sigma h)\big) - e^{(E_k+\sigma h)\tau/\hbar}n_F(E_k+\sigma h)\right]. \tag{A.18c}$$

In contrast to the normal fluid $\mathcal{G}^{\mathrm{MF}}_{\sigma\sigma}(\mathbf{k},\omega_n)$ involves excitations with energies that are given by the positive or negative BCS quasiparticle energy $\pm E_k$ shifted by the Zeeman field $h$. Negative imaginary times follow again from the anti-periodic boundary conditions (4.5) of fermionic Green's functions. Finally, we note that the symmetry $\mathcal{F}_{\sigma\bar{\sigma}}(\mathbf{k},\omega_n) = -\mathcal{F}_{\bar{\sigma}\sigma}(\mathbf{k},\omega_n)$, which arises in the balanced case from the spin-singlet pairing, entails in an isotropic system the additional relation $\mathcal{F}_{\sigma\bar{\sigma}}(\mathbf{k},\beta-\tau) = -\mathcal{F}_{\sigma\bar{\sigma}}(\mathbf{k},\tau)$. This follows from the general properties of the Gorkov Green's functions and can be easily checked for $\mathcal{F}^{\mathrm{MF}}_{\sigma\bar{\sigma}}(\mathbf{k},\tau)$.

## A.3 Luttinger-Ward approach with Nambu structure

### A.3.1 Feynman rules

We summarize the Feynman rules in the symmetry-broken phase both in real and momentum space in Figure A.1. Unlike their normal counterparts, the anomalous Green's function $\mathcal{F}_{\sigma\bar{\sigma}}(\mathbf{x},\tau)$ links points of opposite spin. Moreover, since it is the expectation value of two annihilators $\hat{\Psi}_\sigma$, its particle flow is directed outwards at both endpoints of the line. Analogously, $\mathcal{F}^{+}_{\sigma\bar{\sigma}}(\mathbf{x},\tau)$ shows a purely inward flow. Nevertheless, each end point of every interaction line has a definite spin index with one creation and one annihilation operator. Therefore, each of these points has one line of incoming and one of outgoing particle flow.

### A.3.2 Ladder approximation for the superfluid phase

The first order diagrams in the symmetry-broken state also admit a Fock diagram. Whereas the Hartree diagram vanishes in the $\Lambda \to \infty$ limit, the Fock diagram remains finite, because the gap parameter itself has to be renormalized according to equation (4.8). As a result, we find an additional mean-field contribution to the

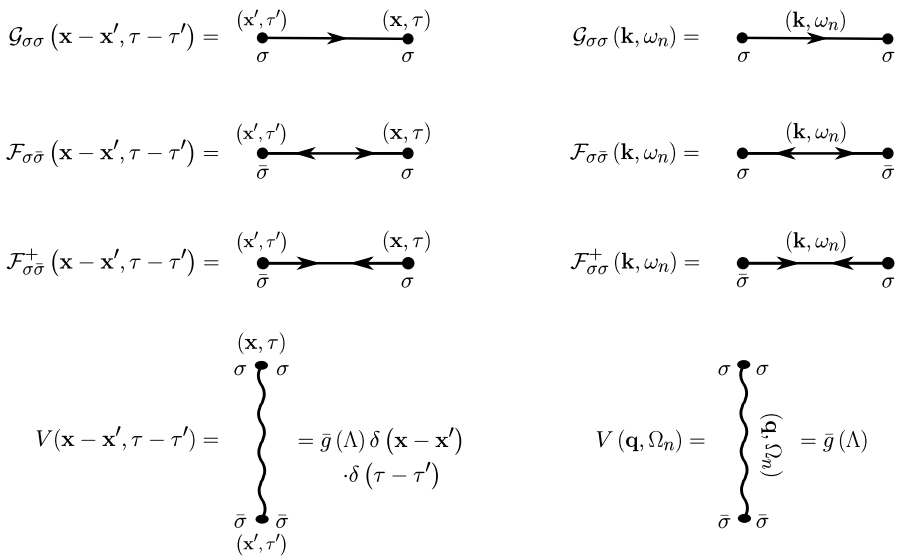


Figure A.1: The Feynman rules, including the anomalous propagator.

grand-potential

$$\begin{aligned}\Omega_{\mathrm{F}} = &-\frac{\bar{g}(\Lambda)}{2}\int d^3x\, \mathcal{F}_{\uparrow\downarrow}\left(\mathbf{0},\tau=0^-\right)\mathcal{F}^{+}_{\downarrow\uparrow}\left(-\mathbf{0},\tau=0^-\right)\\ &-\frac{\bar{g}(\Lambda)}{2}\int d^3x\, \mathcal{F}_{\downarrow\uparrow}\left(\mathbf{0},\tau=0^-\right)\mathcal{F}^{+}_{\uparrow\downarrow}\left(-\mathbf{0},\tau=0^-\right) = -\frac{|\Delta|^2}{\bar{g}(\Lambda)}V\,,\end{aligned} \tag{A.19}$$

where the volume $V$ ensures that $\Omega_F$ is an extensive quantity. In fact, this term is identical to the constant contribution to the mean-field potential $\hat{V}_{\mathrm{MF}}$ (A.9) and gives rise to the mean-field Dyson equation (A.15), when one computes the self-energy via $\delta\Omega_F/\delta G$.

Regarding the higher order diagrams, we follow the procedure introduced by Haussmann [150] and consider ladders of arbitrary length with identical Green's functions in both legs between any two subsequent rungs. This admits four building blocks for the ladder diagrams. First of all, we have the combination $\mathcal{G}_{\uparrow\uparrow}\mathcal{G}_{\downarrow\downarrow}$ with back and forward propagating flows, which is the generalization of the particle-particle bubble $\chi(\mathbf{Q},\Omega_n)$ from the normal phase above $T_c$. Furthermore, we have to consider the purely anomalous pair propagators, which consist either of the combination $\mathcal{F}_{\uparrow\downarrow}\,\mathcal{F}_{\downarrow\uparrow}$ or $\mathcal{F}^{+}_{\uparrow\downarrow}\,\mathcal{F}^{+}_{\downarrow\uparrow}$. These two combinations are not invariant under a gauge transformation themselves but can be closed in a gauge-invariant manner, which yields admissible contributions to the grand potential $\Omega[G]$. Notice that $\Omega$ itself must not depend on the specific choice of the phase of the order parameter, as it is directly related to the pressure. Combinations of a diagonal and an off-diagonal Green's functions between two adjacent rungs are forbidden by the constraints on the spin and Nambu indices, whereas pairs of $\mathcal{F}_{\sigma\bar{\sigma}}\mathcal{F}^{\dagger}_{\bar{\sigma}\sigma}$ can only be closed by

exchange ladders. Their momentum structure resembles particle-hole ladders in the normal phase and cannot be described in terms of the center-of-mass variables only and therefore they have to be neglected. Formally, the four fundamental blocks taken into account for the particle-particle ladders can be organized in a $4 \times 4$ matrix for the bubble diagram in Nambu space, which in the presence of finite $h$ reads

$$\underline{\chi}\left(\mathbf{Q}, \Omega_n\right) = \begin{pmatrix} \chi^{(1)}\left(\mathbf{Q}, \Omega_n\right) & 0 \\ 0 & \chi^{(2)}\left(\mathbf{Q}, \Omega_n\right) \end{pmatrix} . \tag{A.20}$$

Due to the spin symmetry of the interaction potential both $2 \times 2$ components of the particle-particle bubble coincide, i.e. $\chi^{(1)}\left(\mathbf{Q}, \Omega_n\right) = \chi^{(2)}\left(\mathbf{Q}, \Omega_n\right)$, where

$$\chi^{(1)}_{\alpha\beta}\left(\mathbf{Q}, \Omega_n\right) = \int \frac{d^3k}{(2\pi)^3} \left[ \frac{1}{\beta} \sum_m G^{(1)}_{\alpha\beta}(\mathbf{k}, \omega_m)\, G^{(2)}_{\alpha\beta}(\mathbf{Q}-\mathbf{k}, \Omega_n - \omega_m) \right] , \tag{A.21}$$

while the $2 \times 2$ Green's functions $G^{(1,2)}$ are defined in eq. (A.8). Note that the approximation described above entails a component-wise product without summation over the Nambu indices $\alpha, \beta = 1, 2$ on the right-hand side. The resulting Luttinger-Ward functional $\Phi[G]$ in the presence of a superfluid order parameter is topologically equivalent to Fig. 4.2 from the symmetric phase, however the lines are now given by the Nambu pair propagator $\chi_{\alpha\beta}\left(\mathbf{Q}, \Omega_n\right)$. Hence, the summation of all contributions to the Luttinger-Ward functional can be performed in analogy to Sec. 4.4.2, which yields

$$\begin{aligned} \frac{\Omega[\underline{G}]}{V} =& \frac{1}{2\beta} \int \frac{d^3k}{(2\pi)^3} \sum_n \mathrm{Tr} \left\{ \log\left[\underline{G}\left(\mathbf{k}, \omega_n\right)\right] + \left[1 - \underline{G}^{(0)}\left(\mathbf{k}, \omega_n\right)^{-1} \underline{G}\left(\mathbf{k}, \omega_n\right)\right] \right\} \\ & - \frac{1}{2} \bar{g}(\Lambda) \mathcal{F}_{\uparrow\downarrow}(\mathbf{x}=0, \tau=0^+) \mathcal{F}^+_{\downarrow\uparrow}(\mathbf{x}=0, \tau=0^+) \\ & - \frac{1}{2} \bar{g}(\Lambda) \mathcal{F}_{\downarrow\uparrow}(\mathbf{x}=0, \tau=0^+) \mathcal{F}^+_{\uparrow\downarrow}(\mathbf{x}=0, \tau=0^+) \\ & + \frac{1}{2\beta} \int \frac{d^3Q}{(2\pi)^3} \sum_n \mathrm{Tr}\left[\log\left(1 + \bar{g}(\Lambda) \underline{\chi}\left(\mathbf{Q}, \Omega_n\right)\right)\right] . \end{aligned} \tag{A.22}$$

The trace now contains a sum over the indices of $(\underline{G})_{ab}$, with $a, b = 1, ..., 4$ and the normalization has been adjusted in order to recover the result of a two-component ideal Fermi gas if one sets $\bar{g} = 0$. In the following subsection we bring the self-consistent Dyson equation for the Green's function $\underline{G}$ in a form that is equivalent to the normal phase, discussed in Sec. 4.6.2. To simplify the necessary steps, we will mostly use the representation based on the $2 \times 2$ submatrices.

### A.3.3 Self-consistent loop

Like in Chap. 4, the first step in the self-consistent loop is the computation of the bubble diagram $\underline{\chi}$, which below $T_c$ has a non-trivial Nambu structure. Further-

more, it has to be renormalized, due to the asymptotics of the mean-field Green's function (A.14). Again, we denote the physical function as $\underline{M} = \mathrm{diag}(M^{(1)}, M^{(2)})$, with

$$M^{(1)}_{\alpha\beta}\left(\mathbf{Q},\Omega_n\right) = \int \frac{d^3k}{(2\pi)^3}\left[\frac{1}{\beta}\sum_m G^{(1)}_{\alpha\beta}(\mathbf{k},\omega_m)\, G^{(2)}_{\alpha\beta}(\mathbf{Q}-\mathbf{k},\Omega_n-\omega_m) - \frac{\delta_{\alpha\beta}}{2\varepsilon_k}\right] , \quad \text{(A.23)}$$

while the property $M^{(1)}\left(\mathbf{Q},\Omega_n\right) = M^{(2)}\left(\mathbf{Q},\Omega_n\right)$ is inherited from $\underline{\chi}\left(\mathbf{Q},\Omega_n\right)$ given in eqs. (A.20) and (A.21). Note that the dominant asymptotics $\overline{\mathcal{F}} \sim 1/\omega_n^2$ from eq. (A.14) renders the off-diagonal elements finite from the beginning, whereas we have inserted the renormalization prescription of eq. (2.29) to obtain well-defined diagonal components in the zero-range limit. For the numerical implementation we again use the real space representation of the unrenormalized function

$$\chi_{\alpha\beta}\left(\mathbf{x},\tau\right) = G^{(1)}_{\alpha\beta}\left(\mathbf{x},\tau\right) G^{(2)}_{\alpha\beta}\left(\mathbf{x},\tau\right) , \quad \text{(A.24)}$$

since interpreting the $\tau \to \Omega_n$ transformation in terms of a generalized Fourier transformation automatically introduces the correctly renormalized forms, as we have already argued below equation 7.20. The vertex function follows from the solving the Bethe-Salpeter equation, which still can be depicted as in Fig. 4.3. Its solution, however, now requires the inversion of a $2 \times 2$ matrix

$$\Gamma^{(1)}_{\alpha\beta}\left(\mathbf{Q},\Omega_n\right) = \left(\frac{1}{g} + M^{(1)}\left(\mathbf{Q},\Omega_n\right)\right)^{-1}_{\alpha\beta} , \quad \text{(A.25)}$$

while the spin symmetry again entails for the form of the vertex function in the extended Nambu basis $\underline{\Gamma} = \mathrm{diag}(\Gamma^{(1)}, \Gamma^{(2)})$, with $\Gamma^{(1)} = \Gamma^{(2)}$. Finally, the self-energy is given by the componentwise product

$$\Sigma^{(A)}_{\alpha\beta}\left(\mathbf{k},\omega_n\right) = \int \frac{d^3Q}{(2\pi)^3}\frac{1}{\beta}\sum_m \Gamma^{(1)}_{\alpha\beta}\left(\mathbf{Q},\Omega_m\right) G^{(\bar{A})}_{\beta\alpha}\left(\mathbf{Q}-\mathbf{k},\Omega_m-\omega_n\right) . \quad \text{(A.26)}$$

The spin restriction from the s-wave interaction is incorporated by the possible pairs $(A,\bar{A}) = (1,2)$ or $(A,\bar{A}) = (2,1)$, while the special combination of exchanged Nambu indices on the Green's function in comparison to the vertex function results from the original truncation of the Luttinger-Ward functional considered in Section A.3.2. The convolution will again be computed in real space

$$\Sigma^{(A)}_{\alpha\beta}\left(\mathbf{x},\tau\right) = \Gamma^{(1)}_{\alpha\beta}\left(\mathbf{x},\tau\right) G^{(\bar{A})}_{\beta\alpha}\left(-\mathbf{x},-\tau\right) . \quad \text{(A.27)}$$

We can solve the resulting loop self-consistently in the same fashion as in the normal fluid, depicted in Fig. 4.5. Apart from Fourier transforms and multiplications one now has to invert the $2 \times 2$-matrices to obtain the vertex (A.25) and in the solution for the updated Green's function

$$G^{(A)}_{\alpha\beta}\left(\mathbf{k},\omega_n\right) = \left((G^{(0)})^{(A)}\left(\mathbf{k},\omega_n\right) - \Sigma^{(A)}\left(\mathbf{k},\omega_n\right)\right)^{-1}_{\alpha\beta} , \quad \text{(A.28)}$$

which results from inserting the self-energy into the standard form of the Dyson equation.

Below $T_c$ a more fundamental problem, however, arises from the number of variables and physical constraints. The additional parameter $\Delta$ is fixed by the gap equation eq. (4.8). Furthermore, the spontaneously broken symmetry implies the Thouless criterion eq. (4.29), which is connected to the existence of gapless Goldstone modes in the superfluid phase. Since this type of excitation dominates the thermodynamics in the $T \to 0$ limit, it is quite important to satisfy the Thouless criterion. Unfortunately, the ladder approximation violates this equation by a term of order $\mathcal{O}(\Delta^3)$ on the right-hand side [150]. A possible resolution of this problem, developed by Haussmann et al. [37], is to release the gap equation by the introduction of a so-called modified coupling constant via

$$\Delta = g_{\mathrm{mod}} \int \frac{d^3k}{(2\pi)^3} \left( \mathcal{F}(\mathbf{k}, \tau = 0^-) + \frac{\Delta}{2\varepsilon_k} \right) . \tag{A.29}$$

As is detailed in Ref. [37], one can partially cure this ad-hoc definition with a further modified coupling constant $\tilde{g}_{\mathrm{mod}}$ in the mean-field part $\Omega_F$ of the Luttinger-Ward functional, defined in eq. (A.19). This procedure leads to differences between the three interaction strengths $g, g_{\mathrm{mod}}$ and $\tilde{g}_{\mathrm{mod}}$ of about $\gtrsim 10\%$ around the strong coupling limit and it spoils the scale invariance at unitarity on the level of a few percent. Nevertheless, thermodynamic properties can still be obtained in good agreement with the experimental data. For example one finds $\xi_s \simeq 0.36$ for the Bertsch parameter [37].

## A.4 Subtraction Scheme for the Self-consistent Loop in the Superfluid Phase

In this section we repeat the procedure of creating suitable subtractions for the Green's and vertex functions in the presence of a finite order parameter $\Delta$. Fortunately, we can transfer all of the results from the normal fluid case, addressed in Sec. 7.2. The additional anomalous contributions turn out to allow for a much simpler treatment due to the asymptotic $\mathcal{F} \simeq \omega_n^{-2}$ on the mean-field level, see equation (A.14), such that we only have to discuss two new terms. We return now to the dimensionless representation from Sec. 7.1 and we additionally define $\hat{\Delta} = \beta\Delta$. Similarly to the the normal case we do not write the carets explicitly, as there exists no possibility of confusion.

### A.4.1 Green's Function

In the normal-fluid problem all the non-integrable asymptotics arise from the properties of the bare Green's function $\mathcal{G}^{(0)}_{\sigma\sigma}$. In the ordered phase the mean-field Green's functions provide a starting point for the self-consistent loop. By inspection of the

exact function $\mathcal{G}^{\mathrm{MF}}_{\sigma\sigma}(\mathbf{k},\tau)$ in equation (A.18a), we infer that for $k^2 \gg \mu, h, \Delta$ it can be approximated by

$$\mathcal{G}^{\mathrm{MF}}_{\sigma\sigma}(\mathbf{k},\tau) \to -\left(1 - \frac{\Delta^2}{4k^4} + \mathcal{O}(k^{-6})\right) e^{-\left(k^2 - \mu_\sigma + \mathcal{O}\left(k^{-2}\right)\right)\tau}, \tag{A.30}$$

plus exponentially small terms from the Fermi functions. This leads to the limiting behavior $\mathcal{G}\left(k^2 \gg \mu, h, \Delta, \tau \to 0^+\right) \to -1$, which is identical to what we have found for $\mathcal{G}^{(0)}_{\sigma\sigma}(\mathbf{k},\tau)$ in equation (4.10). The next correction $\Delta^2/(4k^2)$ is algebraic in the momentum, in contrast to the purely Gaussian decay in case of $\mathcal{G}^{(0)}_{\sigma\sigma}(\mathbf{k},\tau)$. This reflects the fact that in the symmetry-broken phase even the interactions at the mean-field level give rise to a finite contact parameter that results in the high-momentum tail $\delta\mathcal{C}_{\mathrm{SF}}/k^4 = m^2|\Delta|^2/(\hbar^4 k^4)$ of the momentum distribution $n_\sigma(k) = \mathcal{G}_{\sigma\sigma}(k, \tau \to 0^-)$, as discussed below eq. (2.57). Regarding the relation $\mathcal{C} = -m^2\Gamma(\mathbf{0}, 0^-)/\hbar^4 + \delta\mathcal{C}_{\mathrm{SF}}$ with the short-distance and short-time limit of the vertex function via eq. (4.28) reveals that $\delta\mathcal{C}_{\mathrm{SF}}$ corresponds to the disconnected, anomalous contraction arising from the microscopic definition of the contact density $\mathcal{C} = \lim_{\Lambda\to\infty} \bar{g}^2(\Lambda)\langle\hat{\psi}^\dagger_\uparrow(\mathbf{x})\hat{\psi}^\dagger_\downarrow(\mathbf{x})\hat{\psi}_\downarrow(\mathbf{x})\hat{\psi}_\uparrow(\mathbf{x})\rangle$ (see eq. (2.53)). Apart from the appearance of $\Gamma(\mathbf{0}, 0^-)$, it has to be noted that $\delta\mathcal{C}_{\mathrm{SF}}$ itself also acquires corrections from the beyond-mean field interactions, because they influence $\mathcal{F}_{\sigma\bar{\sigma}}(\mathbf{x},\tau)$ and consequently change the value of $\Delta$.

However, since $k^{-4}$ decays fast enough to be Fourier transformed numerically, we only have to take care of the leading order that exactly agrees with the behavior of the bare Green's function $\mathcal{G}^{(0)}_{\sigma\sigma}(\mathbf{k},\tau)$. Therefore, we can inherit the definitions for the analytical part $\mathcal{G}^{\mathrm{ana}}_{\sigma\sigma}(\mathbf{k},\tau)$ from the subtraction scheme applied above $T_c$, see Sec. 7.2. All functions $\mathcal{G}^{\mathrm{ana}}_{\sigma\sigma}(\mathbf{k},\omega_n), \mathcal{G}^{\mathrm{ana}}_{\sigma\sigma}(\mathbf{k},\tau)$ and $\mathcal{G}^{\mathrm{ana}}_{\sigma\sigma}(\mathbf{x},\tau)$ can be found in eq. (7.13) for the BCS ($\beta\mu \geqslant -2$) or in eq. (7.11) for the BEC code ($\beta\mu < -2$). In total, the decomposition of analytical and numerical parts for the diagonal elements of the Green's function reads as before

$$\mathcal{G}_{\sigma\sigma}(\mathbf{k},\tau) = \mathcal{G}^{\mathrm{ana}}_{\sigma\sigma}(\mathbf{k},\tau) + \mathcal{G}^{\mathrm{num}}_{\sigma\sigma}(\mathbf{k},\tau), \tag{A.31}$$

where the numerical part is now given by the function

$$\mathcal{G}^{\mathrm{num}}_{\sigma\sigma}(\mathbf{k},\tau) = \left(\mathcal{G}^{\mathrm{MF}}_{\sigma\sigma}(\mathbf{k},\tau) - \mathcal{G}^{\mathrm{ana}}_{\sigma\sigma}(\mathbf{k},\tau)\right) + \delta\mathcal{G}_{\sigma\sigma}(\mathbf{k},\tau). \tag{A.32}$$

Again $\delta\mathcal{G}_{\sigma\sigma}(\mathbf{k},\tau)$ denotes the Fourier transform of the genuine interaction contributions $\delta\mathcal{G}_{\sigma\sigma}(\mathbf{k},\omega_n) = \mathcal{G}_{\sigma\sigma}(\mathbf{k},\omega_n) - \mathcal{G}^{\mathrm{MF}}_{\sigma\sigma}(\mathbf{k},\omega_n)$. The transformation to real space follows then in analogy to the normal phase.

Next, we have to consider the anomalous Green's function $\mathcal{F}^{\mathrm{MF}}_{\sigma\bar{\sigma}}(\mathbf{k},\tau)$, given in (A.18b), whose real space and imaginary time equivalent is not known in closed form. From now on, we choose a positive value of the gap parameter, without loss of generality. Both endpoints of the imaginary time interval give rise to algebraic

tails for large momenta $k^2 \gg \mu, h, \Delta$, which read

$$\mathcal{F}^{\mathrm{MF}}_{\sigma\bar{\sigma}}(\mathbf{k},\tau) \to \begin{cases} -\left(\frac{\sigma\Delta}{2k^2} + \mathcal{O}\left(k^{-4}\right)\right) e^{-\left(k^2-\mu_\sigma+\mathcal{O}\left(k^{-2}\right)\right)\tau} & , \ \tau \to 0^+ \\ \left(\frac{\sigma\Delta}{2k^2} + \mathcal{O}\left(k^{-4}\right)\right) e^{-\left(k^2-\mu_\sigma+\mathcal{O}\left(k^{-2}\right)\right)(1-\tau)} & , \ \tau \to 1^- \end{cases} . \tag{A.33}$$

The integration measure of the effectively one-dimensional $\mathbf{k} \leftrightarrow \mathbf{x}$ Fourier transformation (4.16) turns the leading $\pm\Delta/(2k^2)$ term encountered at the boundaries of the imaginary time interval to a nonintegrable $1/k$ decay. Consequently, we also have to construct a suitable subtraction scheme for the off-diagonal components of $\underline{G}(\mathbf{k},\tau)$, which involves only integrable functions in the numerical parts. We define the analytical function as

$$\mathcal{F}^{\mathrm{ana}}_{\sigma\bar{\sigma}}(\mathbf{k},\tau) = -\frac{\sigma\Delta}{2k^2}\left(e^{-k^2\tau} - e^{-k^2(1-\tau)}\right) , \tag{A.34}$$

where we not only discard the next-to-leading order algebraic $k^{-4}$ tail, but also the complete dependence on the chemical potentials. In the normal Green's function $\mathcal{G}^{\mathrm{ana}}_{\sigma\sigma}$, $\mu$ and $h$ had to be considered at least to first order to be able to deal with $\tau^{-1/2}$ divergences in the self-energy $\Sigma^{\mathrm{ana}}_{\sigma\sigma}(\mathbf{x},\tau)$ analytically. Here, in contrast, the $k^{-2}$ factor prevents such singularities in the self-energy and we only retain the leading asymptotics. Thus merely a dependence on $\Delta$ remains in form of a simple prefactor. This fact will prove to be crucial for the computation of the anomalous particle-particle diagram in the next section. Eventually, the suspicious $\Delta/(2k^2)$ term in eq. (A.34) does not give rise to an artificial divergence in the limit $k \to 0$, because the bracket renders the function well-defined. Based on this definition we find

$$\mathcal{F}^{\mathrm{ana}}_{\sigma\bar{\sigma}}(\mathbf{k},\omega_n) = -\frac{\sigma\Delta}{\omega_n^2 + k^4}\left(1 + e^{-k^2}\right) \tag{A.35a}$$

$$\mathcal{F}^{\mathrm{ana}}_{\sigma\bar{\sigma}}(\mathbf{k},\tau) = -\frac{\sigma\Delta}{2k^2}\left(e^{-k^2\tau} - e^{-k^2(1-\tau)}\right) \tag{A.35b}$$

$$\mathcal{F}^{\mathrm{ana}}_{\sigma\bar{\sigma}}(\mathbf{x},\tau) = -\frac{\sigma\Delta}{8\pi r}\left[\mathrm{erf}\left(\frac{r}{2\sqrt{\tau}}\right) - \mathrm{erf}\left(\frac{r}{2\sqrt{1-\tau}}\right)\right] . \tag{A.35c}$$

To obtain the $(\mathbf{x},\tau)$ representation, one has to regularize the $\mathbf{k}$-integral in the sense of generalized functions, according to eq. (C.12). However, in this case one has to treat both positive and negative values $k$ separately and to shift the nonzero integration boundary $\to \pm\infty$. Sending $r \to 0$ leads to

$$\mathcal{F}^{\mathrm{ana}}_{\sigma\bar{\sigma}}(\mathbf{x}=\mathbf{0},\tau) = \frac{-\sigma\Delta}{8\pi^{3/2}}\left[\frac{1}{\sqrt{\tau}} - \frac{1}{\sqrt{1-\tau}}\right] , \tag{A.36}$$

where we have made use of the Taylor expansion of the error function, given in eq. (C.3). The latter form acquires singularities for $\tau \to 0^+$ or $\tau \to 1^-$. Basically, this behavior rephrases the non-integrability of the analytic part (A.35b) in these

limits. However, $\mathcal{F}^{\mathrm{ana}}_{\sigma\bar{\sigma}}(\mathbf{x},\tau)$ diverges more weakly than $\mathcal{G}^{\mathrm{ana}}_{\sigma\sigma}(\mathbf{x}=\mathbf{0},\tau\to 0^-)\sim\tau^{-3/2}$, giving rise to much more convenient properties of the particle-particle bubble, which we discuss below. Before doing so, we introduce the subtraction scheme for the anomalous propagator

$$\mathcal{F}_{\sigma\bar{\sigma}}(\mathbf{x},\tau)=\mathcal{F}^{\mathrm{ana}}_{\sigma\bar{\sigma}}(\mathbf{x},\tau)+\mathcal{F}^{\mathrm{num}}_{\sigma\bar{\sigma}}(\mathbf{x},\tau)\,, \tag{A.37}$$

with

$$\mathcal{F}^{\mathrm{num}}_{\sigma\bar{\sigma}}(\mathbf{x},\tau)=\left(\mathcal{F}^{\mathrm{MF}}_{\sigma\bar{\sigma}}(\mathbf{x},\tau)-\mathcal{F}^{\mathrm{ana}}_{\sigma\bar{\sigma}}(\mathbf{x},\tau)\right)+\delta\mathcal{F}_{\sigma\bar{\sigma}}(\mathbf{x},\tau) \tag{A.38}$$

where $\delta\mathcal{F}_{\sigma\bar{\sigma}}(\mathbf{x},\tau)$ denotes the interaction effects beyond mean-field.

### A.4.2 Particle-particle bubble

To compute the particle bubble diagram in Nambu space, we first recall that the full matrix can be written as a block-diagonal matrix $\underline{\chi}=\mathrm{diag}(\chi^{(1)},\chi^{(1)})$ with two identical $2\times 2$ subblocks. Next we note that $\chi^{(1)}_{\alpha\beta}(\mathbf{Q},\Omega_n)$, defined in eq. (A.21) consists only of two independent functions: one diagonal, normal function equivalent to the case above $T_c$ and one anomalous off-diagonal part. To see this, we begin with the convolution for $\chi^{(1)}_{22}(\mathbf{Q},\Omega_n)$. A transformation of the integration variable and a reordering of the Matsubara sum reveal

$$\chi_{22}(\mathbf{Q},\Omega_n)=\chi^{(1)}_{11}(-\mathbf{Q},-\Omega_n)\,, \tag{A.39}$$

such that knowledge of one diagonal element of $\chi^{(1)}$ immediately determines the other one by complex conjugation. In a similar manner, we find for the off-diagonal part

$$\chi^{(1)}_{21}(\mathbf{Q},\Omega_n)=\chi^{(1)}_{12}(-\mathbf{Q},-\Omega_n)^*\,. \tag{A.40}$$

Therefore, we concentrate in the following on the computation of $\chi^{(1)}_{11}(\mathbf{Q},\Omega_n)$ and $\chi^{(1)}_{12}(\mathbf{Q},\Omega_n)$ and use these two relations to achieve the full matrix $\underline{\chi}$. This also reduces the numerical effort.

Regarding the computation of $\chi_{11}(\mathbf{Q},\Omega_n)$, there are no changes compared to the symmetric phase, since we use the identical $\mathcal{G}^{\mathrm{ana}}_{\sigma\sigma}(\mathbf{x},\tau)$ as basis of all the decompositions. The off-diagonal function includes the terms

$$\begin{aligned}\chi^{(1)}_{12}(\mathbf{x},\tau)=\;&\mathcal{F}^{\mathrm{ana}}_{\sigma\bar{\sigma}}(\mathbf{x},\tau)\,\mathcal{F}^{\mathrm{ana}}_{\bar{\sigma}\sigma}(\mathbf{x},\tau)+\mathcal{F}^{\mathrm{ana}}_{\sigma\bar{\sigma}}(\mathbf{x},\tau)\,\mathcal{F}^{\mathrm{num}}_{\bar{\sigma}\sigma}(\mathbf{x},\tau)\\&+\mathcal{F}^{\mathrm{num}}_{\sigma\bar{\sigma}}(\mathbf{x},\tau)\,\mathcal{F}^{\mathrm{ana}}_{\bar{\sigma}\sigma}(\mathbf{x},\tau)+\mathcal{F}^{\mathrm{num}}_{\sigma\bar{\sigma}}(\mathbf{x},\tau)\,\mathcal{F}^{\mathrm{num}}_{\bar{\sigma}\sigma}(\mathbf{x},\tau)\,,\end{aligned} \tag{A.41}$$

where the purely analytic term unfortunately contains the squares of error functions, whose Fourier transforms are not available in closed form. To solve this problem one could try to further subtract appropriate approximations from the

product $\mathcal{F}^{\mathrm{ana}}_{\sigma\bar{\sigma}}(\mathbf{x},\tau)\,\mathcal{F}^{\mathrm{ana}}_{\bar{\sigma}\sigma}(\mathbf{x},\tau)$. This, however, turns out to be difficult, because one has to take into account both the exponential behavior at large $x \gg \sqrt{\tau}$ and simultaneously the $1/\tau$ and $1/(1-\tau)$ singularities in the opposite limit $x \ll \sqrt{\tau}$. Any expansion around either limit breaks down in the other one and leads to large errors. Since $\mathcal{F}^{\mathrm{ana}}_{\sigma\bar{\sigma}}(\mathbf{x},\tau)$ does not depend on the thermodynamic parameters except for the prefactor and we first integrate over $\mathbf{x}$, we compute $\mathcal{FT}_{r\to Q}\left[\left(\mathcal{F}^{\mathrm{ana}}_{\sigma\bar{\sigma}}\mathcal{F}^{\mathrm{ana}}_{\bar{\sigma}\sigma}\right)(\mathbf{x},\tau)\right]$ only once during the initialization on a sufficiently dense grid and store the values for the iterations in the self-consistent loop. Furthermore, we estimate the scaling $\mathcal{FT}_{r\to Q}\left[\left(\mathcal{F}^{\mathrm{ana}}_{\sigma\bar{\sigma}}\mathcal{F}^{\mathrm{ana}}_{\bar{\sigma}\sigma}\right)(\mathbf{x},\tau)\right] \sim \sqrt{\tau}$ in the limit $\tau \to 0^+$, which follows from rescaling the Fourier integral of $(\Delta/8\pi r)^2\,\mathrm{erf}^2(r/2\sqrt{\tau})$, which exhibits the worst divergence in the regime of small $\tau$. The nonanalytic $\sqrt{\tau}$ behavior resembles the subtraction in the normal phase that gives rise to $E_2(\mathbf{Q},\Omega_n)$ defined in eq. (7.20). However, since $\mathcal{F}^{\mathrm{ana}}_{\sigma\bar{\sigma}}(\mathbf{x},\beta-\tau) = -\mathcal{F}^{\mathrm{ana}}_{\sigma\bar{\sigma}}(\mathbf{x},\tau)$, we conclude for the convolution

$$\chi^{(1)\mathrm{ana}}_{12}(\mathbf{Q},\Omega_n) = \mathcal{FT}_{\tau\to\Omega_n, r\to Q}\left[\left(\mathcal{F}^{\mathrm{ana}}_{\sigma\bar{\sigma}}\mathcal{F}^{\mathrm{ana}}_{\bar{\sigma}\sigma}\right)(\mathbf{x},\tau)\right] = \chi^{(1)\mathrm{ana}}_{12}(\mathbf{Q},-\Omega_n)\,,$$

which rules out a contribution of $1/\Omega_n$ to the asymptotic behavior and we encounter a decay of at least $\chi^{(1)\mathrm{ana}}_{12}(\mathbf{Q},\Omega_n) \sim \Omega_n^{-3/2}$. Furthermore, we have verified the latter power law numerically. Consequently, for the computation of the vertex functions and the self-energies, which appear in the following steps of the self-consistent loop, we can directly use the equations outlined in the previous subsection. We apply again the scheme developed in Chap 7, since the dominant asymptotics always originates from the diagonal elements and coincides with the normal phase. On the other hand, the new anomalous terms always vanish fast enough to be treated numerically.

# Appendix B

# Matsubara sums

## B.1 General framework

The evaluation of fermionic or bosonic Matsubara sums $\sum_n f(\hbar\omega_n)$ or $\sum_n f(\hbar\Omega_n)$, is a standard problem in finite-temperature equilibrium field theory both in frameworks with Galilean [67, 154] and Lorentz invariance [187]. In addition, this technique can be applied to obtain statements about the analytical properties and error estimates of the LFT, confer Section 6.1.2. Usually one rewrites the sum of interest as a contour integral in the complex frequency plane, where the contour $\gamma$ encircles the imaginary axis in the mathematically positive sense (see Fig. B.1). Provided that $f(z)$ itself has no singularities for imaginary $z$, this procedure reads

$$\frac{1}{\beta}\sum_n f(\hbar\omega_n) = -\oint_\gamma \frac{dz}{2\pi i} g(z) f(z) \qquad \text{or} \qquad \frac{1}{\beta}\sum_n f(\hbar\Omega_n) = \oint_\gamma \frac{dz}{2\pi i} g(z) f(z)\,, \tag{B.1}$$

with an auxiliary function $g(z)$ that has first order poles with known residues at the fermionic or bosonic Matsubara frequencies. Standard choices for $g(z)$ are

$$g(z) = \begin{cases} n_F(z) \\ -n_F(-z) \end{cases} \quad \text{(Fermions)} \qquad \text{or} \qquad g(z) = \begin{cases} n_B(z) \\ -n_B(-z) \end{cases} \quad \text{(Bosons)}\,, \tag{B.2}$$

where $n_F(z)$ denotes the Fermi-Dirac and $n_B(z)$ the Bose-Einstein distribution

$$n_{F,B}(z) = \frac{1}{e^{\beta z} \pm 1}\,, \tag{B.3}$$

and the upper (lower) sign refers to Fermions (Bosons). The distribution functions have residues of $\mp 1/\beta$ at the $\omega_n$ or $\Omega_n$, respectively, which legitimates equation (B.1). This identity allows to deform the contour by the help of Cauchy's theorem and thereby to compute the integrals via the residue theorem and related techniques from complex analysis, e.g in the presence of branch cuts. For convenience one tries to choose $g(z)$ such that the contour does not contribute anymore once it is shifted towards infinity.

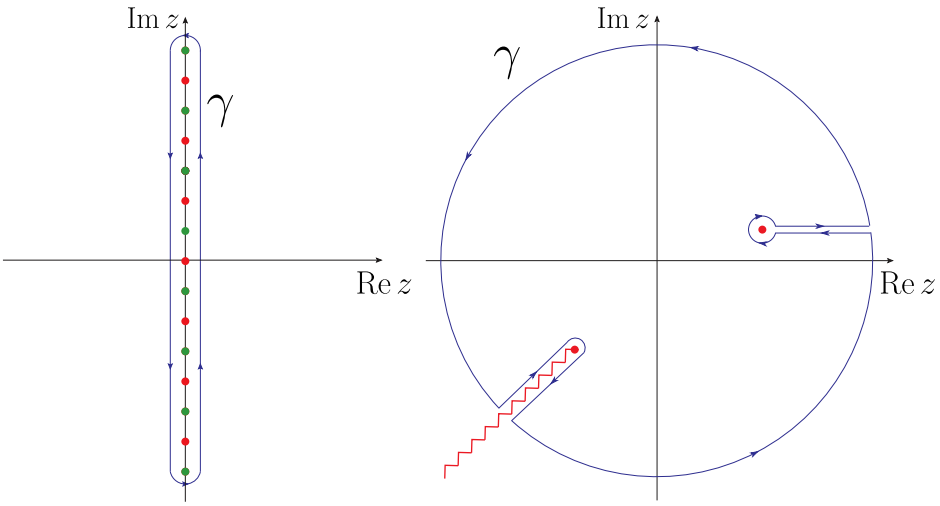


Figure B.1: Graphical representation of the contour integration for Matsubara sums: Left initial contour $\gamma$ that encircles the fermionic (green) or bosonic (red) Matsubara frequencies. Right: Example for a deformed $\gamma$ that includes one pole (red point) and one branch cut (red line).

## B.2 Mean-field Green's functions

As a concrete example, we will compute the diagonal mean-field Green's functions $\mathcal{G}^{\mathrm{MF}}_{\sigma\sigma}(\mathbf{k},\tau)$ in the symmetry-broken phase for $\tau > 0$ from the imaginary frequency solution to the mean-field equations (A.14a). We use (B.1) to write for the Fourier transformation

$$\begin{aligned}\mathcal{G}^{\mathrm{MF}}_{\sigma\sigma}(\mathbf{k},\tau) &= \frac{1}{\beta}\sum_n e^{-i\omega_n\tau}\mathcal{G}^{\mathrm{MF}}_{\sigma\sigma}(\mathbf{k},\omega_n) \\ &= \oint_\gamma \frac{dz}{2\pi i} n_F(-z)\frac{e^{-z\tau/\hbar}\,(z+\varepsilon_k-\bar{\sigma}h)}{(z-(E_k-\sigma h))\,(z+(E_k+\sigma h))}\,.\end{aligned} \tag{B.4}$$

In this case we use $g(z) = -n_F(-z)$ such that the integrand shows an exponential decay both for $\mathrm{Re}\, z \to \pm\infty$, since $\tau > 0$. Now we can deform $\gamma$ to a circle in the limit of infinite radius, as depicted in Fig. B.1. Because of the asymptotics the integral along the arcs vanishes and we can evaluate the integral by virtue of the residue theorem

$$\mathcal{G}^{(0)}_{\sigma\sigma}(\mathbf{k},\tau) = -\mathrm{Res}_{z_1} - \mathrm{Res}_{z_2}\,, \tag{B.5}$$

where $z_1 = E_k - \sigma h$ and $z_2 = -E_k - \sigma h$ refer to the simple poles of the integrand and the sign is due to orientation of the contour. Inserting the residues recovers the result (A.18a). The anomalous functions from eqs. (A.18b) and (A.18c) can be obtained along the same lines.

# Appendix C

# Generalized Fourier transformations and analytical results

In this appendix we prove many of the analytic expressions for the Fourier transforms between imaginary time and Matsubara frequencies. In particular, we show how to deal with the non-integrable function $\chi^{\mathrm{ana}}(\mathbf{Q},\tau) \sim \tau^{-3/2}$ for $\tau \to 0^+$ that we encountered in eq. (7.15) in the self-consistent loop of the Luttinger-Ward formalism.

## C.1 Properties of the error function

Before we start with the Fourier transforms we state several mathematical properties of the error function, that are required later. The error function, which has already appeared quite frequently, is an entire function defined by [167]

$$\mathrm{erf}(z) = \frac{2}{\sqrt{\pi}} \int_0^z dt\, e^{-t^2} \,. \tag{C.1}$$

In particular, it converges exponentially to one for asymptotically large arguments, or more precisely [167]

$$\mathrm{erf}(z) \simeq 1 - \frac{e^{-z^2}}{\sqrt{\pi} z} \,, \tag{C.2}$$

for $|z| \to \infty$ and $|\arg(z)| < 3\pi/4$. Note that we always encounter $\mathrm{erf}\,(\sqrt{z})$ in this thesis, where the square root restricts the phase to the first and fourth quadrant of the complex $z$-plane and we never leave the range of validity of the last result. Finally, we state the Taylor series of the error function [167]

$$\mathrm{erf}(z) = \frac{2}{\sqrt{\pi}} \sum_{n=0}^{\infty} \frac{(-1)^n z^{2n+1}}{n!(2n+1)} \,. \tag{C.3}$$

For positive $z$ one can relate the error and the Gamma functions by the identity

$$\mathrm{erf}(\sqrt{z}) = \frac{1}{\sqrt{\pi}} \left[ \Gamma\left(\frac{1}{2}\right) - \Gamma\left(\frac{1}{2}, z\right) \right] \,, \tag{C.4}$$

which can be verified by transforming the integration variable in the definition (C.1) via $t \to u^2$ and rewriting the integral in terms of the Gamma and the incomplete Gamma function

$$\Gamma(a) = \int_0^\infty t^{a-1} e^{-t} \tag{C.5a}$$

$$\Gamma(a,z) = \int_x^\infty t^{a-1} e^{-t} \,. \tag{C.5b}$$

## C.2 Generalized Fourier transforms

In this section we follow the book by Gel'fand and Shilov [155], who discuss the theory of generalized functions, which are also called distributions, and their Fourier transforms in detail. Here we will focus on the properties that are necessary to understand the origin of the analytic formulas encountered in Secs. 7.2 and 7.3. From a physicist's perspective a generalized function $f$ acts on a set of suitable test functions $\varphi : \mathbb{R} \to \mathbb{C}$ via a scalar product

$$\langle f|\varphi\rangle \in \mathbb{C} \,. \tag{C.6}$$

If $f$ is an ordinary function this bilinear form is identified with the integral

$$\langle f|\varphi\rangle = \int dx\, f^*(x)\varphi(x) \,. \tag{C.7}$$

Possible test functions are the Schwarz functions, which are both analytic and asymptotically decay faster than any polynomial. Therefore, the Schwarz space is a subset of $L^1[\mathbb{R}]$ and the Fourier transform $\hat{\varphi}(k) = \mathcal{FT}_{x\to k}(\varphi(x))$ exists[1]. A standard example for a Schwarz function is given by $\exp(-x^2)$, while the most frequently encountered distribution, which cannot be considered as an ordinary function is the Dirac $\delta$-distribution, which satisfies

$$\langle \delta|\varphi\rangle = \varphi(0) \,. \tag{C.8}$$

Regarding the Fourier transform $\hat{f}$ of a distribution $f$, the following defining identity holds [155]

$$\begin{aligned} \langle f|\varphi\rangle &= \int dx\, f^*(x)\varphi(x) = \int dx f^*(x) \left[\int \frac{dk}{2\pi} \hat{\varphi}(k) e^{ikx}\right] \\ &= \int \frac{dk}{2\pi} \hat{\varphi}(k) \left[\int dx f(x) e^{-ikx}\right]^* = \frac{1}{2\pi}\int dk \hat{f}(k)\hat{\varphi}(k) = \frac{1}{2\pi}\langle \hat{f}|\hat{\varphi}\rangle \,, \end{aligned} \tag{C.9}$$

[1] In this short section we use the sign convention of the Fourier transformation between a one-dimensional position argument $x$ and the conjugated momentum $k$.

which is equivalent to Parseval's theorem for ordinary functions. In particular, we can deduce the Fourier transform of the $\delta$ distribution by imposing the last condition

$$\langle\hat{\delta}|\hat{\varphi}\rangle = \langle\delta|\varphi\rangle = \varphi(0) = \int \frac{dk}{2\pi}\hat{\varphi}(k) = \frac{1}{2\pi}\langle 1|\hat{\varphi}\rangle\,, \tag{C.10}$$

which indeed yields $\hat{\delta} = 1$. Apart from the definition (C.9) one can also show that the rules that apply to Fourier transforms of ordinary functions extend to the more general framework, as is shown in further detail in [155]. For example the Fourier transform of a distribution can be inverted and regarding derivatives we have

$$\begin{aligned} \frac{d}{dk}\mathcal{FT}_{x\to k}(f) &= \mathcal{FT}_{x\to k}(ixf) \\ \mathcal{FT}_{x\to k}(\frac{d}{dx}f) &= (-ik)\mathcal{FT}_{x\to k}(f) \end{aligned} \tag{C.11}$$

The last concept from the theory of generalized functions, that we require for the imbalanced Fermi gas, concerns the regularization of functionals with algebraic divergences. In particular, we consider the case of the unit interval, corresponding to the range of dimensionless imaginary times. Given the generalized function $f(x) = x^\lambda p(x)$, with $\lambda > -1$ and an arbitrary real and analytic function $p(x)$, the scalar product with the test function $\varphi$ can be written as

$$\begin{aligned} \langle x^\lambda p(x)|\varphi(x)\rangle &= \int_0^1 dx\, x^\lambda p(x)\varphi(x) = \\ &= \int_0^1 dx\, x^\lambda \Big( p(x)\varphi(x) - p(0)\varphi(0) - x\frac{d}{dx}p(x)\varphi(x)\big|_{x=0} + \\ &\qquad\qquad \ldots - \frac{x^{(n-1)}}{(n-1)!}\frac{d^{n-1}}{dx^{n-1}}p(x)\varphi(x)\big|_{x=0}\Big) \\ &\quad + \frac{1}{\lambda+1}p(0)\varphi(0) + \frac{1}{\lambda+2}\frac{d}{dx}p(x)\varphi(x)\big|_{x=0} + \ldots \\ &\qquad\qquad \ldots + \frac{1}{(n-1)!(\lambda+n)}\frac{d^{n-1}}{dx^{n-1}}p(x)\varphi(x)\big|_{x=0}\,, \end{aligned} \tag{C.12}$$

for any integer $n \geqslant 0$, which can be seen from repeated partial integration. Since the right-hand side is an analytic function of $\lambda > -1$, we can analytically continue the above result to the extended domain $\lambda \notin \mathbb{Z}_-$ and merely have to exclude the poles at negative integers, as discussed in Ref. [155]. Thus we have created a well-defined interpretation of functionals that do not exist in the ordinary sense of integrals. In practice, one takes as many terms into account on the right-hand side as are required to regularize the expression and the integral exists.

## C.3 Generalized Fourier transforms in the context of the imbalanced Fermi gas

Being equipped with these notions we can go ahead and confirm the form of the various analytical terms that appeared during the construction of the subtraction scheme in Chap. 7. To keep the notation simple, we return to the temperature units from Sec 7.1, where we have set $\beta = 1$. First, we calculate the Fourier transform of $\tau^{-1/2}e^{-A\tau}$ to an arbitrary real frequency $\omega$, which can be set to a Matsubara frequency later on. Here $A \in \mathbb{R}$ represents any combination of the variables $k^2, Q^2$ or $d$. The corresponding mathematical expression can be understood as a function $h$ of the complex variable $A - i\omega$

$$h(A - i\omega) = \mathcal{FT}_{\tau\to\omega}(\tau^{-1/2}e^{-A\tau}) = \int_0^1 d\tau\, \tau^{-1/2}e^{i\omega\tau}e^{-A\tau}\,, \tag{C.13}$$

which is well-defined due to the compact integral and the integrability of $1/\sqrt{\tau}$.

Instead of considering this integral on the real axis, we can equivalently interpret it as a contour integral

$$h(A - i\omega) = (A - i\omega)^{-1/2} \int_{\gamma[A-i\omega]} du\, u^{-1/2}e^{-u}\,, \tag{C.14}$$

where $\gamma[A-i\omega]$ describes the straight line from the origin to $A-i\omega$ in the complex $u$ plane. In particular, for $\omega = 0$ and $A \in \mathbb{R}^+$ the expression reduces to a real integral, which can be identified with the definition (C.1)

$$h(A) = A^{-1/2} \int_0^A u^{-1/2}e^{-u} = \sqrt{\pi}\,\frac{\mathrm{erf}(\sqrt{A})}{\sqrt{A}} \tag{C.15}$$

Since this equation is valid for all $A \in \mathbb{R}^+$ and the expression on the right-hand side is analytic on this set we can analytically continue the function to complex arguments with finite imaginary part $i\omega$, as is explained e.g. in the book by Freitag and Busam [165]. Due to the uniqueness of the analytic continuation, we have determined the Fourier transform of

$$\mathcal{FT}_{\tau\to\omega}(\tau^{-1/2}e^{-A\tau}) = \sqrt{\pi}\,\frac{\mathrm{erf}(\sqrt{A - i\omega})}{\sqrt{A - i\omega}}\,, \tag{C.16}$$

which we have already used for the definitions of $E_0\,(\mathbf{Q}, \Omega_n)$ in eq. (7.20) or in eq. (7.57) for the analytic part of the self-energy. We can draw even further important insights from this result. According to equation (C.11) we can increase the power of $\tau$ in eq. (C.16) by steps of one and obtain the Fourier transform by taking derivatives with respect to $\omega$ on the right-hand side. For example we find

$$\mathcal{FT}_{\tau\to\omega}\left(\tau^{1/2}e^{-A\tau}\right) = -\frac{e^{-(A-i\omega)}}{A - i\omega} - \frac{\sqrt{\pi}}{2}\sqrt{\pi}\frac{\mathrm{erf}(\sqrt{A - i\omega})}{\sqrt{A - i\omega}^3}\,, \tag{C.17}$$

which has been used for the function $E_2(\mathbf{Q}, \Omega_n)$ in eq. (7.20). Moreover, we note that taking higher derivatives or equivalently increasing the power of $\tau$ does not give rise to a faster asymptotics for $|\omega| \to \infty$, since the first term always gives rise to a $1/\omega$-decay. The latter originates form the finite value of the integrand at $\tau = \beta$, which implies a discontinuity, when one extends the bosonic function periodically to the entire imaginary time axis.

Let us finally come to the non-integrable case of $\tau^{-3/2}\exp(-A\tau)$. According to the notion of regularization from eq. (C.12), we have to use the first order subtraction, with $p = \exp(-A\tau)$. In mathematical terms we get

$$\langle \tau^{-3/2} e^{-A\tau} | \varphi(\tau) \rangle = \int_0^1 d\tau \frac{1}{\tau^{3/2}} \left[ e^{-A\tau}\varphi(\tau) - \varphi(0) \right] - 2\varphi(0)\,. \tag{C.18}$$

Partial integration leads to

$$\begin{aligned} \langle \tau^{-3/2} e^{-A\tau} | \varphi(\tau) \rangle &= -2e^{-A}\varphi(1) + 2\int_0^1 d\tau \frac{1}{\sqrt{\tau}} \left[ -Ae^{-A\tau}\varphi(\tau) + e^{-A\tau}\varphi'(\tau) \right] \\ &= -2\langle \delta(\tau-1) e^{-A\tau} | \varphi(\tau) \rangle + 2\langle \tau^{-1/2} e^{-A\tau} | -A\varphi(\tau) + \varphi'(\tau) \rangle\,, \end{aligned} \tag{C.19}$$

where the prime indicates the derivative with respect to $\tau$. Using the defining identity of the Fourier transforms we can write this expression as

$$\begin{aligned} &\langle \tau^{-3/2} e^{-A\tau} | \varphi(\tau) \rangle = \langle \mathcal{FT}_{\tau\to\omega} \left( \tau^{-3/2} e^{-A\tau} \right)(\omega) | \hat{\varphi}(\omega) \rangle \\ &= -2\langle e^{-A} e^{i\omega} | \hat{\varphi}(\omega) \rangle + 2\langle \mathcal{FT}_{\tau\to\omega} \left( \tau^{-1/2} e^{-A\tau} \right) | -A\hat{\varphi}(\omega) + \mathcal{FT}_{\tau\to\omega}[\varphi'(\tau)](\omega) \rangle\,. \end{aligned} \tag{C.20}$$

Assuming a periodic test function $\varphi(\tau + 1) = \varphi(\tau)$ and $\omega = \Omega_n$, which is the relevant case for the particle-particle bubble $\chi$ that carries bosonic arguments, the Fourier transform of the derivative brings an additional factor of $-i\omega$. Since this identity holds true for an arbitrary periodic $\varphi$, we conclude

$$\mathcal{FT}_{\tau\to\Omega_n} \left( \tau^{-3/2} e^{-A\tau} \right) = -2e^{-(A-i\Omega_n)} - 2\sqrt{\pi}\sqrt{A - i\Omega_n}\,\mathrm{erf}\,\sqrt{A - i\Omega_n}\,, \tag{C.21}$$

where we have inserted the previous result (C.16). Indeed, this Fourier transform is of the form of $E_0$, defined in (7.20).

# Appendix D

# Additional explanations and definitions for the Luttinger-Ward computations

## D.1 Computation of $\Gamma_b^{\text{sub}}(\mathbf{x}, \tau)$

We briefly discuss how to obtain the function $\Gamma_b^{\text{sub}}(\mathbf{x}, \tau)$ given in eq. (7.47c). First of all, we note

$$\frac{e^{-(Q^2+d)\tau}}{Q^2+d} = \int_\tau^\infty d\tau' e^{-(Q^2+d)\tau'} \,. \tag{D.1}$$

Computing the $k \to r$ Fourier transform of this expression yields

$$\begin{aligned} &\int_\tau^\infty \frac{e^{-\frac{r^2}{4\tau'-d\tau'}}}{8\pi^{3/2}(\tau')^{3/2}} \\ &\quad = \frac{e^{-\sqrt{d}r}}{8\pi r}\left[1 + \operatorname{erf}\left(\frac{r-2\sqrt{d}\tau}{2\sqrt{\tau}}\right) - e^{2\sqrt{d}x}(1 - \operatorname{erf}\left(\frac{r+2\sqrt{d}\tau}{2\sqrt{\tau}}\right))\right] . \end{aligned} \tag{D.2}$$

The result in the second line can be easily verified by taking the $\tau$ derivative in order to recover the integrand. The definitions required for the error function are given in the beginning of the previous appendix. The remaining terms can be treated analogously, where we have also made use of the identity (C.4) that relates the error function and the incomplete Gamma function on the real axis.

## D.2 Auxiliary functions for the thermodynamic quantities

We list all the auxiliary functions required for the precise computation of $H_2[G]$ in Sec 7.3.4. We begin with the various contributions to the first semi-analytic term defined in eq. (7.81), which does not depend on whether the BCS or BEC code

runs.

$$h^{\text{s-a}}_{(1),11}(\mu_\sigma,\mathbf{k}) = \frac{16\sqrt{\pi}e^{-\frac{1}{2}(k^2+d)}}{(d-k^2+2\mu_\sigma)^{3/2}}\Bigg[2^{3/2}(k^2-\mu_\sigma)\sqrt{d-k^2+2\mu_\sigma} + e^{\frac{1}{2}(d-k^2+2\mu_\sigma)}\sqrt{\pi}\,\mathrm{erf}\left(\sqrt{\frac{1}{2}(d-k^2+2\mu_\sigma)}\right) \cdot\left(-2k^4-4\mu_\sigma^2+d(-1+2k^2-2\mu_\sigma)+k^2(-1+6\mu_\sigma)\right)\Bigg] \tag{D.3a}$$

$$h^{\text{s-a}}_{(1),12}(\mu_\sigma,\mathbf{k}) = \frac{128\pi^2 e^{-\frac{1}{2}(k^2+d)}}{(d-k^2+2\mu_\sigma)^2}\Bigg[2(d+3k^2-2\mu_\sigma)-2e^{\frac{1}{2}(d-k^2+2\mu_\sigma)} \cdot\left(2k^4+k^2(3-6\mu_\sigma)+2\mu_\sigma(-1+2\mu_\sigma)+(1-2k^2+2\mu_\sigma)\right)\Bigg] \tag{D.3b}$$

$$h^{\text{s-a}}_{(1),13}(\mu_\sigma,\mathbf{k}) = \frac{16\sqrt{\pi}e^{-\frac{1}{2}(k^2+d)}}{(d-k^2+2\mu_\sigma)^{5/2}}\Bigg[\frac{5}{\sqrt{2}}(d-k^2+2\mu_\sigma)^{3/2} + 3\sqrt{2}(d+\mu_\sigma)\sqrt{d-k^2+2\mu_\sigma} + \frac{\sqrt{\pi}}{2}e^{\frac{1}{2}(d-k^2+2\mu_\sigma)}\,\mathrm{erf}\left(\sqrt{\frac{1}{2}(d-k^2+2\mu_\sigma)}\right) \cdot\left(-2k^4+d(-1+2k^2-2\mu_\sigma)-4\mu_\sigma(-1+\mu_\sigma)+k^2(-5+6\mu_\sigma)\right)\Bigg] \tag{D.3c}$$

$$h^{\text{s-a}}_{(1),21}(\mu_\sigma,\mathbf{k}) = \frac{32\pi e^{-k^2+\mu_\sigma}(k^2-\mu_\sigma)\,\mathrm{erf}\left(\sqrt{\frac{d+2\mu_\sigma-k^2}{2}}\right))}{\sqrt{d+2\mu_\sigma-k^2}} \tag{D.3d}$$

$$h^{\text{s-a}}_{(1),22}(\mu_\sigma,\mathbf{k}) = \frac{512\pi^2(\mu_\sigma-k^2)(e^{\frac{1}{2}(d+2\mu_\sigma-k^2)}-1)}{k^2-2\mu_\sigma-d}e^{-\frac{1}{2}(d+k^2)} \tag{D.3e}$$

$$h^{\text{s-a}}_{(1),23}(\mu_\sigma,\mathbf{k}) = -\frac{16e^{-\frac{1}{2}(k^2+d)}(k^2-\mu_\sigma)}{(d-k^2+2\mu_\sigma)^{3/2}} \cdot\left[\sqrt{2\pi}\sqrt{d-k^2+2\mu_\sigma}-e^{\frac{1}{2}(d-k^2+2\mu_\sigma)}\pi\,\mathrm{erf}\left(\sqrt{\frac{1}{2}(d-k^2+2\mu_\sigma)}\right)\right] \tag{D.3f}$$

### BCS code

Next, we turn to the second semi-analytic term from eq. (7.82) in the BCS scheme

$$\begin{aligned} h^{\text{s-a}}_{(2),1}(\mu,h,\mathbf{k}) = \frac{-1}{(h-2k^2+\mu)^3}\Big( & -4hk^2+2(2h-\mu)(h+\mu) \\ & - e^{h-2k^2+\mu}\big[ \\ & 8k^6\big((1-h+\mu) \\ & \quad +(h+\mu)(h+3(h-\mu)+\mu+3(\mu^2-h^2)+2(\mu+h)^2)(-1+h-\mu)\big) \\ & 4k^4(-5h+h^2-\mu(3+4\mu)) \\ & 2k^2(-h+\mu+(\mu+h)(-1+9h-5h^2+\mu+5\mu^2))\big]\Big) \end{aligned} \tag{D.4}$$

$$\begin{aligned} h^{\text{s-a}}_{(2),2}(\mu,h,\mathbf{k}) = & -\frac{2(h-k^2+\mu)}{(h-2k^2+\mu)^2} \\ & \cdot\Big(2k^2-2h+e^{(h-2k^2+\mu)}(2h+\mu^2-h^2-2k^2(1+\mu-h))\Big). \end{aligned} \tag{D.5}$$

### BEC code

It remains to give the new definitions in the BEC scheme. First of all, the purely analytical contributions have to be adjusted, which yields

$$\begin{aligned} h_1^{\text{ana}}(\mu_{\bar\sigma},\mathbf{k}) = -\frac{\sqrt{2}}{\pi}\Bigg( & \frac{4(k^2-\mu_\sigma)}{2\mu_\sigma-k^2}e^{-\frac{k^2+d}{2}} \\ & - e^{-k^2+\mu_\sigma} \\ & \frac{\sqrt{2\pi}(2k^4+4\mu_\sigma^2+d(-1+2k^2-2\mu_\sigma)+k^2(1-6\mu_\sigma))\operatorname{erf}\left[\sqrt{d+\mu_\sigma-\frac{k^2}{2}}\right]}{(2\mu_\sigma-k^2)^{3/2}}\Bigg) \end{aligned} \tag{D.6}$$

and

$$h_2^{\text{ana}}(\mu_{\bar\sigma},\mathbf{k}) = \frac{4(\mu_\sigma-k^2)}{\sqrt{\pi}\sqrt{d-k^2+2\mu_\sigma}}\operatorname{erf}\left[\sqrt{\frac{d-k^2+2\mu_\sigma}{2}}\right]. \tag{D.7}$$

Furthermore the auxiliary functions for the second semi-analytic term read

$$h^{\text{s-a}}_{(2),1}(\mu,h,\mathbf{k}) = \frac{e^{-(k^2-\mu+h)}}{4(k^2-\mu)^2}\Big(-4(k^2-\mu)^2-2h(-1+e^{2(k^2-\mu)}-2k^2+2\mu)\Big) \tag{D.8}$$

$$h^{\text{s-a}}_{(2),2}(\mu,h,\mathbf{k}) = \frac{2e^{-h}(h-k^2+\mu)\sinh(k^2-\mu)}{\mu-k^2}\,. \tag{D.9}$$

## D.3 Calculation of the first analytic Parseval term

Finally, we show how one achieves the result for the first analytical Parsival term $P_{10}^{\text{ana}}$ defined in eq. (7.92). We consider the corresponding integral without prefactors, which reads

$$\begin{aligned}&\int_0^1 d\tau\,\frac{e^{d\tau/2}-1}{\tau^{3/2}\sqrt{1-\tau}}\\ &\qquad=\frac{\pi d}{2}e^{d/2}-\frac{d^2}{2}\int_0^1 d\tau\,\sqrt{(1-\tau)\tau}e^{d\tau/2}-\frac{d^2}{2}\int_0^1 d\tau\,\arcsin(\sqrt{\tau})e^{d\tau/2}\,.\end{aligned} \tag{D.10}$$

To obtain the form on the right-hand side we have partially integrated the denominator two times in a row. Next we focus on the first integral, where we shift the integration interval from $\tau\in[0,1]$ to the symmetric choice $\tau\in[-1/2,1/2]$, before rescaling to $\tau\in[-1,1]$. Then we have

$$-\frac{d^2}{2}\int_0^1 d\tau\,\sqrt{(1-\tau)\tau}e^{d\tau/2}=-\frac{d^2}{8}e^{d/4}\int_{-1}^1 d\tau\,\sqrt{1-\tau^2}e^{d\tau/4}=-\frac{\pi d}{2}e^{d/4}I_1(d/4)\,, \tag{D.11}$$

where we have used the definition (9.6.18) for the modified Bessel functions from Ref. [167]. The second integral can be solved by transforming the integration variable via $\sin\theta=\sqrt{\tau}$, which yields

$$-\frac{d^2}{2}\int_0^1 d\tau\,\arcsin(\sqrt{\tau})e^{d\tau/2}=-\frac{d^2}{2}\int_0^{\pi/2}d\theta\sin(2\theta)\theta e^{d/4(1-\cos(2\theta))}\,. \tag{D.12}$$

We rescale the integration interval to $\theta\in[0,\pi]$ and notice the convenient rewriting

$$-\frac{d^2}{8}e^{d/4}\int_0^\pi d\theta\,\theta\frac{d}{d\theta}\left(\frac{4}{d}e^{-d/4\cdot\cos\theta}\right)\,, \tag{D.13}$$

such that one last partial integration results in

$$-\frac{\pi d}{2}e^{d/2}+\frac{d}{4}e^{d/4}\int_0^\pi d\theta\,e^{-d/4\cos\theta}=-\frac{\pi d}{2}e^{d/2}+\pi\frac{d}{2}e^{d/4}I_0(d/4)\,. \tag{D.14}$$

In the last step we have applied defintion (9.6.19) from Ref. [167]. Note that the first term cancels the remaining constant in eq. (D.10) and we obtain

$$\int_0^1 d\tau\,\frac{e^{d\tau/2}-1}{\tau^{3/2}\sqrt{1-\tau}}=\frac{\pi}{2}de^{d/4}\left(I_0(d/4)-I_1(d/4)\right)\,, \tag{D.15}$$

which indeed is of the form of $P_{10}^{\text{ana}}$.

# Appendix E

# List of publications

During the PhD-project the following papers have been published (in chronological order):

- J. Lang, B. Frank and J. C. Halimeh: "Concurrence of dynamical phase transitions at finite temperature in the fully connected transverse-field Ising model", *Phys. Rev. B.* 97, 174401 (2018)

- B. Frank, J. Lang and W. Zwerger "Universal phase diagram and scaling functions of imbalanced Fermi gases", *ArXiv e prints* arXiv:1804.03035
  JETP 127(5), 812 (2018) (special issue in honor of L. P. Piteavskii's 85th birthday)
  For the extended abstract see: *JETP* Vol. 154 (5), 953 (2018)

- J. Lang, B. Frank and J. C. Halimeh: "Dynamical Quantum Phase Transitions: A Geometric Picture", *Phys. Rev. Lett.* 121, 130603 (2018)

- J. Lang and B. Frank: "Fast logarithmic Fourier-Laplace transform of non-integrable functions", *ArXiv e prints* arXiv:1812.09575

# Bibliography


[1] P. Nikolić and S. Sachdev. Renormalization-group fixed points, universal phase diagram, and 1/N expansion for quantum liquids with interactions near the unitarity limit. *Phys. Rev. A*, 75(3):033608–14, 2007.

[2] D. T. Son and M. A. Stephanov. Phase diagram of a cold polarized Fermi gas. *Phys. Rev. A*, 74:013614, 2006.

[3] M. Greiner, C. A. Regal, and D. S. Jin. Emergence of a molecular Bose-Einstein condensate from a Fermi gas. *Nature*, 426:537, 2003.

[4] S. Jochim, M. Bartenstein, A. Altmeyer, G. Hendl, S. Riedl, C. Chin, J. Hecker-Denschlag, and R. Grimm. Bose-Einstein Condensation of Molecules. *Science*, 302:2101, 2003.

[5] M. W. Zwierlein, C. A. Stan, C. H. Schunck, S. M. F. Raupach, S. Gupta, Z. Hadzibabic, and W. Ketterle. Observation of Bose-Einstein Condensation of Molecules. *Phys. Rev. Lett.*, 91:250401, 2003.

[6] H. K. Onnes. The resistance of pure mercury at helium temperatures. *Commun. Phys. Lab. Univ. Leiden*, 12:120, 1911.

[7] J. Bardeen, L. N. Cooper, and J. R. Schrieffer. Theory of Superconductivity. *Phys. Rev.*, 108(5):1175, 1957.

[8] L. N. Cooper. Bound Electron Pairs in a Degenerate Fermi Gas. *Phys. Rev.*, 104:1189–1190, 1956.

[9] J. G. Bednorz and K. A. Müller. Possible high Tc superconductivity in the Ba-La-Cu-O system. *Zeitschrift für Physik B Condensed Matter*, 64(2):189–193, 1986.

[10] A. P. Drozdov, M. I. Eremets, I. A. Troyan, V. Ksenofontov, and S. I. Shylin. Conventional superconductivity at 203 kelvin at high pressures in the sulfur hydride system. *Nature*, 525:73–76, 2015.

[11] A. Schilling, M. Cantoni, J. D. Guo, and H. R. Ott. Superconductivity above 130 K in the Hg-Ba-Ca-Cu-O system. *Nature*, 363:56–58, 1993.

[12] B. Keimer, S. A. Kivelson, M. R. Norman, S. Uchida, and J. Zaanen. From quantum matter to high-temperature superconductivity in copper oxides. *Nature*, 518:179–186, 2015.

[13] D. D. Osheroff, R. C. Richardson, and D. M. Lee. Evidence for a New Phase of Solid $^3$He. *Phys. Rev. Lett.*, 28:885–888, Apr 1972.

[14] D. D. Osheroff, W. J. Gully, R. C. Richardson, and D. M. Lee. New Magnetic Phenomena in Liquid $^3$He below 3 mK. *Phys. Rev. Lett.*, 29:920–923, Oct 1972.

[15] D. Vollhardt and P. Wölfle. *The Superfluid Phases of Helium 3.* Taylor & Francis, London, 1990.

[16] C. Pethick and H. Smith. *Bose-Einstein Condensation in Dilute gases.* Cambridge University Press, 2nd edition, 2008.

[17] L. P. Pitaevskii and S. Stringari. *Bose-Einstein Condensation.* Oxford University Press, Oxford, UK, 2003.

[18] C. Chin, R. Grimm, P. Julienne, and E. Tiesinga. Feshbach Resonances in Ultracold Gases. *Rev. Mod. Phys.*, 82:1225, 2010.

[19] D. M. Eagles. Possible Pairing without Superconductivity at Low Carrier Concentrations in Bulk and Thin-Film Superconducting Semiconductors. *Phys. Rev.*, 186:456–463, 1969.

[20] A. J. Leggett. Cooper Pairing In Spin-Polarized Fermi Systems. *J. Phys. Colloques*, 41:C7–19–C7–26, 1980.

[21] P. Nozières and S. Schmitt-Rink. Bose condensation in an attractive fermion gas: from weak to strong coupling superconductivity. *J. Low Temp. Phys.*, 59(3/4):195–211, 1985.

[22] T.-L. Ho. Universal Thermodynamics of Degenerate Quantum Gases in the Unitarity Limit. *Phys. Rev. Lett.*, 92:090402, 2004.

[23] Y. Nishida and D. T. Son. Nonrelativistic conformal field theories. *Phys. Rev. D*, 76(8):086004, 2007.

[24] A. M. Clogston. Upper Limit for the Critical Field in Hard Superconductors. *Phys. Rev. Lett.*, 9(6):266, 1962.

[25] B. S. Chandrasekhar. A Note on the Maximum Critical Field of High-Field Superconductors. *Appl. Phys. Lett.*, 1:7, 1962.

[26] G. Sarma. On the influence of a uniform exchange field acting on the spins of the conduction electrons in a superconductor. *J. Phys. Chem. Solids*, 24:1029, 1963.

[27] P. Fulde and R. A. Ferrell. Superconductivity in a Strong Spin-Exchange Field. *Phys. Rev.*, 135:A550, 1964.

[28] A. J. Larkin and Y. N. Ovchinnikov. Inhomogeneous state of superconductors. *Zh. Eksp. Teor. Fiz.*, 47:1136, 1964.

[29] A. Lebed, editor. *The Physics of Organic Superconductors and Conductors*. Springer Series in Materials Science. Springer-Verlag Berlin Heidelberg, 1 edition, 2008.

[30] G. B. Partridge, W. Li, R. I. Kamar, Y. Liao, and R. G. Hulet. Pairing and Phase Separation in a Polarized Fermi Gas. *Science*, 311(5760):503–505, 2006.

[31] G. B. Partridge, W. Li, Y. A. Liao, R. G. Hulet, M. Haque, and H. T. C. Stoof. Deformation of a Trapped Fermi Gas with Unequal Spin Populations. *Phys. Rev. Lett.*, 97:190407, 2006.

[32] M. W. Zwierlein, A. Schirotzek, C. H. Schunck, and W. Ketterle. Fermionic Superfluidity with Imbalanced Spin Populations. *Science*, 311:492–496, 2006.

[33] Y. Shin, M. W. Zwierlein, C. H. Schunck, A. Schirotzek, and W. Ketterle. Observation of Phase Separation in a Strongly Interacting Imbalanced Fermi Gas. *Phys. Rev. Lett.*, 97:030401, 2006.

[34] Y. Shin, C. H. Schunck, A. Schirotzek, and W. Ketterle. Phase diagram of a two-component Fermi gas with resonant interactions. *Nature*, 451(7179):689–693, 2008.

[35] Y. Shin. Determination of the equation of state of a polarized Fermi gas at unitarity. *Phys. Rev. A*, 77(4):041603–4, 2008.

[36] N. Navon, S. Nascimbène, F. Chevy, and C. Salomon. The equation of state of a low-temperature Fermi gas with tunable interactions. *Science*, 328:729, 2010.

[37] R. Haussmann, W. Rantner, S. Cerrito, and W. Zwerger. Thermodynamics of the BCS-BEC crossover. *Phys. Rev. A*, 75(2):023610, 2007.

[38] S. Tan. Energetics of a strongly correlated Fermi gas. *Ann. of Phys.*, 323(12):2952–2970, 2008.

[39] S. Tan. Large momentum part of a strongly correlated Fermi gas. *Ann. of Phys.*, 323(12):2971–2986, 2008.

[40] S. Tan. Virial and pressure relations of a strongly correlated Fermi gas. *Ann. of Phys.*, 323(12):2987–2990, 2008.

[41] I. Bloch, J. Dalibard, and W. Zwerger. Many-body physics with ultracold gases. *Rev. Mod. Phys.*, 80(3):885–80, 2008.

[42] W. Zwerger. Strongly interacting Fermi gases. In M. Inguscio, W. Ketterle, S. Stringari, and G. Roati, editors, *Quantum matter at ultralow temperatures, Proceedings of the International School of Physics "Enrico Fermi", Course 191, Varenna, 7-15 July 2014*, pages 63–141. IOS Press, Amsterdam, 2016.

[43] K. Gottfried and T.-M. Yan. *Quantum Mechanics : Fundamentals / K. Gottfried, T.-M. Yan.* 01 2003.

[44] G. F. Gribakin and V. V. Flambaum. Calculation of the scattering length in atomic collisions using the semiclassical approximation. *Phys. Rev. A*, 48:546, 1993.

[45] V. V. Flambaum, G. F. Gribakin, and C. Harabati. Analytical calculation of cold-atom scattering. *Phys. Rev. A*, 59(3):1998, 1999.

[46] H. Feshbach. Unified theory of nuclear reactions. *Annals of Physics*, 5(4):357 – 390, 1958.

[47] U. Fano. Effects of Configuration Interaction on Intensities and Phase Shifts. *Phys. Rev.*, 124:1866–1878, 1961.

[48] E. Tiesinga, B. J. Verhaar, and H. T. C. Stoof. Threshold and resonance phenomena in ultracold ground-state collisions. *Phys. Rev. A*, 47:4114–4122, 1993.

[49] P. O. Fedichev, Y. Kagan, G. V. Shlyapnikov, and J. T. M. Walraven. Influence of Nearly Resonant Light on the Scattering Length in Low-Temperature Atomic Gases. *Phys. Rev. Lett.*, 77:2913–2916, 1996.

[50] M. Theis, G. Thalhammer, K. Winkler, M. Hellwig, G. Ruff, R. Grimm, and J. Hecker Denschlag. Tuning the Scattering Length with an Optically Induced Feshbach Resonance. *Phys. Rev. Lett.*, 93:123001, 2004.

[51] G. Zürn, T. Lompe, A. N. Wenz, S. Jochim, P. S. Julienne, and J. M. Hutson. Precise Characterization of $^6$Li Feshbach Resonances Using Trap-Sideband-Resolved RF Spectroscopy of Weakly Bound Molecules. *Phys. Rev. Lett.*, 110:135301, 2013.

[52] M. Holland, S. J. J. M. F. Kokkelmans, M. L. Chiofalo, and R. Walser. Resonance Superfluidity in a Quantum Degenerate Fermi Gas. *Phys. Rev. Lett.*, 87:120406, 2001.

[53] E. Timmermans, K. Furuya, P. W. Milonni, and A. K. Kerman. Prospect of creating a composite Fermi Bose superfluid. *Phys. Lett. A*, 285:228, 2001.

[54] F. Werner, L. Tarruell, and Y. Castin. Number of closed-channel molecules in the BEC-BCS crossover. *Eur. Phys. J. B*, 68(3):401–415, 2009.

[55] Y. Castin. Basic theory tools for degenerate Fermi gases. In M. Inguscio, W. Ketterle, and C. Salomon, editors, *Proceedings of the International School of Physics "Enrico Fermi" on Ultra-Cold Fermi gases*, pages 1–60. SIF Bologna, Bologna, 2007.

[56] R. Schmidt, S. P. Rath, and W. Zwerger. Efimov physics beyond universality. *Euro. Phys. J. B*, 85:386, 2012.

[57] K. Góral, T. Köhler, S. A. Gardiner, E. Tiesinga, and P. S. Julienne. Adiabatic association of ultracold molecules via magnetic-field tunable interactions. *J. Phys. B*, 37:3457, 2004.

[58] M. J. H. Ku, A. T. Sommer, L. W. Cheuk, and M. W. Zwierlein. Revealing the Superfluid Lambda Transition in the Universal Thermodynamics of a Unitary Fermi Gas. *Science*, 335(6068):563–567, 2012.

[59] S. Nascimbène, N. Navon, K. S. Jiang, F. Chevy, and C. Salomon. Exploring the thermodynamics of a universal Fermi gas. *Nature*, 463:1057–1060, 2010.

[60] D. S. Petrov, C. Salomon, and G. V. Shlyapnikov. Weakly bound dimers of fermionic atoms. *Phys. Rev. Lett.*, 93:090404, 2004.

[61] C. A. Regal, M. Greiner, and D. S. Jin. Lifetime of molecule-atom mixtures near a Feshbach resonance in $^{40}$K. *Phys. Rev. Lett.*, 92:083201, 2004.

[62] T. Bourdel, L. Khaykovich, J. Cubizolles, J. Zhang, F. Chevy, M. Teichmann, L. Tarruell, S. J. J. M. F. Kokkelmans, and C. Salomon. Experimental Study of the BEC-BCS Crossover Region in Lithium-6. *Phys. Rev. Lett.*, 93:050401, 2004.

[63] W. Ketterle and M. W. Zwierlein. Making, probing and understanding ultracold Fermi gases. In M. Inguscio, W. Ketterle, and C. Salomon, editors, *Ultracold Fermi Gases, Proceedings of the International School of Physics "Enrico Fermi", Course CLXIV, Varenna, 20 - 30 June 2006*. IOS Press, Amsterdam, 2008.

[64] D. S. Petrov, C. Salomon, and G. V. Shlyapnikov. Scattering properties of weakly bound dimers of fermionic atoms. *Phys. Rev. A*, 71:012708, 2005.

[65] I. V. Brodsky, M. Y. Kagan, A. V. Klaptsov, R. Combescot, and X. Leyronas. Exact diagrammatic approach for dimer-dimer scattering and bound states of three and four resonantly interacting particles. *Phys. Rev. A*, 73:032724, 2006.

[66] J. Levinsen and V. Gurarie. Properties of strongly paired fermionic condensates. *Phys. Rev. A*, 73:053607, 2006.

[67] A. L. Fetter and J. D. Walecka. *Quantum Theory of Many-Particle Systems.* McGraw-Hill, New York, 1971.

[68] M. M. Parish, F. M. Marchetti, A. Lamacraft, and B. D. Simons. Finite-temperature phase diagram of a polarized Fermi condensate. *Nature Physics*, 3(2):124–128, 2007.

[69] D. E. Sheehy and L. Radzihovsky. BEC-BCS Crossover in "Magnetized" Feshbach-Resonantly Paired Superfluids. *Phys. Rev. Lett.*, 96:060401, Feb 2006.

[70] M. Veillette, D. Sheehy, and L. Radzihovsky. Large-N expansion for unitary superfluid Fermi gases. *Phys. Rev. A*, 75:043614, 2007.

[71] E. Braaten and H. W. Hammer. Universality in few-body systems with large scattering length. *Physics Reports*, 428:259, 2006.

[72] S. Sachdev. *Quantum Phase Transitions, Second Edition.* Cambridge University Press, Cambridge, UK, 2011.

[73] S. Sachdev. The BCS-BEC Crossover and the Unitary Fermi Gas. In W. Zwerger, editor, *The BCS-BEC Crossover and the Unitary Fermi Gas*, chapter Dilute Fermi and Bose Gases. Springer, Berlin, 2012.

[74] W. Zwerger, editor. *The BCS-BEC Crossover and the Unitary Fermi Gas.* Lecture Notes in Physics, Vol. 836, Springer, Berlin, Heidelberg, 2012.

[75] S. Giorgini, L. P. Pitaevskii, and S. Stringari. Theory of ultracold atomic Fermi gases. *Rev. Mod. Phys.*, 80:1215–1274, Oct 2008.

[76] M. Randeria and E. Taylor. Crossover from Bardeen-Cooper-Schrieffer to Bose-Einstein Condensation and the Unitary Fermi Gas. *Annu. Rev. Condens. Matter Phys.*, 5(1):209–232, 2014.

[77] S. J. Blundell and K. M. Blundell. *Concepts in Thermal Physics.* OUP Oxford, 2010.

[78] B. Frank, J. Lang, and W. Zwerger. Universal phase diagram and scaling functions of imbalanced Fermi gases. *JETP*, 127(5):812, 2018.

[79] A. Bulgac and M. Forbes. Zero-temperature thermodynamics of asymmetric Fermi gases at unitarity. *Phys. Rev. A*, 75(3):031605, 2007.

[80] F. Chevy. Universal phase diagram of a strongly interacting Fermi gas with unbalanced spin populations. *Phys. Rev. A*, 74(6):063628, 2006.

[81] D. T. Son. Vanishing Bulk Viscosities and Conformal Invariance of the Unitary Fermi Gas. *Phys. Rev. Lett.*, 98(2):020604–4, 2007.

[82] K. M. O'Hara, S. L. Hemmer, M. E. Gehm, S. R. Granade, and J. E. Thomas. Observation of a Strongly Interacting Degenerate Fermi Gas of Atoms. *Science*, 298:2179, 2002.

[83] M. Bartenstein, A. Altmeyer, S. Riedl, S. Jochim, C. Chin, J. Hecker-Denschlag, and R. Grimm. Crossover from a molecular Bose-Einstein condensate to a degenerate Fermi gas. *Phys. Rev. Lett.*, 92:120401, 2004.

[84] C. A. Regal, M. Greiner, and D. S. Jin. Observation of Resonance Condensation of Fermionic Atom Pairs. *Phys. Rev. Lett.*, 92(4):040403, 2004.

[85] M. W. Zwierlein, C. A. Stan, C. H. Schunck, S. M. F. Raupach, A. J. Kerman, and W. Ketterle. Condensation of Pairs of Fermionic Atoms near a Feshbach Resonance. *Phys. Rev. Lett.*, 92:120403, 2004.

[86] C. Chin, M. Bartenstein, A. Altmeyer, S. Riedl, S. Jochim, J. Hecker-Denschlag, and R. Grimm. Observation of the Pairing Gap in a Strongly Interacting Fermi Gas. *Science*, 305:1128, 2004.

[87] R. Haussmann. Properties of a Fermi liquid at the superfluid transition in the crossover region between BCS superconductivity and Bose-Einstein condensation. *Phys. Rev. B*, 49(18):12975, 1994.

[88] E. Burovski, N. Prokof'ev, B. Svistunov, and M. Troyer. Critical Temperature and Thermodynamics of Attractive Fermions at Unitarity. *Phys. Rev. Lett.*, 96:160402, 2006.

[89] O. Goulko and M. Wingate. Thermodynamics of balanced and slightly spin-imbalanced Fermi gases at unitarity. *Phys. Rev. A*, 82:053621, 2010.

[90] O. Goulko and M. Wingate. Numerical study of the unitary Fermi gas across the superfluid transition. *Phys. Rev. A*, 93:053604, 2016.

[91] Y. Nishida and D. T. Son. Epsilon Expansion for a Fermi Gas at Infinite Scattering Length. *Phys. Rev. Lett.*, 97(5):050403, 2006.

[92] Y. Nishida and D. T. Son. Fermi gas near unitarity around four and two spatial dimensions. *Phys. Rev. A*, 75(6):063617–22, 2007.

[93] K. Van Houcke, F. Werner, E. Kozik, N. V. Prokof'ev, B. V. Svistunov, M. Ku, A. Sommer, L. W. Cheuk, A. Schirotzek, and M. W. Zwierlein. Feynman Diagrams versus Fermi-gas Feynman emulator. *Nature Physics*, 8:366–370, 2012.

[94] H. T. C. Stoof, M. Houbiers, C. A. Sackett, and R. G. Hulet. Superfluidity of Spin-Polarized $^6$Li. *Phys. Rev. Lett.*, 76(1):10, 1996.

[95] L.P. Gor'kov and T.K. Melik-Barkhudarov. Contribution to the Theory of Superfluidity in an Imperfect Fermi Gas. *Zh. Eskp. Theor. Fiz.*, 40:1452, 1961.

[96] H. Heiselberg, C. J. Pethick, H. Smith, and L. Viverit. Influence of Induced Interactions on the Superfluid Transition in Dilute Fermi Gases. *Phys. Rev. Lett.*, 85(12):2418, 2000.

[97] G. Baym, J.-P. Blaizot, M. Holzmann, F. Laloë, and D. Vautherin. The Transition Temperature of the Dilute Interacting Bose Gas. *Phys. Rev. Lett.*, 83(9):1703, 1999.

[98] G. Baym, J.-P. Blaizot, and J. Zinn-Justin. The transition temperature of the dilute interacting Bose gas for N internal states. *Europhys. Lett.*, 49(2):150–155, 2000.

[99] G. Baym, J.-P. Blaizot, M. Holzmann, F. Laloë, and D. Vautherin. Bose-Einstein transition in a dilute interacting gas. *Eur. Phys. J. B*, 24(1):107–124, 2001.

[100] P. Arnold and G. Moore. BEC Transition Temperature of a Dilute Homogeneous Imperfect Bose Gas. *Phys. Rev. Lett.*, 87(12):120401, 2001.

[101] V. A. Kashurnikov, N. V. Prokof'ev, and B. V. Svistunov. Critical Temperature Shift in Weakly Interacting Bose Gas. *Phys. Rev. Lett.*, 87(12):120402, 2001.

[102] P. C. Hohenberg and P. C. Martin. Microscopic theory of superfluid helium. *Annals of Physics*, 34(2):291–359, 1965.

[103] Z. Nussinov and S. Nussinov. Triviality of the BCS-BEC crossover in extended dimensions: Implications for the ground state energy. *Physical Review A*, 74(5):053622–9, 2006.

[104] Y. Nishida and D. T. Son. Unitary Fermi Gas, $\epsilon$ Expansion and Nonrelativistic Conformal Field Theories. In W. Zwerger, editor, *The BCS-BEC Crossover and the Unitary Fermi Gas*, pages 233–275. Lecture Notes in Physics, Vol. 836, Springer, Berlin, Heidelberg, 2012.

[105] P. Arnold, J. E. Drut, and D. T. Son. Next-to-next-to-leading-order epsilon-expansion for a Fermi gas at infinite scattering length. *Phys. Rev. A*, 75(4):043605, 2007.

[106] Y. Nishida. Ground-state energy of the unitary Fermi gas from the epsilon expansion. *Phys. Rev. A*, 79(1):013627–5, 2009.

[107] R. Rossi, T. Ohgoe, K. Van Houcke, and F. Werner. Resummation of diagrammatic series with zero convergence radius for strongly correlated fermions. *ArXiv e-prints*, arXiv1802.07717, 2018.

[108] R. Rossi. *Contributions to unbiased diagrammatic methods for interacting fermions*. Theses, Ecole Normale Supérieure (ENS), 2017.

[109] T. Enss. Quantum critical transport in the unitary Fermi gas. *Phys. Rev. A*, 86:013616, 2012.

[110] D. Saint-James, G. Sarma, and E. J. Thomas. *Type II Superconductivity*. Commonwealth and International Library. Liberal Studies Divi. Elsevier Science & Technology, 1969.

[111] A. I. Buzdin and H. Kachkachi. Generalized Ginzburg-Landau theory for nonuniform FFLO superconductors. *Phys. Lett. A*, 225(4):341 – 348, 1997.

[112] R. Combescot and C. Mora. Transition to Fulde-Ferrel-Larkin-Ovchinnikov phases near the tricritical point: an analytical study. *Eur. Phys. J. B*, 28(4):397–406, 2002.

[113] R. Casalbuoni and G. Nardulli. Inhomogeneous superconductivity in condensed matter and QCD. *Rev. Mod. Phys.*, 76:263–320, 2004.

[114] L. Rammelmüller, A. C. Loheac, J. E. Drut, and J. Braun. Finite-temperature equation of state of polarized fermions at unitarity. *ArXiv e-prints*, arXiv1807.04664, July 2018.

[115] M. Barth and W. Zwerger. Tan relations in one-dimension. *Annals of Physics*, 326:2544, 2011.

[116] F. Werner and Y. Castin. General relations for quantum gases in two and three dimensions: Two-component fermions. *Phys. Rev. A*, 86:013626, 2012.

[117] E. Braaten and L. Platter. Exact Relations for a Strongly Interacting Fermi Gas from the Operator Product Expansion. *Phys. Rev. Lett.*, 100(20):205301, 2008.

[118] E. Braaten. Universal Relations for Fermions with Large Scattering Length. In W. Zwerger, editor, *The BCS-BEC Crossover and the Unitary Fermi Gas*, pages 193–231. Lecture Notes in Physics, Vol. 836, Springer, Berlin, Heidelberg, 2012.

[119] R. Balian, D. Haar, and J. F. Gregg. *From Microphysics to Macrophysics: Methods and Applications of Statistical Physics*. Number Bd. 1 in Theoretical and Mathematical Physics. Springer Berlin Heidelberg, 2006.

[120] E. D. Kuhnle, S. Hoinka, P. Dyke, H. Hu, P. Hannaford, and C. J. Vale. Temperature Dependence of the Universal Contact Parameter in a Unitary Fermi Gas. *Phys. Rev. Lett.*, 106:170402, 2011.

[121] S. Hoinka, M. Lingham, K. Fenech, H. Hu, C. J. Vale, J. E. Drut, and S. Gandolfi. Precise Determination of the Structure Factor and Contact in a Unitary Fermi Gas. *Phys. Rev. Lett.*, 110:055305, 2013.

[122] M. Punk, P. T. Dumitrescu, and W. Zwerger. Polaron-to-molecule transition in a strongly imbalanced Fermi gas. *Phys. Rev. A*, 80(5):053605–10, 2009.

[123] J. Zinn-Justin. *Phase Transitions and Renormalization Group*. Oxford Graduate Texts, Oxford University Press, 2010.

[124] M. W. Zwierlein. Thermodynamics of strongly interacting Fermi gases. In M. Inguscio, W. Ketterle, S. Stringari, and G. Roati, editors, *Quantum matter at ultralow temperatures, Proceedings of the International School of Physics "Enrico Fermi", Course 191, Varenna, 7-15 July 2014*, pages 63–141. IOS Press, Amsterdam, 2016.

[125] N. W. Ashcroft and N. D. Mermin. *Solid State Physics*. Holt, Rinehardt and Winston, New York, 1976.

[126] T.-L. Ho and E. J. Mueller. High Temperature Expansion applied to Fermions near Feshbach Resonance. *Phys. Rev. Lett.*, 92:160404, 2004.

[127] M. Y. Kagan and A. V. Chubukov. Increase in superfluid transition temperature in Polarized Fermi gas with repulsion. *JETP Letters*, 50:483–485, 1989.

[128] K. R. Patton and D. E. Sheehy. Induced $p$-wave superfluidity in strongly interacting imbalanced Fermi gases. *Phys. Rev. A*, 83:051607, 2011.

[129] S. Nascimbène, N. Navon, S. Pilati, F. Chevy, S. Giorgini, A. Georges, and C. Salomon. Fermi-Liquid Behavior of the Normal Phase of a Strongly Interacting Gas of Cold Atoms. *Phys. Rev. Lett.*, 106(21):215303, 2011.

[130] S. Sachdev and K. Yang. Fermi surfaces and Luttinger's theorem in paired fermion systems. *Phys. Rev. B*, 73(17):174504–6, 2006.

[131] N. Prokof'ev and B. Svistunov. Fermi-polaron problem: Diagrammatic Monte Carlo method for divergent sign-alternating series. *Phys. Rev. B*, 77(2):020408, 2008.

[132] C. Lobo, A. Recati, S. Giorgini, and S. Stringari. Normal State of a Polarized Fermi Gas at Unitarity. *Phys. Rev. Lett.*, 97(20):200403–4, 2006.

[133] I. Boettcher, J. Braun, T. K. Herbst, J. M. Pawlowski, D. Roscher, and C. Wetterich. Phase structure of spin-imbalanced unitary Fermi gases. *Phys. Rev. A*, 91:013610, 2015.

[134] D. Roscher, J. Braun, and J. E. Drut. Phase structure of mass- and spin-imbalanced unitary Fermi gases. *Phys. Rev. A*, 91:053611, May 2015.

[135] S. Pilati and S. Giorgini. Phase Separation in a Polarized Fermi Gas at Zero Temperature. *Phys. Rev. Lett.*, 100(3):030401, 2008.

[136] M. Punk and W. Zwerger. Theory of rf-Spectroscopy of Strongly Interacting Fermions. *Phys. Rev. Lett.*, 99(17):170404, 2007.

[137] F. Chevy and C. Mora. Ultra-cold Polarized Fermi Gases. *Reports on Progress in Physics*, 73:112401, 2010.

[138] J. M. Luttinger and J. C. Ward. Ground-State Energy of a Many-Fermion System. II. *Phys. Rev.*, 118:1417–1427, 1960.

[139] A. A. Abrikosov, L. P. Gor'kov, and I. E. Dzyaloshinski. *Methods of Quantum Field Theory in Statistical Physics*. Dover Publications, New York, 1975.

[140] G. Baym and L. P. Kadanoff. Conservation Laws and Correlation Functions. *Phys. Rev.*, 124:287–299, 1961.

[141] D. J. Amit. *Field Theory, the Renormalization Group, and Critical Phenomena*. World Scientific Publishing Co Pte Ltd, 1984.

[142] C. De Dominicis and P. C. Martin. Stationary Entropy Principle and Renormalization in Normal and Superfluid Systems. I. Algebraic Formulation. *Journal of Mathematical Physics*, 5(1):14–30, 1964.

[143] C. De Dominicis and P. C. Martin. Stationary Entropy Principle and Renormalization in Normal and Superfluid Systems. II. Diagrammatic Formulation. *Journal of Mathematical Physics*, 5(1):31–59, 1964.

[144] S. Cerrito. *Thermodynamics of the BCS-BEC crossover*. Thesis, TU München, 2007.

[145] V. M. Galitskii. The Energy Spectrum of a non-ideal Fermi Gas. *JETP*, 34:151–162, 1958.

[146] C. A. R. Sá de Melo, M. Randeria, and J. R. Engelbrecht. Crossover from BCS to Bose superconductivity: Transition temperature and time-dependent Ginzburg-Landau theory. *Phys. Rev. Lett.*, 71:3202–3205, 1993.

[147] R. B. Diener, R. Sensarma, and M. Randeria. Quantum Fluctuations in the Superfluid State of the BCS-BEC Crossover. *Phys. Rev. A*, 77:023626, 2008.

[148] R. Combescot, A. Recati, C. Lobo, and F. Chevy. Normal State of Highly Polarized Fermi Gases: Simple Many-Body Approaches. *Phys. Rev. Lett.*, 98:180402, 2007.

[149] R. Haussmann. Crossover from BCS superconductivity to Bose-Einstein condensation: a self-consistent theory. *Z. Phys. B*, 91:291, 1993.

[150] R. Haussmann. *Self-consistent Quantum Field Theory and Bosonization for Strongly Correlated Electron Systems.* Lecture Notes in Physics. Springer Verlag, Berlin, 1999.

[151] R. Haussmann, M. Punk, and W. Zwerger. Spectral functions and rf response of ultracold fermionic atoms. *Physical Review A*, 80(6):063612, 2009.

[152] D. J. Thouless. Perturbation theory in statistical mechanics and the theory of superconductivity. *Ann. of Phys.*, 10(4):553 – 588, 1960.

[153] K. Van Houcke, F. Werner, N. Prokof'ev, and B. Svistunov. Bold diagrammatic Monte Carlo for the resonant Fermi gas. *ArXiv e-prints*, arXiv1305.3901, 2013.

[154] A. Altland and B. Simons. *Condensed Matter Field Theory.* Cambridge University Press, 2010.

[155] I.M. Gel'fand and G.E. Shilov. *Generalized Functions, Volume 1:.* AMS Chelsea Publishing. American Mathematical Society, 2016.

[156] J. Cooley and J. Tukey. An Algorithm for the Machine Calculation of Complex Fourier Series. *Mathematics of Computation*, 19(90):297–301, 1965.

[157] W. H. Press and W. T. Vetterling. *Numerical Recipes in C: The Art of Scientific Computing.* Number bk. 4. Cambridge University Press, 1992.

[158] G. V. Haines and Alan G. Jones. Logarithmic Fourier transformation. *Geophysical Journal International*, 92(1):171–178, 1988.

[159] W. Steffen, A. Patkowski, H. Gläser, G. Meier, and E. W. Fischer. Depolarized-light-scattering study of orthoterphenyl and comparison with the mode-coupling model. *Phys. Rev. E*, 49:2992–3002, Apr 1994.

[160] J. Lang and B. Frank. Fast logarithmic Fourier-Laplace transform of nonintegrable functions. *ArXiv e-prints*, arXiv1812.09575.

[161] W. Götze and R. Haussmann. Further phase transition scenarios described by the self consistent current relaxation theory. *Z. Phys. B: Condens. Matter*, 72:403.

[162] J. Spouge. Computation of the Gamma, Digamma, and Trigamma Functions. *SIAM Journal on Numerical Analysis*, 31(3):931–944, 1994.

[163] T. W. Körner. *Fourier Analysis*. Cambridge University Press, 1989.

[164] E. C. Titchmarsh. *Introduction to the Theory of Fourier Integrals*. Clarendon Press, 1975.

[165] E. Freitag and R. Busam. *Complex Analysis*. Lecture notes in mathematics. Springer, 2005.

[166] J. H. Ahlberg, E. N. Nilson, J. L. Walsh, and R. Bellman. *The Theory of Splines and Their Applications: Mathematics in Science and Engineering: A Series of Monographs and Textbooks*. Number Bd. 38. Elsevier Science, 2016.

[167] M. Abramowitz and I. A. Stegun. *Handbook of Mathematical Functions: With Formulas, Graphs, and Mathematical Tables*. Applied mathematics series. Dover Publications, 1965.

[168] P. Zhang. Quantum Chaos for the Unitary Fermi Gas from the Generalized Boltzmann Equations. *ArXiv e-prints*, arXiv1809.01303, 2018.

[169] H. Smith and H. H. Jensen. *Transport Phenomena*. Oxford University Press, New York, 1989.

[170] T. Enss and J. H. Thywissen. Universal Spin Transport and Quantum Bounds for Unitary Fermions. *ArXiv e-prints*, arXiv1805.05354, 2018.

[171] D. Forster. *Hydrodynamic Fluctuations, Broken Symmetry and Correlation Functions*. Frontiers in Physics. W. A. Benjamin, Advanced Book Program, Reading, Massachusetts, 1975.

[172] E. Elliott, J. A. Joseph, and J. E. Thomas. Observation of Conformal Symmetry Breaking and Scale Invariance in Expanding Fermi Gases. *Phys. Rev. Lett.*, 112:040405, 2014.

[173] T. Enss, R. Haussmann, and W. Zwerger. Viscosity and scale invariance in the unitary Fermi gas. *Ann. Phys. (NY)*, 326(3):770–796, 2011.

[174] W. D. Goldberger and Z. U. Khandker. Viscosity sum rules at large scattering lengths. *Phys. Rev. A*, 85:013624, 2012.

[175] G. M. Bruun and H. Smith. Shear viscosity and damping for a Fermi gas in the unitarity limit. *Phys. Rev. A*, 75(4):043612, 2007.

[176] R. Balian. *From Microphysics to Macrophysics, Vol. II*. Spinger Berlin, 1992.

[177] J. A. Joseph, E. Elliott, and J. E. Thomas. Shear Viscosity of a Unitary Fermi Gas Near the Superfluid Phase Transition. *Phys. Rev. Lett.*, 115:020401, 2015.

[178] L. D. Landau and I. M. Khalatnikov. *Sov. Phys. JETP*, 19:637, 1949.

[179] G. Rupak and T. Schäfer. Shear viscosity of a superfluid Fermi gas in the unitarity limit. *Phys. Rev. A*, 76(5):053607–9, 2007.

[180] T. Schäfer and D. Teaney. Nearly perfect fluidity: from cold atomic gases to hot quark gluon plasmas. *Rep. Prog. Phys.*, 72:126001, 2009.

[181] G. Policastro, D. T. Son, and A. O. Starinets. Shear Viscosity of Strongly Coupled $N = 4$ Supersymmetric Yang-Mills Plasma. *Phys. Rev. Lett.*, 87:081601, 2001.

[182] P. K. Kovtun, D. T. Son, and A. O. Starinets. Viscosity in Strongly Interacting Quantum Field Theories from Black Hole Physics. *Phys. Rev. Lett.*, 94(11):111601, 2005.

[183] M. Ammon and J. Erdmenger. *Gauge/Gravity Duality*. Cambridge University Press, 2015.

[184] J. Jäckle. *Einführung in die Transporttheorie*. Vieweg, Braunschweig, 1978.

[185] M. Braby, J. Chao, and T. Schäfer. Thermal conductivity and sound attenuation in dilute atomic Fermi gases. *Phys. Rev. A*, 82:033619, 2010.

[186] M. Rangamani, S. F. Ross, D. T. Son, and E. G. Thompson. Conformal non-relativistic hydrodynamics from gravity. *JHEP*, 2009(01):075, 2009.

[187] M. Le Bellac. *Thermal Field Theory*. Cambridge Monographs on Mathematical Physics. Cambridge University Press, 1996.

# Acknowledgments

Zuallererst möchte ich mich bei Prof. Zwerger für die Betreuung meiner Promotion bedanken. Zum einen hat mich seine Themenstellung zu den ultrakalten Fermigasen sehr fasziniert, da sie theoretisch und experimentell relevant ist. Weiterhin sind zur Bearbeitung sowohl analytische als auch numerische Methoden notwendig, wobei ich in beiden Bereichen viel lernen konnte. Außerdem möchte ich Danke sagen für die Geduld, da die Projekte und auch das Zusammenschreiben der Dissertation immer länger gedauert haben als geplant. Abgesehen von den physikalischen Inhalten war die Arbeitsatmospäre an seinem Lehrstuhl T34 immer sehr angenehm und alle Anliegen konnten persönlich, schnell und unkompliziert geklärt werden.

Zum letzten Punkt hat natürlich auch die gesamte Arbeitsgruppe beigetragen, an die ebenfalls ein großes Dankeschön geht. Insbesondere die wissenschaftlichen und nicht-wissenschaftlichen Diskussionen mit Daniela Neufang, Marcus Barth, Christian Langmack, Félix Rosé, Johannes Oberreuther, Simon Weidinger und Johannes Lang werden mir immer in guter Erinnerung an meine Doktorandenzeit bleiben.

Ein besonders herzliches Dankeschön geht an Johannes Lang, mit dem ich mir ein Büro geteilt habe. Aus unserer Zusammenarbeit sind viele der wissenschaftlichen Ergebnisse in dieser Arbeit entstanden. Darüberhinaus hat sich eine Freundschaft entwickelt, die über Physik hinausgeht und auch Umzüge und Junggesellenabschiede umfasst. Außerdem können wir auch mal gemeinsam Blödsinn machen und einen "Wer darf die Bürotür aufschließen"-Wettbewerb zu führen. Danke dafür!

Vielen Dank auch an Jad Halimeh für die erfolgreiche Kooperation gemeinsam mit Johannes Lang zu Loschmidt-Echos und dynamischen Phasenübergängen. Wir sehen uns bald in Dresden.

Vielen Dank auch an Matthias Punk für die Begutachtung meiner Dissertation.

Meiner Familie, besonders meinen Eltern und Schwiegereltern, möchte ich ebenfalls Danke sagen für die Unterstüzung, Ratschläge und die Aufmunterung in allen Lebenslagen und gerade wenn es mit der Doktorarbeit etwas langsamer voranging. Es ist gut zu wissen, dass man sich immer auf euch verlassen kann.

Der letzte Dank geht an meine Frau Manuela, deren Geduldsfaden durch die vielen Stunden und Nachtschichten mit der Dissertation auf eine harte Probe gestellt worden, aber nie gerissen ist. Danke, dass du Teil meines Lebens geworden bist, für mich da bist, wenn ich dich brauche. Ich freue mich auf die kommenden Herausforderungen, die wir gemeinsam meistern werden, auch wenn es wieder schlaflose Nächte geben wird.